中国计量大学新增博士研究生指导教师申请表

申请一级学科：　　　仪器科学与技术

　　除表中另有说明外，所填报各项与时间相关的内容均截至 2021 年 12 月 30 日，"近五年"的统计时间为 2017 年 1 月 1 日至 2021 年 12 月 30 日。

一、基本情况

姓名	秦来顺	性别	男	出生年月	1978.10
高层次人才和申报新增博士点时学术带头人、学术骨干				联系方式	13221413235
最高学位及授予单位	博士，中科院上海硅酸盐研究所				
最高学历，毕业时间，毕业单位	博士，2006.07，中科院上海硅酸盐研究所				
职称，获得职称年月	教授，2013.12				
目前所在学院和一级学科	材料与化学学院，材料科学与工程学科				
主要研究方向	辐射探测材料与器件，光电材料与传感，材料评价与标准				

主要学习和工作经历，从研究生开始

自何年月	至何年月	单位	学习或工作
2001.09	2006.07	中科院上海硅酸盐研究所	硕士博士研究生
2006.08	2013.12	中国计量学院理学院、材料学院	讲师、副教授
2014.01	至今	中国计量大学材料学院	教授

二、指导研究生情况

序号	年级	研究生姓名（层次）	本人担任的主要工作	研究生培养单位	学院审核人
1	2017 级	周佳波（硕士生）	第一指导教师	中国计量大学	
2	2018 级	宁佩（硕士生）	第一指导教师	中国计量大学	
3	2019 级	何君雨、李雯（硕士生）	第一指导教师	中国计量大学	

4	2020 级	向鹏、俞晨斌（硕士生）	第一指导教师	中国计量大学	
5	2021 级	舒昶、郑中秋（硕士生）	第一指导教师	中国计量大学	

三、近五年立项主持的代表性科研项目

序号	项目名称及编号	项目来源（项目类型）	起止时间	经费（万元）	本人排名/总人数	学院审核人
1	双读出闪烁晶体 $Cs_2LiLaBr_6:Ce$ 的结晶行为与高光学质量单晶生长（编号：51972291）	国家自然科学基金（面上项目）	2020.01—2023.12	60	1/6	
2	面向成像诊疗技术的高性能射线探测材料与元件产业化关键技术（编号：2022C01046）	浙江省"尖兵计划"	2022.01—2024.12	130/350（财政）/1000（总）	4/6	
3	用于中子/伽马双读出的大尺寸、高质量 CLLB:Ce 闪烁晶体的研制（编号：ICNM-2021-ZH-13）	国防科技工业核材料技术创新中心（重点项目）	2021.01—2022.12	50	1/6	
4	红外光响应的多元金属氧化物光催化制氢材料的构建（LY19E02003）	浙江省自然科学基金（一般项目）	2019.01—2021.12	10	1/5	
5	材料计量与标准化特色创新人才的培养，jg20190197	浙江省高等教育"十三五"第二批教学改革研究项目	2020.01—2021.12	2	1/5	
6	重稀土扩散 NdFeB 基体研究（编号：H221070）	科技合作项目（横向）	2022.03—2023.03	100	1/5	
近五年到账总经费：					（万元）	

四、近五年发表的代表性学术论文

序号	论文名称	刊物名称	发表时间	SCI（中科院分区）、SSCI 收录	本人排名/总人数	学院审核人
1	2D Heterostructure of Amorphous CoFeB Coating Black Phosphorus Nanosheets with Optimal Oxygen Intermediate Absorption for Improved Electrocatalytic Water Oxidation	ACS Nano	2021, 15, 12418-12428	SCI（中科院 1 区）	通讯作者	
2	Tunable electronic band structure, luminescence properties and thermostability of $(Gd_{1-x}La_x)_2Si_2O_7:Ce$ scintillator by adjusting La/Gd ratio	Journal of Rare Earths	2021，39：657-665	SCI（中科院 2 区）	通讯作者	

序号						
3	Hydrogenated ZnIn$_2$S$_4$ microspheres: boosting photocatalytic hydrogen evolution by sulfur vacancy engineering and mechanism insight	Physical Chemistry Chemical Physics	2019, 21(45): 25484-25494	SCI（中科院2区）	通讯作者	
4	Facile synthesis of Er-doped BiFeO$_3$ nanoparticles for enhanced visible light photocatalytic degradation of tetracycline hydrochloride	Journal of Sol-Gel Science and Technology	2019, 90(3): 535-546	SCI（中科院3区）	通讯作者	
5	Photoassisted Electrodeposition of Cobalt-Phosphate Cocatalyst on BiFeO$_3$ Thin Film Photoanode for Highly Efficient Photoelectrochemical Performances of Water Oxidation	Journal of the Electrochemical Society	2019,166(8): D308-D314	SCI（中科院2区）	通讯作者	
6	Decoration of WS$_2$ as an effective noble-metal free cocatalyst on ZnIn$_2$S$_4$ for enhanced visible light photocatalytic hydrogen evolution	International Journal of Hydrogen Energy	2018, 43, 18261-18269	SCI（中科院2区）	通讯作者	
7	Facile synthesis of Sm-doped BiFeO$_3$ nanoparticles for enhanced visible light photocatalytic performance	Materials Science and Engineering B	2017，220：1-12	SCI（中科院2区）	通讯作者	
8	Defective BiFeO$_3$ with surface oxygen vacancies: Facile synthesis and mechanism insight into photocatalytic performance	Solar Energy Materials and Solar Cells	2017，171：24–32	SCI（中科院2区）	通讯作者	

五、近五年出版的学术专著

序号	专著名称	出版社名称，时间	本人排名/总人数	学院审核人
1	标准样品概论	中国标准出版社，2021.11	编著者之一(1/33)	
2				
3				

六、近五年获省部级及以上科研成果奖

序号	获奖名称	授予单位，获奖等级，时间	本人排名/总人数	学院审核人
1				
2				

七、近五年授权发明专利

序号	专利名称 （国别及专利号）	授权 时间	专利有效 期止	技术转让 到账经费 （万元）	本人排名/ 总人数	学院 审核人
1						
2						
3						
4						
5						
专利技术转让到校总经费：				（万元）		

八、近五年主持制定并颁布实施的规程/规范/标准

序号	成果名称（编号）	发布单位	发布时间及类别	本人排名/ 总人数）	学院 审核人
1					
2					
3					

九、近五年获正省（部）级及以上领导肯定性批示

序号	成果名称	批示领导及职务	批示时间	本人排名/ 作者人数	学院 审核人
1					
2					

与学位授权点学科方向契合的成果（至少填一项）	第＿＿二＿＿项，第_1、3_条 第＿＿＿＿项，第＿＿＿＿条 第＿＿＿＿项，第＿＿＿＿条	第＿＿＿＿项，第＿＿＿＿条 第＿＿＿＿项，第＿＿＿＿条 第＿＿＿＿项，第＿＿＿＿条

本人以上填写内容真实性、准确性无误，工作中未有学术不端行为，自觉践行"四个统一"，做学生成长成才的指导者和引路人。

申请人签名：　　　　　　　　　　年　　月　　日

申请人所在学院、党委审核推荐意见（明确填写是否符合博士生导师任职资格条件，是否同意推荐）：

院长签名：　　　　（学院盖章）　　　　党委书记签名：　　　　（党委盖章）
　　　　年　　月　　日　　　　　　　　　　　　　　　　年　　月　　日

学科委员会意见	应到委员人数	实到委员人数	同意票数	反对票数	弃权票数
	是否推荐：是□　否□　　委员会主任签名：　　　　年　　月　　日				

研究生院复核意见：

（研究生院盖章）

分管领导签名：　　　　　　年　　月　　日

校外专家评审结果	评审专家数	强烈推荐	推荐	一般推荐	不推荐

校学科建设委员会意见	应到委员人数	实到委员人数	同意票数	反对票数	弃权票数
	是否通过：是□　否□　　委员会主任签名：　　　　年　　月　　日				

学校意见：

（签章）

年　　月　　日

佐 证 材 料

一、近五年立项主持的代表性科研项目，包括：合同首页、参加人员页、经费页、签名盖章页。

二、近五年发表的代表性学术论文，包括：检索证明、封面、目录、正文首页、刊号。

三、近五年出版的学术专著，包括：封面、目录、相关内容。

四、近五年获省部级及以上科研成果奖：获奖证书。

五、近五年授权发明专利：专利证书。

六、近五年主持制定并颁布实施的规程/规范/标准：相关材料全文。

七、近五年获省（部）级正职以上领导肯定性批示：相关材料全文。

八、学校引育的高层次人才：相关证明材料。

ARTICLE

2D Heterostructure of Amorphous CoFeB Coating Black Phosphorus Nanosheets with Optimal Oxygen Intermediate Absorption for Improved Electrocatalytic Water Oxidation

Huayu Chen, Junxiang Chen, Pei Ning, Xin Chen, Junhui Liang, Xin Yao, Da Chen,* Laishun Qin,* Yuexiang Huang, and Zhenhai Wen*

Cite This: *ACS Nano* 2021, 15, 12418−12428

Read Online

ACCESS | 📊 Metrics & More | 📖 Article Recommendations | 🄪 Supporting Information

ABSTRACT: The oxygen evolution reaction (OER) plays a paramount role in a variety of electrochemical energy conversion devices, and the exploration of highly active, stable, and low-cost electrocatalysts is one of the most important topics in this field. The exfoliated black phosphorus (EBP) nanosheet with a two-dimensional (2D) layered structure has high carrier mobility but is limited by excessive oxygen-containing intermediate absorption and fast deterioration in air. We here report the fabrication of nanohybrids of amorphous CoFeB nanosheets on EBP nanosheets (EBP/CoFeB). The 2D/2D heterostructure, thanks to the electronic interactions and oxygen affinity difference between EBP and CoFeB nanosheets, is capable of balancing the oxygen-containing intermediate absorption to an optimal status for facilitating the OER process. While the crystalline EBP contributes to the improved conductivity, the amorphous coating protects EBP and thus ensures the catalytic stability. The EBP/CoFeB electrocatalyst shows excellent OER performance with an ultralow overpotential of 227 mV at 10 mA cm^{-2} with an ultrasmall Tafel slope of 36.7 mV dec^{-1} with excellent stability. This study may inspire more researches to develop heterostructured nanohybrid electrocatalysts for a diversity of electrochemical reactions.

KEYWORDS: 2D heterostructure, amorphous CoFeB, black phosphorus nanosheets, electrocatalyst, oxygen evolution reaction
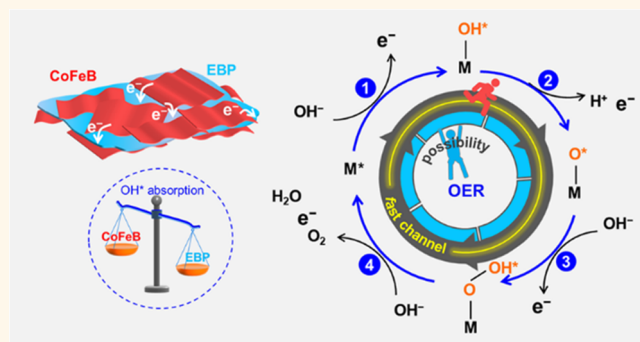
The development of renewable energy can greatly reduce our reliance on fossil fuels and address the emerging environmental issues inevitably arising from the development of industry.[1,2] In recent years, tremendous works have been devoted to technologies of hydrogen energy[3] and carbon neutralization.[4,5] Electrocatalytic H$_2$ generation is one of the most efficient and ecofriendly routes to achieve this goal especially by synergy with renewable solar energy or wind.[6−8] Nevertheless, the anodic oxygen evolution reaction (OER) is sluggish in kinetics and thermodynamically has a high energy barrier even when using benchmarked precious Ir- or Ru-based electrocatalysts.[9,10] Therefore, the development of nonprecious electrocatalysts for OER with high activity and stability is urgently desired.

Black phosphorus (BP) nanosheets, as a recently developed two-dimensional (2D) material, feature the common merits of a 2D material (*e.g.*, high specific surface area to expose active

sites)[11,12] and possess high carrier mobility,[13,14] which is conducive to OER electrocatalysis. Unfortunately, BP nanosheets likely interact with oxygen-containing species too strongly[15,16] and suffer from poor OER intrinsic activity and instability due to defects on the edge and surface.[17] It has been recently reported that the exfoliated BP (EBP) nanosheet with a 2D layered structure has a high carrier mobility favorable for OER electrocatalysis but suffers from too strong absorption of hydroxyl groups[18] and fast deterioration in air.[19] In this context, it is essential to modulate the oxygen-containing
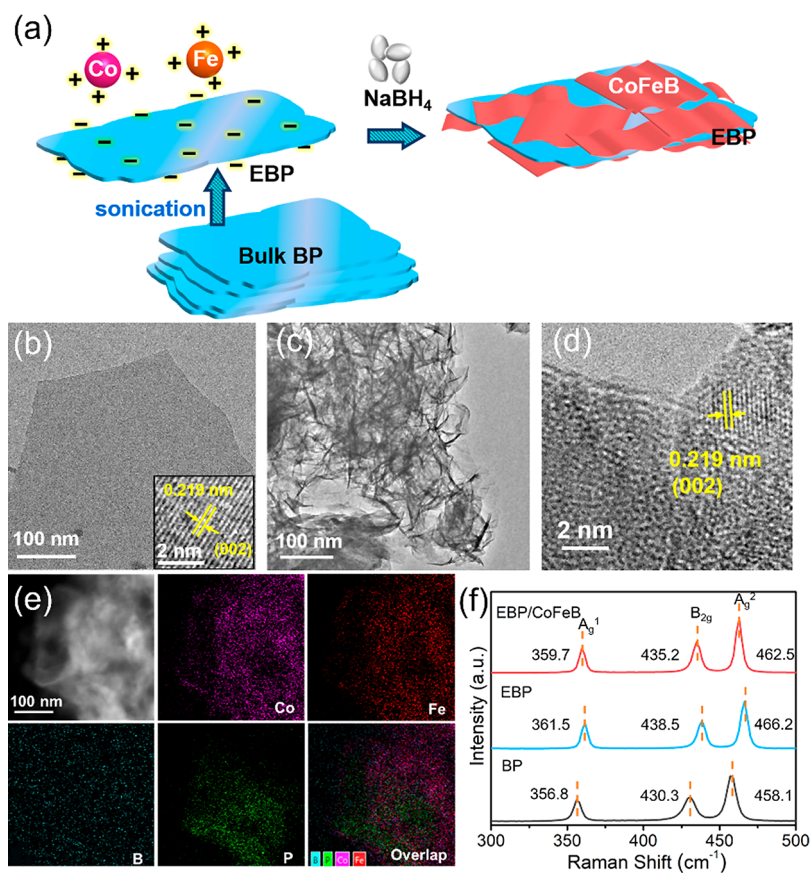
Figure 1. (a) Schematic diagram of the synthesis of the EBP/CoFeB sample. (b) TEM image of EBP nanosheets (inset: HRTEM image). (c, d) TEM and HRTEM images of the EBP/CoFeB sample. (e) HAADF-STEM image and STEM-EDX mapping of Co, Fe, B, and P of the EBP/CoFeB sample. (f) Raman scattering spectra of the bulk BP, EBP, and EBP/CoFeB samples.

intermediate absorption of EBP and protect the EBP surface by coating it with an air-stable material with weaker absorption capacity. Previous works generally focused on suppressing the deterioration of BP *via* constructing a heterostructure of BP and a metal-based material. Researchers designed nickel nitride (Ni₃N)-BP,[20] Ni₂P nanocrystals-BP,[21] Co₃O₄ nanoparticles/BP (Co₃O₄@BP),[22] and BP/Co₂P heterostructure,[23] most of which were of 0D/2D structure, devoted to passivating the defects of BP as well as regulating the conductivity and charge transfer.[24−26] In these cases, however, the modulation of oxygen-containing intermediate absorption is usually not the major concern, and the overpotentials for OER among nonprecious materials are still large.

Given that the main factor inducing phosphorene degradation is oxygen in air,[27,28] the 2D/2D structure may be more effective for blocking the few-layer BP nanosheet from oxygen as well as facilitating electron transfer at the interface. We therefore strive to find 2D metal-based materials with weaker oxygen-containing intermediate absorption capacity that can perfectly match BP. Recently, amorphous transition metal boride (TMB) nanosheets have been reported to possess high OER activity, as the boron can weaken the metal−metal bonds to further diminish the energy barrier for formation of OOH species. However, the oxygen intermediate adsorption of TMB tends to be strengthened and thus favorable for further improving the performance.[29,30] By developing TMB hybrids with BP, the phosphorus, with high electronegativity and O affinity,[15,31] may innovate the electronic structure of TMB and strengthen the oxygen-containing intermediate absorption to

an optimal condition. Besides, the metal-based material in amorphous phase often possesses abundant active sites; however, its poor conductivity unfavorably maximizes the electrocatalytic activity.[31−33]

Bearing these points in mind, in this work, amorphous CoFeB nanosheets were directly grown on the liquid EBP nanosheets to form a 2D/2D nanosheet hybrid electrocatalyst for OER. Such a heterostructure could achieve the following desired effects. First, the heterostructure would optimize the oxygen-containing intermediate absorption since the absorption capacity is relatively strong for EBP but rather weak for CoFeB nanosheets. The first-principal analysis verifies that amorphous CoFeB can generate a "fast channel" (with no exothermic step) but is limited by its low probability, while the EBP offers extra active sites whose affinity to OH* fulfills the demands of the "fast channel". Second, the EBP (crystalline) and CoFeB (amorphous) hybrid displays the superiorities of quick charge carrier transfer[34] and abundant reactive sites, respectively. Third, the CoFeB nanosheets protect the EBP from degradation in the ambient environment to promote the electrochemical stability. Hence the as-prepared EBP/CoFeB heterostructure shows excellent catalytic performance for OER with a small overpotential of 227 mV at 10 mA cm⁻², fast kinetics with a small Tafel slope of 36.7 mV dec⁻¹, and long-term durability.

RESULTS AND DISCUSSION

The synthesis of a 2D/2D EBP/CoFeB catalyst was implemented by three steps under a N₂ atmosphere (Figure
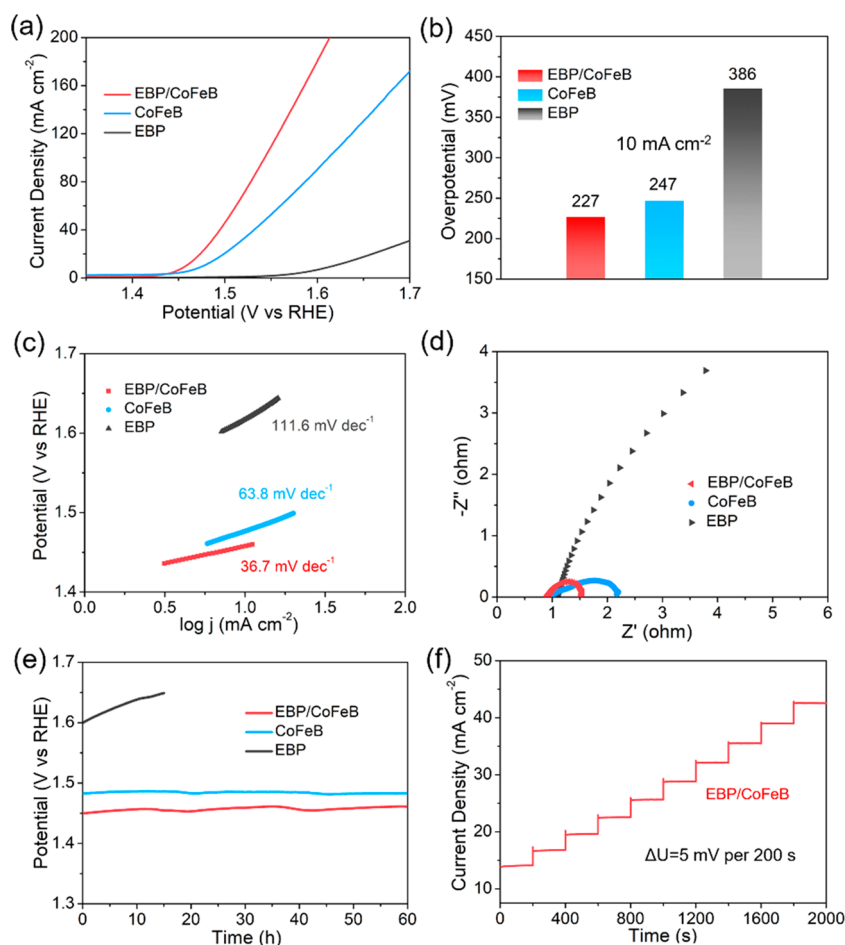
Figure 2. (a) OER curves of samples with a scan rate of 5 mV s^{-1} (without *iR* compensation). (b) Overpotentials for OER at a current density of 10 mA cm^{-2}. (c) Tafel plots and (d) EIS measurement results of all the samples. (e) Chronopotentiometry tests for OER at a current density of 10 mA cm^{-2}. (f) Multipotential process of the EBP/CoFeB. The potential starts at 1.460 V and ends at 1.505 V with an increment of 5 mV per 200 s. All the measurements were operated in 1 M KOH solution.

1a). First, the EBP (Figure S1) was obtained from bulk phosphorus by a liquid exfoliation method; then metal ions (Co^{2+}, Fe^{2+}) were absorbed on the surface of the EBP by electrostatic interaction, as P has lone-pair electrons;[35] finally CoFeB nanosheets were grown on the EBP *via* chemical reduction triggered by NaBH$_4$. Transmission electron microscopy (TEM) (Figure 1b) and high-resolution TEM (HRTEM) (inset of Figure 1b) images show that the EBP sample exhibits 2D nanosheets with an interplanar distance of 0.219 nm, corresponding well to the (002) plane of black phosphorus. The atomic force microscopy (AFM) image (Figure S2) of EBP nanosheets further reveals the thickness is below 10 nm. The pristine CoFeB sample exhibits the morphology of wrinkled nanosheets (Figure S3a) without lattice fringes in the HRTEM image (Figure S3b), which implies an amorphous characteristic of CoFeB. The AFM image of CoFeB nanosheets is also shown in Figure S4, and the line scan of the height is consistent with a wrinkled surface morphology. The TEM image of the EBP/CoFeB composite is also displayed in Figure 1c. The HRTEM (Figure 1d) image shows the amorphous structure is overlapped with clear lattice fringes, indicating that the amorphous CoFeB nanosheets are grown on the EBP nanosheets to form 2D/2D nanosheets. ICP-OES analysis (Table S1) reveals that the EBP/CoFeB comprises Co (39.42 wt %), Fe (17.53 wt %), B (2.17 wt %), and P (17.92 wt %),

the rest being mostly oxygen and carbon, which corresponds to a P to Co atomic ratio of 1:1.16.

X-ray diffraction (XRD) patterns also prove that the CoFeB nanosheets are amorphous, as no obvious diffraction peak appears (Figure S5).[36] All the diffraction peaks of EBP/CoFeB can be indexed to the BP (JCPDS 73-1358).[23] The peaks located at 16.9°, 26.5°, 34.2°, 35.0°, 41.1°, and 52.4° are assigned to the (020), (021), (040), (111), (002), and (060) planes of BP, respectively. The weak diffraction peak of BP may be ascribed to the few-layer structure. Element mapping analysis reveals the uniform dispersion of Co, Fe, B, and P elements (Figure 1e) and highlights that the EBP nanosheet is covered by the CoFeB nanosheet in the EBP/CoFeB. The variations in the Raman spectra from the bulk BP to the EBP/CoFeB heterostructure are shown in Figure 1f; three characteristic peaks of bulk BP centered at 356.8, 430.3, and 458.1 cm^{-1} correspond to A$_g^1$, B$_{2g}$, and A$_g^2$ vibrational modes,[37] where the A$_g^1$ represents the out-of-plane vibration and the latter two represent the in-plane vibrations.[23] After exfoliation, three characteristic Raman peaks exhibit an obvious red-shift, indicating the reduction of thickness and formation of few-layer EBP nanosheets. The EBP/CoFeB shows a blue-shift in the peaks' position due to the interaction between EBP and CoFeB nanosheets. It should be noticed that the in-plane vibrations (B$_{2g}$ and A$_g^2$) have a more obvious blue-shift (about
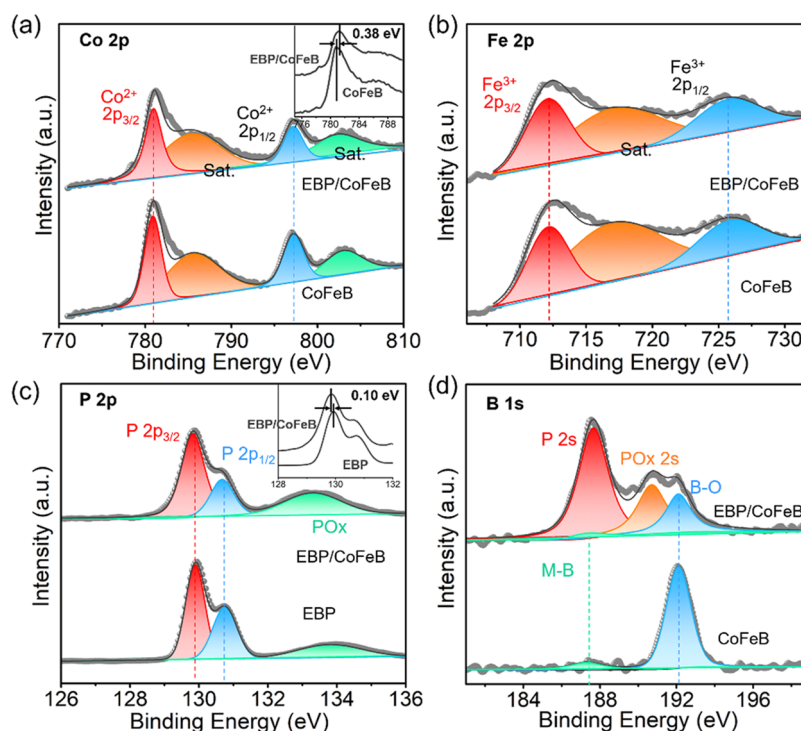
Figure 3. XPS data of the (a) Co 2p peak, (b) Fe 2p peak, (c) P 2p peak, and (d) B 1s peak of the as-prepared samples.

3.5 cm^{-1}) than that of the out-of-plane vibration (A$_g^1$) (about 1.8 cm^{-1}), which suggests that CoFeB grows on the surface of EBP and the layered structure of EBP is not destroyed.

The oxygen evolution activities of the electrocatalysts were evaluated by a series of electrochemical measurements in an aqueous electrolyte of 1 M KOH. Linear sweep voltammetry (LSV) curves (Figure 2a) show that the EBP/CoFeB catalyst is the most efficient and has the smallest onset potential, superior to those of the pure CoFeB and the EBP samples. The overpotentials of the CoFeB and EBP catalyst are 247 and 386 mV at a current density of 10 mA cm^{-2} (Figure 2b), respectively. By contrast, the EBP/CoFeB heterostructure only requires an overpotential of 227 mV to reach the same current density (surpasses most of the BP- and metal boride-based materials, Figure S6), which demonstrates that the OER activity at the heterostructure is mostly derived from the synergistic effect between the two parts. The overpotentials for all the samples at the current density of 100 mA cm^{-2} are shown in Figure S7, and the EBP/CoFeB catalyst also displays the highest activity, requiring only 313 mV to reach 100 mA cm^{-2}. In a two-electrode cell configuration, the EBP/CoFeB catalyst also presents an excellent performance (Figure S8). Figure 2c shows that the Tafel slope of EBP/CoFeB is 36.7 mV dec^{-1}, which is less than those of CoFeB (63.6 mV dec^{-1}) and BP (111.6 mV dec^{-1}), indicating that the EBP/CoFeB displays the fastest kinetics. The EBP/CoFeB presents a smaller semicircle radius of impedance arc than that of CoFeB during electrochemical impedance spectroscopy (EIS) measurement (Figure 2d), which means the electron transfer is significantly facilitated when the EBP support is introduced. We speculate that the crystalline−amorphous structure can simultaneously promote the conductivity and activity.

The stability tests were performed by chronopotentiometry at a current density of 10 mA cm^{-2}. The potential on EBP sample continuously increases due to the poor stability, in

contrast to the EBP/CoFeB nanosheet heterostructure, which shows good durability without obvious change in potential during a 60 h run (Figure 2e), thanks to CoFeB nanosheets' coating protection of the EBP that leads to desired electrochemical stability. The multipotential curve of EBP/CoFeB (Figure 2f) shows that the current density increases with the increase of potential (increment = 5 mV per 200 s) and remains almost unchanged when the applied potential is constant. The trends of the current densities under all the potentials are similar, implying that the EBP/CoFeB has good transport properties. We also investigated the electrochemical active surface area (ECSA) by the electrochemical double-layer capacitance (C$_{dl}$)[38] to further elucidate the origin of the superior performance of the EBP/CoFeB heterostructure. The C$_{dl}$ values are determined by the slope of the linear relationship between the current density in cyclic voltammetry (CV) curves and the scan rates (Figure S9).[39] The C$_{dl}$ value of EBP/CoFeB (129.86 mF cm^{-2}) is 16.2-fold that for EBP (8.04 mF cm^{-2}) (Figure S10), suggesting the existence of much more active sites after combining with CoFeB. The C$_{dl}$ value of pure CoFeB (160.12 mF cm^{-2}) is relatively higher than that of the heterostructure, revealing that the active sites of the heterostructure mainly originate from the metal sites in boride, and the intrinsic activity of the active site is improved after the construction of the heterostructure.

The chemical and electronic states of the catalysts were characterized by X-ray photoelectron spectroscopy (XPS).[40] The XPS survey scan spectra (Figure S11) of the samples manifest the existence of Co, Fe, B, P, and O elements. In the high-resolution Co 2p spectra (Figure 3a), the peaks at binding energies of 781.0 and 797.2 eV correspond to the Co 2p$_{3/2}$ and Co 2p$_{1/2}$ levels of Co^{2+}, which is consistent with previous reports.[41,42] It can be seen that the Co 2p peak shifts positively to higher binding energy (about 0.38 eV) after loading on the EBP, which means Co has a higher interaction strength with
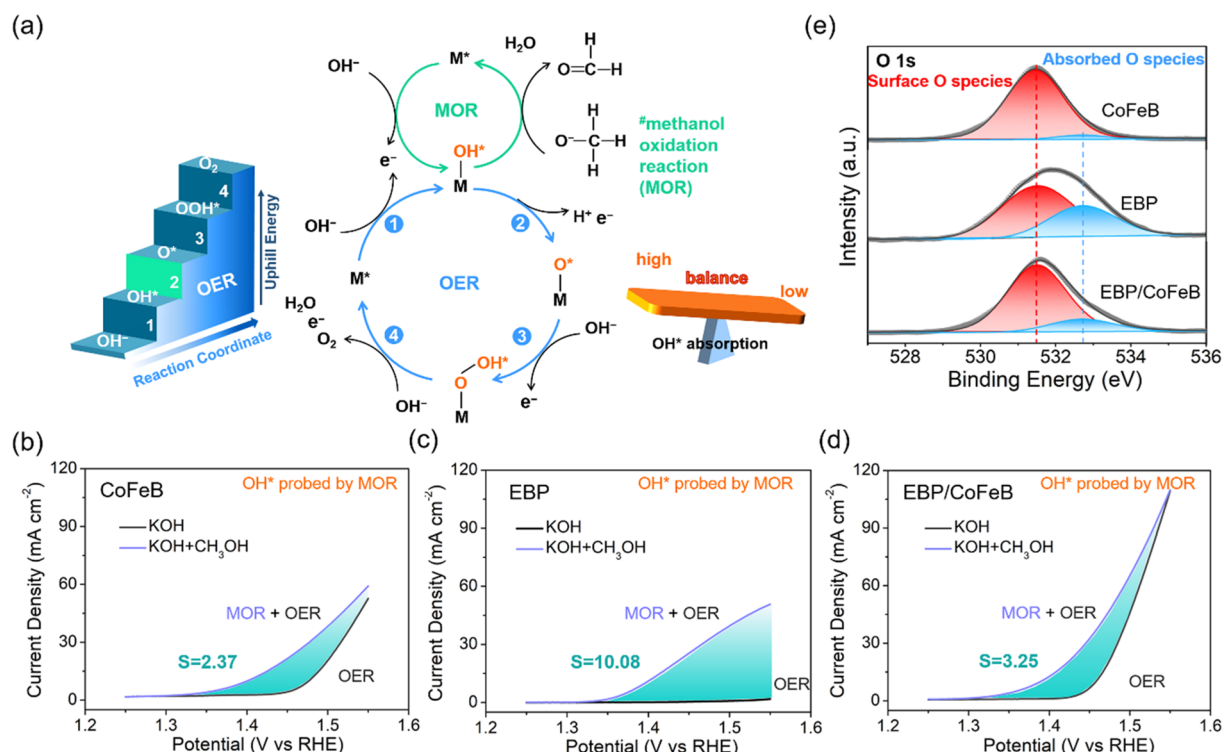
Figure 4. (a) Schematic diagram of the typical processes for OER and MOR. (b−d) Study of oxygen intermediates by methanol oxidation on CoFeB, EBP, and EBP/CoFeB. The LSV curves were collected in 1 M KOH (black) and 1 M KOH + CH_3OH (purple), scan rate: 50 mV s^{-1}. Filled area shows the current difference caused by MOR. (e) XPS data of the O 1s peak for the samples.

OER intermediates[43] and may improve the OER activity.[44] The positive shift can be ascribed to the electronegativity difference between element P and other elements (Co, Fe, and B) in consideration that P has the strongest electronegativity and can extract electrons from the metal elements. As for the Fe 2p XPS peaks (Figure 3b), two fitted peaks located at 712.1 and 725.7 eV are assigned to the Fe $2p_{3/2}$ and Fe $2p_{1/2}$ levels of high-valent Fe^{3+}.[45,46] The combination with EBP does not give rise to an obvious change in chemical valence of Fe, probably because that the Fe in pristine CoFeB is already in the highest valence state that is available for OER. Hence the metal sites (main active sites) are more favorable for OER after introducing the EBP. In the high-resolution P 2p spectra (Figure 3c), peaks located at 129.8 and 130.7 eV correspond to the original state of BP.[47,48] The oxidation peak at 133.3 eV is attributed to P−O and is enhanced after coating with the CoFeB nanosheets, which indicates slight surface oxidation occurred during the synthesis procedures to form more P−O bonds. A similar phenomenon was also reported for the BP/Co$_2$P heterostructures.[23] The peak of the P 2p level shows a slight negative shift compared with the EBP, confirming the electronic extraction from CoFeB. The XPS peaks (Figure 3d) of B 1s (187.3, 192.1 eV)[49] also confirm the formation of metal boride, where the peak related to the B−O bond reveals the characteristic surface oxidation of metal boride[50] to further drive the water oxidation process. The peaks for the oxidation of B and P are obvious for the sample after the OER test (Figure S12), especially for the POx in pure EBP sample, revealing that the black phosphorus nanosheet in EBP is more easily degraded than that in the EBP/CoFeB sample.

To further explore the origin of the high OER performance of the EBP/CoFeB heterostructure, we analyze the absorption properties of catalysts toward OER intermediates that are

closely related to the OER kinetics under the operating condition. The previously reported works have indicated that the OER on metal boride undergoes a process similar to that on the metal oxide due to its surface oxidation feature, and boron may accelerate the surface restructuring.[51,52] As shown in Figure 4a, the active site of OER acts as an electrophile in an uphill four-step catalytic cycle to continuously absorb hydroxyl ions and release the electrons to an external circuit. XPS and Raman spectra confirm this process: the characteristic peaks related to oxyhydroxide (XPS: 780.1 eV in Co 2p, 529.5 eV in O 1s; Raman: two peaks at around 600 cm^{-1}) emerged after the OER (Figures S13 and S14). It is widely acknowledged that OH* is a significant intermediate in the OER catalytic cycle, and the binding energy of it is correlated with binding energies of other oxygen intermediates (e.g., O* and OOH*).[53] Thus, it is very important to achieve a balanced bonding energy of OH* for the OER catalyst.

It was reported that OH* can be probed by the methanol oxidation reaction (MOR) under real operating conditions of the OER process because the intermediates of OH* are electrophiles that can be probed by reaction with nucleophiles such as methanol molecules. The pathways of MOR and OER are shown in Figure 4a.[54] As such, the LSV curves are tested in 1 M KOH solution with or without methanol (1 M). The current difference caused by MOR can reflect the extent of surface coverage of OH* to further embody the OH* adsorption ability. The filled areas (Figure 4b−d) between the curves were calculated (S_{CoFeB} = 2.37, S_{EBP} = 10.08, and $S_{EBP/CoFeB}$ = 3.25) to quantify the current difference during the reaction process (the area is proportional to the transferred charge that reflects the extent of reaction; see details in the Supporting Information), indicating that the absorption strength toward OH* varies in the trend EBP > EBP/CoFeB
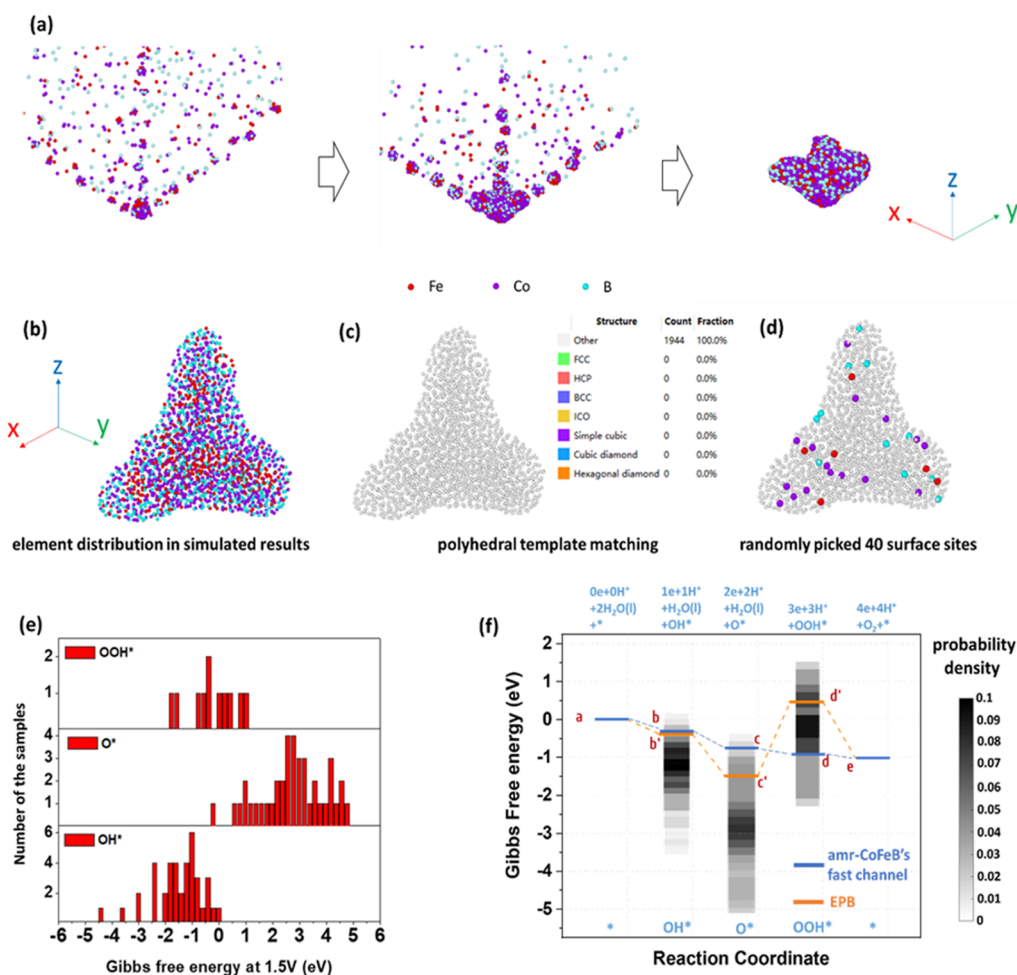
Figure 5. (a) The simulated synthesis process of amorphous CoFeB, with the details shown in Synthesis Simulation Details. For (a)−(d), the red, purple, and blue balls represent Fe, Co, and B elements. (b) Element distribution for the simulated CoFeB. (c) Result of the polyhedral template matching. The fully white colors indicate there is no ordered structure formed. (d) Positions for the randomly chosen 40 surface sites. (e) Energy distribution of the adsorption free energy of OOH*, O*, and OH* (G_{OOH*}, G_{O*}, G_{OH*}), which are the statistical results of the associated values on all 40 sites. The definitions of G_{OOH*}, G_{O*}, and G_{OH*} are the formation energies of the associated adsorbates from H_2O. Their specific expressions are given in eqs 11−13. The probability density in (f) is based on the data of (e). (f) Free energy diagram (FED) of OER on EPB and amorphous CoFeB. The "fast channel" FED with no exothermic step is shown by blue, while that of EPB is shown by orange (see Figure S18 for structures and computational details). The appearing probabilities of the G_{OOH*}, G_{O*}, and G_{OH*} levels are shown by a gray-scale map, with the darker color suggesting a higher appearing probability.

> CoFeB. Therefore, the lower OER activity of CoFeB and EBP can be attributed to the fact that the adsorption of OH* on CoFeB is too weak while that of EBP is too strong. The combination with EBP for CoFeB nanosheets strengthens the OH* absorption. The improved catalytic performance of EBP/CoFeB nanosheets may originate from the balanced bonding energy of the O intermediate. The medium Tafel slope of the EBP/CoFeB in MOR also confirms the moderate absorption strength (Figure S15). Moreover, CV curves were measured in KOH containing methanol to investigate the redox processes (Figure S16). The redox peaks between 1.0 and 1.2 V vs RHE represent the transformation between Co^{2+} and $Co^{3+/4+}$ [52,55], and the currents at the potentials above 1.2 V are majorly contributed by OER and MOR (related to OH* adsorption). As marked by the dashed lines, the onset potentials for MOR at the set of electrocatalysts trend as CoFeB (1.45 V vs RHE) > EBP/CoFeB (1.41 V vs RHE) > EBP (1.35 V vs RHE), indicating a balanced adsorption energy of OH* for EBP/CoFeB because the more positive oxidation potential signifies a

more difficult oxidation process, which is in agreement with the above discussion.

The O 1s XPS spectra were further studied (Figure 4e), and the peaks in the XPS spectra can be deconvoluted into two peaks: the peak at 531.5 eV can be assigned to the surface O species, and the peak at higher binding energy (532.7 eV) is attributed to the adsorbed O species.[36,51] Similarly, the absorption of O species for CoFeB is too weak, resulting in a low OER performance, whereas the absorption ability for the EBP/CoFeB is the most appropriate. After the OER process, new peaks at the binding energies of 780.1 eV (Figure S13a) and 529.5 eV (Figure S13b) appear, both corresponding to the oxyhydroxide. The proportion of oxyhydroxide (Tables S2 and S3) deduced from XPS results (Figure S13) for EBP/CoFeB is higher than that of CoFeB, which also arises from the enhanced absorption of OH*.

First-principals-based analysis is proposed to discuss the role of EPB in activity improvement. To begin with, CoFeB has an amorphous structure that is a metastable state in thermodynamics. As shown in Figure 1a, the formation of CoFeB can be

viewed as a quick gathering of Co, Fe, and B atoms that are randomly distributed in space. To simulate such a process, we employed high-dimension neutral network atomic potentials (HDNNPs)[56]-based molecular dynamics (MD). The schematic process is shown in Figure 5a, with the full movie provided in the Supporting Information. The atomic spatial distribution can be found in Figure 5b, which matches well with the electron diffraction (EDX) results. Besides, the polyhedral template matching[57] result is shown in Figure 5c, where we found no short-term ordered structure formed; this again confirms the structure we obtained by simulated synthesis matches the experimental results. Besides, we found the nucleation process should be very fast, because Fe will gather on the surface if it is a slow process (Synthesis Simulation Details section and Figure S17 and movie S2.gif in the Supporting Information), which is quite different from that predicted by EDX. So when we discuss the activity, we start from randomly picked surface sites in this structure (Activity Study by the Cut Model section). The positions of those sites are drawn in Figure 5d. The adsorption free energies of reaction intermediates of the OER, namely, O*, OH*, and OOH*, were calculated based on Norksov's approach[58] (detailed in the OER Activity Study Based on the Computational Hydrogen Electrode (CHE) Method section) and listed in Figure 5e. From it we saw a distribution of adsorption energies. On the basis of these values, we compose a free energy diagram (FED) of OER on amorphous CoFeB in Figure 5f. The black energy levels in the steps represent the average Gibbs free energy. And the free energy distributions are shown with a gray-scale map. On the other hand, the FED of BP was also plotted by orange steps in Figure 5f.

From Figure 5f we found two important facts that are consistent with experiments. (1) About the activity of amorphous CoFeB, for amorphous CoFeB, it can generate a "fast channel" (with no exothermic step) along the blue FED ($a \rightarrow b \rightarrow c \rightarrow d \rightarrow e$) in Figure 5f. Within such a channel, amorphous CoFeB will give a higher OER activity than EPB, which is consistent with Figure 4. (2) According to Figure 5f, one can see the step of levels b and c is located in the lighter colored areas, indicating the unlikely formation of such a "fast channel", as the amount of active sites that possess suitable adsorption energies of OH* and O* is rather low. However, when constructing hybrids of EBP/CoFeB, extra active sites can be offered for binding OH*, as indicated by level b′ in Figure 5f. That may be the key factor for EBP/CoFeB outperforming CoFeB in OER catalysis.

CONCLUSIONS

In summary, a 2D/2D EBP/CoFeB electrocatalyst was fabricated to optimize the adsorption/desorption of oxygen-containing intermediate products during the OER process. The interactions between EBP and CoFeB nanosheets give rise to high-performance active sites with balanced oxygen intermediate absorption. The crystalline EBP contributed to the enhanced conductivity, while the CoFeB nanosheets can protect the degradable EBP from the ambient environment to achieve long-term electrochemical stability. This work sheds light on the facile tuning of oxygen-containing intermediate absorption for BP-based heterostructures and guides the design of heterostructured nanohybrids for efficient and durable electrocatalysis.

MATERIALS AND METHODS

Chemicals. Bulk black phosphorus (99.99%) was purchased from Zhongke Materials Co., Ltd. Cobalt nitrate ($Co(NO_3)_2 \cdot 6H_2O$, 99%) and potassium hydroxide (95%) were purchased from Aladdin Chemical Reagent Co., Ltd. N-Methylpyrrolidone (NMP, 99%) was purchased from Macklin Biochemical Co., Ltd. Ferrous sulfate heptahydrate ($FeSO_4 \cdot 7H_2O$, 99%) was purchased from Gaojing Chemical Co., Ltd. Sodium borohydride ($NaBH_4$, 96%) was purchased from Sinopharm Chemical Reagent Co., Ltd. All chemicals were used as received without any further purification.

Synthesis of EBP. Exfoliated black phosphorus nanosheets were synthesized by a simple liquid exfoliation method using the solvent NMP. In brief, 40 mg of bulk black phosphorus was ground in a N_2-filled glovebox and transferred to an NMP solution (200 mL). The mixture was put in continuous water-bath sonication at 18 kHz for 12 h and centrifuged at 6000 rpm for 15 min. The obtained supernatant was centrifuged at 10 000 rpm for 15 min and washed with N_2-saturated ethanol and deionized water to get EBP. The EBP can be well redispersed in N_2-saturated deionized water and sealed.

Synthesis of EBP/CoFeB and CoFeB. For the adsorption of metal ions on the surface of negatively charged EBP nanosheets, $Co(NO_3)_2 \cdot 6H_2O$ (0.067 M) and $FeSO_4 \cdot 7H_2O$ (0.033 M) were dissolved in N_2-saturated deionized water to form a homogeneous solution, and this solution was used as solvent to replace the deionized water during the centrifugation of EBP. The EBP with absorbed ions was then immersed in deionized water to remove the weakly bonded ions and redispersed in N_2-saturated deionized water (50 mL). Excess $NaBH_4$ (0.6 M, 5 mL) solution (serving as a reducing agent and boron source) was slowly injected into the aqueous dispersion under an ice bath. The surface of the EBP became darker colored. The precipitate (denoted as EBP/CoFeB) was washed by deionized water to remove the unreacted $NaBH_4$ and vacuum-dried at 60 °C for 6 h.

For the preparation of pure CoFeB, excess $NaBH_4$ (0.6 M, 5 mL) solution was directly added into a N_2-saturated mixed solution of $Co(NO_3)_2 \cdot 6H_2O$ (0.0067 M) and $FeSO_4 \cdot 7H_2O$ (0.0033 M) (the volume was 100 mL) under an ice bath. The precipitate was also washed by deionized water and vacuum-dried at 60 °C for 6 h.

Characterizations. X-ray diffraction patterns were recorded by an X-ray diffractometer (D8 Advanced, Bruker, Germany). The morphologies of the samples, the high-angle annular dark-field scanning transmission electron microscopic (HAADF-STEM) images, and energy dispersion spectra were obtained by a transmission electron microscope (JEM-2010F, JEOL, Japan). Atomic force microscopy was carried out on a Si substrate loaded with nanosheets by the atomic force microscope (Multimode 8, Bruker, Germany) in the tapping mode to measure the thickness of the nanosheets. Chemical valence analysis was performed by X-ray photoelectron spectroscopy (Escalab 250Xi, Thermo Scientific, America), and the XPS spectra were referenced to C 1s emission at 284.8 eV. Raman spectra were recorded by a Raman spectrometer (InVia-Reflex, Renishaw, UK) equipped with a 514 nm laser. The evaluations of electrochemical activities were performed by an electrochemical workstation (CHI 660E, Chenhua, China).

Electrochemical Measurements. A 5 mg amount of catalyst powder was dispersed in a mixture of water (100 μL) and ethanol (300 μL), and then 20 μL of Nafion solution (5 wt % in water) was added to this suspension. After ultrasonic stirring for 30 min, 80 μL of the homogeneous ink was deposited onto a 1×1 cm^2 Ni foam substrate (catalyst loading was about 1.0 mg cm^{-2}). The Ni foam was pretreated with diluted H_2SO_4 solution and washed by distilled water until the pH of the water was neutral.

Electrochemical performance was evaluated by an electrochemical workstation. All the measurements were carried out in a 1.0 M KOH aqueous solution. For the three-electrode configuration, the reference electrode was a Ag/AgCl electrode, and the counter electrode was a Pt mesh electrode. The potential (vs Ag/AgCl) was converted to the reversible hydrogen electrode (RHE) according to the following equation:

$$E_{RHE} = E_{Ag/AgCl} + 0.059 \times pH + 0.198 \text{ V} \qquad (1)$$

The linear sweep voltammetry test was performed at a scan rate of 5 mV s^{-1}. All the LSV curves were recorded without being iR-corrected. Double-layer capacitance values were deduced from cyclic voltammetry measurements, which were cycled between 1.20 and 1.30 V (vs RHE) at different scan rates. The electrochemical impedance spectra were measured at 1.50 V (vs RHE) from 1×10^6 to 0.1 Hz in the same configuration as the LSV measurements. For the methanol probe experiments, 1 M methanol was added into the KOH aqueous electrolyte.

Quantification of the Extent of Methanol Oxidation Reaction. The area (S) in Figure 4b–d is calculated according to the following equations:

$$U(\text{V}) = \text{scan rate} \times t \text{ (s)} = 0.05 \text{ (V s}^{-1}) \times t \text{ (s)} \qquad (2)$$

$$Q \text{ (C)} = I \text{ (A)} \times t \text{ (s)} \qquad (3)$$

$$S \text{ (mA V cm}^{-2}) = \int I \text{ (mA cm}^{-2}) \, dU \text{ (V)}$$
$$= \int I \text{ (mA cm}^{-2}) \, d[0.05 \text{ (V s}^{-1}) \times t \text{ (s)}] = 0.05 \text{ (V s}^{-1}) \times$$
$$\int I \text{ (mA cm}^{-2}) \, dt \text{ (s)} = 0.05 \times \int I \text{ (A)} \, dt \text{ (s)}$$
$$(10^{-3} \text{V s}^{-1} \text{ cm}^{-2}) = 0.05 \times 10^{-3} Q \text{ (C)} \text{ (V s}^{-1} \text{ cm}^{-2}) \qquad (4)$$

Thus, the area (S) is proportional to the charge transfer (Q).

Machine Learning Details. When the details of the synthesis process are demanded, ab initio molecular dynamics (AIMD) is usually called for. However, AIMD is prohibitively expensive. One of the best solutions to this now is the introduction of a neural network (NN). It is able to represent functions of many variables in a continuous way and to interpolate within the training set. Thus, it will allow obtaining a faithful representation of the ab initio potential energies and forces, at a much reduced cost.[59] So we could say NN-based MD is an "equivalently accurate, but faster" AIMD. Until today, the structure of NN used to represent DFT results has gradually reached a paradigm, that is, the high-dimensional neutral network potentials proposed by Behler and Parrinello.[59,60] It decouples the total energy of the system to a sum of atomic energies and, using the concept of "nearsightedness" to regard the atomic potentials as functionals of the local chemical environment up to a cutoff radius, are computed by individual atomic neural networks.

In this paper, to simulate the synthesis of amorphous CoFeB, we will also introduce such HDNNPs. To begin with, we downloaded a coordinate file of CoFeB unit cells from the Web site of the material project[61] (ID: mp-1224984). From this structure, we created bulk and surface models to train the NN. Specifically, we built the bulk model by a supercell of $2 \times 2 \times 2$, and we built surface models by cleaving facets of 011, 100, and 210, with thicknesses of 4.19, 4.84, and 5.97 Å, respectively, and extended them all by 2×2 supercells. Finally, we deleted half of Fe and a quarter of B from all these models, to create a 2:1:1.5 stoichiometry of Co, Fe, and B. The total numbers of atoms are 72 for bulk structures (16Fe, 32Co, and 24B), 54 for 011 surface structures (12Fe, 24Co, and 18B), 36 for 100 surface structures (8Fe, 16Co, and 12B), and 54 for 210 surface structures (12Fe, 24Co, and 18B).

On the basis of these models, we use DFTMD to generate the DFT data set (details for the parameters chosen are given in the DFT and DFTMD Details). Three temperatures, namely, 300, 900, and 3000 K, were chosen, where 500 data were generated for each temperature; that is, we obtained 6000 DFT data in total to train the NN.

Among the many NN-based methods for constructing accurate force fields, we chose here the DeePMD kit package.[62] The codes achieve a high-dimensional neutral network that preserves all the natural symmetries during structure analysis. While efficiently being indistinguishable from the DFT-based data, it will generate a small volume of the force field. During the learning process, the cutoff radius is set to 5 Å. The maximum number of neighbor atoms that are treated by full relative coordinates is set as 50, 32, and 32 for Fe, Co,

and B. The smoothing is set to begin from 1/5 to 2. The number of neurons in each hidden layer numbers of the embedding nets is 10, 20, and 40, and those of the hidden layer numbers of the fitting net are 240, 240, and 240. The prefactors of energy and force loss at the start of the training are set to be 0.02 and 1000, while those at the limit of the training are set to be 2 and 1. The starting learning rate, the decay step, and the decay rate are set as 0.001, 1000, and 0.95.

DFT and DFTMD Details. All the DFT calculations are implemented via Quantum Espresso.[63] Spin-polarized DFT calculations were performed with periodic supercells under the generalized gradient approximation (GGA) using the Perdew–Burke–Ernzerhof (PBE) functional for exchange–correlation and the ultrasoft pseudopotentials for nuclei and core electrons. The Kohn–Sham orbitals were expanded in a plane-wave basis set with a kinetic energy cutoff of 30 Ry and the charge-density cutoff of 300 Ry. The Fermi-surface effects were treated by the smearing technique of Methfessel and Paxton, using a smearing parameter of 0.02 Ry. For all of the structures, the convergence criteria are set as 10^{-4} Ry/bohr of Cartesian force components acting on each atom and 10^{-4} Ry of total energy. For surface structures, the k-points are set to be $3 \times 3 \times 1$, while those of the bulk structure are $3 \times 3 \times 3$.

For DFTMD calculation, the time step is set to be 1 fs. The canonical ensemble condition was imposed by a Nose thermostat with a target temperature. For each structure, we have three target temperatures. They are 300, 900, and 3000 K, respectively. All of the structures are performed by 500 fs. All the snapshots are recorded for NN training.
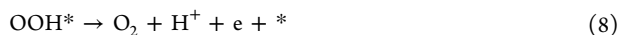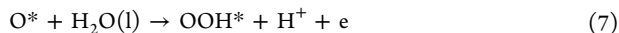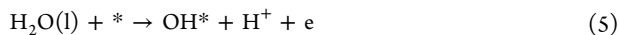
Synthesis Simulation Details. The synthesis simulation is done by large-scale atomic/molecular massively parallel simulator (LAMMPS),[64] with the force field generated by the DeePMD kit. During the simulation, we put six hard plates with the expressions of z = 0 and 400, x = 0 and 400, and y = 0 and 400 to set the boundary of the atoms, and we use a Morse potential to describe the interaction between these plates and the atoms near them, so that every atom approaching this plate will rebound by the Morse potential, such that all the atoms are restricted inside a cubic box. Additionally, we have included a gravity for all the atoms, with the direction of [−1, −1, −1]. This means that if the temperature is low enough, all the atoms will gradually gather at one corner of the box.

The simulation begins from a bulk structure with 1944 atoms. During the MD, a canonical ensemble condition (NVT) was imposed by a Nose thermostat with a target temperature of 32 000 K for 200 ps, then cooling to 600 K for another 200 ps, and finally stabilized at 300 K for the last 200 ps. In particular, for the cooling process, the temperature of the thermostat was set to be 600 K, and the temperature was relaxed every 1 fs. We record the evolution process made by such a simulation in movie files S1.gif and S3.gif, Supporting Information.

As a comparison, we also simulated the process with a much slower cooling process, where the temperature of the thermostat was also set to be 600 K, but the relaxation frequency was decreased to one time per 20 fs. The evolution processes are recorded in movies S2.gif and S4.gif, Supporting Information. We found that in such a process, while amorphous structures can still be formed, Fe, Co, and B will not follow a uniform random distribution. Instead, Fe and Co tend to locate inside, leaving B on the periphery. This could be inferred from Figure S17, and it was not consistent with the experimental EDX results. This proves the amorphous structure used in the paper was generated by a fast cooling process.

Activity Study by the Cut Model. After obtaining the above-mentioned model, it is necessary to discuss the activities on the surface sites. To do this, we first randomly pick 40 surface sites, then cut the sites along with their neighbor atoms with a cutoff radius of 4 Å. Such a cluster is put in the center of a periodic box of $10 \times 10 \times 10$ Å^3. We make these cutoff models to simulate the impact from the selected site, as well as its surroundings. The associated structure is given in movie file S5.gif, Supporting Information. When implementing DFT calculations on these clusters, half of the atoms on the bottom are fixed in order to keep the structures in the amorphous CoFeB.

OER Activity Study Based on the Computational Hydrogen Electrode (CHE) Method. When discussing the OER mechanism, the OER is assumed to follow a classical four-proton coupled electron transfer (PCET) process[65] that is written as

$$H_2O(l) + * \rightarrow OH* + H^+ + e \tag{5}$$

$$OH* \rightarrow O* + H^+ + e \tag{6}$$

$$O* + H_2O(l) \rightarrow OOH* + H^+ + e \tag{7}$$

$$OOH* \rightarrow O_2 + H^+ + e + * \tag{8}$$

The asterisk stands for the site on the surface of a certain catalyst. The free energies of $O_2(g)$ are calculated by the equilibrium

$$O_2 + 4H^+(aq) + 4e \rightarrow OH* + 2H_2O(l) \tag{9}$$
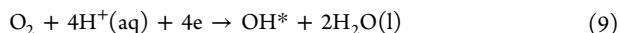
at 1.23 V to avoid the error of DFT energy caused by the high spin of O_2.[66,67] The chemical potential of $H^+(aq)$ is calculated by $1/2H_2(g)$ on the basis of the CHE method.[58]

The chemical potentials of adsorbates X* are calculated by the following expression:

$$\mu_{X*} = E_{X*} - E_* + ZPE_{X*} - TS_{X*} \tag{10}$$

The E_{X*} and E_* are the DFT-based total energies of active sites with and without the adsorbates X*. ZPE and TS are the contributions from zero points and entropies of adsorbates, whose values are listed in Table S4. The formation free energies of OH*, O*, and OOH*, denoted as G_{OH*}, G_{O*}, and G_{OOH*}, are defined as

$$G_{OH*} = \mu_{OH*} + 1/2\mu_{H_2*} - Ue - \mu_{H_2O} \tag{11}$$

$$G_{O*} = \mu_{O*} + \mu_{H_2*} - 2Ue - \mu_{H_2O} \tag{12}$$

$$G_{OOH*} = \mu_{OOH*} + 3/2\mu_{H_2*} - 3Ue - 2\mu_{H_2O} \tag{13}$$

When calculating the values in Figure 5e and f, U is set as 1.5 V. The associated G_{OH*}, G_{O*}, and G_{OOH*} values for picked sites are gathered in Table S5, with the associated optimized structures listed in Figure S18 and Figure S19, for CoFeB and EBP, respectively.

ASSOCIATED CONTENT

Ⓢ Supporting Information

The Supporting Information is available free of charge at https://pubs.acs.org/doi/10.1021/acsnano.1c04715.

> Photos of samples during the exfoliation process; AFM images of EBP and CoFeB nanosheets; TEM image of CoFeB nanosheets; XRD patterns of EBP/CoFeB and CoFeB nanosheets; research status; overpotentials for all the samples at a current density of 100 mA cm^{-2}; LSV curve for two-electrode configuration; CV curves for ECSA; XPS survey scan; XPS spectra of the P 2p, B 1s, Co 2p, Fe 2p, and O 1s for the samples after the OER process; Raman spectra of the samples before and after the OER process; Tafel plots for MOR; CV curves for MOR; element distribution for the simulated sample; side views of selected surface sites; optimized structures of OER intermediates on EBP (PDF)
>
> Movie videos as described in the text (ZIP)

AUTHOR INFORMATION

Corresponding Authors

Da Chen − *College of Materials and Chemistry, China Jiliang University, Hangzhou 310018 Zhejiang, People's Republic of China;* ⓞ orcid.org/0000-0001-7854-7135; Email: dchen_80@hotmail.com

Laishun Qin − *College of Materials and Chemistry, China Jiliang University, Hangzhou 310018 Zhejiang, People's Republic of China;* Email: qinlaishun@cjlu.edu.cn

Zhenhai Wen − *CAS Key Laboratory of Design and Assembly of Functional Nanostructures, Fujian Provincial Key Laboratory of Nanomaterials, Fujian Institute of Research on the Structure of Matter, Chinese Academy of Sciences, Fuzhou 350002, People's Republic of China;* ⓞ orcid.org/0000-0002-2340-9525; Email: wen@fjirsm.ac.cn

Authors

Huayu Chen − *College of Materials and Chemistry, China Jiliang University, Hangzhou 310018 Zhejiang, People's Republic of China*

Junxiang Chen − *CAS Key Laboratory of Design and Assembly of Functional Nanostructures, Fujian Provincial Key Laboratory of Nanomaterials, Fujian Institute of Research on the Structure of Matter, Chinese Academy of Sciences, Fuzhou 350002, People's Republic of China*

Pei Ning − *College of Materials and Chemistry, China Jiliang University, Hangzhou 310018 Zhejiang, People's Republic of China*

Xin Chen − *TJU-NIMS International Collaboration Laboratory, School of Material Science and Engineering, Tianjin University, Tianjin 300072, People's Republic of China*

Junhui Liang − *College of Materials and Chemistry, China Jiliang University, Hangzhou 310018 Zhejiang, People's Republic of China;* ⓞ orcid.org/0000-0002-0508-8297

Xin Yao − *College of Optical and Electronic Technology, China Jiliang University, Hangzhou 310018 Zhejiang, People's Republic of China*

Yuexiang Huang − *College of Materials and Chemistry, China Jiliang University, Hangzhou 310018 Zhejiang, People's Republic of China*

Complete contact information is available at:
https://pubs.acs.org/10.1021/acsnano.1c04715

Notes

The authors declare no competing financial interest.

REFERENCES

(1) Zhao, D.; Zhuang, Z.; Cao, X.; Zhang, C.; Peng, Q.; Chen, C.; Li, Y. Atomic Site Electrocatalysts for Water Splitting, Oxygen Reduction and Selective Oxidation. *Chem. Soc. Rev.* **2020**, *49*, 2215−2264.

(2) Fei, H.; Dong, J.; Chen, D.; Hu, T.; Duan, X.; Shakir, I.; Huang, Y.; Duan, X. Single Atom Electrocatalysts Supported on Graphene or Graphene-Like Carbons. *Chem. Soc. Rev.* **2019**, *48*, 5207−5241.

(3) Zhu, J.; Hu, L.; Zhao, P.; Lee, L. Y. S.; Wong, K.-Y. Recent Advances in Electrocatalytic Hydrogen Evolution Using Nanoparticles. *Chem. Rev.* **2020**, *120*, 851−918.

(4) Franco, F.; Rettenmaier, C.; Jeon, H. S.; Roldan Cuenya, B. Transition Metal-Based Catalysts for the Electrochemical CO$_2$ Reduction: From Atoms and Molecules to Nanostructured Materials. *Chem. Soc. Rev.* **2020**, *49*, 6884−6946.

(5) Li, X.; Yu, J.; Jaroniec, M.; Chen, X. Cocatalysts for Selective Photoreduction of CO$_2$ into Solar Fuels. *Chem. Rev.* **2019**, *119*, 3962−4179.

(6) Chang, C.-J.; Zhu, Y.; Wang, J.; Chen, H.-C.; Tung, C.-W.; Chu, Y.-C.; Chen, H. M. *In Situ* X-Ray Diffraction and X-Ray Absorption Spectroscopy of Electrocatalysis for the Energy Conversion Reactions. *J. Mater. Chem. A* **2020**, *8*, 19079−19112.

(7) Nitopi, S.; Bertheussen, E.; Scott, S. B.; Liu, X.; Engstfeld, A. K.; Horch, S.; Seger, B.; Stephens, I. E. L.; Chan, K.; Hahn, C.; Nørskov, J. K.; Jaramillo, T. F.; Chorkendorff, I. Progress and Perspectives of Electrochemical CO$_2$ Reduction on Copper in Aqueous Electrolyte. *Chem. Rev.* **2019**, *119*, 7610−7672.

(8) Francke, R.; Schille, B.; Roemelt, M. Homogeneously Catalyzed Electroreduction of Carbon Dioxide-Methods, Mechanisms, and Catalysts. *Chem. Rev.* **2018**, *118*, 4631−4701.

(9) Song, J.; Wei, C.; Huang, Z.-F.; Liu, C.; Zeng, L.; Wang, X.; Xu, Z. J. A Review on Fundamentals for Designing Oxygen Evolution Electrocatalysts. *Chem. Soc. Rev.* **2020**, *49*, 2196−2214.

(10) Shi, Z.; Wang, X.; Ge, J.; Liu, C.; Xing, W. Fundamental Understanding of the Acidic Oxygen Evolution Reaction: Mechanism Study and State-of-the-Art Catalysts. *Nanoscale* **2020**, *12*, 13249−13275.

(11) Zhang, W.; Zhou, K. Ultrathin Two-Dimensional Nano-structured Materials for Highly Efficient Water Oxidation. *Small* **2017**, *13*, 1700806.

(12) Di, J.; Yan, C.; Handoko, A. D.; Seh, Z. W.; Li, H.; Liu, Z. Ultrathin Two-Dimensional Materials for Photo- and Electrocatalytic Hydrogen Evolution. *Mater. Today* **2018**, *21*, 749−770.

(13) Sang, D. K.; Wang, H.; Guo, Z.; Xie, N.; Zhang, H. Recent Developments in Stability and Passivation Techniques of Phosphorene toward Next-Generation Device Applications. *Adv. Funct. Mater.* **2019**, *29*, 1903419.

(14) Cai, Y.; Gao, J.; Chen, S.; Ke, Q.; Zhang, G.; Zhang, Y.-W. Design of Phosphorene for Hydrogen Evolution Performance Comparable to Platinum. *Chem. Mater.* **2019**, *31*, 8948−8956.

(15) Ren, X.; Zhou, J.; Qi, X.; Liu, Y.; Huang, Z.; Li, Z.; Ge, Y.; Dhanabalan, S. C.; Ponraj, J. S.; Wang, S. Few-Layer Black Phosphorus Nanosheets as Electrocatalysts for Highly Efficient Oxygen Evolution Reaction. *Adv. Energy Mater.* **2017**, *7*, 1700396.

(16) Liang, Q.; Zhong, L.; Du, C.; Luo, Y.; Zheng, Y.; Li, S.; Yan, Q. Achieving Highly Efficient Electrocatalytic Oxygen Evolution with Ultrathin 2D Fe-Doped Nickel Thiophosphate Nanosheets. *Nano Energy* **2018**, *47*, 257−265.

(17) Dinh, K. N.; Zhang, Y.; Zhu, J.; Sun, W. Phosphorene-Based Electrocatalysts. *Chem. - Eur. J.* **2020**, *26*, 6437.

(18) Qiao, H.; Liu, H.; Huang, Z.; Ma, Q.; Luo, S.; Li, J.; Liu, Y.; Zhong, J.; Qi, X. Black Phosphorus Nanosheets Modified with Au Nanoparticles as High Conductivity and High Activity Electrocatalyst for Oxygen Evolution Reaction. *Adv. Energy Mater.* **2020**, *10*, 2002424.

(19) Li, X.; Xiao, L.; Zhou, L.; Xu, Q.; Weng, J.; Xu, J.; Liu, B. Adaptive Bifunctional Electrocatalyst of Amorphous CoFe Oxide@2D Black Phosphorus for Overall Water Splitting. *Angew. Chem., Int. Ed.* **2020**, *59*, 21106−21113.

(20) Wu, T.; Zhang, S.; Bu, K.; Zhao, W.; Bi, Q.; Lin, T.; Huang, J.; Li, Y.; Huang, F. Nickel Nitride-Black Phosphorus Heterostructure Nanosheets for Boosting the Electrocatalytic Activity towards the Oxygen Evolution Reaction. *J. Mater. Chem. A* **2019**, *7*, 22063−22069.

(21) Luo, Z.-Z.; Zhang, Y.; Zhang, C.; Tan, H. T.; Li, Z.; Abutaha, A.; Wu, X.-L.; Xiong, Q.; Khor, K. A.; Hippalgaonkar, K.; Xu, J.; Hng, H. H.; Yan, Q. Multifunctional 0D-2D Ni$_2$P Nanocrystals-Black Phosphorus Heterostructure. *Adv. Energy Mater.* **2017**, *7*, 1601285.

(22) Shi, F.; Huang, K.; Wang, Y.; Zhang, W.; Li, L.; Wang, X.; Feng, S. Black Phosphorus-Modified Co$_3$O$_4$ through Tuning the Electronic Structure for Enhanced Oxygen Evolution Reaction. *ACS Appl. Mater. Interfaces* **2019**, *11*, 17459−17466.

(23) Wang, J.; Liu, D.; Huang, H.; Yang, N.; Yu, B.; Wen, M.; Wang, X.; Chu, P. K.; Yu, X.-F. In-Plane Black Phosphorus/Dicobalt

Phosphide Heterostructure for Efficient Electrocatalysis. *Angew. Chem., Int. Ed.* **2018**, *57*, 2600−2604.

(24) Sun, H.; Tian, C.; Fan, G.; Qi, J.; Liu, Z.; Yan, Z.; Cheng, F.; Chen, J.; Li, C.-P.; Du, M. Boosting Activity on Co$_4$N Porous Nanosheet by Coupling CeO$_2$ for Efficient Electrochemical Overall Water Splitting at High Current Densities. *Adv. Funct. Mater.* **2020**, *30*, 1910596.

(25) Yeo, B. S. Oxygen Evolution by Stabilized Single Ru Atoms. *Nat. Catal.* **2019**, *2*, 284−285.

(26) Zhang, J.; Liu, J.; Xi, L.; Yu, Y.; Chen, N.; Sun, S.; Wang, W.; Lange, K. M.; Zhang, B. Single-Atom Au/NiFe Layered Double Hydroxide Electrocatalyst: Probing the Origin of Activity for Oxygen Evolution Reaction. *J. Am. Chem. Soc.* **2018**, *140*, 3876−3879.

(27) Zhang, T.; Wan, Y.; Xie, H.; Mu, Y.; Du, P.; Wang, D.; Wu, X.; Ji, H.; Wan, L. Degradation Chemistry and Stabilization of Exfoliated Few-Layer Black Phosphorus in Water. *J. Am. Chem. Soc.* **2018**, *140*, 7561−7567.

(28) Huang, Y.; Qiao, J.; He, K.; Bliznakov, S.; Sutter, E.; Chen, X.; Luo, D.; Meng, F.; Su, D.; Decker, J.; Ji, W.; Ruoff, R. S.; Sutter, P. Interaction of Black Phosphorus with Oxygen and Water. *Chem. Mater.* **2016**, *28*, 8330−8339.

(29) Gupta, S.; Patel, M. K.; Miotello, A.; Patel, N. Metal Boride-Based Catalysts for Electrochemical Water-Splitting: A Review. *Adv. Funct. Mater.* **2020**, *30*, 1906481.

(30) Chen, X.; Yu, Z.; Wei, L.; Zhou, Z.; Zhai, S.; Chen, J.; Wang, Y.; Huang, Q.; Karahan, H. E.; Liao, X.; Chen, Y. Ultrathin Nickel Boride Nanosheets Anchored on Functionalized Carbon Nanotubes as Bifunctional Electrocatalysts for Overall Water Splitting. *J. Mater. Chem. A* **2019**, *7*, 764−774.

(31) Ren, H.; Sun, X.; Du, C.; Zhao, J.; Liu, D.; Fang, W.; Kumar, S.; Chua, R.; Meng, S.; Kidkhunthod, P.; Song, L.; Li, S.; Madhavi, S.; Yan, Q. Amorphous Fe-Ni-P-B-O Nanocages as Efficient Electro-catalysts for Oxygen Evolution Reaction. *ACS Nano* **2019**, *13*, 12969−12979.

(32) Han, H.; Choi, H.; Mhin, S.; Hong, Y.-R.; Kim, K. M.; Kwon, J.; Ali, G.; Chung, K. Y.; Je, M.; Umh, H. N.; Lim, D.-H.; Davey, K.; Qiao, S.-Z.; Paik, U.; Song, T. Advantageous Crystalline-Amorphous Phase Boundary for Enhanced Electrochemical Water Oxidation. *Energy Environ. Sci.* **2019**, *12*, 2443−2454.

(33) Tian, T.; Zheng, M.; Lin, J.; Meng, X.; Ding, Y. Amorphous Ni-Fe Double Hydroxide Hollow Nanocubes Enriched with Oxygen Vacancies as Efficient Electrocatalytic Water Oxidation Catalysts. *Chem. Commun.* **2019**, *55*, 1044−1047.

(34) Jeong, S.; Hu, K.; Ohto, T.; Nagata, Y.; Masuda, H.; Fujita, J.-i.; Ito, Y. Effect of Graphene Encapsulation of NiMo Alloys on Oxygen Evolution Reaction. *ACS Catal.* **2020**, *10*, 792−799.

(35) Zhou, Q.; Chen, Q.; Tong, Y.; Wang, J. Light-Induced Ambient Degradation of Few-Layer Black Phosphorus: Mechanism and Protection. *Angew. Chem., Int. Ed.* **2016**, *55*, 11437−11441.

(36) Nsanzimana, J. M. V.; Gong, L.; Dangol, R.; Reddu, V.; Jose, V.; Xia, B. Y.; Yan, Q.; Lee, J.-M.; Wang, X. Tailoring of Metal Boride Morphology *via* Anion for Efficient Water Oxidation. *Adv. Energy Mater.* **2019**, *9*, 1901503.

(37) Yuan, Z.; Li, J.; Yang, M.; Fang, Z.; Jian, J.; Yu, D.; Chen, X.; Dai, L. Ultrathin Black Phosphorus-on-Nitrogen Doped Graphene for Efficient Overall Water Splitting: Dual Modulation Roles of Directional Interfacial Charge Transfer. *J. Am. Chem. Soc.* **2019**, *141*, 4972−4979.

(38) Zhong, X.; Sun, Y.; Chen, X.; Zhuang, G.; Li, X.; Wang, J.-G. Mo Doping Induced More Active Sites in Urchin-Like W$_{18}$O$_{49}$ Nanostructure with Remarkably Enhanced Performance for Hydrogen Evolution Reaction. *Adv. Funct. Mater.* **2016**, *26*, 5778−5786.

(39) Li, W.; Watzele, S.; El-Sayed, H. A.; Liang, Y.; Kieslich, G.; Bandarenka, A. S.; Rodewald, K.; Rieger, B.; Fischer, R. A. Unprecedented High Oxygen Evolution Activity of Electrocatalysts Derived from Surface-Mounted Metal-Organic Frameworks. *J. Am. Chem. Soc.* **2019**, *141*, 5926−5933.

(40) Huang, J.; Sun, Y.; Du, X.; Zhang, Y.; Wu, C.; Yan, C.; Yan, Y.; Zou, G.; Wu, W.; Lu, R.; Li, Y.; Xiong, J. Cytomembrane-Structure-

Inspired Active Ni-N-O Interface for Enhanced Oxygen Evolution Reaction. *Adv. Mater.* **2018**, *30*, e1803367.

(41) He, D.; Song, X.; Li, W.; Tang, C.; Liu, J.; Ke, Z.; Jiang, C.; Xiao, X. Active Electron Density Modulation of Co_3O_4-Based Catalysts Enhances Their Oxygen Evolution Performance. *Angew. Chem., Int. Ed.* **2020**, *59*, 6929−6935.

(42) Liu, J.; Ji, Y.; Nai, J.; Niu, X.; Luo, Y.; Guo, L.; Yang, S. Ultrathin Amorphous Cobalt-Vanadium Hydr(oxy)oxide Catalysts for the Oxygen Evolution Reaction. *Energy Environ. Sci.* **2018**, *11*, 1736−1741.

(43) Jin, Y.; Huang, S.; Yue, X.; Du, H.; Shen, P. K. Mo- and Fe-Modified $Ni(OH)_2$/NiOOH Nanosheets as Highly Active and Stable Electrocatalysts for Oxygen Evolution Reaction. *ACS Catal.* **2018**, *8*, 2359−2363.

(44) Li, N.; Bediako, D. K.; Hadt, R. G.; Hayes, D.; Kempa, T. J.; von Cube, F.; Bell, D. C.; Chen, L. X.; Nocera, D. G. Influence of Iron Doping on Tetravalent Nickel Content in Catalytic Oxygen Evolving Films. *Proc. Natl. Acad. Sci. U. S. A.* **2017**, *114*, 1486.

(45) Chen, H.; Song, L.; Ouyang, S.; Wang, J.; Lv, J.; Ye, J. Co and Fe Codoped $WO_{2.72}$ as Alkaline-Solution-Available Oxygen Evolution Reaction Catalyst to Construct Photovoltaic Water Splitting System with Solar-to-Hydrogen Efficiency of 16.9%. *Adv. Sci.* **2019**, *6*, 1900465.

(46) Niu, S.; Jiang, W.-J.; Wei, Z.; Tang, T.; Ma, J.; Hu, J.-S.; Wan, L.-J. Se-Doping Activates FeOOH for Cost-Effective and Efficient Electrochemical Water Oxidation. *J. Am. Chem. Soc.* **2019**, *141*, 7005−7013.

(47) Shao, L.; Sun, H.; Miao, L.; Chen, X.; Han, M.; Sun, J.; Liu, S.; Li, L.; Cheng, F.; Chen, J. Facile Preparation of NH_2-Functionalized Black Phosphorene for the Electrocatalytic Hydrogen Evolution Reaction. *J. Mater. Chem. A* **2018**, *6*, 2494−2499.

(48) Liu, D.; Wang, J.; Lu, J.; Ma, C.; Huang, H.; Wang, Z.; Wu, L.; Liu, Q.; Jin, S.; Chu, P. K.; Yu, X.-F. Direct Synthesis of Metal-Doped Phosphorene with Enhanced Electrocatalytic Hydrogen Evolution. *Small Methods* **2019**, *3*, 1900083.

(49) Nsanzimana, J. M. V.; Dangol, R.; Reddu, V.; Duo, S.; Peng, Y.; Dinh, K. N.; Huang, Z.; Yan, Q.; Wang, X. Facile Synthesis of Amorphous Ternary Metal Borides-Reduced Graphene Oxide Hybrid with Superior Oxygen Evolution Activity. *ACS Appl. Mater. Interfaces* **2019**, *11*, 846−855.

(50) Nsanzimana, J. M. V.; Reddu, V.; Peng, Y.; Huang, Z.; Wang, C.; Wang, X. Ultrathin Amorphous Iron-Nickel Boride Nanosheets for Highly Efficient Electrocatalytic Oxygen Production. *Chem. - Eur. J.* **2018**, *24*, 18502−18511.

(51) Masa, J.; Weide, P.; Peeters, D.; Sinev, I.; Xia, W.; Sun, Z.; Somsen, C.; Muhler, M.; Schuhmann, W. Amorphous Cobalt Boride (Co_2B) as a Highly Efficient Nonprecious Catalyst for Electrochemical Water Splitting: Oxygen and Hydrogen Evolution. *Adv. Energy Mater.* **2016**, *6*, 1502313.

(52) Chen, H.; Ouyang, S.; Zhao, M.; Li, Y.; Ye, J. Synergistic Activity of Co and Fe in Amorphous Cox-Fe-B Catalyst for Efficient Oxygen Evolution Reaction. *ACS Appl. Mater. Interfaces* **2017**, *9*, 40333−40343.

(53) Wang, Q.; Xu, C.-Q.; Liu, W.; Hung, S.-F.; Bin Yang, H.; Gao, J.; Cai, W.; Chen, H. M.; Li, J.; Liu, B. Coordination Engineering of Iridium Nanocluster Bifunctional Electrocatalyst for Highly Efficient and pH-Universal Overall Water Splitting. *Nat. Commun.* **2020**, *11*, 4246.

(54) Tao, H. B.; Xu, Y.; Huang, X.; Chen, J.; Pei, L.; Zhang, J.; Chen, J. G.; Liu, B. A General Method to Probe Oxygen Evolution Intermediates at Operating Conditions. *Joule* **2019**, *3*, 1498−1509.

(55) Burke, M. S.; Kast, M. G.; Trotochaud, L.; Smith, A. M.; Boettcher, S. W. Cobalt-Iron (Oxy)hydroxide Oxygen Evolution Electrocatalysts: The Role of Structure and Composition on Activity, Stability, and Mechanism. *J. Am. Chem. Soc.* **2015**, *137*, 3638−48.

(56) Behler, J.; Parrinello, M. Generalized Neural-Network Representation of High-Dimensional Potential-Energy Surfaces. *Phys. Rev. Lett.* **2007**, *98*, 146401.

(57) Larsen, P. M.; Schmidt, S.; Schiøtz, J. Robust Structural Identification *via* Polyhedral Template Matching. *Modell. Simul. Mater. Sci. Eng.* **2016**, *24*, 055007.

(58) Nørskov, J. K.; Logadottir, A.; Lindqvist, L.; Kitchin, J. R.; Bligaard, T.; Jonsson, H. Origin of the Overpotential for Oxygen Reduction at a Fuel-Cell Cathode. *J. Phys. Chem. B* **2004**, *108*, 17886−17892.

(59) Behler, J. First Principles Neural Network Potentials for Reactive Simulations of Large Molecular and Condensed Systems. *Angew. Chem., Int. Ed.* **2017**, *56*, 12828−12840.

(60) Behler, J.; Parrinello, M. Generalized Neural-Network Representation of High-Dimensional Potential-Energy Surfaces. *Phys. Rev. Lett.* **2007**, *98*, 146401.

(61) Jain, A.; Ong, S. P.; Hautier, G.; Chen, W.; Richards, W. D.; Dacek, S.; Cholia, S.; Gunter, D.; Skinner, D.; Ceder, G.; Persson, K. A. The Materials Project: A Materials Genome Approach to Accelerating Materials Innovation. *APL Mater.* **2013**, *1*, 011002.

(62) Wang, H.; Zhang, L.; Han, J.; Weinan, E. DeePMD-Kit: A Deep Learning Package for Many-Body Potential Energy Representation and Molecular Dynamics. *Comput. Phys. Commun.* **2018**, *228*, 178−184.

(63) Giannozzi, P.; Baroni, S.; Bonini, N.; Calandra, M.; Car, R.; Cavazzoni, C.; Ceresoli, D.; Chiarotti, G. L.; Cococcioni, M.; Dabo, I.; Corso, A. D.; de Gironcoli, S.; Fabris, S.; Fratesi, G.; Gebauer, R.; Gerstmann, U.; Gougoussis, C.; Kokalj, A.; Lazzeri, M.; Martin-Samos, L.; et al. Quantum Espresso: A Modular and Open-Source Software Project for Quantum Simulations of Materials. *J. Phys.: Condens. Matter* **2009**, *21*, 395502.

(64) Plimpton, S. Fast Parallel Algorithms for Short-Range Molecular Dynamics. *J. Comput. Phys.* **1995**, *117*, 1−19.

(65) Man, I. C.; Su, H. Y.; Calle-Vallejo, F.; Hansen, H. A.; Martínez, J. I.; Inoglu, N. G.; Kitchin, J.; Jaramillo, T. F.; Nørskov, J. K.; Rossmeisl, J. Universality in Oxygen Evolution Electrocatalysis on Oxide Surfaces. *ChemCatChem* **2011**, *3*, 1159−1165.

(66) Kurth, S.; Perdew, J. P.; Blaha, P. Molecular and Solid-State Tests of Density Functional Approximations: LSD, GGAs, and Meta-GGAs. *Int. J. Quantum Chem.* **1999**, *75*, 889−909.

(67) Jones, R. O.; Gunnarsson, O. The Density Functional Formalism, Its Applications and Prospects. *Rev. Mod. Phys.* **1989**, *61*, 689−746.

Tunable electronic band structure, luminescence properties and thermostability of (Gd$_{1-x}$La$_x$)$_2$Si$_2$O$_7$:Ce scintillator by adjusting La/Gd ratio[☆]

Qinhua Wei [a, †], Zhenzhen Zhou [b, †], Weijie Zhang [a], Gao Tang [a], Qian Liu [b], Laishun Qin [a, *], Hongsheng Shi [c, **]

[a] College of Materials and Chemistry, China Jiliang University, Hangzhou 310018, China
[b] State Key Laboratory of High Performance Ceramics and Superfine Microstructure, Shanghai Institute of Ceramics, Chinese Academy of Sciences, Shanghai 200050, China
[c] Xinjiang Technical Institute of Physics & Chemistry, Chinese Academy of Sciences, Urumqi 830011, China

ARTICLE INFO

ABSTRACT

Mixed crystal strategy is an effective approach of improving the luminescence properties of optical materials and has been adopted widely in many systems. In this paper, the La-mixed Gd$_2$Si$_2$O$_7$:Ce polycrystalline samples were successfully synthesized by a sol-gel method. The crystal structure and luminescence properties were confirmed and discussed by XRD, UV-Vis luminescence spectra, and XEL, respectively. The vacuum ultraviolet excitation spectra and thermoluminescence glow curves were also systematically investigated and discussed at varied temperature. A combination of the first-principles calculations and optical characterization experiments was employed to study the electronic band structure of host material, revealing that the band gap is narrowed and the 5d$_1$ level of Ce^{3+} shifts to higher energy as the La content increases. The luminescence thermo-stability and activation energy were also measured and calculated. It indicates that thermo-stability is strongly dependent on the La concentration. An effective approach is developed to tune the electronic band structure, luminescence properties and thermostability of (Gd$_{1-x}$La$_x$)$_2$Si$_2$O$_7$:Ce scintillator by adjusting La/Gd ratio.

© 2020 Chinese Society of Rare Earths. Published by Elsevier B.V. All rights reserved.

1. Introduction

Because of high light output and good energy resolution, Ce^{3+} doped rare-earth pyrosilicate materials are promising scintillation and optical materials, such as Gd$_2$Si$_2$O$_7$:Ce (GPS:Ce), Lu$_2$Si$_2$O$_7$:Ce (LPS:Ce), and La$_2$Si$_2$O$_7$:Ce (LaPS:Ce).[1–3] However, there are two disadvantages: high-temperature phase transformation and incongruently melting. It is difficult to obtain large size single crystal directly from its melt and the research works were constrained. Mixed crystal strategy is regarded as an effective way to stabilize the pyrosilicate phase while it can also improve the luminescence properties of material.[4] As previously reported, the mixed crystal strategy has been applied in different materials, such as Sc^{3+} admixed LuBO$_3$:Ce,[5] Y^{3+} admixed Gd$_3$ (Al,Ga)$_5$O$_{12}$:Ce,Pr,[6] Ga^{3+} admixed Y$_3$Al$_5$O$_{12}$:Ce,[7] La(Br,Cl)$_3$:Ce and K(Ca,Sr)I$_3$:Eu single crystals.[8,9] Mixing Sc^{3+} was adopted to optimize LuBO$_3$:Ce properties by tuning the 5d states location of Ce^{3+} relative to the conduction band bottom.[9] The improved light output of Ga^{3+} admixed LuAG:Ce results from the elimination of the Lu$_{Al}^{3+}$ antisite defects by suppressing the shallow electron traps.[10,11] Besides, because of the decrease of energy for creation of one electron-hole pair, the scintillation efficiency can also be enhanced by narrowing the host band gap. The band gap and scintillation efficiency of K(Ca,Sr)I$_3$:Eu crystal were varied for different constituents.[8] As we known, the splitting of 5d levels of Ce^{3+} or Eu^{2+} is greatly affected by the location environment and electronic band structure,[12] which plays an important role on the luminescence properties. Thus, the positive effect is achieved by modifying the electronic band structure[9,13,14] or decreasing the thermalization length of electron-hole

pairs.[15,16] A conclusion was proofed that the host band gap and the energy levels of luminescence centers are mainly related with the electronic structure of material. The band gap is a critical parameter and can be tunable when the values of host's constituents are varying.

In GPS:Ce system, the different crystal structures of tetragonal, orthorhombic and triclinic modifications of GPS:Ce were obtained by varying the doping concentration and sintering temperature. The problems of crystal structure instability and incongruent melting can also be solved through replacing gadolinium with optically inactive lanthanum (La^{3+}).[17,18] In our previous reports,[19] a combinatorial method was employed to rapidly screen the effects of La, Ce co-doping on the luminescent properties of $Gd_2Si_2O_7$. Meantime, the phase transformation and scintillation properties were discussed. Compared with GPS:Ce crystal, the La^{3+} admixed GPS:Ce crystal presents a higher light output (42000 ph/MeV) and more excellent energy resolution (FWHM) (5% at 662 keV).[20,21] However, the researches focus on the crystal growth, crystal structure, temperature effect and incongruent melting problem.[21–24] The study on electronic structure and energy levels of luminescence centers is rare. An empirical factor has been developed,[25] namely, the relationship between (L_{ex}/L_{veg}) and (R_a/R_b).[3] L_{ex} is the experimental light yield and L_{veg} is the Vegard's law prediction data. The R_a/R_b is the ratio of ionic radii between substitution and host ions. The maximum value of (L_{ex}/L_{veg}) tends to decrease when (R_a/R_b)[3] is above 1.5 and the limit of the solubility range is at $R_a/R_b = 1.15$, which is in accordance with Goldschmidt's rules. Based on that, the ionic radius ratio of R_{La}/R_{Gd} is about 1.1, which is close to the empirical criterion value of 1.15[25]. Therefore, choosing La^{3+} as the substitution ion is reasonable and beneficial. But, the electronic structure of $(Gd,La)_2Si_2O_7$:Ce is not fully clear. The ionization energy and the change trend of energy separation between the trivalent lanthanide lowest 5d state and the conduction band (CB) were also uncertain.

In this paper, the effects of lanthanum substitution on the electronic structure, band gap, luminescence properties and thermo-stability of GPS:Ce were investigated and discussed precisely. The first-principle calculation and optical method were employed to study the electronic structure and band gap of La-GPS. The thermoluminescence (TL), vacuum ultraviolet (VUV) and X-ray excited luminescence (XEL) spectra, and photoluminescence (PL) as a function of temperature were also discussed. Finally, the luminescence thermostability and activation energy for thermal quenching were also presented.

2. Experimental

2.1. Samples preparation

High-purity (99.99%) Gd_2O_3, La_2O_3, Ce $(NO_3)_3$ and nitric acid (A.R.), TEOS (A.R.) were used as starting materials. The 1 mol% Ce^{3+} doped $(Gd_{1−x}La_x)_2Si_2O_7$ ($x = 0.1, 0.3, 0.5, 1.0$) crystalline powders were synthesized by a sol-gel method. This gel was dried at 120 °C and then calcined in a muffle furnace at 600 °C for 2 h. The pulverous mixtures were ground in an agate mortar, and then reacted at 1400 °C for 10 h in Al_2O_3 crucibles in a weak reducing atmosphere, the detail could be seen in our previous report.[12,19] The crystal structure and phase purity of the powder samples were analyzed by X-ray diffraction (XRD) with Cu Kα radiation ($\lambda = 0.1541$ nm) made by Bluke.

2.2. First-principle calculation methods

The crystal structural optimization and electronic structures of $(Gd_{1−x}La_x)_2Si_2O_7$ were calculated based on the crystal structure of

triclinic $Gd_2Si_2O_7$ (98723-ICSD). $(Gd_{1−x}La_x)_2Si_2O_7$ was modeled by building a cell including four structural units (44 atoms) with Gd atoms. There are four lattice sites for Gd atom in triclinic $Gd_2Si_2O_7$, as shown in Fig. S1. One Gd atom at Gd1 site is replaced by one La atom in model of $(Gd_{1−x}La_x)_2Si_2O_7$ ($x = 0.125$) (Fig. S2(a)). Based on model of $(Gd_{1−x}La_x)_2Si_2O_7$ ($x = 0.125$), another remote Gd atom at Gd2 site is replaced by one La atom in model of $(Gd_{1−x}La_x)_2Si_2O_7$ ($x = 0.25$) (Fig. S2(b)) to avoid the interaction between La atoms as much as possible. Based on that, the other two Gd atoms at Gd3 and Gd4 sites respectively are replaced by two La atoms in model of $(Gd_{1−x}La_x)_2Si_2O_7$ ($x = 0.50$) in considering about all lattice sites of Gd atom as much as possible (Fig. 2, Fig. S2(c)). First principle calculation was performed using density function theory (DFT) in Perdew-Burke-Ernzerhof generalized gradient approximation (PBE-GGA) for the exchange correlation functional, with projector augmented-wave (PAW) pseudo-potentials, as implemented in the Vienna *ab initio* simulation package (VASP).[26,27] The geometry optimizations were performed until the total energies and the Hellmann−Feynman forces on the atoms converged to 5×10^{-5} eV and 0.2 eV/nm, respectively. The optimized lattice structures were used for calculation both band structures and density of states (DOS). A plane wave cutoff energy of 520 eV was used throughout the calculation. The k-point meshes for Brillouin zone sampling were $8 \times 8 \times 4$, according to the Monkhorst-Pack scheme.[28]

2.3. Optical property measurements

The VUV-UV excitation and emission spectra were measured at the Beijing Synchrotron Radiation Facility (BSRF) VUV spectroscopy workstation on a U24 beam line from 10 to 296 K. The specific measurement details could be found in Ref.29.

The PL spectra and photoluminescence excitation (PLE) spectra under UV light were recorded on a Hitachi F-4600 spectrometer. The temperature dependence of PL intensity was measured in a range from room temperature (RT) to 250 °C. The sample was kept at each temperature for at least 30 min to stabilize the intensity. The slits for both excitation and emission measurements were all set as 2.5 nm and the scan speed was fixed at 240 nm/min.

The XEL was measured on an XEL spectrometer, assembled at the Shanghai Institute of Ceramics. The X-ray tube was operated at the condition of $V = 70$ kV and $I = 2$ mA. The TL glow curves of crystals were determined through an FJ-427A1 TL spectrometer with a linear heating rate of 1 °C/s from RT to 400 °C. Prior to each TL measurement, the samples were irradiated under X-ray for 90 s.

3. Results and discussion

The phase formation process of $(Gd_{1−x}La_x)_2Si_2O_7$:Ce samples calcined at 600, 1100, 1200, 1300 and 1400 °C has been discussed in our previous work.[12,19] In this paper, the $(Gd_{1−x}La_x)_2Si_2O_7$:Ce ($x = 0.1, 0.3, 0.5, 1.0$) crystalline samples were prepared at 1400 °C. The room temperature XRD patterns of samples are consistent with the Refs. 30−33, which had a triclinic structure with $P/1$ space group (JCPDS 23-247). Although the La-GPS structure is identical to that of triclinic GPS, the lattice parameter distortion might have occurred when the La^{3+} ion is substituted in the Gd^{3+} site, which has a larger ionic radius by 10% than that of Gd^{3+}. The monoclinic phase structure of $La_2Si_2O_7$:Ce was obtained by comparison with the lanthanum pyrosilicate ($La_2Si_2O_7$, ICSD card No.71807) when Gd^{3+} is replaced by La^{3+} completely (see Fig. S3).

3.1. Electronic band structure

As previously discussed, the luminescence property is related with the electronic band structure, which is affected by co-doping

La^{3+}. The VUV-UV excitation spectra of $(Gd_{1-x}La_x)_2Si_2O_7$:Ce ($x = 0.1$, 0.3, 0.5) crystalline at 296 K and the enlarged spectra are shown in Fig. 1. The different excitation bands were obtained in the excitation spectra of Ce^{3+}, which can be assigned to five electronic transitions from the 4f ground state to the 5d level of Ce^{3+}, labeled as 5d$_1$, 5d$_2$, 5d$_3$, 5d$_4$ and 5d$_5$ in the spectra. The excitation peak of 274 nm should be ascribed to electronic transitions from $^8S_{7/2}$ to ^6I_x of Gd^{3+}. From the enlarged Gaussian fitting spectra of Fig. 1(b), it can be found that the 5d$_1$ excited state has a slightly shift to high energy (from 3.63 to 3.71 eV) when the La content is increased, as listed in Table 1. Fig. 2 presents the VUV spectra of $(Gd_{1-x}La_x)_2Si_2O_7$:Ce ($x = 0.1$, 0.3, 0.5) samples measured at 10 K, monitored at $\lambda_{em} = 313$ nm and $\lambda_{em} = 367$ nm, respectively. The wavelength range is from 125 to 210 nm. Combining Figs. 1 and 2, the dominant excitation band, located at 168 nm (higher energy side), should be assigned to the host excitation. With the increase of La content, the dominant band of 168 nm shifts to longer wavelength (low energy). It means that the band gap of the $(Gd_{1-x}La_x)_2Si_2O_7$:Ce host becomes narrower. The specific values are also listed in Table 1. Besides, a new excitation band of 177 nm is also observed. Referring to the data of Li$_3$Gd(BO$_3$)$_3$ system,[34,35] the excitation band of 177 nm should correspond to the electronic transitions from $^8S_{7/2}$ to $^6G_{13/2}$ of Gd^{3+}. Obviously, it has a heavy overlap with the band of 168 nm. As the La content increases, the overlaps are enhanced while the peak intensity of 177 nm is decreased sharply. Thus, a case occurs that the edge of the conduction band is narrowing and merging the energy level of 177 nm when the La content is increased, as discussed in Ga^{3+} admixed LuAG:Ce system. To further validate the changes of host band gap, the TL measurement and first-principle calculation were adopted. Usually, in the same system, the featured point defect of material should exist in all samples. Therefore, the trap depth trend as a function of La content was adopted to study the change of band gap. The two-dimensional TL of $(Gd_{1-x}La_x)_2Si_2O_7$:Ce ($x = 0.1$, 0.3, 0.5) crystalline were studied

Table 1
The optical and calculated parameter of $(Gd_{1-x}La_x)_2Si_2O_7$:Ce samples derived from VUV-UV excitation spectra and PBE method.

Gd/La ratio	9:1	7:3	5:5
Energy of 5d$_1$ (eV)	3.63	3.66	3.71
Optical data (eV)	7.08	7.04	6.88
Calculated data (eV)	4.49	4.48	4.41

and the glow curves are presented in Fig. 3. Three featured point defects are observed in all samples at testing temperature, labeled A, B and C. The entire glow curve has an obvious shift to lower temperature as La content increased, qualitatively indicating that the conduction band edge of host becomes lower, as reported in Refs. 9,14.

The density of states and band structure of $(Gd_{1-x}La_x)_2Si_2O_7$ ($x = 0.125$, 0.25, 0.5) were calculated by PBE method and are shown in Fig. 4. In order to clarity, the Fermi level was set to be zero. With La content increasing, the band gap energy (E_g) was obtained, located at 4.49, 4.48 and 4.41 eV, respectively. Because of the nature of PBE method, it is rational that the calculated absolute value deviates from the experiment data, determined by optical method. In view of the density of states, the valence band maximum (VBM) consists of O-2p orbitals while the conduction band minimum (CBM) consists of Gd-5d and La-4f orbitals. The Si states have no contribution on the VBM and CBM. The host absorption band of 168 nm, as plotted in Figs. 1 and 2, can be ascribed to O-2p, -La-4f and Gd-5d electron transitions. From Fig. 4, it is found that as the La contents are raised, the CBM becomes lower, which is well in agreement with the VUV and TL data (trap depths). The E_g of experiment and calculation versus the La^{3+} content is presented in Fig. 5(a-b). The band gap is decreased clearly as La^{3+} concentration increases. It is important that the band gap variation trend is the
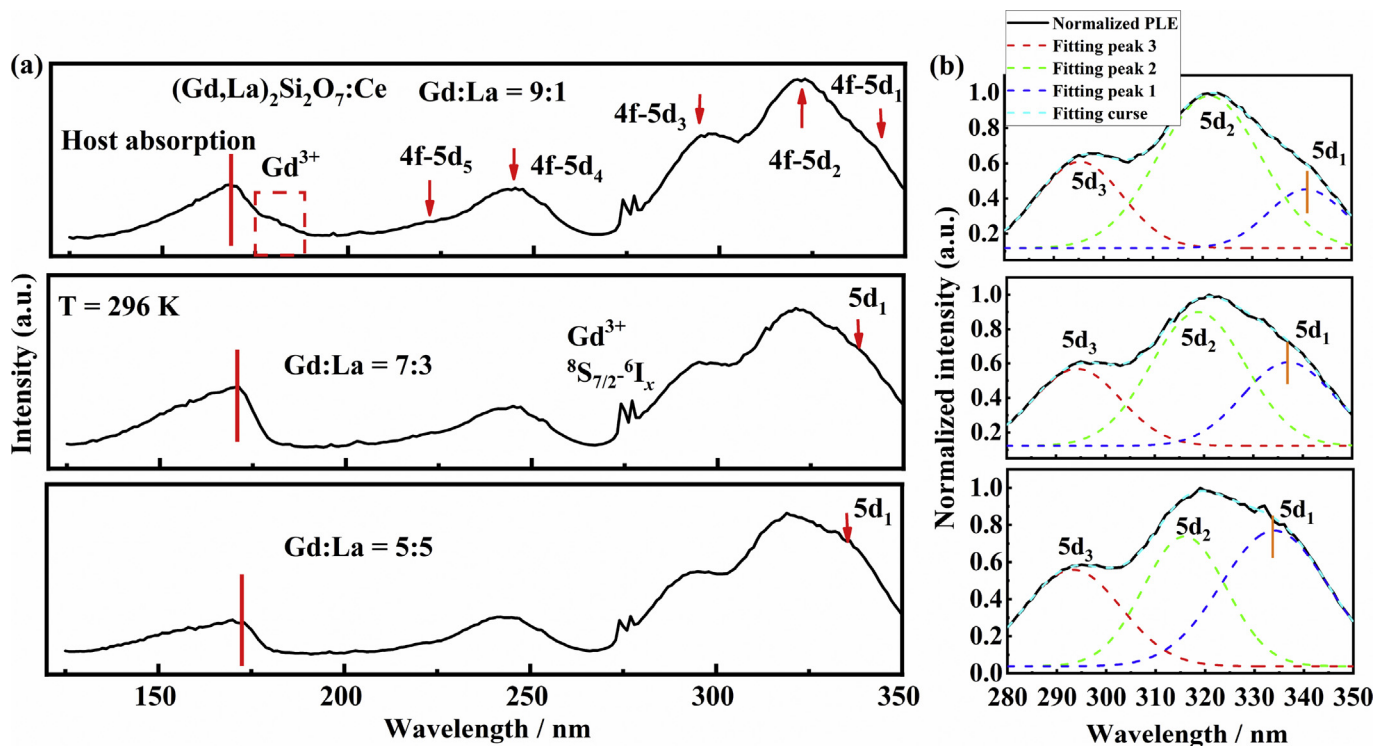

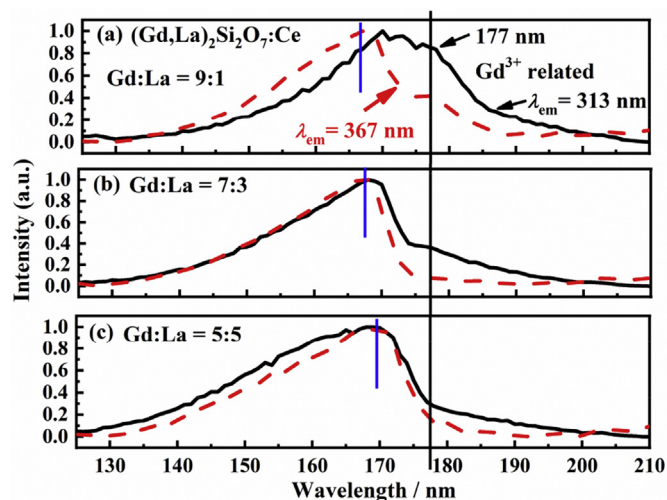**Fig. 1.** The VUV-UV excitation spectra (a) and enlarged spectra (b) of $(Gd_{1-x}La_x)_2Si_2O_7$:Ce ($x = 0.1$, 0.3, 0.5) samples at 296 K, monitored at $\lambda_{em=}$367 nm.

Fig. 2. VUV excitation spectra of $(Gd_{1-x}La_x)_2Si_2O_7$:Ce ($x = 0.1, 0.3, 0.5$) samples at 10 K, monitored at $\lambda_{em} = 313$ and 367 nm, the detection range is from 125 to 210 nm.

same for the three different methods (optical method, TL and PBE method). According to the above analysis, the Gd^{3+} related energy band of 177 nm is near to the bottom of conduction band. The energy separation becomes smaller as La content increases. Thus, the lower conduction band edge is merging the energy band of 177 nm. As discussed above, the $5d_1$ excited state of Ce^{3+} has a blue-shift and the $5d_1$ level position becomes higher in the forbidden gap with the increase of La content. The bottom of conduction band and the $5d_1$ state of Ce^{3+} present an opposite moving direction, which will narrow the energy separation ΔE (ionization energy). The schematic diagram is shown in Fig. 5(c). The similar electronic structure change is also observed in the $(Gd_xLu_{1-x})_3(Ga_xAl_{1-x})_5O_{12}$:Ce and K(Ca,Sr)I$_3$ crystals.[8,10] Normally, the narrower energy separation indicates that the enhancing unwanted excited-state ionization of emission center will cause the luminescence efficiency deteriorated with the increase of La content. The luminescence properties are discussed in the next.
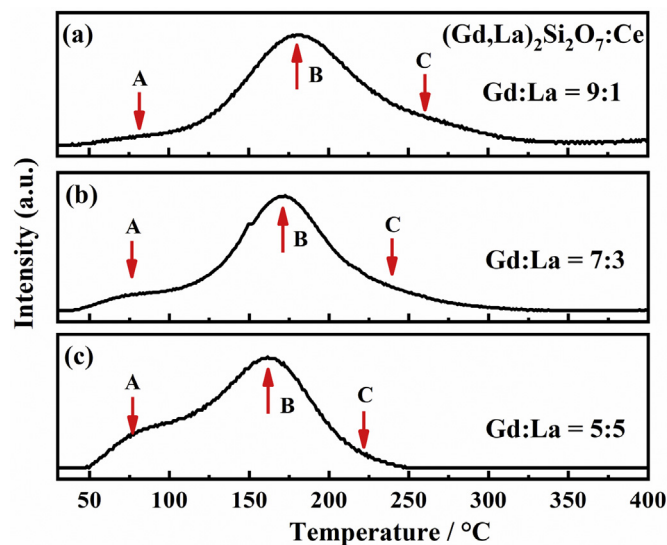

Fig. 3. Two-dimensional TL grow curves of $(Gd_{1-x}La_x)_2Si_2O_7$:Ce ($x = 0.1, 0.3, 0.5$) powders. A, B and C are TL peak of featured point defects for different temperatures, respectively.

3.2. Luminescence properties

The emission spectra, excitation spectra and normalized spectra of $(Gd_{1-x}La_x)_2Si_2O_7$:Ce ($x = 0.1, 0.3, 0.5, 1.0$) samples ($\lambda_{ex} = 320$ nm, $\lambda_{em} = 366$ nm) were tested and are shown in Fig. 6(a−c), the inset is intensity of I_{second}/I_{max} of different samples. From Fig. 6(a, b), two emission peaks, located at 367 and 387 nm for the $(Gd_{0.9}La_{0.1})_2$-Si_2O_7:Ce sample (Gd:La = 9:1), are assigned to the Ce^{3+} electron transition from the lowest 5d level to $^2F_{5/2}$ and $^2F_{7/2}$ of 4f sublevels.[36] I_{max} and I_{second} correspond to the intensity of the maximum emission peak (367 nm) and the second emission peak (387 nm) of Ce^{3+}, respectively. Six main excitation peaks can be found, which are located at 218, 245, 272, 291, 318 and 340 nm, respectively. Obviously, the peak of 272 nm is ascribed to the $^8S_{7/2}$-^6I_J electron transition of Gd^{3+} while the other peaks are ascribed to the 4f-5d electron transition of Ce^{3+}. As La^{3+} concentration increases, the excitation peaks have a shift to shorter wavelength (blue-shift), which is well in agreement with the VUV-UV excitation spectra. Except that, the luminescence efficiency is deteriorated while the blue-shifting of main emission peaks of 367 and 387 nm happens, as shown in Fig. 6(c). As described above, the type of lanthanide ions greatly affect the energy of 5d electron of Ce^{3+}. Therefore, when Gd^{3+} (9.38 nm) is replaced partly by the larger La^{3+} (10.32 nm), the binding energy and covalence between Ce^{3+} and anion ligands are both decreased, which leads to change of the surrounding crystal field environment of Ce^{3+}. Hence, the blue-shifting of spectra can be ascribed to the weaker crystal-field splitting. In other words, the moderate lattice disorder results in the blue-shifting. It is also approved that the $5d_1$ level position of Ce^{3+} becomes higher as La concentration increases. Secondly, the value of I_{second}/I_{max} is enhanced for higher La concentration sample as shown in inset of Fig. 6(c). In this system, different independent sites can be occupied by Ce ions and the emission bands are overlapped. Therefore, the re-absorption of different sites Ce ions occurs. This phenomenon will have positive contribution to the luminescence thermo-stability, as observed and reported in Refs. 37-39. Fig. 6(d) presents the emission spectra of different proportions of Gd/La under 272 nm excited at room temperature, the inset is the enlarged spectra. From Fig. 6(d), the emission peaks of 367 and 313 nm, corresponding to Ce^{3+} and Gd^{3+} electron transition, respectively, are rather related with the La^{3+} concentration. Especially for 313 nm, it is increased first and then becomes weaker when the La^{3+} content is increased from 10 mol% to 100 mol%. It can be explained by the varied energy transfer process, as observed and discussed in GSO:Ce and $Gd_{9.33}(SiO_4)_6O_2$ system.[40,41] The nearest neighbor distance of Gd^{3+}-Gd^{3+} is small at low La^{3+} concentration (Gd/La ratio is 9:1). There is a high nonradiative energy transfer rate among Gd^{3+} ions, resulting in a weak emission peak of 313 nm. As the La concentration increased gradually (Gd/La ratio is 3:7 and 5:5), it leads to the separation between the Gd^{3+} ions. The strength of resonant energy transfer between Gd^{3+} ions is reduced accordingly and the emission intensity is enhanced. But, the lower emission intensity of 313 nm can be assigned to the lower Gd^{3+} concentration for the higher La concentration samples. The luminescence properties and complicated energy transfer processes (Gd^{3+}-Gd^{3+}, Gd^{3+}-Ce^{3+} and Ce^{3+}-Ce^{3+}) are varied as La^{3+} content changed. However, the further mechanism is not yet clear and more experiments need to be done.

The XEL properties of $(Gd_{1-x}La_x)_2Si_2O_7$:Ce ($x = 0.1, 0.3, 0.5, 1.0$) samples were determined and are shown in Fig. 7. $La_2Si_2O_7$:1 mol% Ce (LaPS:Ce) is chosen as a reference sample. According to the integration value of the Ce^{3+} emission intensity in XEL spectra, the output of $(Gd_{1-x}La_x)_2Si_2O_7$:Ce samples is deteriorated as La content increased. The $(Gd_{0.9}La_{0.1})_2Si_2O_7$:Ce sample presents the highest output (about 3.6 times of LaPS:Ce sample). Through Gaussian fitting, it is also found that the value of I_{second}/I_{max} is enhanced and

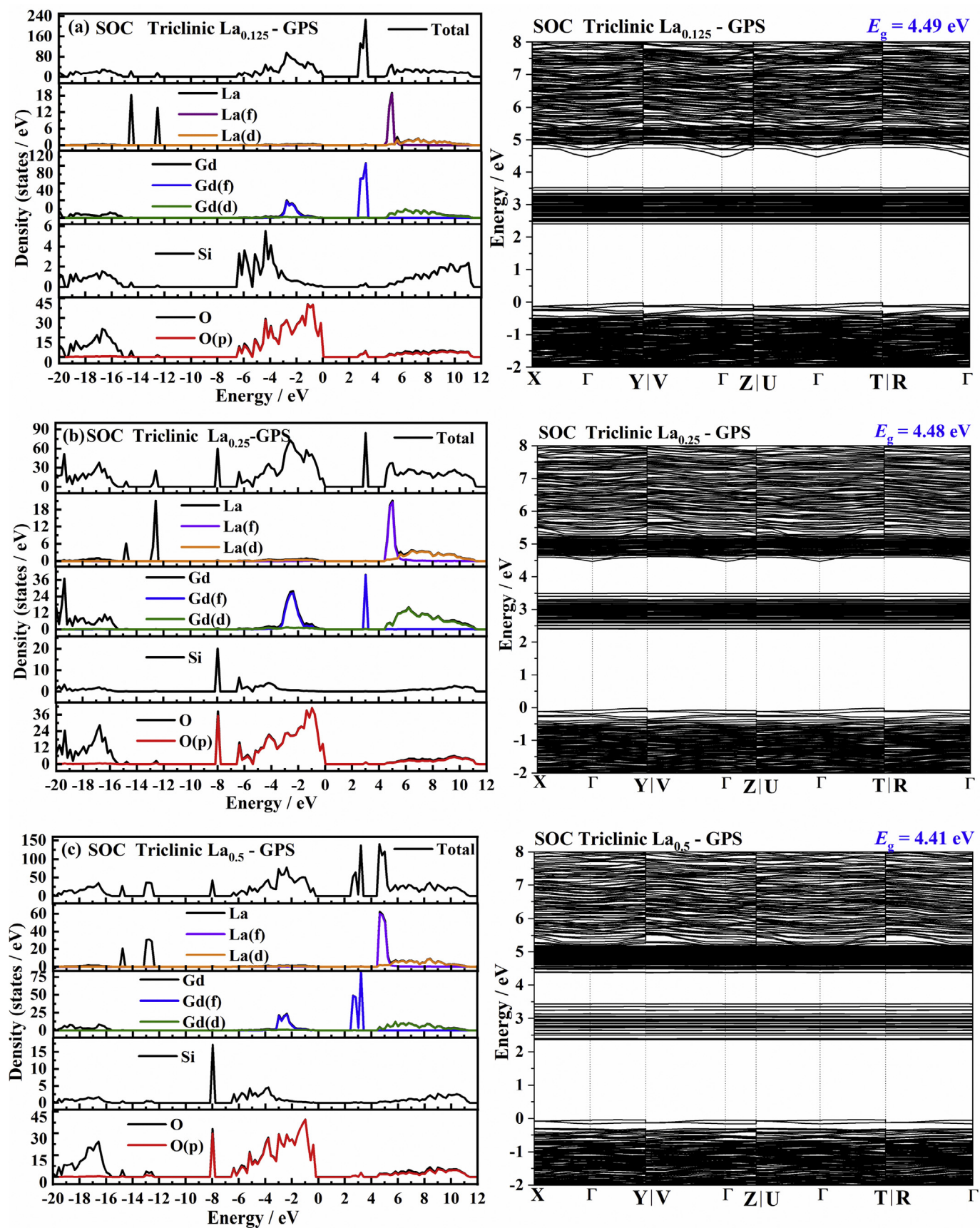**Fig. 4.** Projected density of states and band gap of $(Gd_{1-x}La_x)_2Si_2O_7$ ($x = 0.125, 0.25, 0.5$) samples.
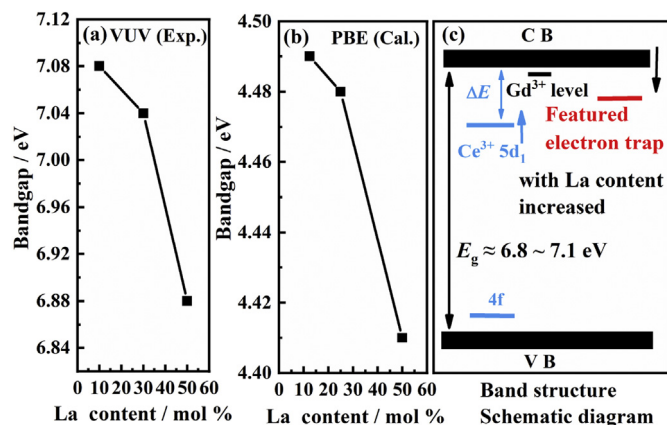
Fig. 5. The energy band gap values determined by optical methods (a), and PBE calculation methods (b) and the schematic diagram (c) of band structure with the variation of La content in $(Gd_{1-x}La_x)_2Si_2O_7$.

the varied trend of emission peaks in XEL spectra is consistent with that of the UV excitation. Combined with the electron band structure result, it is rational and approved that the luminescence efficiency becomes much worse as La^{3+} concentration increased. In a

word, the deteriorated luminescence efficiency results from the narrower energy separation.

3.3. Thermo-stability

The temperature dependence of Ce^{3+} emission spectra was measured under the optimum excitation wavelength and is given in Fig. 8(a–c). It is clear that the main emission peak of 367 nm originates from the 5d-4f electron transition of Ce^{3+}. As testing temperature is raised, the full width at half maximum (FWHM) of the emission band is increased, which results from the improved electron−phonon interaction. Meanwhile, the emission peak has a shift toward longer wavelength (red-shift) at the higher temperature as shown in the inset of Fig. 8. Based on the emission spectra of the Ce^{3+} luminescence, the integral emission intensity versus temperature for different proportions of Gd/La samples was also measured and is presented in Fig. 8(d). Usually, the thermal quenching temperature (T_{50}) is defined as the temperature at which the emission intensity is 50% of that at room temperature (RT).[42] The variation trend of thermal quenching temperature can be seen obviously as La^{3+} content rises. Thermal quenching temperatures of all samples are over 500 K. It means that these samples present an excellent thermo-stability. Except that, the luminescence yields of $La_{0.1}$-GPS:Ce and $La_{0.3}$-GPS:Ce samples are increased

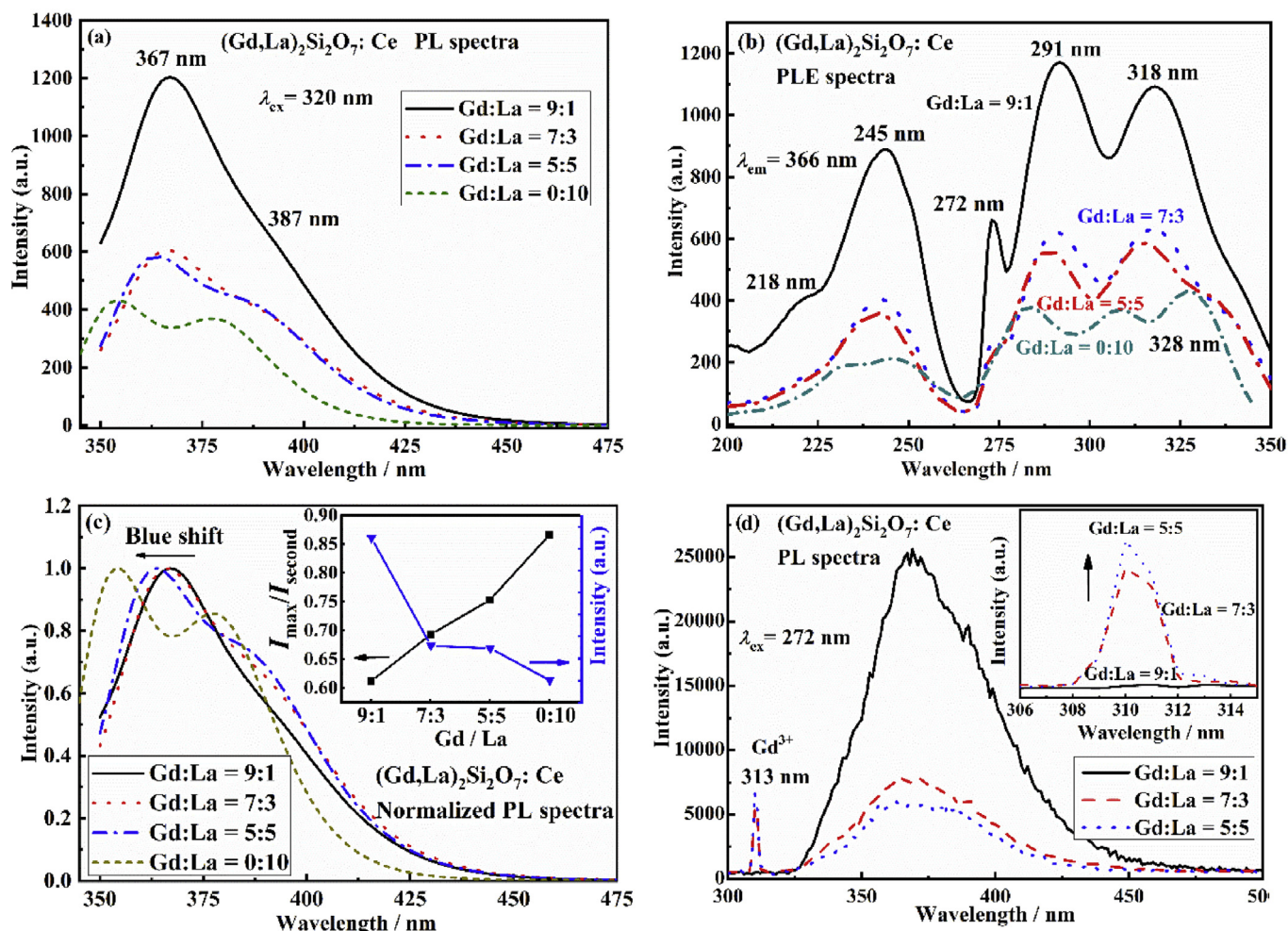**Fig. 6.** Emission spectra (a), excitation spectra (b) and normalized spectra (c) of $(Gd_{1-x}La_x)_2Si_2O_7$:Ce ($x = 0.1, 0.3, 0.5, 1.0$) samples ($\lambda_{ex} = 320$ nm, $\lambda_{em} = 366$ nm), the inset is intensity of I_{second}/I_{max} of different samples; (d) Emission spectra of $(Gd_{1-x}La_x)_2Si_2O_7$:Ce ($x = 0.1, 0.3, 0.5$) samples ($\lambda_{ex} = 272$ nm).
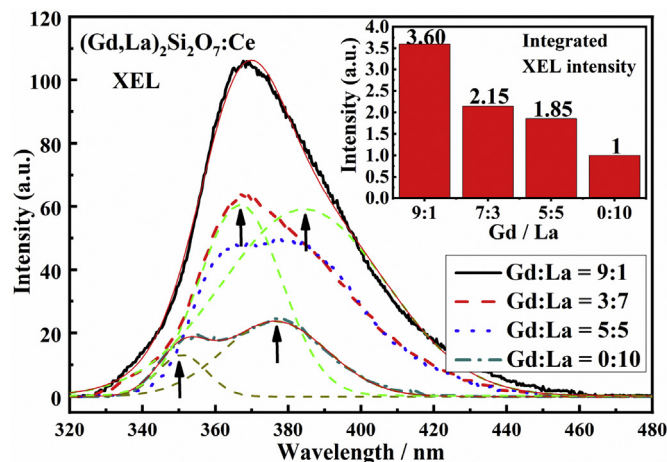
Fig. 7. XEL spectra of $(Gd_{1-x}La_x)_2Si_2O_7$:Ce (x = 0.1, 0.3, 0.5, 1.0) samples and the inset is normalized integrated intensity.

by 5% while the $La_{0.5}$-GPS:Ce sample is about 10%−15% when the temperature is raised from RT to 100 °C. This phenomenon was also observed and discussed in other pyrosilicate and β-SiAlON

phosphor.[43] This is an important advantage for applications under severe temperature conditions (well logging, nuclear stations, etc.)

Usually, a high value of activation energy ($\Delta E'$) means good thermo-stability. Based on the data of temperature-dependent PL spectra, the activation energy of various samples was fitted and calculated by the Arrhenius equation,[44] the results are shown in Fig. 9.

$$I(T) \approx \frac{I_0}{1 + c\exp\frac{-\Delta E'}{kT}} \tag{1}$$

In Eq. (1), $\Delta E'$ is the thermal quenching activation energy. I_0 and $I(T)$ are luminescence intensity of initial temperature and T temperature, respectively, c is constant and k is Boltzmann's constant. From Fig. 9, the activation energy of $(Gd_{1-x}La_x)_2Si_2O_7$:Ce (x = 0.1, 0.3, 0.5, 1.0) can be tuned between 0.38 and 0.95 eV by varying La^{3+} concentration. The results show that La^{3+} has positive contribution to the luminescence thermo-stability. The thermal excitation of 5d electrons has a strong effect on the thermal quenching of Ce^{3+} emission. Normally, the decrease of ΔE should lead to the decrease of the activation energy $\Delta E'$ and present a worse luminescence thermo-stability. However, the variation trend of thermal quenching deviates from the typical quenching model in our experiments. It is interesting that this phenomenon was also found in some other Ce^{3+} or Eu^{2+} doped compounds systems.[45,46] To further
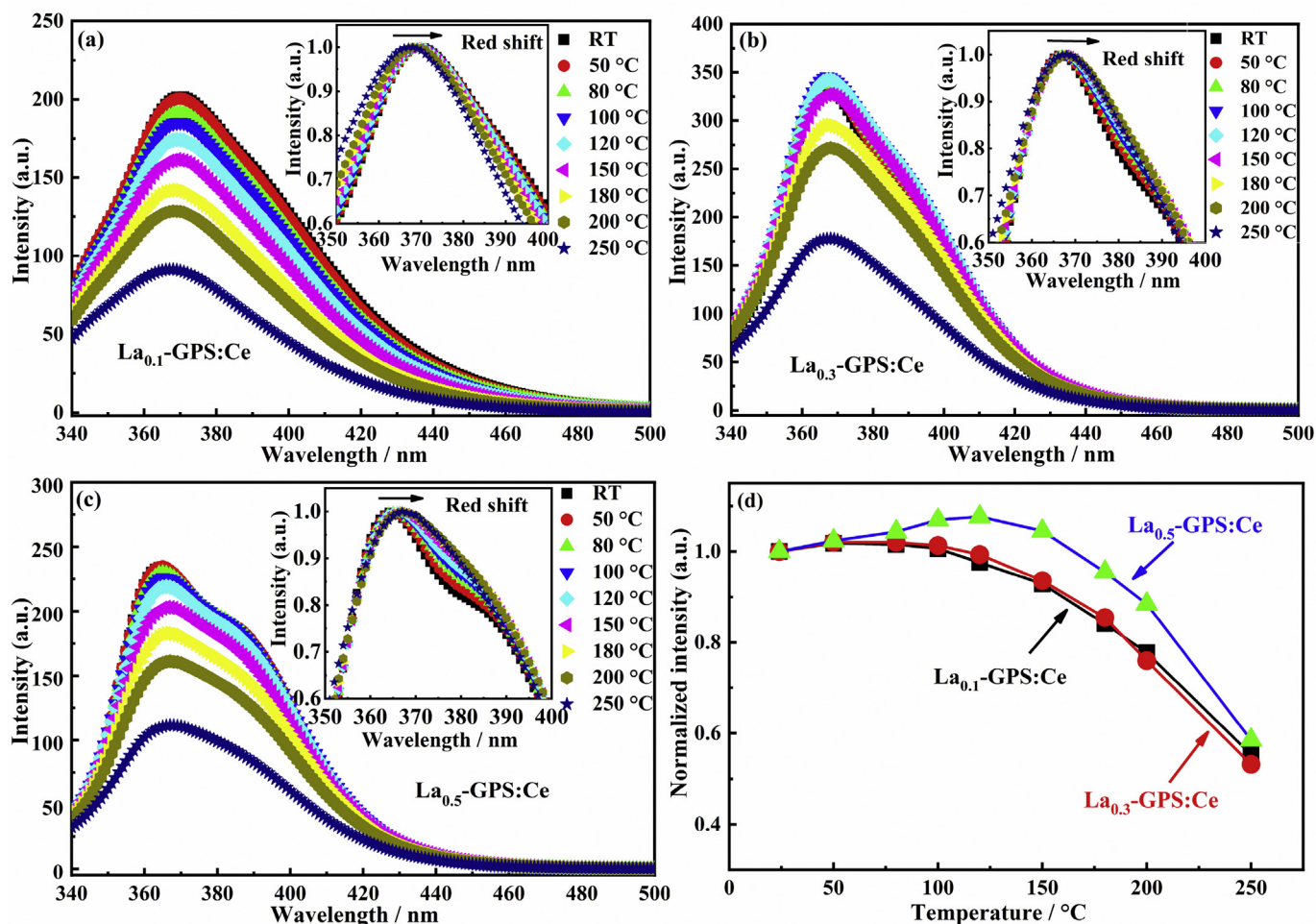

Fig. 8. Temperature-dependent PL spectra of $(Gd_{1-x}La_x)_2Si_2O_7$:Ce (x = 0.1, 0.3, 0.5) recorded at an excitation wavelength of 291 nm (a−c) and integral intensity results for different testing temperatures (d).
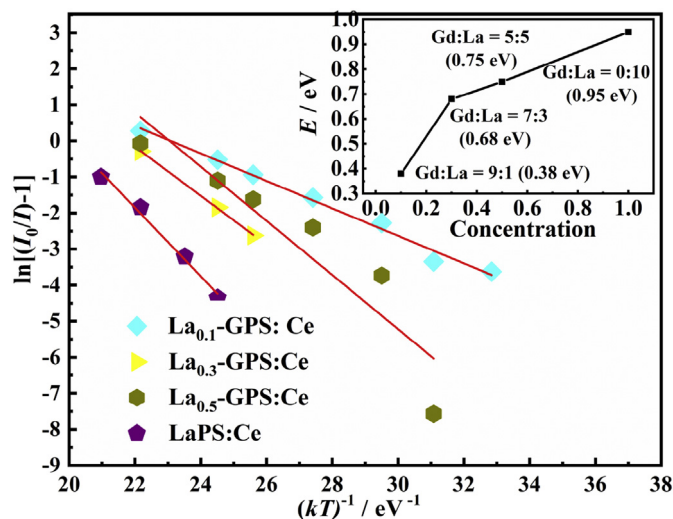
Fig. 9. Activation energy of $(Gd_{1-x}La_x)_2Si_2O_7$:Ce (x = 0.1, 0.3, 0.5,1.0) samples.

study the thermo-stability, the temperature dependence of normalized emission intensity under different excitation wavelengths was investigated, as shown in Fig. S4. The luminescence thermo-stability is varied under different excitation wavelengths, but they have the same evolution tendency. The excitation wavelength of 273 nm, ascribed to the $^8S_{7/2}$-^6I_J electron transition of Gd^{3+}, shows the best luminescence thermo-stability for the entire wavelength. Based on the experiment data and literature[35,37,38,41], the abnormal variation trend of thermal quenching can be explained as below:

In La-mixed GPS:Ce system, two types of overlapped spectra of Ce^{3+} - Ce^{3+} and Ce^{3+} - Gd^{3+} are observed, indicating that the emitted light of Gd^{3+} and Ce^{3+} will be re-absorbed by Ce^{3+}. Besides, the electron that escaped from Gd^{3+} or relaxed to $5d_1$ state of Ce^{3+}, will recombine with the Ce^{3+} center at later time, and then emit light, as reported in Ref.38. Those processes have benefit to enhanced luminescence thermo-stability. On the other hand, the resonant energy transfer is strongly related to the environment temperature. In this system, there are several different resonant energy transfer processes (including Gd^{3+}- Gd^{3+}, Gd^{3+} - Ce^{3+} and Ce^{3+}- Ce^{3+}). For the low La^{3+} concentration sample (Gd/La = 9:1), the resonant energy transfer between Gd^{3+} ions is dominant. The more energy is wasted by resonant energy transfer and shows a worse thermo-stability. With the La^{3+} content increasing, the resonant energy transfer is reduced and the dipole-dipole energy migration is dominant. Compared with resonant energy transfer, the dipole-dipole energy migration has a weaker relationship with the environment temperature, indicating a better thermo-stability, as observed and reported in Ref.41. The abnormal variation trend of thermal quenching is rational and acceptable. However, more experiments need to be done.

4. Conclusions

In summary, the $(Gd_{1-x},La_x)_2Si_2O_7$:1 mol%Ce polycrystallines were synthesized by a sol-gel method. The UV, VUV, XEL spectra, and TL were investigated systematically. The first-principles DFT-based theoretical calculation and optical experiments demonstrate that the band gap of $(Gd_{1-x},La_x)_2Si_2O_7$:Ce material and the relative position of $5d_1$ state of Ce^{3+} are varied by co-doping La^{3+}. Meantime, the energy separation ΔE becomes smaller when La^{3+} concentration is increased, leading to the deteriorated luminescence

efficiency. The result of luminescence thermo-stability indicates that the method of co-doping La^{3+} has a positive effect on improving the luminescence thermo-stability. The activation energy $\Delta E'$ is altered between 0.38 and 0.95 eV. In a word, the electronic band structure, luminescence properties and activation energy of $(Gd_{1-x},La_x)_2Si_2O_7$:Ce are tuned successfully by adjusting La/Gd ratio. More importantly, this work should be helpful to understand the relationship among composition, electronic structure and luminescence properties.

Appendix A. Supplementary data

Supplementary data to this article can be found online at https://doi.org/10.1016/j.jre.2020.09.011.

References

1. Baumer V, Gerasymov I, Sidletskiy O, Voloshina O, Neicheva S. Growth and characterization of tetragonal structure modification of beta-Gd2Si2O7:Ce. *J Alloys Compd*. 2011;509:8478.
2. Feng H, Ding DZ, Li HY, Lu S, Pan SK, Chen XF, et al. Growth and luminescence characteristics of cerium-doped yttrium pyrosilicate single crystal. *J Alloys Compd*. 2010;489:645.
3. Wei QH, Liu GH, Zhou ZZ, Wan JQ, Yang H, Liu Q. Preparation and spectroscopic properties of Ce-doped La2Si2O7 as novel scintillator materials. *Mater Lett*. 2014;126:178.
4. Gektin AV, Belsky AN, Vasil'ev AN. Scintillation efficiency improvement by mixed crystal. *IEEE Trans Nucl Sci*. 2014;61:262.
5. Wu YT, Ren GH, Ding DZ, Yang F, Pan SK. Effects of scandium on the bandgap and location of Ce^{3+} levels in Lu1-xScxBO3:Ce scintillators. *Appl Phys Lett*. 2012;100:021904.
6. Ou YY, Zhou WJ, Ma FK, Liu CM, Zhou RF, Su F, et al. Luminescence tuning of Ce^{3+}, Pr^{3+} activated (Y,Gd)AGG system by band gap engineering and energy transfer. *J Rare Earths*. 2020;5:514.
7. Boiko V, Zeler J, Markowska M, Dai Z, Gerus A, Bolek P, et al. Persistent luminescence from Y3Al2Ga3O12 doped with Ce^{3+} and Cr^{3+} after X-ray and blue light irradiation. *J Rare Earths*. 2019;11:1200.
8. Bao HB, Qin LS, Ding YG, Li ZG, Shi HS, Shu KY. Growth and scintillation properties of La(Cl0.05Br0.95)3:Ce crystal. *Chin Phys Lett*. 2013;30: 088101.
9. Wu YT, Li Q, Chakoumakos BC, Zhuravleva M, Lindsey AC, Johnson II JA, et al. Quaternary iodide K(Ca,Sr)I3:Eu^{2+} single-crystal scintillators for radiation detection: crystal structure, electronic structure, and optical and scintillation properties. *Adv Opt Mater*. 2016;4:1518.
10. Nikl M, Pejchal J, Mihokova E, Mares JA, Ogino H, Yoshikawa A, et al. Antisite defect-free Lu3(GaxAl1-x)5O12:Pr scintillator. *Appl Phys Lett*. 2006;88:141916.
11. Fasoli M, Vedda A, Nikl M, Jiang C, Uberuaga BP, Andersson DA, et al. Band-gap engineering for removing shallow traps in rare-earth Lu3Al5O12 garnet scintillators using Ga^{3+} doping. *Phys Rev B*. 2011;84:081102.
12. Wei QH, Shi HS, Zhou ZZ, Liu GH, Chen Z, Qin LS, et al. A study on the structure, luminescence and thermo-stability of polycrystalline Gd2Si2O7:Ce and (Gd,La)2Si2O7:Ce. *J Mater Chem C*. 2017;5:1443.
13. Kamada K, Endo T, Tsutumi K, Yanagida T, Fujimoto Y, Fukabori A, et al. Composition engineering in Cerium-doped (Lu,Gd)3(Ga,Al)5O12 single-crystal scintillators. *Cryst Growth Des*. 2011;11:4484.
14. Bessiere A, Dorenbos P, van Eijk CWE, Kramer KW, Gudel HU, Mello DC, et al. Luminescence and scintillation properties of the small band gap compound LaI3:Ce^{3+}. *Nucl Instrum Methods Phys Res A*. 2005;537:22.
15. Birowosuto MD, Dorenbos P, Kramer KW, Gudel HU. Ce^{3+} activated LaBr3 - xIx: high-light-yield and fast-response mixed halide scintillators. *J Appl Phys*. 2008;103:103517.
16. Sidletskiy O, Belsky A, Gektin A, Neicheva S, Kurtsev D, Kononets V, et al. Structure-property correlations in a Ce-doped (Lu,Gd)2SiO5:Ce scintillator. *Cryst Growth Des*. 2012;12:4411.
17. Jary V, Nikl M, Kurosawa S, Shoji Y, Mihokova E, Beitlerova A, et al. Luminescence characteristics of the Ce^{3+}-doped pyrosilicates: the case of La-admixed Gd2Si2O7 single crystals. *J Phys Chem C*. 2014;118:26521.
18. Murakami R, Kurosawa S, Yamane H, Horiai T, Shoji Y, Yokota Y, et al. Crystal structure of Ce-doped (La,Gd)2Si2O7, grown by the Czochralski process. *J Alloys Compd*. 2018;748:404.
19. Wei QH, Wan JQ, Liu GH, Zhou ZZ, Yang H, Wang JC, et al. Combinatorial optimization of La, Ce-co-doped pyrosilicate phosphors as potential scintillator materials. *ACS Comb Sci*. 2015;17:217.

20. Suzuki A, Kurosawa S, Shishido T, Pejchal J, Yokota Y, Futami Y. A Fast and high-energy-resolution oxidescintillator: Ce-doped $(La,Gd)_2Si_2O_7$. *Appl Phys Exp*. 2012;5:102601.
21. Kurosawa S, Horiai T, Murakami R, Shoji Y, Pejchal J, Yamaji A, et al. Comprehensive study on Ce-doped $(Gd,La)_2Si_2O_7$ scintillator. *IEEE Trans Nucl Sci*. 2018;65:2136.
22. Youichi T, Kaneko JH, Mikio H, Moyuru M, Hiroyuki I. Crystal growth and scintillation properties of $La_{0.2}Ce_{0.05}Gd_{1.75}Si_2O_7$ single crystal with triclinic structure. *Opt Mater*. 2014;36:665.
23. Horiai T, Kurosawa S, Murakami R, Shoji Y, Pejchal J, Yamaji A, et al. Crystal growth and temperature dependence of light output of Ce-doped $(Gd, La, Y)_2Si_2O_7$ single crystals. *J Cryst Growth*. 2018;486:173.
24. Kurosawa S, Shishido T, Sugawara T, Nomura A, Yubuta K, Suzuki A, et al. Scintillation properties of $Ce:(La,Gd)_2Si_2O_7$ at high temperatures. *Nucl Instrum Methods Phys Res A*. 2015;772:72.
25. Sidletskiy O, Gektin A, Belsky A. Light-yield improvement trends in mixed scintillation crystals. *Phys Status Solidi A*. 2014;211:2384.
26. Kresse G, Furthmuller J. Efficient iterative schemes for *ab initio* total-energy calculations using a plane-wave basis set. *Phys Rev B*. 1996;54:169.
27. Kresse G, Joubert D. From ultra-soft pseudo potentials to the projector augmented-wave method. *Phys Rev B*. 1999;59:1758.
28. Monkhorst HJ, Pack JD. Special points for brillonin-zone integrations. *Phys Rev B*. 1976;13:5188.
29. Wu YT, Ding DZ, Pan SK, Yang F, Ren GH. The luminescence and energy transfer in Pr^{3+}-Ce^{3+} co-doped $Lu_{0.8}Sc_{0.2}BO_3$ crystals. *J Lumin*. 2012;132:251.
30. Shinde S, Pitale S, Singh SG, Ghosh M, Tiwari B, Sen S, et al. Structural and luminescence properties of $Gd_2Si_2O_7$:Ce prepared by solution combustion followed by heat treatment. *J Alloys Compd*. 2015;630:68.
31. Horiai T, Kurosawa S, Murakami R, Yamaji A, Shoji Y, Ohashi Y, et al. Temperature dependence of Ce-doped $(Gd_{0.6}La_{0.4})_2Si_2O_7$ scintillators. *Opt Mater*. 2017;65:56.
32. Kawamura S, Higuchi M, Kaneko JH, Nishiyama S, Haruna J, Saeki S, et al. Phase relations around the pyrosilicate phase in the Gd_2O_3-Ce_2O_3-SiO_2 System. *Cryst Growth Des*. 2009;9:1470.
33. Kawamura S, Kaneko JH, Higuchi M, Fujita F, Homma A, Haruna J, et al. Investigation of Ce-doped $Gd_2Si_2O_7$ as a scintillator material. *Nucl Instrum Methods Phys Res Sect A*. 2007;583:356.
34. Ogorodnikov IN, Pustovarov VA, Omelkov SI, Vostrov DO, Isaenko LI. Optical and luminescence spectroscopy studies of electronic structure of $Li_6GdB_3O_9$ single crystals. *Opt Mater*. 2014;36:1060.
35. Yan F, Pan SK, Ding DZ, Wu YT, Ren GH. Optical characterization of neutron detection crystal $Li_6Gd(BO_3)_3$. *Acta Phys Sin*. 2011;60:113301.
36. Mu ZF, Wang YH, Hu YH, Wu HY, Deng LY, Xie W, et al. The afterglow and thermoluminescence properties of $Y_3Al_5O_{12}$:Ce^{3+}. *Acta Phys Sin*. 2011;60:013201.
37. Feng H, Jary V, Mihokova E, Ding DZ, Nikl M, Ren GH, et al. Temperature dependence of luminescence characteristics of $Lu_{2(1-x)}Y_{2x}SiO_5$:Ce^{3+} scintillator grown by the Czochralski method. *J Appl Phys*. 2010;108:033519.
38. Wang TT, Ding DZ, Chen XP, Hou W, Shi JJ. Exploring the energy transfer processes in $Lu_{2(1-x)}Y_{2x}SiO_5$:Ce crystals. *J Rare Earths*. 2018;36:685.
39. Ning LX, Lin LH, Li LL, Wu CB, Duan CK, Zhang YF, et al. Electronic properties and 4f-5d transitions in Ce-doped Lu_2SiO_5: a theoretical investigation. *J Mater Chem*. 2012;22:13723.
40. Suzuki H, Tombrello TA, Melcher CL, Schweitzer JS. Energy-transfer mechanism in $Gd_2(SiO_4)O$:Ce scintillators. *IEEE Trans Nucl Sci*. 1994;41:681.
41. Wei QH, Liu YQ, Miao YT, Li YX, Shi HS, Qin LS. Effects of lanthanum substitution on the luminescence properties and energy transfer mechanism of $Gd_{9.33}(SiO_4)_6O_2$:Ce polycrystalline. *J Lumin*. 2018;194:610.
42. Xie RJ, Hirosaki N, Kimura N, Sakuma KM. 2-phosphor-converted white light-emitting diodes using oxynitride/nitride phosphors. *Appl Phys Lett*. 2007;90:191101.
43. Liu TC, Cheng BM, Hu SF, Liu RS. Highly stable red oxynitride β-SiAlON:Pr^{3+} phosphor for light-Emitting diodes. *Chem Mater*. 2011;23:3698.
44. Bhushan S, Chukichev MV. Temperature dependent studies of cathodoluminescence of green band of ZnO crystals. *J Mater Sci Lett*. 1988;7:319.
45. Liu CM, Qi ZM, Ma CG, Dorenbos P, Hou DJ, Zhang S, et al. High light yield of $Sr_8(Si_4O_{12})Cl_8$:Eu^{2+} under X-ray excitation and its temperature-dependent luminescence characteristics. *Chem Mater*. 2014;26:3709.
46. Ueda J, Dorenbos P, Bos AJ, Meijerink JA, Tanabe S. Insight into the thermal quenching mechanism for $Y_3Al_5O_{12}$:Ce^{3+} through thermo luminescence excitation spectroscopy. *J Phys Chem C*. 2015;119:25003.

Check for updates

Hydrogenated ZnIn$_2$S$_4$ microspheres: boosting photocatalytic hydrogen evolution by sulfur vacancy engineering and mechanism insight†

Yanze Wang, [ID] Da Chen, [ID] * Laishun Qin,* Junhui Liang [ID] and Yuexiang Huang

In some oxide photocatalysts, changing their surface structure rather than crystal structure by introducing some defects (such as oxygen vacancies) has been proven to be effective in enhancing the separation efficiency of photogenerated carriers and thus photocatalytic activity. To the best of our knowledge, however, such a surface defect engineering strategy for sulfide photocatalysts has rarely been verified. The present work shows the first case of employing pressure hydrogenation to prepare hydrogenated ZnIn$_2$S$_4$ (H-ZIS) microspheres with surface-deficient porous structures, which are favorable for furnishing sufficient surface sulfur vacancies to realize excellent photocatalytic hydrogen evolution reactions. The hydrogen evolution rate (HER) of H-ZIS is as high as 1.9 mmol h^{-1} g^{-1} (nearly 8.6 times that of the pristine ZIS sample), which rivals or exceeds those of previously-reported ZIS-based photocatalysts under visible light irradiation. Meanwhile, the inherent correlation between surface sulfur vacancies and photocatalytic activities of H-ZIS is also explored. Thus, this work demonstrates the feasibility of enhancing the hydrogen evolution capability of sulfide photocatalysts by the formation of sulfur vacancies through a pressure hydrogenation process.

1. Introduction

Interest in converting solar energy into hydrogen through direct photocatalytic water splitting arises due to its potential application in solving two critical global issues of fossil energy shortage and environmental pollution.[1–3] It is known that direct photocatalytic water splitting for the hydrogen evolution reaction involves several crucial steps, namely light absorption by photocatalysts, transport of photogenerated carriers, and redox reactions on the surface of photocatalysts.[4] Apparently, the hydrogen evolution efficiency largely depends on the type of photocatalyst, the separation mechanism for photogenerated carriers, and surface reactivity. Among the currently developed semiconductor photocatalysts, ZnIn$_2$S$_4$ (ZIS), a typical ternary sulfur compound, is regarded as a promising candidate for the hydrogen evolution reaction by direct photocatalytic water splitting due to its appropriate band gap, relatively high photocatalytic activity, and attractive chemical stability.[5,6] Considerable investigations on the hydrogen evolution reaction by the ZIS photocatalyst have been carried out,[7–9] and a relatively high hydrogen evolution rate (HER) of 600–700 μmol h^{-1} g^{-1} for pure ZIS was obtained by Xia *et al.*[10] Such a HER value, however,

is far below the expectation for meaningful commercial applications. Therefore, it is still a big challenge for scientists to further improve the photocatalytic activity of ZIS and subsequently to increase its HER.

Considering that a photocatalytic reaction takes place on the surface of photocatalyst particles and that the surface is not only the reaction site but also the transport route for photogenerated carriers, the surface structure of catalysts would play a key role in determining the final HER value. In some oxide photocatalysts, changing their surface structure rather than crystal structure by introducing some defects was found to be effective in enhancing the separation efficiency of photogenerated carriers and thus photocatalytic activity. For instance, Chen *et al.*[11] reported that the hydrogen evolution reaction capability of TiO$_2$ photocatalysts could be significantly improved by introducing oxygen vacancy defects into nanocrystalline TiO$_2$ photocatalysts by high temperature and pressure hydrogenation. The formation of surface oxygen vacancy defects during the hydrogenation process could alter the band gap structure of TiO$_2$ and promote the generation, separation and migration process of photogenerated carriers. Recently, it has been reported that the introduction of oxygen vacancy defects in In$_2$O$_3$ porous ultrathin sheets could not only enhance the visible light absorption ability, but also improve the separation efficiencies of photogenerated carriers. The obtained visible light photocurrent density of the In$_2$O$_3$ porous ultrathin sheets with rich oxygen vacancies was 15 times higher than that of the pristine In$_2$O$_3$ ultrathin sheets.[12] Similar effects were also found

College of Materials and Chemistry, China Jiliang University, Hangzhou, 310018, Zhejiang, China. E-mail: dchen_80@hotmail.com, qinlaishun@cjlu.edu.cn

in other oxide photocatalysts such as ZnO,[13] SrTiO$_3$,[14] BiFeO$_3$,[15] *etc.* by introducing surface defects though the effect scale may differ significantly. Further studies[16,17] also revealed that the concentration of surface oxygen vacancies which is determined by the hydrogenation methods and conditions is also an important factor affecting the photocatalytic activities of hydrogenated photocatalysts. Considering the fact that sulfur and oxygen are in the same main-group and have similar chemical properties, it is reasonable to expect that the hydrogen evolution reaction activity of ZIS photocatalysts could be enhanced by introducing surface defects such as sulfur vacancies into ZIS photocatalysts. Very recently, Zhu *et al.*[18] reported the *in situ* hydrogenated ZIS nanosheets (H$_x$ZIS), which were obtained at room temperature under UV-vis light illumination within several hours. The optimized H$_x$ZIS exhibited the best photocatalytic performance with a ten-fold H$_2$ production enhancement compared to pristine ZIS nanosheets, demonstrating the feasibility of using hydrogenation engineering to enhance the photocatalytic activities of sulfide photocatalysts. Though the hydrogenation of ZIS was reported in their work, to the best of our knowledge, the pressure hydrogenation induced surface defect engineering strategy for ZIS photocatalysts as well as the corresponding photocatalytic mechanism has not been previously reported and verified in the literature.

Herein, the ZIS microsphere particles were prepared by a hydrothermal method and a pressure hydrogenation process was employed to obtain hydrogenated ZIS photocatalysts. The ZIS surface structure evolution, effect of surface defects and hydrogen evolution reaction performance of the hydrogenated ZIS microspheres are characterized and discussed. The correlation between the hydrogenation-induced surface defect structure and photocatalytic activity of hydrogenated products was tentatively proposed. It was found that the stability of hydrogenation-induced sulfur vacancies on the surface of hydrogenated ZIS was poor, thus leading to the poor photocatalytic stability of hydrogenated ZIS. The essential reasons for the instability of surface sulfur vacancies are still unclear and need further exploration. This work is important to increase our understanding on the effect of surface defects on the separation of photogenerated carriers and surface reactivity of photocatalysts. Such a surface defect engineering strategy may also expand to other photocatalyst materials.

2. Experimental

2.1 Preparation of pristine ZnIn$_2$S$_4$

All chemicals were of analytical grade and used without further purification. 50 mL of a mixed aqueous solution containing ZnCl$_2$ (2 mmol), In(NO$_3$)$_3$·H$_2$O (4 mmol) and thioacetamide (TAA, 8 mmol) was placed in a Teflon-lined stainless steel autoclave. The autoclave was sealed and maintained at 160 °C for 6 hours. After the autoclave was cooled to room temperature, the obtained precipitate was collected and washed several times with ethanol and deionized water. After drying in an oven at 60 °C for 24 hours, the final product of pristine ZIS particles was obtained.

2.2 Hydrogenation of ZnIn$_2$S$_4$

Hydrogenation of ZIS was performed in a home-built hydrogenation furnace. Typically, 0.5 g of the as-prepared ZIS powder was put in a stainless steel hydrogenation reactor (with a height of 93.5 mm and an inner diameter of 8.5 mm, possessing an effective volume of ~5 mL, as shown in Fig. S1, ESI†) in connection with the vacuum system. After being evacuated to 10 Pa, the reactor was heated to 300 °C at a heating rate of 10 °C min^{-1} and was then filled with hydrogen (purity higher than 99.999%) at a pressure of 2.0 MPa. The inlet valve at the top of the reactor was subsequently closed, and the reactor was kept at high temperature and high pressure for 4 h. The total amount of hydrogen in the reactor used for hydrogenation treatment was calculated to be about 2 mmol according to the ideal gas equation ($PV = nRT$, where P, V, T, n and R are the pressure, volume, absolute temperature, the molar amount of gas, and the ideal gas constant, respectively).[19] After hydrogenation treatment, the reactor was cooled down to room temperature and the high pressure hydrogen within the reactor was subsequently released. The hydrogenated ZIS (H-ZIS) product was then taken out from the reactor.

2.3 Material characterization

X-ray powder diffraction (XRD) patterns were obtained on a Bruker D2 Advance X-ray diffractometer using Cu K_α irradiation. The morphological microstructures of the products were measured by field emission scanning electron microscopy (FESEM, Hitachi-SU8010) and transmission electron microscopy (TEM, JEOL JEM-2100F). The elemental binding energies of the products were analyzed by X-ray photo-electron spectroscopy (XPS, Al-K$_\alpha$ 1063, Thermo Fisher Scientific). The UV-visible diffuse reflectance spectra (DRS) of the products were carried out by an UV-visible spectrophotometer (Shimadzu UV-3600), using BaSO$_4$ as the reference. The steady state photoluminescence (PL) spectra and time-resolved transient photoluminescence (TRPL) decay spectra were collected on a Hitachi High-Tech F-7000 fluorescence spectrophotometer with a xenon lamp as an excitation source (λ = 300 nm). The Brunauer–Emmett–Teller (BET) specific surface area and pore structure of the samples were characterized by a Micromeritics Gemini VII 2390 porosimeter. The electron spin resonance (ESR) signals were examined on a Bruker model ESR A300 spectrometer.

2.4. Photocatalytic and photoelectrochemical measurements

Photocatalytic H$_2$ evolution experiments were performed in a Lab-H$_2$ photocatalytic system, where a 300 W xenon arc lamp assembled with an optical filter ($\lambda \geq$ 420 nm) was used as a visible light source and placed vertically on top of a quartz glass photocatalytic reactor. In a typical process, 0.2 g of the photocatalyst was dispersed in 100 mL of NaSO$_3$ (0.25 M) and Na$_2$S (0.35 M) mixed aqueous solution under stirring in the reactor, which was cooled by refluxing water to eliminate any thermal catalytic effect. A certain amount of H$_2$PtCl$_6$·6H$_2$O aqueous solution was then added into the dispersion to deposit the desired amount of Pt cocatalyst (*i.e.*, 0.5 wt%) on the surface of

This journal is © the Owner Societies 2019

Phys. Chem. Chem. Phys., 2019, **21**, 25484–25494 | 25485

the photocatalyst by an *in situ* photodeposition method. Prior to irradiation, the system was evacuated several times to remove the residual air inside, and then the dispersion was continuously stirred in the dark for 30 min to reach the absorption equilibrium. The light source was thereafter switched on to initiate the photocatalytic reaction for hydrogen production, and the hydrogen production amount was intermittently collected and analyzed online using a gas chromatography mass spectrometer (GEL-SPJZN GC-7820, nitrogen as a carrier gas) with a thermal conductivity detector (TCD). By contrast, no appreciable amount of H_2 was produced when the photocatalytic experiments were performed in the dark or without the photocatalyst. To evaluate the photocatalytic stability, the remaining photocatalyst powder in the suspension was carefully recovered by centrifugation and washing and used for another photocatalytic reaction. All the reported photocatalytic data in this paper are based on the average values of three parallel experiments, and the error bars are based on the standard deviations of three parallel experiments.

For photoelectrochemical measurements, the working photo-electrodes were fabricated by doctor blading a slurry, which was prepared by mixing the obtained photocatalyst powder and a polymer binder (PVDF) at a weight ratio of 90:10 using *N*-methyl-2-pyrrolidinone (NMP) as a solvent, on an F-doped SnO_2 (FTO) conductive glass. The prepared photoelectrodes were then dried in a vacuum oven at 60 °C for 10 h. The active area of the photoelectrodes was found to be 1.0×2.0 cm^2. Photoelectro-chemical measurements were recorded on an electrochemical station (CHI660E, Shanghai Chenhua Co.) using the standard three-electrode system with the working photoelectrode, a saturated calomel electrode (SCE) as the reference electrode, and a platinum wire as the counter electrode in 0.5 M Na_2SO_4 aqueous solution. The photocurrent measurements were performed under inter-mittent visible light ($\lambda \geq 420$ nm) irradiation. Electrochemical impedance spectra (EIS) were recorded by applying an AC voltage with 5 mV amplitude in the frequency range from 0.01 Hz to 100 kHz under visible light ($\lambda \geq 420$ nm) irradiation.

3. Results and discussion

3.1 Structure evolution

To reveal the crystal structure evolution during high temperature and pressure hydrogenation processes, the XRD measurements for the ZIS and H-ZIS samples were performed. As shown in Fig. 1, all the diffraction peaks of the pristine ZIS sample could be well indexed to the hexagonal phase of ZIS (JCPDS card No. 065-2023).[20] The XRD pattern of the H-ZIS sample was similar to that of the pristine ZIS, indicating that the crystal structure of ZIS did not change during hydrogenation treatment. Fig. 2(A) and (B) show the FESEM images of the pristine ZIS and H-ZIS samples. Both samples were composed of petaloid microspheres with an average diameter of about 5 μm, and their surface was made up of a large number of interlaced petaloid nanosheets. It can be seen that the morphological structure of the ZIS sample was nearly unchanged after hydrogenation treatment, implying that the hydrogenation process would not significantly alter the
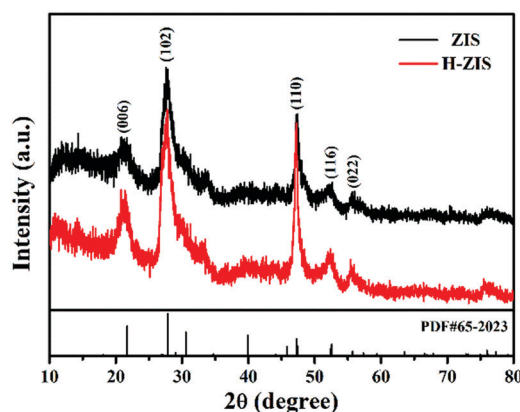

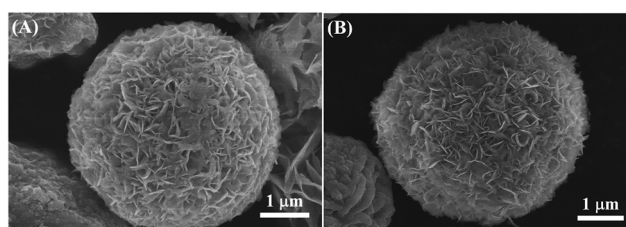Fig. 1 X-ray diffraction patterns of the prepared pristine ZIS and H-ZIS samples.

Fig. 2 FESEM images of the (A) pristine ZIS and (B) H-ZIS samples.

morphological feature of the ZIS sample. Meanwhile, the BET measurements show that the specific surface area of the H-ZIS sample was 93.2 m^2 g^{-1} which was close to that of the pristine ZIS sample (90.9 m^2 g^{-1}), further confirming that the hydro-genation treatment would not significantly change the morpho-logical structure of the pristine ZIS sample.

Fig. 3 shows the TEM images of the petal-like ultrathin nanosheets on the surface of ZIS and H-ZIS microspheres. As seen in Fig. 3(A) and (C), both the prepared ZIS and H-ZIS samples consisted of petal-like ultrathin nanosheets, and the morphological feature of the ultrathin nanosheets in the H-ZIS sample was similar to that of the ZIS sample, which was in agreement with the SEM results. Meanwhile, these ultrathin nanosheets both in the prepared ZIS and H-ZIS samples possessed a multilayered laminar structure (Fig. 3(B) and (D)), where the presence of lattice fringes with a lattice spacing of 0.324 nm corresponding to the {102} lattice plane of the ZIS crystal was clearly observed, confirming that the hydrogenation treatment would not change the high crystallinity of ZIS. It is interesting to note that the HRTEM images of the ZIS and H-ZIS samples (respectively for Fig. 3(B) and (D)) demonstrate that the multilayered laminar structure of the prepared ZIS was con-tinuously free of defects, whereas many microscopic defects (such as micropores) as denoted by the green dashed line on the top layer and the yellow dashed line on the bottom layer were found on the multilayered laminar structure of the pre-pared H-ZIS sample. The observed porous feature of the pre-pared H-ZIS sample was probably due to the massive loss of sulfur[21] caused by the high temperature and high pressure
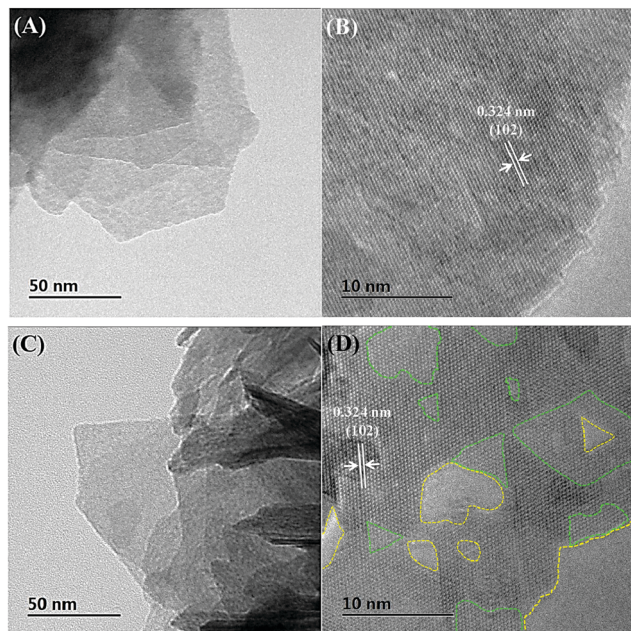
Fig. 3 TEM and HRTEM images of the (A and B) pristine ZIS and (C and D) H-ZIS samples.

hydrogenation treatment, and thereby surface defects of sulfur vacancies would be formed in the H-ZIS sample as will be discussed below.

3.2 Sulfur vacancies

It is well known that the ESR study can provide useful information for identifying the formation of different kinds of vacancy defects.[21,22] To corroborate the formation of sulfur vacancies on the surface of H-ZIS, ESR analysis was performed. Obviously, as shown in Fig. 4, both the pristine ZIS and H-ZIS samples displayed one typical single Lorentzian line in the same magnetic field region with a g-value of 2.003. This signal could be attributed to the unpaired electrons on the sulfur atoms of the sulfide, demonstrating the presence of sulfur vacancies.[21,23] Moreover, the ESR intensity was markedly strengthened after hydrogenation, indicating that more electrons were captured by
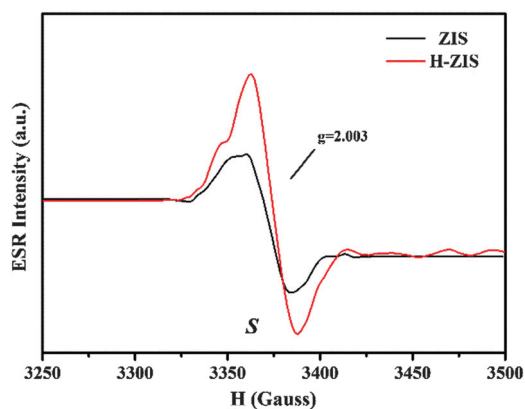

Fig. 4 ESR spectra of the prepared pristine ZIS and H-ZIS samples.

sulfur vacancies.[15,23–26] These results indicate that the hydrogenation treatment could contribute to the generation of sulfur vacancies in the sulfide, and that the sulfur vacancies are capable of trapping free electrons, which helps accelerate the transfer rate of electron–hole pairs.

To further verify the presence of sulfur vacancies in the H-ZIS sample, XPS measurements were taken to comparatively analyze the chemical states of the prepared ZIS and H-ZIS samples. As can be seen from Fig. 5(A), the XPS survey spectrum of the H-ZIS sample was similar to that of the pristine ZIS sample, indicating that the hydrogenation process would not change the chemical composition of ZIS. The survey spectra confirmed the presence of Zn, In, and S elements in the prepared ZIS and H-ZIS samples, while the other weak peaks detected at 531.78 eV and 284.28 eV corresponding to O 1s and C 1s were probably ascribed to adventitious carbon and oxygen as confirmed by the unchanged peak positions in these two samples (Fig. S3, ESI†). As shown in Fig. 5(B), the Zn 2p spectra of pristine ZIS consisted of the two binding energies around 1044.87 eV and 1021.78 eV corresponding to the Zn $2p_{1/2}$ and Zn $2p_{3/2}$ spectra, respectively, confirming the valence state of Zn^{2+}.[27,28] For the In 3d spectra (Fig. 5(C)), the two characteristic peaks of pristine ZIS centered at 452.17 eV and 444.61 eV could be identified as the binding energies of In $3d_{3/2}$ and In $3d_{5/2}$, respectively, which was correlated to the In^{3+} valence state.[27, 28] Fig. 5(D) shows the S 2p spectra for the pristine ZIS and H-ZIS samples. The binding energies of S $2p_{1/2}$ and S $2p_{3/2}$ in the pristine ZIS sample were located at 162.46 and 161.26 eV, respectively, which could be assigned to S^{2-}.[24] Nevertheless, some slight peak shifts toward higher binding energies were observed in the Zn 2p, In 3d and S 2p spectra of H-ZIS. The shift of these XPS peaks could probably be attributed to the formation of porous defects (e.g., sulfur vacancies) induced by hydrogenation treatment, which would facilitate the transfer of electrons from ZIS to sulfur vacancies and thus decrease the equilibrium electron cloud density to make the binding energies increase.[29,30] In addition, from the XPS characterization the atomic ratios of Zn/In/S in the pristine ZIS and H-ZIS samples were determined to be 1:2.07:3.89 and 1:2.05:3.42, respectively. The sulfur content in H-ZIS decreased obviously compared to that in the pristine ZIS sample, further proving the formation of the sulfur vacancies in the H-ZIS sample. In combination with the above TEM and ESR results, it can be deduced that the hydrogenation treatment could cause a massive loss of sulfur atoms, thereby forming the observed porous defects on the H-ZIS surface, which could be ascribed to those hydrogenation-induced sulfur vacancies, and that such formed sulfur vacancies could be prone to capture the electrons transferred from ZIS, thereby promoting the separation and migration of charge carriers within the H-ZIS sample.

3.3 Effect of sulfur vacancies

To investigate the influence of the hydrogenation-induced sulfur vacancies on the photocatalytic performance of ZIS, the visible light photocatalytic hydrogen production activities of the prepared ZIS and H-ZIS samples were examined. As shown
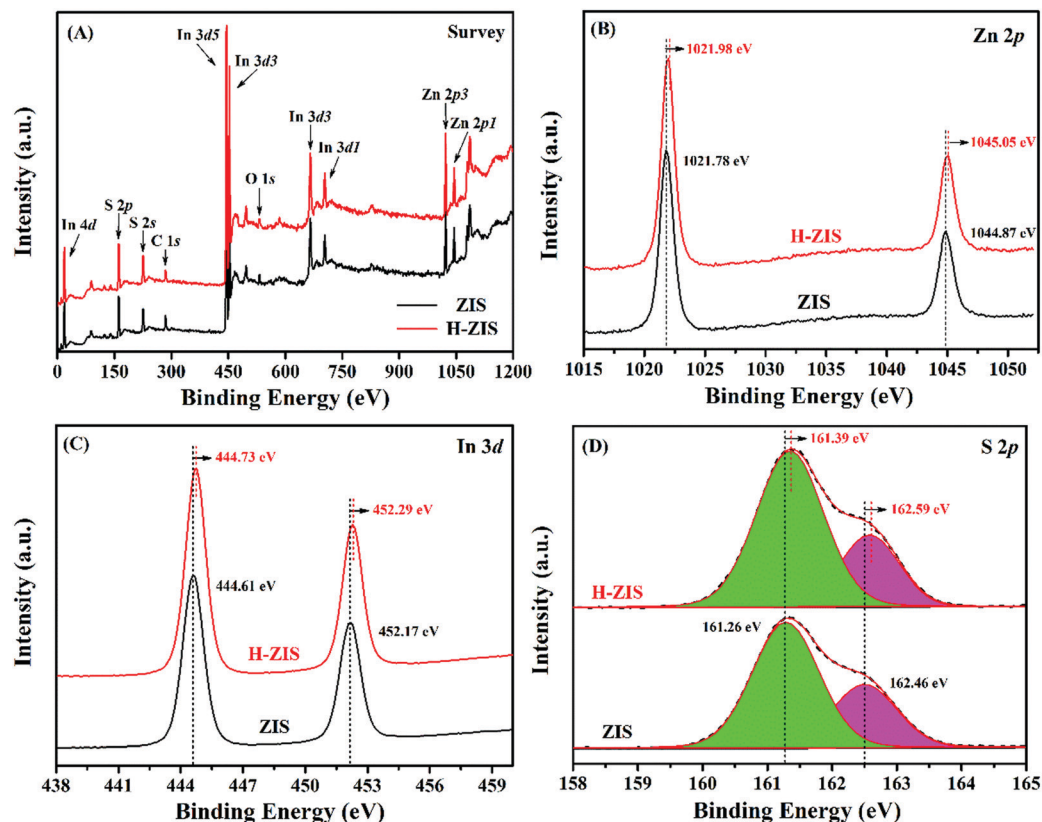
This journal is © the Owner Societies 2019

Phys. Chem. Chem. Phys., 2019, 21, 25484–25494 | 25487

Fig. 5   XPS spectra of pristine ZIS and H–ZIS samples: (A) Survey, (B) Zn 2p, (C) In 3d, and (D) S 2p.

in Fig. 6, the average HER value of the pristine ZIS sample was 218.6 μmol h^{-1} g^{-1}, which is in agreement with the previous reports.[31] In contrast, the H-ZIS sample exhibited an enhanced photocatalytic activity with an average HER of 1905.5 μmol h^{-1} g^{-1}, which is more than eight times higher than that of the pristine ZIS sample and is also comparable to or even higher than the HER data collected for the previously-reported ZIS-based photocatalysts[10,32–38] as summarized in Table 1. Apparently, the hydrogenation-induced sulfur vacancies could significantly increase the photocatalytic hydrogen evolution activity of ZIS. In addition, to test whether

Fig. 6   Photocatalytic H$_2$ evolution performances of the prepared pristine ZIS and H–ZIS samples under visible light irradiation.

any hydrogen molecules were desorbed from the surface of the H-ZIS sample during the photocatalytic process, we used the H-ZIS sample to perform the hydrogen evolution test in isotope D$_2$O, and used a high-resolution Gas Chromatography Mass Spectrometer (GCT Premier, GC-MS) to detect D$_2$. As shown in Fig. S2 (ESI†), a peak associated with D$_2$ was detected at a retention time of about 2.7 min, and with the increase of time, the D$_2$ amount produced from the photocatalytic D$_2$ evolution was also increased. More importantly, no H$_2$ peak appeared during the whole retention time, indicating that H$_2$ could not be generated by H-ZIS in D$_2$O and no H$_2$ was desorbed from the H-ZIS surface during the photocatalytic process. This also proves that the adsorption of H$_2$ on the H-ZIS surface during hydrogenation treatment could be negligible.

One important factor that influences the photocatalytic performance of a given photocatalyst is its optical absorption properties. Fig. 7(A) displays the UV-vis DRS absorption spectra of the pristine ZIS and H-ZIS samples. The absorption edge of the pristine ZIS sample was located at about 550 nm, indicating that the pristine ZIS sample could respond to visible light for photocatalytic reactions. Compared to the pristine ZIS sample, the H-ZIS sample exhibited much higher visible light absorption intensity with a red-shifted absorption edge at *ca.* 600 nm, implying that the hydrogenation treatment could expand the light absorption band of ZIS. Meanwhile, the color of ZIS turned from orange to yellowish-brown after hydrogenation treatment (the inset of Fig. 7(A)), also confirming the extended light absorption capability by hydrogenation. In addition, the
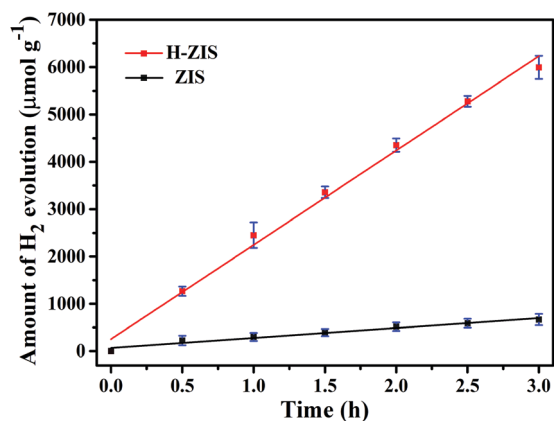
Table 1 Photocatalytic hydrogen evolution rate (HER) of H-ZIS in this work in comparison with those of the previously reported ZIS-based photocatalysts

Photocatalysts	Modification method	HER (μmol h^{-1} g^{-1})	Ref.
Hydrogenated ZIS	Pressure hydrogenation treatment	1905.5	Our work
RGO(3%)-CoO$_x$/BMO/ZIS	Z-scheme Heterojunction	740.4	32
MoS$_2$/ZIS	Heterojunction	1889	33
CQDs/ZIS	Quantum dots loading	1767.7	10
RGO(1%)/ZIS	RGO composites	132.3	34
AgIn$_5$S$_8$/ZIS	Heterojunction	949.9	35
CdS QDs(5%)/ZIS	Quantum dots loading	1020	36
NH$_2$-MIL-125(Ti) (30%)/ZIS	Heterojunction	1705.6	37
g-C$_3$N$_4$/nanocarbon/ZIS	Z-scheme Heterojunction	1006.4	38
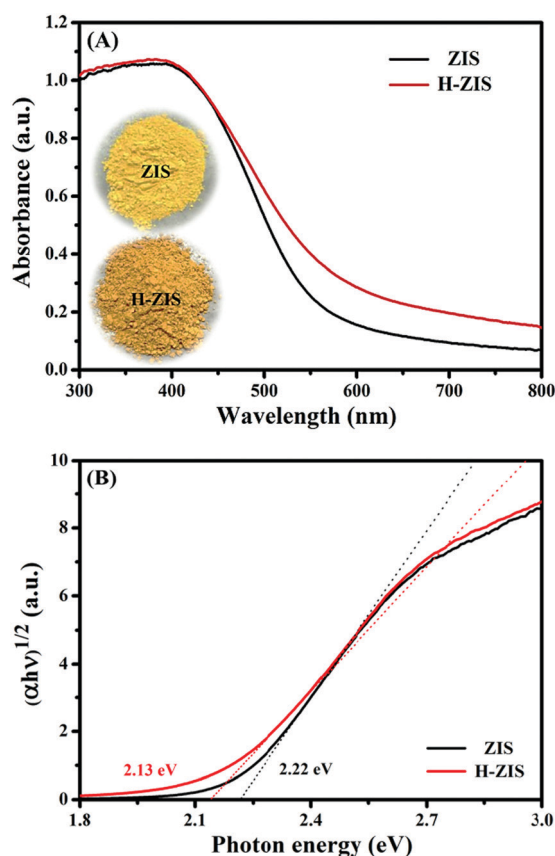
Fig. 7 (A) UV-vis diffuse reflectance spectra (DRS) of the prepared pristine ZIS and H-ZIS samples (insets are photographs of the prepared ZIS and H-ZIS powders). (B) Plots of $(\alpha h\nu)^{1/2}$ vs. $(h\nu)$ derived from the DRS spectra for the pristine ZIS and H-ZIS samples to determine their band gap values.

bandgap values of the prepared pristine ZIS and H-ZIS samples can be calculated from the following classical Tauc plot:[39,40]

$$(\alpha h\nu)^{1/n} = A(h\nu - E_g)$$

where α, h, ν, E_g, A and n are the absorption coefficient, Planck constant, the incident photon frequency, the optical band gap, the absorption constant, and the index value, respectively. Among them, n is dependent on the characteristics of the transition in a semiconductor,[41,42] i.e., direct transition (n = 1/2) or indirect transition (n = 2). Thus, the band-gap energy (E_g) of the semiconducting photocatalyst can be estimated from a plot of $(\alpha h\nu)^2$ or $(\alpha h\nu)^{1/2}$ versus photon energy ($h\nu$) for direct and indirect transition, respectively, and the intercept of the tangent to the X axis can be regarded as the bandgap value of the sample. Since ZIS is a direct bandgap semiconductor,[40] the band gap energy (E_g) of the prepared ZIS and H-ZIS photocatalysts could be estimated from a plot of $(\alpha h\nu)^2$ versus photon energy ($h\nu$), as presented in Fig. 7(B). According to the plots, the bandgap values for the pristine ZIS and H-ZIS photocatalysts were calculated as 2.22 and 2.13 eV, respectively. Therefore, it can be concluded that the hydrogenation-induced sulfur vacancies could reduce the band gap of ZIS to some extent probably due to the occurrence of defect levels[43] within the H-ZIS sample and thus improve the visible light absorption, which could make some important contribution to the enhanced photocatalytic activity of H-ZIS.

3.4 Proposed mechanism

To elucidate the photocatalytic mechanism of H-ZIS for enhanced photocatalytic hydrogen evolution activity, the photoelectrochemical (PEC) measurements were carried out. The transient photocurrent behaviors of the photocatalysts may be directly related to the separation and migration efficiency of photogenerated carriers.[24,44] Fig. 8(A) shows the transient photocurrent behaviors of the prepared pristine ZIS and H-ZIS samples under intermittent visible light irradiation ($\lambda \geq$ 420 nm). Upon irradiation, both pristine ZIS and H-ZIS could generate strong photocurrent signals, confirming their visible light response. More importantly, the photocurrent intensity of H-ZIS was much higher than that of pristine ZIS, implying more efficient photo-induced charge separation and transfer processes and a longer lifetime of the photogenerated carriers in the H-ZIS sample. It is worth noting that when the light was switched on, the instantaneous over-high photocurrent spike (blue dashed box) was observed on the H-ZIS sample due to the flux of photoinduced carriers into the surface where they were trapped or captured by sulfur vacancies.[45,46] This also demonstrates the role of sulfur vacancies in capturing photogenerated electrons. Moreover, the charge separation efficiencies of the pristine ZIS and H-ZIS samples were further investigated by the typical EIS Nyquist diagrams shown in Fig. 8(B). The smaller arc radius in the EIS Nyquist diagram generally means a smaller charge transfer resistance at the interface and a higher separation efficiency of the photogenerated carriers.[47] As seen, the arc
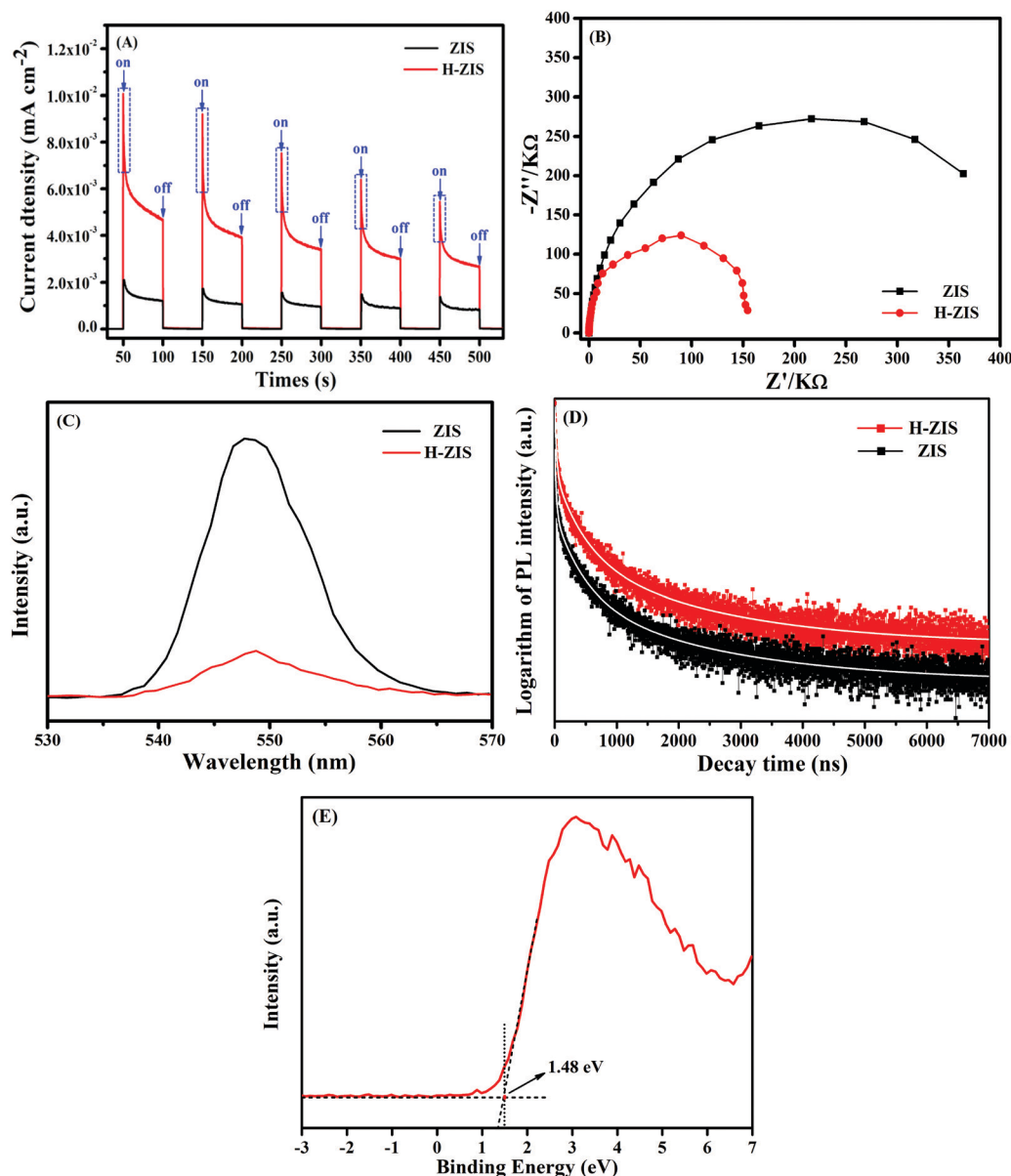
Fig. 8 (A) Transient photocurrent responses, (B) EIS Nyquist plots, (C) steady-state PL spectra, (D) TRPL decay spectra of pristine ZIS and H-ZIS, and (E) VB XPS spectra of H-ZIS.

radius of the prepared H-ZIS sample was much smaller than that of the pristine ZIS sample, indicating that the hydrogenation-induced S vacancies could significantly promote the separation and migration of photogenerated carriers in the H-ZIS sample.

In addition, the recombination probability of photogenerated electrons and holes can usually be reflected from the photoluminescence (PL) emission intensity, and a lower PL emission intensity means a lower recombination probability.[48] To explore the influence of sulfur vacancies on the recombination probability of photogenerated electrons and holes, the steady-state PL spectra of the prepared ZIS and H-ZIS samples were comparatively studied. As can be seen from Fig. 8(C), the pristine ZIS sample exhibited a strong PL emission peak at about 550 nm, which was attributed to the emission of band

gap transition of ZIS.[49] In contrast, the PL emission intensity of H-ZIS was much lower than that of the pristine ZIS sample, probably due to the suppressed recombination of photoexcited electrons and holes via band-to-band emission transition[50] as well as the non-radiative decay of the excited charge carriers to the native defect (surface) states induced by hydrogenation.[51] In consideration of the detrimental effect of non-radiative decay of the excited charge carriers on the photocatalytic activity,[52] in our case, the decreased PL emission intensity of H-ZIS should be dominantly affected by the band-to-band emission transition. This indicates that the recombination of photogenerated holes and electrons was greatly suppressed in the H-ZIS sample. Furthermore, the TRPL spectra of the prepared ZIS and H-ZIS samples were also measured to evaluate

25490 | Phys. Chem. Chem. Phys., 2019, 21, 25484–25494

This journal is © the Owner Societies 2019

the lifetime of the photogenerated carriers. The average emission lifetime (τ_{avg}) could be calculated by fitting the TRPL decay spectra:[24]
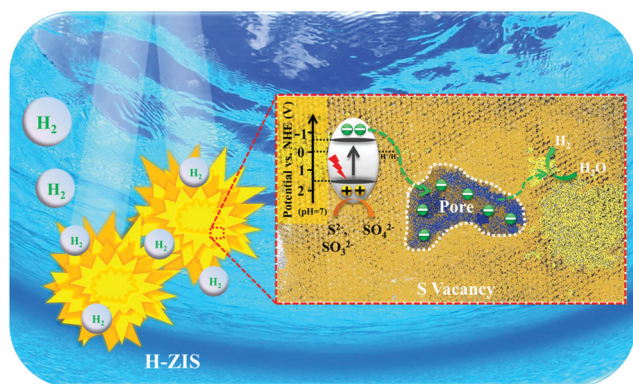
$$\tau_{avg} = \frac{A_1\tau_1^2 + A_2\tau_2^2 + A_3\tau_3^2}{A_1\tau_1 + A_2\tau_2 + A_3\tau_3}$$

where τ is the lifetime and A is the pre-exponential factor with subscripts 1, 2 and 3 representing various species. According to the fitting data shown in Fig. 8(D), the decay-time constants could be obtained and the results are summarized in Table S1 (ESI†). It can be seen that at an excitation wavelength of 300 nm, the PL lifetime of the H-ZIS sample (67.38 ns) was approximately twice that of the pristine ZIS sample (35.01 ns). The longer PL decay lifetime further revealed the lower recombination rate of the photogenerated carriers in the H-ZIS sample, indicative of the more efficient separation and migration of the photogenerated carriers after hydrogenation.

In order to clarify the photocatalytic mechanism of H-ZIS for hydrogen evolution, the valence band (VB) position of H-ZIS was also verified using XPS measurements. As shown in Fig. 8(E), the maximum VB position of the H-ZIS sample was determined to be about +1.48 eV, which is consistent with the previous results.[53] Combined with the calculated band gap value of H-ZIS from the DRS data in Fig. 7(B), the minimum conduction band (CB) energy of H-ZIS was determined to be about −0.65 eV. On the basis of the above discussion, the photocatalytic mechanism of the prepared H-ZIS sample for enhanced photocatalytic hydrogen evolution was schematically illustrated in Scheme 1. After high pressure hydrogenation processes, surface sulfur vacancies were generated on the ZIS sample, and thus the band gap structure was altered. Upon visible light irradiation, many more photogenerated electrons and holes would be produced on the surface of the prepared H-ZIS photocatalyst, thanks to its narrowed band gap in comparison with the pristine ZIS sample. The hydrogenation-induced surface sulfur vacancies within the H-ZIS sample could act as trapping centers for photogenerated electrons, which would on one hand become redox active sites for promoting the photocatalytic hydrogen production process and on the other hand facilitate the separation and migration of photogenerated

Scheme 1 Schematic illustration of the photocatalytic mechanism of H-ZIS for enhanced photocatalytic hydrogen evolution performance.

electron–hole pairs. Simultaneously, the photogenerated holes would be ceaselessly consumed by reacting with the sacrificial agent (e.g. SO_3^{2-}, S^{2-}) in the aqueous solution, which is also favorable for the separation and migration of photogenerated carriers within the H-ZIS sample. The suppression of charge recombination would further strengthen the photocatalytic activity of H-ZIS for hydrogen production. All these factors ultimately contributed to the observed enhanced photocatalytic activity of the hydrogenated ZIS sample for hydrogen production.

Meanwhile, of great concern was the stability of surface sulfur vacancies in H-ZIS, which was closely correlated to the photocatalytic stability of H-ZIS. Fig. 9(A) shows the photocatalytic hydrogen production results of H-ZIS under visible light irradiation for five cycles. As seen, the HER of H-ZIS was gradually decreased from 1902.79 μmol h^{-1} g^{-1} at the first cycling test to 870.76 μmol h^{-1} g^{-1} at the fifth cycling test. Apparently, after five cycles the photocatalytic activity of H-ZIS was markedly decreased, revealing the poor photocatalytic stability of H-ZIS. As a control, the pristine ZIS sample showed much better photocatalytic stability with a photocatalytic activity only reduced by ∼12% after 5 cycles (Fig. S4(A), ESI†). Fig. 9(B) shows the XRD patterns of the prepared H-ZIS sample before and after the photocatalytic hydrogen production experiment. As seen, though the intensities of the diffraction peaks of H-ZIS were decreased after the photocatalytic hydrogen production, the positions of the diffraction peaks of H-ZIS after photocatalytic hydrogen production were almost identical to those before photocatalytic hydrogen production, suggesting that the crystal structure of H-ZIS was nearly unchanged before and after the photocatalytic experiment. The decreased intensities of diffraction peaks of H-ZIS after photocatalytic hydrogen production were probably due to the adsorbents or partial photocorrosion[54] on the surface of the H-ZIS sample during the photocatalytic hydrogen production. Meanwhile, similar phenomena were also observed in the XRD patterns of the pristine ZIS sample before and after photocatalytic hydrogen production (Fig. S4(B), ESI†). Moreover, the XPS survey spectrum of the H-ZIS sample after photocatalytic hydrogen production (Fig. S5, ESI†) was basically the same as that before photocatalytic hydrogen production. Therefore, it can be deduced that the photocatalytic hydrogen production process does not alter the crystal structure of ZIS. In addition, the ESR results (Fig. 9(C)) clearly show that the ESR intensity of the H-ZIS sample after the photocatalytic hydrogen production experiment was much lower than that of the H-ZIS sample before the photocatalytic experiment, indicating that the sulfur vacancy concentration on the surface of H-ZIS was significantly reduced after the photocatalytic experiment. This means that the stability of the hydrogenation-induced surface sulfur vacancies in H-ZIS was poor, thus leading to the poor photocatalytic stability of H-ZIS. In fact, the instability of sulfur vacancies in H-ZIS could also be reflected from the gradual decrease of the photocurrent intensity of the H-ZIS sample with increasing visible light irradiation time (Fig. 8(A)). Nevertheless, the essential reasons for the poor stability of the hydrogenation-induced sulfur vacancies on the surface of H-ZIS are still

This journal is © the Owner Societies 2019

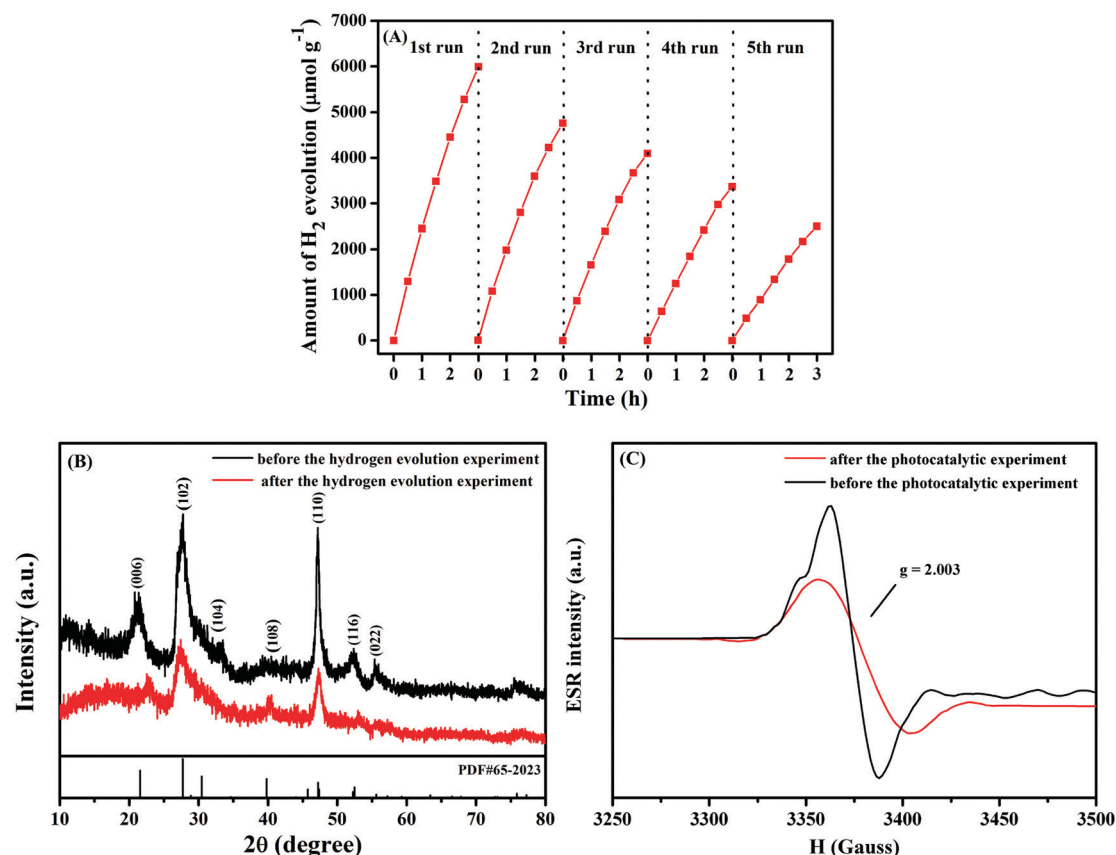Phys. Chem. Chem. Phys., 2019, 21, 25484–25494 | 25491

Fig. 9 (A) Photocatalytic H$_2$ evolution over the prepared H–ZIS sample for several cycles under visible light illumination; (B) XRD patterns and (C) ESR spectra of the H–ZIS sample measured before and after the photocatalytic cycling tests.

unknown, which needs to be further explored, and improvements in the stability of the sulfur vacancies of H-ZIS are also under way.

4. Conclusions

In summary, sulfur vacancies were introduced into the hydrothermally-synthesized ZIS sample by a high pressure hydrogenation process. The formation of sulfur vacancies on the surface of ZIS during the hydrogenation process was verified by HRTEM, XPS, and ESR analysis. The presence of surface sulfur vacancies in H-ZIS was found to significantly improve the photocatalytic hydrogen production activity, and the photocatalytic hydrogen evolution rate of H-ZIS was more than eight times higher than that of ZIS. The enhanced photocatalytic performance of H-ZIS could be attributed to the fact that the hydrogenation-induced sulfur vacancies could act as trapping centers for photogenerated electrons, thus facilitating the photoinduced charge separation and transfer processes and also suppressing the recombination of photogenerated electrons and holes. Meanwhile, the as-formed surface sulfur vacancies in H-ZIS were unstable during the photocatalytic process, thus leading to the poor photocatalytic stability of H-ZIS. Improvements in the photocatalytic stability of H-ZIS are still underway.

Conflicts of interest

There are no conflicts to declare.

Acknowledgements

References

1 A. Kudo and Y. Miseki, Heterogeneous Photocatalyst Materials for Water Splitting, *Chem. Soc. Rev.*, 2009, **38**, 253–278.
2 X. P. Dong and F. X. Cheng, Recent development in exfoliated two-dimensional g-C$_3$N$_4$ nanosheets for photocatalytic applications, *J. Mater. Chem. A*, 2015, **3**, 23642–23652.
3 Y. Ma, X. Wang, Y. Jia, X. Chen, H. Han and C. Li, Titanium Dioxide-Based Nanomaterials for Photocatalytic Fuel Generations, *Chem. Rev.*, 2014, **114**, 9987–10043.
4 J. R. Ran, J. Zhang, J. G. Yu, M. Jaroniec and S. Z. Qiao, Earth-abundant Cocatalysts for Semiconductor-based Photocatalytic Water Splitting, *Chem. Soc. Rev.*, 2014, **43**, 7787–7812.

25492 | *Phys. Chem. Chem. Phys.*, 2019, **21**, 25484–25494

This journal is © the Owner Societies 2019

5   S. Li, D. Dai, L. Ge, Y. Gao, C. Han and N. Xiao, Synthesis of Layer-like Ni(OH)$_2$ Decorated ZnIn$_2$S$_4$ Sub-microspheres with Enhanced Visible-light Photocatalytic Hydrogen Production Activity, *Dalton Trans.*, 2017, **46**, 10620–10629.

6   J. Wang, Y. Chen, W. Zhou, G. Tian, Y. Xiao and H. Fu, Cubic Quantum Dot/Hexagonal Microsphere ZnIn$_2$S$_4$ Heterophase Junctions for Exceptional Visible-light-driven Photocatalytic H$_2$ Evolution, *J. Mater. Chem. A*, 2017, **5**, 8451–8460.

7   Z. B. Lei, W. S. You, M. Y. Liu, G. H. Zhou, T. Takata, M. Hara, K. Domen and C. Li, Photocatalytic Water Reduction under Visible Light on a Novel ZnIn$_2$S$_4$ Catalyst Synthesized by Hydrothermal Method, *Chem. Commun.*, 2003, 2142–2143.

8   J. Shen, J. T. Zai, Y. P. Yuan and X. F. Qian, 3D Hierarchical ZnIn$_2$S$_4$: The Preparation and Photocatalytic Properties on Water Splitting, *Int. J. Hydrogen Energy*, 2012, **37**, 16986–16993.

9   L. Shang, C. Zhou, T. Bian, H. J. Yu, L. Z. Wu, C. H. Tung and T. R. Zhang, Facile Synthesis of Hierarchical ZnIn$_2$S$_4$ Submicrospheres Composed of Ultrathin Mesoporous Nanosheets as a Highly Efficient Visible-light-driven Photocatalyst for H$_2$ Production, *J. Mater. Chem. A*, 2013, **1**, 4552–4558.

10 Y. Xia, Q. Li, K. L. Lv, D. G. Tang and M. Li, Superiority of Graphene Over Carbon Analogs for Enhanced Photocatalytic H$_2$-production Activity of ZnIn$_2$S$_4$, *Appl. Catal., B*, 2017, **206**, 344–352.

11 X. B. Chen, L. Liu, P. Y. Yu and S. S. Mao, Increasing Solar Absorption for Photocatalysis with Black Hydrogenated Titanium Dioxide Nanocrystals, *Science*, 2011, **331**, 746–750.

12 F. Lei, Y. Sun, K. Liu, S. Gao, L. Liang, B. Pan and Y. Xie, Oxygen Vacancies Confined in Ultrathin Indium Oxide Porous Sheets for Promoted Visible-light Water Splitting, *J. Am. Chem. Soc.*, 2014, **136**, 6826–6829.

13 X. Lu, G. Wang, S. Xie, J. Y. Shi, W. Li, Y. X. Tong and Y. Li, Efficient Photocatalytic Hydrogen Evolution over Hydrogenated ZnO Nanorod Arrays, *Chem. Commun.*, 2012, **48**, 7717–7719.

14 H. Q. Tan, Z. Zhao, W. B. Zhu, E. N. Coker, B. S. Li, M. Zheng, W. X. Yu, H. Y. Fan and Z. C. Sun, Oxygen Vacancy Enhanced Photocatalytic Activity of Pervoskite SrTiO3, *ACS Appl. Mater. Interfaces*, 2014, **6**, 19184–19190.

15 D. Chen, F. Niu, L. S. Qin, S. Wang, N. Zhang and Y. X. Huang, Defective BiFeO$_3$ with Surface Oxygen Vacancies: Facile Synthesis and Mechanism Insight into Photocatalytic Performance, *Sol. Energy Mater. Sol. Cells*, 2017, **171**, 24–32.

16 X. M. Yu, B. Kim and Y. K. Kim, Highly Enhanced Photoactivity of Anatase TiO$_2$ Nanocrystals by Controlled Hydrogenation-Induced Surface Defects, *ACS Catal.*, 2013, **3**, 2479–2486.

17 S. L. Chen, D. Li, Y. X. Liu and W. X. Huang, Morphology-dependent Defect Structures and Photocatalytic Performance of Hydrogenated Anatase TiO$_2$ Nanocrystals, *J. Catal.*, 2016, **341**, 126–135.

18 Y. W. Zhu, L. L. Wang, Y. T. Liu, L. H. Shao and X. N. Xia, *In situ* hydrogenation engineering of ZnIn$_2$S$_4$ for promoted visible-light water splitting, *Appl. Catal., B*, 2019, **241**, 483–490.

19 E. Clapeyron, Memory on the motive power of heat, *J. Ec. Polytech.*, 1834, **14**, 153–190.

20 X. Hu, J. Yu, J. Gong and Q. Li, Rapid Mass Production of Hierarchically Porous ZnIn$_2$S$_4$ Submicrospheres via a Microwave-Solvothermal Process, *Cryst. Growth Des.*, 2016, **7**, 2444–2448.

21 Y. Yin, J. C. Han, Y. M. Zhang, X. H. Zhang, P. Xu, Q. Yuan, L. Samad, X. J. Wang, Y. Wang, Z. H. Zhang, P. Zhang, X. Z. Cao, B. Song and S. Jin, Contributions of Phase, Sulfur Vacancies, and Edges to the Hydrogen Evolution Reaction Catalytic Activity of Porous Molybdenum Disulfide Nanosheets, *J. Am. Chem. Soc.*, 2016, **138**, 7965–7972.

22 Y. S. Chen, H. Y. Guo, J. C. Yang, Y. H. Chu, W. F. Wu and J. G. Lin, Electron Paramagnetic Resonance Probed Oxygen Deficiency in SrTiO$_3$ with Different Cap Layers, *J. Appl. Phys.*, 2012, **112**, 123720.

23 Z. Fang, S. Weng, X. Ye, W. Feng, Z. Zheng, M. Lu, S. Lin, X. Fu and P. Liu, Defect Engineering and Phase Junction Architecture of Wide-Bandgap ZnS for Conflicting Visible Light Activity in Photocatalytic H$_2$ Evolution, *ACS Appl. Mater. Interfaces*, 2015, **7**, 13915–13924.

24 S. Zhang, X. Liu, C. Liu, S. Luo, L. Wang, T. Cai, Y. Zeng, J. Yuan, W. Dong, Y. Pei and Y. Liu, MoS$_2$ Quantum Dot Growth Induced by S Vacancies in a ZnIn$_2$S$_4$ Monolayer: Atomic-Level Heterostructure for Photocatalytic Hydrogen Production, *ACS Nano*, 2018, **12**, 751–758.

25 S. Godefroo, M. Hayne, M. Jivanescu, A. Stesmans, M. Zacharias, O. Lebedev, G. Van Tendeloo and V. Moshchalkov, Classification and Control of the Origin of Photoluminescence from Si Nanocrystals, *Nat. Nanotechnol.*, 2008, **3**, 174–178.

26 Z. S. Luo, M. Zhou and X. C. Wang, Cobalt-based Cubane Molecular Co-catalysts for Photocatalytic Water Oxidation by Polymeric Carbon Nitrides, *Appl. Catal., B*, 2018, **238**, 664–671.

27 S. Peng, P. Zhu, V. Thavasi, S. Mhaisalkar and S. Ramakrishna, Facile Solution Deposition of ZnIn$_2$S$_4$ Nanosheet Films on FTO Substrates for Photoelectric Application, *Nanoscale*, 2011, **3**, 2602–2608.

28 L. Ye, J. Fu, Z. Xu, R. Yuan and Z. Li, Facile One-pot Solvothermal Method to Synthesize Sheet-on-sheet Reduced Graphene Oxide (RGO)/ZnIn$_2$S$_4$ Nanocomposites with Superior Photocatalytic Performance, *ACS Appl. Mater. Interfaces*, 2014, **6**, 3483–3490.

29 J. Yang, E. H. Sargent, S. O. Kelley and J. Y. Ying, A General Phase-transfer Protocol for Metal Ions and its Application in Nanocrystal Synthesis, *Nat. Mater.*, 2009, **8**, 683–689.

30 J. X. Low, B. Z. Dai, T. Tong, C. J. Jiang and J. G. Yu, *In Situ* Irradiated X-Ray Photoelectron Spectroscopy Investigation on a Direct Z-Scheme TiO$_2$/CdS Composite Film Photocatalyst, *Adv. Mater.*, 2019, **31**, 1802981.

31 J. Y. Zhao, X. M. Yan, N. Zhao, X. Li, B. Lu, X. H. Zhang and H. T. Yu, Cocatalyst Designing: a Binary Noble-metal-free Cocatalyst System Consisting of ZnIn$_2$S$_4$ and In(OH)$_3$ for Efficient Visible-light Photocatalytic Water Splitting, *RSC Adv.*, 2018, **8**, 4979–4986.

32 S. Wan, M. Ou, Q. Zhong, S. Zhang and F. Song, Construction of Z-scheme Photocatalytic Systems using ZnIn$_2$S$_4$, CoO$_x$-loaded Bi$_2$MoO$_6$ and Reduced Graphene Oxide Electron

This journal is © the Owner Societies 2019

Phys. Chem. Chem. Phys., 2019, **21**, 25484–25494 | 25493

Mediator and its Efficient Nonsacrificial Water Splitting under Visible Light, *Chem. Eng. J.*, 2017, **325**, 690–699.

33 Y. J. Yuan, J. R. Tu, Z. J. Ye, D. Q. Chen, B. Hu, Y. W. Huang, T. T. Chen, D. P. Cao, Z. T. Yu and Z. G. Zou, MoS_2-graphene/$ZnIn_2S_4$ Hierarchical Microarchitectures with an Electron Transport Bridge between Light-harvesting Semiconductor and Cocatalyst: A Highly Efficient Photocatalyst for Solar Hydrogen Generation, *Appl. Catal., B*, 2016, **188**, 13–22.

34 L. Ye and Z. H. Li, Rapid Microwave-assisted Syntheses of Reduced Graphene Oxide(RGO)/$ZnIn_2S_4$ Microspheres as Superior Noble-metal-free Photocatalyst for Hydrogen Evolutions Under Visible Light, *Appl. Catal., B*, 2014, **160**, 552–557.

35 Z. J. Guan, Z. Q. Xu, Q. Y. Li, P. Wang, G. Q. Li and J. J. Yang, $AgIn_5S_8$ Nanoparticles Anchored on 2D Layered $ZnIn_2S_4$ to form 0D/2D Heterojunction for Enhanced Visible-light Photocatalytic Hydrogen Evolution, *Appl. Catal., B*, 2018, **227**, 512–518.

36 J. G. Hou, C. Yang, H. J. Cheng, Z. Wang, S. Q. Jiao and H. M. Zhu, Ternary 3D Architectures of CdS QDs/Graphene/$ZnIn_2S_4$ Heterostructures for Efficient Photocatalytic H_2 Production, *Phys. Chem. Chem. Phys.*, 2013, **15**, 15660–15668.

37 H. Liu, J. Zhang and D. Ao, Construction of Heterostructured $ZnIn_2S_4$@NH_2-MIL-125(Ti) Nanocomposites for Visible-light-driven H_2 Production, *Appl. Catal., B*, 2018, **221**, 433–442.

38 F. F. Shi, L. L. Chen, M. Chen and D. L. Jiang, g-C_3N_4/Nanocarbon/$ZnIn_2S_4$ Nanocomposite: Artificial Z-Scheme Visible-light Photocatalytic System Using Nanocarbon as the Electron Mediator, *Chem. Commun.*, 2015, **51**, 17144–17147.

39 J. Tauc, R. Grigorovici and A. Vancu, Optical Properties and Electronic Structure of Amorphous Germanium, *Phys. Status Solidi B*, 1966, **15**, 627–637.

40 W. Lim, M. Hong and G. Ho, *In situ* Photo-assisted Deposition and Photocatalysis of $ZnIn_2S_4$/Transition Metal Chalcogenides for Enhanced Degradation and Hydrogen Evolution under Visible Light, *Dalton Trans.*, 2016, **45**, 552–560.

41 E. A. Davis and N. F. Mott, Conduction in non-crystalline systems V. Conductivity, optical absorption and photoconductivity in amorphous semiconductors, *Philos. Mag.*, 1970, **22**, 903–922.

42 F. Niu, D. Chen, L. S. Qin, N. Zhang, J. Y. Wang, Z. Chen and Y. X. Huang, Facile Synthesis of Highly Efficient p–n Heterojunction CuO/$BiFeO_3$ Composite Photocatalysts with Enhanced Visible-Light Photocatalytic Activity, *ChemCatChem*, 2015, **7**, 3279–3289.

43 Z. Zhao, X. Y. Zhang, G. Q. Zhang, Z. Y. Liu, D. Qu, X. Miao, P. Y. Feng and Z. C. Sun, Effect of Defects on Photocatalytic Activity of Rutile TiO_2 Nanorods, *Nano Res.*, 2015, **8**, 4061–4071.

44 P. Qiu, J. Yao, H. Chen, F. Jiang and X. Xie, Enhanced Visible-Light Photocatalytic Decomposition of 2,4-Dichlorophenoxyacetic Acid over $ZnIn_2S_4$/g-C_3N_4 Photocatalyst, *J. Hazard. Mater.*, 2016, **317**, 158–168.

45 Q. J. Xiang, J. G. Yu and M. Jaroniec, Enhanced Photocatalytic H_2 Production Activity of Graphene-Modified Titania Nanosheets, *Nanoscale*, 2011, **3**, 3670–3678.

46 C. Y. Cummings, F. Marken, L. M. Peter, A. A. Tahir and K. G. Wijayantha, Kinetics and Mechanism of Light-Driven Oxygen Evolution at Thin Film α-Fe_2O_3 Electrodes, *Chem. Commun.*, 2012, **48**, 2027–2029.

47 X. Jiao, Z. Chen, X. Li, Y. Sun, S. Gao, W. Yan, C. Wang, Q. Zhang, Y. Lin, Y. Luo and Y. Xie, Defect-Mediated Electron-Hole Separation in One-unit-cell $ZnIn_2S_4$ Layers for Boosted Solar-Driven CO_2 Reduction, *J. Am. Chem. Soc.*, 2017, **139**, 7586–7594.

48 Y. Yao, G. H. Li, S. Ciston, R. M. Lueptow and K. A. Gray, Photoreactive TiO_2/Carbon Nanotube Composites: Synthesis and Reactivity, *Environ. Sci. Technol.*, 2008, **42**, 4952–4957.

49 B. Chai, T. Peng, P. Zeng and X. Zhang, Preparation of a MWCNTs/$ZnIn_2S_4$ Composite and its Enhanced Photocatalytic Hydrogen Production under Visible-light Irradiation, *Dalton Trans.*, 2012, **41**, 1179–1186.

50 S. H. Shen, J. Chen, X. X. Wang, L. Zhao and L. J. Guo, Microwave-assisted hydrothermal synthesis of transition-metal doped $ZnIn_2S_4$ and its photocatalytic activity for hydrogen evolution under visible light, *J. Power Sources*, 2011, **196**, 10112–10119.

51 S. H. Shen, L. Zhao, X. J. Guan and L. J. Guo, Improving visible-ight photocatalytic activity for hydrogen evolution over $ZnIn_2S_4$: A case study of alkaline-earth metal doping, *J. Phys. Chem. Solids*, 2012, **73**, 79–83.

52 Y. P. Yuan, Z. Y. Zhao, J. Zheng, M. Yang, L. G. Qiu, Z. S. Li and Z. G. Zou, Polymerizable complex synthesis of $BaZr_{1-x}Sn_xO_3$ photocatalysts: Role of Sn^{4+} in the band structure and their photocatalytic water splitting activities, *J. Mater. Chem.*, 2010, **20**, 6772–6779.

53 D. Q. Zeng, L. Xiao, W. J. Ong, P. Y. Wu, H. F. Zheng, Y. Z. Chen and D. L. Peng, Hierarchical $ZnIn_2S_4$/$MoSe_2$ Nanoarchitectures for Efficient Noble-Metal-Free Photocatalytic Hydrogen Evolution under Visible Light, *ChemSusChem*, 2017, **10**, 4624–4631.

54 J. Y. Chen, H. M. Zhang, P. R. Liu, Y. B. Li, X. L. Liu, G. Y. Li, P. K. Wong, T. C. An and H. J. Zhao, Cross-linked $ZnIn_2S_4$/rGO composite photocatalyst for sunlight-driven photocatalytic degradation of 4-nitrophenol, *Appl. Catal., B*, 2015, **168**, 266–273.

25494 | *Phys. Chem. Chem. Phys.*, 2019, **21**, 25484–25494

This journal is © the Owner Societies 2019

Facile synthesis of Er-doped BiFeO₃ nanoparticles for enhanced visible light photocatalytic degradation of tetracycline hydrochloride

Jiabo Zhou, Lidong Jiang, Da Chen, Junhui Liang, Laishun Qin, Liqun Bai, Xingguo Sun & Yuexiang Huang

Springer

Springer

ORIGINAL PAPER: SOL-GEL AND HYBRID MATERIALS FOR CATALYTIC, PHOTOELECTROCHEMICAL AND SENSOR APPLICATIONS

Facile synthesis of Er-doped BiFeO₃ nanoparticles for enhanced visible light photocatalytic degradation of tetracycline hydrochloride

Jiabo Zhou[1] · Lidong Jiang[1] · Da Chen 🄳[1] · Junhui Liang[1] · Laishun Qin[1] · Liqun Bai[2,3] · Xingguo Sun[1] · Yuexiang Huang[1]

Abstract

In the present work, Er-doped BiFeO₃ (BFO) nanoparticles ($Bi_{(1-x)}Er_xFeO_3$, where $x = 0.00$, 0.01, 0.03, 0.05) containing different concentrations of Er dopants were successfully prepared through a facile sol gel method. The crystalline structure, morphological features, and chemical compositions of the obtained samples were examined by a variety of characterization techniques, and these samples were then used as photocatalysts for the photocatalytic removal of tetracycline hydrochloride (TC) upon visible light. The Er doping could significantly improve the optical absorption capability of the BFO especially in visible light range, and could also boost the photocatalytic activity of the BFO for TC removal. Among all the prepared photocatalysts, the Er3%-BFO sample yielded the highest photocatalytic efficiency of 75.8% for TC removal, which was nearly 2.78 times that of pure BFO. On the basis of the photocurrent response, electrochemical impedance spectra, and photoluminescence emission results, the contributions made on the significantly boosted photocatalytic activities of Er-doped BFO could be reflected on the following aspects: (i) the improved spectral absorption especially in visible light region, (ii) the promotion of photoinduced charge separation and migration, and (iii) the suppressed recombination probability of photogenerated electron–hole pairs. The present work demonstrates the feasibility of employing rare earth doping to develop highly efficient BFO-based photocatalysts for the photocatalytic removal of antibiotics.

Graphical Abstract

The photocatalytic activity of BiFeO₃ for tetracycline hydrochloride removal was significantly improved by the effective doping of Er^{3+} rare earth ions.

✉ Da Chen
dchen_80@hotmail.com

✉ Laishun Qin
qinlaishun@cjlu.edu.cn

[1] College of Materials Science and Engineering, China Jiliang University, Hangzhou, Zhejiang 310018, China

[2] Zhejiang Provincial Key Laboratory of Chemical Utilization of Forestry Biomass, Zhejiang A & F University, Lin'an, Zhejiang 311300, China

[3] Zhejiang Provincial Key Lab for Chem & Bio Processing Technology of Farm Products, Zhejiang University of Science & Technology, Hangzhou, Zhejiang 310023, China
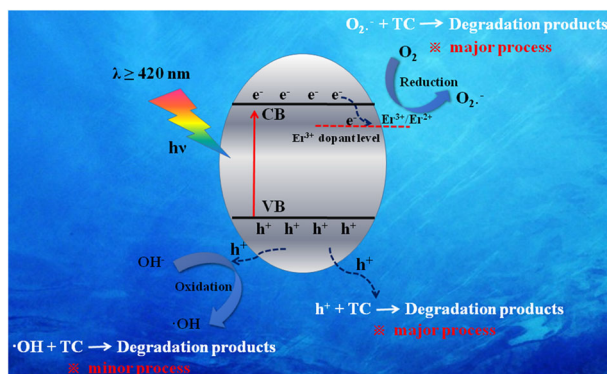
Highlights

- Effective Er doping into BiFeO$_3$ (BFO) nanoparticles was obtained by a facile sol–gel route.
- The optical absorption properties of BFO nanoparticles was improved by Er doping.
- Er-doped BFO nanoparticles showed superior photocatalytic activities for TC removal.
- The possible photocatalytic mechanism of Er-doped BFO nanoparticles was discussed.

Keywords BiFeO$_3$ · Er doping · Sol gel method · Photocatalytic activities · Tetracycline hydrochloride removal

1 Introduction

With the progress and development of the human society, the water pollution problem caused by the unreasonable and nonstandard use of antibiotics has caught more and more attention because of the adverse effects to the aquatic ecosystem as well as the potential threat to human health. However, the removal of antibiotic contaminations from water and wastewater is still not ideal by means of conventional remediation techniques (such as biological processes, coagulation, flocculation, and sedimentation) [1]. Therefore, it is desired to find out an efficient and cost-effective physicochemical method for antibiotics removal. Over the past decade, heterogeneous photocatalysis has been recognized as a promising practical approach for degradation or removal of antibiotics from aqueous matrices in view of its low cost, easy availability, strong oxidation ability, and eco-friendliness [2, 3]. In this approach, the development of highly efficient semiconductor photocatalysts is pivotal for effective photocatalytic removal of antibiotics.

TiO$_2$-based semiconductors have been proven as efficient photocatalysts for photocatalytic degradation of organic pollutant and photocatalytic water splitting because of their relatively high photocatalytic activity, robust chemical stability, low cost, and nontoxicity [4–8]. The drawback of TiO$_2$-based semiconductors lies in their wide band-gap, thus making them only absorb the ultraviolet light, which greatly limits their practical applications. Thus, pursuing inexpensive, earth-abundant, and efficient visible light photocatalysts is still a challenging task. Over the past decade, perovskite-structured bismuth ferrite (BiFeO$_3$, BFO for

short) has shown great potential as an efficient visible light photocatalyst for photocatalytic degradation of pollutants in view of its proper band gap structure (~2.2 eV), low cost, good chemical stability, as well as its unique intrinsic electric polarization field [9–11]. However, the relatively poor photocatalytic performance of BFO restricts its potential application [12], and further improving its photocatalytic activity is imperative for future practical applications. To date, several strategies, such as morphological control [13], elemental doping [14], cocatalyst deposition [15], and heterostructure construction [16], have been employed to modify BFO with the purpose of extending its optical response range and improving its photocatalytic activity. Particularly, the doping of rare earth ions into the photocatalyst has proven effective in enhancing the photocatalytic activity [17], on account of the electron or hole trapping ability of the rare earth dopants within the photocatalyst, thus to facilitate the charge separation and migration of photogenerated carriers [18]. Moreover, the doping of rare earth ions into semiconductors can alter the absorption edge of semiconductors, which would enhance the absorption of low energy photons for effectively improving the visible light photocatalytic activity [19, 20]. Furthermore, the rare earth ions doped into semiconductors can on one hand have a strong complex ability to adsorb various organic pollutants because of the formation of Lewis acid–base complex between these ions and the substrate through their 4f orbitals [21], and on the other hand probably reduce the crystallite size but increase the surface area of oxide photocatalysts [22], which would contribute to the enhancement of the adsorption capacity of photocatalysts for organic pollutants. Thus, it is suggested that the

rare earth doping can provide BFO with better visible light adsorption abilities and higher efficiency photocatalytic performances. In fact, doping of BFO semiconductors is a subject of broad interest for the past few years. Pure BFO nanostructures doped with rare earth ions like Gd, Dy, Sm, Pr, and Nd have been reported for photocatalytic applications in the literature [14, 23–26]. Notably, erbium (Er) is a popular rare earth element for doping semiconductor photocatalysts because of its unique transitions of Er^{3+} intra-f electrons, which leads to sensitization of the photocatalyst to visible light [27]. To our knowledge, however, the application of Er^{3+}-doped BFO nanostructure as a photocatalyst has not been reported yet.

In recent years, a variety of synthetic methods have been developed to prepare BFO powders, such as sol–gel synthesis [28], hydrothermal synthesis [29], solid state reaction [30], rapid liquid-phase sintering [31], co-precipitation [32], microemulsion technique [33], and so on. Among these methods, the sol–gel process is widely used for preparing BFO powders and thin films because it can easily achieve a uniform composition on the atomic or molecular scale at a relatively low synthesis temperature [34]. Herein, Er-doped BFO nanoparticles ($Bi_{(1-x)}Er_xFeO_3$, where $x = 0.00$, 0.01, 0.03, 0.05) containing a different concentration of Er dopants prepared by a facile sol–gel approach were employed as the photocatalysts for visible light photocatalytic removal of tetracycline hydrochloride (TC). To explore the effect of Er doping on the photocatalytic performance of Er-doped BFO nanoparticles, a variety of photoelectrochemical (PEC) techniques including photocurrent action spectra, electrochemical impedance spectra (EIS), and photoluminescence (PL) emission spectra were then carried out. According to the PEC results, the possible mechanism of Er-doped BFO nanoparticles for enhanced photocatalytic TC removal was tentatively discussed.

2 Experimental section

2.1 Sol–gel synthesis of Er-doped BFO nanoparticles

Er-doped BFO nanoparticles containing different concentrations of Er dopants ($Bi_{1-x}Er_xFeO_3$, where $x = 0$, 0.01, 0.03, or 0.05) were synthesized through a simple sol–gel approach, which were labeled as BFO, Er1%-BFO, Er3%-BFO, and Er5%-BFO, respectively. In a typical synthesis, 0.1 mol of tartaric acid was dissolved in 100 mL of ethylene glycol under magnetically stirring. Subsequently, the desired stoichiometric amounts of $Bi(NO_3)_3 \cdot 5H_2O$ (10× (1−x) mmol), $Fe(NO_3)_3 \cdot 9H_2O$ (10 mmol), and $Er(NO_3)_3 \cdot 5H_2O$ (10×(x) mmol) were added to the above solution, respectively, and carefully dissolved under magnetically

stirring for 2 h. The homogeneous precursor sol at a concentration of 0.1 M was then obtained. After being heated at 80 °C, the sol was dried into a gel. The gel was powdered, and then calcined at 550 °C for 2 h in order to form a high crystalline rhombohedral structure [35]. After the calcined powders were naturally cooled to room temperature, the final product (i.e., the BFO or Er-doped BFO nanoparticles) was thus obtained.

2.2 Materials characterizations

The crystalline phases of the prepared BFO and Er-doped BFO samples were examined on a Bruker D2 X-ray diffractometer using Cu K_α radiation ($\lambda = 1.5418$ Å). The average crystalline sizes of the prepared samples were estimated from line broadening of the corresponding X-ray diffraction peaks using the Scherrer equation. The morphological features, microstructures, and element mapping of the prepared samples were analyzed by field emission scanning electron microscopy (FESEM, Hitachi SU 8010) attached with energy dispersive X-ray spectroscopy (EDS), and a transmission electron microscopy (TEM, JEOL JEM-2100 Japan). The inductively coupled plasma mass spectrometry (ICP-MS) measurements were performed on an ICP-MS spectrometry (PE NexION 300X) to determine the actual Er doping contents in the prepared samples. Specific surface areas of the prepared samples were measured by Brunauer–Emmett–Teller (BET) nitrogen adsorption–desorption (Shimadzu, Micromeritics ASAP 2010) instrument. The X-ray photoelectron spectra (XPS) of the prepared samples were performed on a PHI 5000 Versa Probe with a monochromatic Al K_α source and a charge neutralizer in the high vacuum analysis chamber of 10^{-9} Torr. All the binding energies were calibrated to the adventitious C 1s peak at 284.8 eV. The ultraviolet–visible (UV–vis) diffuse reflectance spectra (DRS) and the PL emission spectra were acquired by using a Shimadzu UV-3600 spectrometer and a fluorescence spectrophotometer (Hitachi High-Tech F-7000), respectively. The total organic carbon (TOC) content of the samples was analyzed by a TOC-VCPH analyzer (Shimadzu, Japan).

2.3 Photocatalytic evaluation

To assess their photocatalytic activities, the prepared BFO or Er-doped BFO nanoparticles were used as the photocatalyst for photocatalytic TC removal upon visible light ($\lambda \geq 420$ nm) irradiation. The irradiance was produced by a 300 W Xe lamp with a cutoff filter. In a typical process, 0.2 g of the prepared BFO or Er-BFO photocatalyst powder was well dispersed in 100 mL of TC solution (30 mg/L) in a home-built photoreaction vessel under magnetically stirring. After the suspension was kept stirring in dark for 0.5 h, the

photocatalytic reaction was initiated by visible light irradiation. At intervals, 4 mL of the suspension was taken out and the catalyst powder was removed from the solution using a 0.22 µm nitrocellulose filter. The TC removal efficiency was then estimated by detecting the absorbance of each collected supernatant at maximum wavelength (i.e., 356 nm) on a UV–visible spectrometer (model 722, Shanghai Precision Instruments Co., Ltd., China). The reusability and stability of the prepared Er-doped BFO photocatalyst were also investigated by recycling the photocatalyst powders in suspension for another four catalytic reactions. All the photocatalytic data were the average values of three parallel experiments with the error bars based on their standard deviations.

2.4 Photoelectrochemical measurements

The PEC measurements (i.e., photocurrent response current and EIS) were carried out on an electrochemical workstation using a home-built three-electrode quartz cell in an electrolyte solution of 0.5 M Na_2SO_4, where the fabricated samples photoelectrode, a platinum wire, and a saturated calomel electrode (SCE) were used as the working electrode, the counter electrode, and the reference electrode, respectively. To fabricate the working photoelectrode (the active area of $1 \times 1 \, cm^2$), a slurry was firstly prepared by mixing the obtained sample powder (90%) and polymer binder (polyvinylidene fluoride, 10%) in N-methyl-2-pyrrolidinone (NMP), and was then doctor bladed onto the surface of FTO conductive glass. After vacuum drying at 60 °C overnight, the working photoelectrode was thus obtained. A Xe lamp (300 W) assembled with a cutoff filter ($\lambda \geq 420$ nm), which was placed at 12 cm away from the working photoelectrode, was used as the visible light source. The photocurrent response spectra were detected upon an on–off intermittent visible irradiation. The EIS plots of the samples were acquired using a sinusoidal ac perturbation of 10 mV upon visible light irradiation.

3 Results and discussion

The crystalline phases of the prepared samples were determined by XRD patterns, as shown in Fig. 1a. As for the pure BFO, all diffraction peaks were readily indexed to the rhombohedral phase with R3c space group (JCPDS No. 86-1518), indicating that the rhombohedral crystalline BFO could be successfully synthesized through the present sol–gel process. Meanwhile, the diffraction patterns of the Er-doped BFO samples were similar to that of the pure BFO, validating that Er doping would not affect the crystal structure of BFO. The magnified XRD patterns (Fig. 1b) show that the separated (104) and (110) diffraction peaks
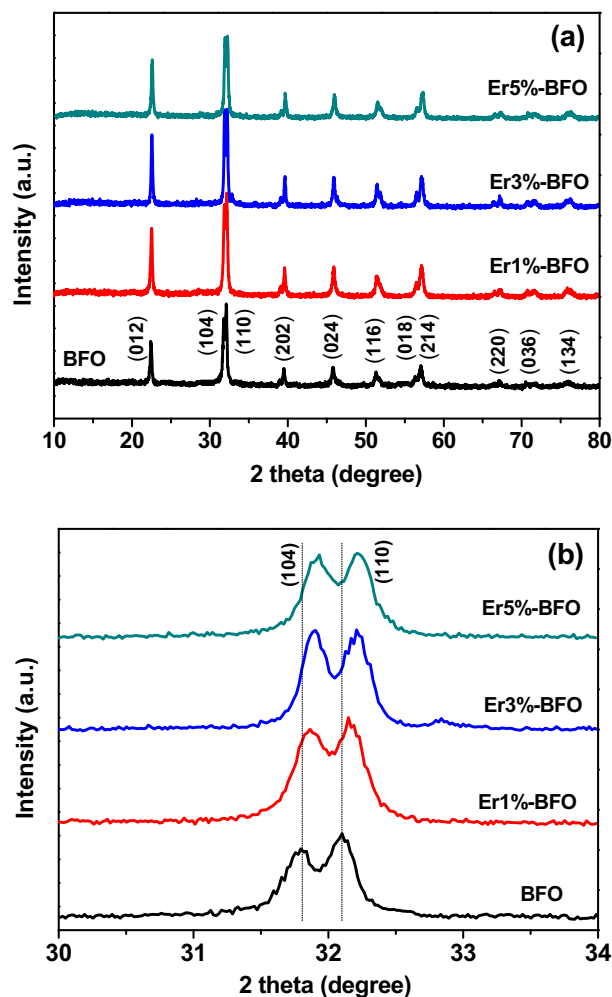

Fig. 1 a XRD patterns of the prepared BFO and Er-doped BFO samples containing different Er doping contents; **b** the magnified XRD patterns ranging from 30° to 34°

Table 1 Unit cell parameters of the prepared BFO and Er-doped BFO samples, and the actual Er doping contents in the BFO and Er-doped BFO samples

Samples	Unit cell parameters			ICP-MS (Er doping content)	
	$a = b$ (Å)	c (Å)	Cell volume (Å^3)	Weight ratio (mg/kg)	Molar ratio (%)
BFO	5.5758	13.8665	374.57	0	0
Er1%-BFO	5.5745	13.8595	373.31	5140	0.96
Er3%-BFO	5.5732	13.8474	372.45	14,868	2.77
Er5%-BFO	5.5727	13.8398	372.16	24,697	4.59

located at around 32° had an obvious shift toward higher 2θ values as increasing the Er dopant concentration, which could be due to the structural distortion induced by the substitution of smaller sized Er^{3+} ions (0.88 Å) for Bi^{3+} ions (1.03 Å) into the lattice of $BiFeO_3$ [36]. The structural

Fig. 2 FESEM images of the prepared **a** pure BFO, **b** Er1%-BFO, **c** Er3%-BFO, and **d** Er5%-BFO, respectively; and **e** Er elemental mapping of Er3%-BFO sample
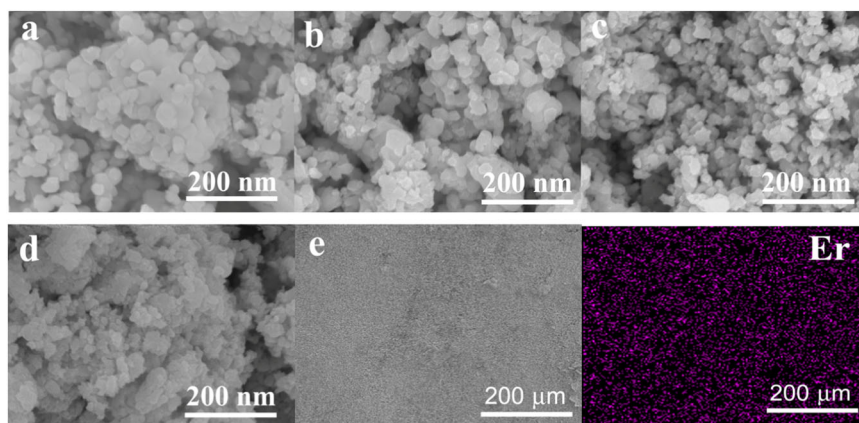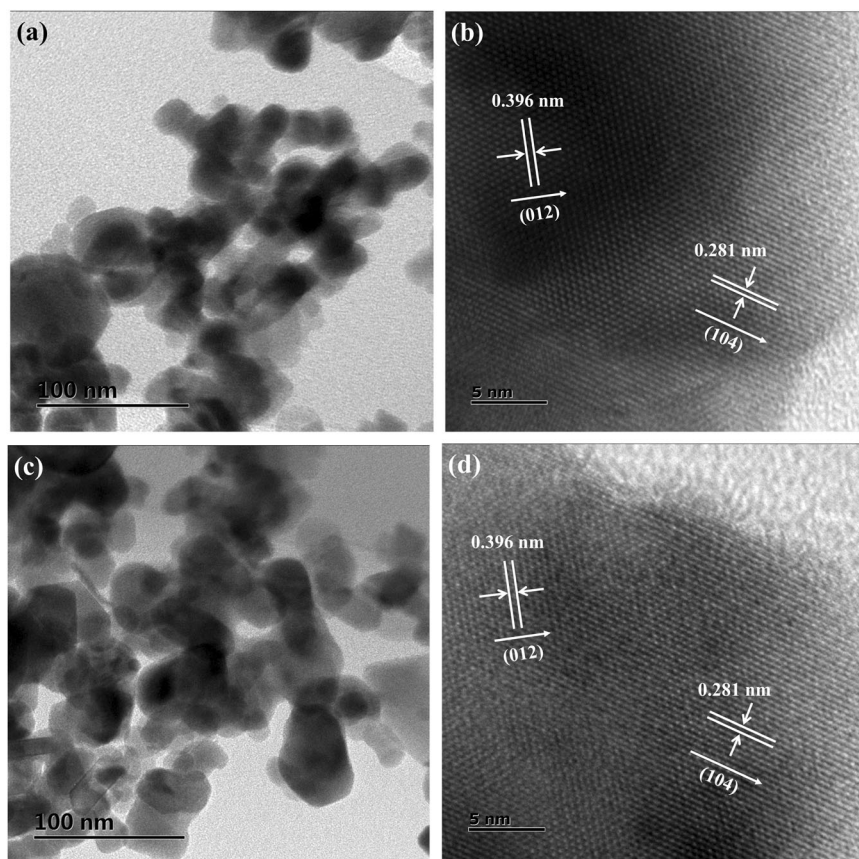

Fig. 3 TEM and HRTEM images of the prepared **a**, **b** BFO and **c**, **d** Er3%-BFO samples

distortion in BFO derived from Er substitution might bring about the contraction in lattice parameters, unit cell, and volume, as verified by the calculated unit cell parameters in Table 1. In addition, the crystalline sizes were calculated from the XRD patterns using Scherer's formula to be 52.45, 43.82, 39.51, and 36.35 nm for pure BFO, Er1%-BFO, Er3%-BFO, and Er5%-BFO, respectively, confirming the crystalline size of Er-doped BFO was slightly reduced with increasing the Er doping content. This further reveals the structural distortion of BFO induced by the Er doping.

The general morphologies and particle sizes of as-prepared BFO and Er-doped BFO samples were examined by FESEM, as shown in Fig. 2a–d. The prepared pure BFO (Fig. 2a) exhibited agglomeration of the particles with an irregular shape in an average particle size of 40–100 nm. As for Er-doped BFO samples (Fig. 2b–d), each Er-doped BFO sample also consisted of irregular nanoparticles, similar to those of BFO, indicating that the Er-doping had no obvious effect on the morphology of products. Meanwhile, the uniform distribution of Er dopant element in the BFO host

Table 2 The average crystalline size, BET surface area, simple TC adsorption efficiency in dark, and photodegradation efficiency of the prepared photocatalyst samples

Samples	Average crystalline size (nm)[a]	BET surface area (m²/g)[b]	Simple TC adsorption in dark (%)	Photodegradation efficiency (TC) (%)
BFO	52.4	21.4	2.2	27.3
Er1%-BFO	43.8	24.6	3.1	49.0
Er3%-BFO	39.5	27.1	3.5	75.8
Er5%-BFO	36.3	28.5	3.6	57.8

[a]Calculated from XRD results by Scherrer formula

[b]Measured from Brunauer–Emmett–Teller (BET) nitrogen adsorption–desorption instrument

was verified by the Er elemental mapping of the Er3%-BFO sample (Fig. 2e). According to the ICP-MS results in Table 1, the actual Er doping contents in the prepared Er-doped BFO samples were found to be 0, 0.96%, 2.77%, and 4.59% for BFO, Er1%-BFO, Er3%-BFO, and Er5%-BFO, respectively, which were close to the theoretical Er doping contents, further demonstrating the effective doping of Er^{3+} ions in Er-doped BFO samples. In addition, the morphological microstructures of the prepared BFO and Er-doped BFO samples were further examined by TEM and high-resolution TEM (HRTEM) measurements, as presented in Fig. 3. It can be seen that both the prepared BFO (Fig. 3a) and the Er3%-BFO samples (Fig. 3c) were composed of irregular particles with an average particle size of ~50 nm, which were prone to aggregate, in accordance with the FESEM results. To further manifest the crystalline phase of BFO and Er-doped BFO sample, the HRTEM images of both the BFO and Er3%-BFO samples (Fig. 3c, d) were acquired. The interplanar spacings for the pure BFO and Er3%-BFO were 0.396 and 0.281 nm, which could be corresponding to the (012) and (104) crystal planes of the rhombohedral BFO, respectively. The HRTEM data further confirm the rhombohedral crystal structure of pure BFO and Er3%-BFO nanoparticles, in accordance with the XRD result. In addition, the specific surface areas of the prepared pure BFO, Er1%-BFO, Er3%-BFO, and Er5%-BFO were determined from the BET measurements to be 21.4, 24.6, 27.1, and 28.5 m²/g, respectively. The larger specific surface area of Er-doped BFO samples in comparison with the pure BFO sample would result in a stronger adsorption capacity (as presented in Table 2), which could play a positive role in photocatalytic activity [37].

To clarify the elemental chemical states of the prepared Er-doped BFO sample, we carried out the XPS measurements. As seen in the survey spectrum of Er3%-BFO sample (Fig. 4a), the prepared Er3%-BFO sample was composed of Bi, Fe, O, and Er elements (Note: the C 1s peak should be ascribed to the adventitious carbon for calibration during XPS measurement [38, 39]). The core-level XPS spectrum for Er 4d (Fig. 4b) reveals that the Er 4d peaks centered at 168.80 eV could be associated with trivalent oxidation state of erbium [40, 41], suggesting that Er^{3+} was effectively doped into BFO nanoparticles.
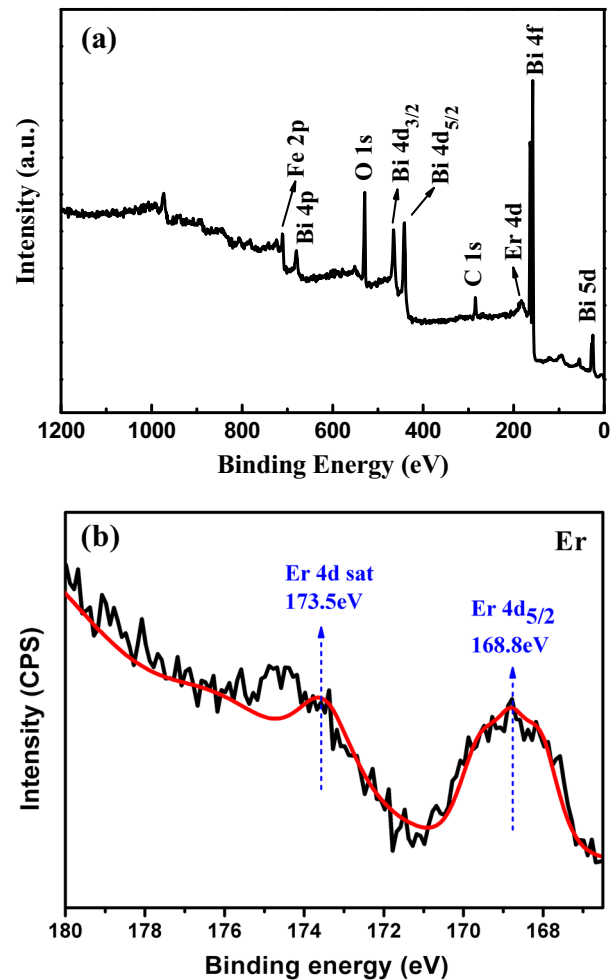
Fig. 4 XPS spectra of Er3%-doped BFO nanoparticles: **a** survey spectrum, **b** the core level spectrum of Er 4d

Moreover, the corresponding surface quantitative analysis revealed that the measured Er content was close to its theoretical value, indicating a homogeneous distribution of Er^{3+} ions in Er3%-BFO sample. The XPS results further confirmed the successful preparation of Er-doped BFO nanoparticles.

The optical absorption properties of the prepared BFO and Er-doped BFO samples were examined by the UV–vis DRS spectra, and the results are displayed in Fig. 5. The prepared BFO nanoparticles showed strong spectral
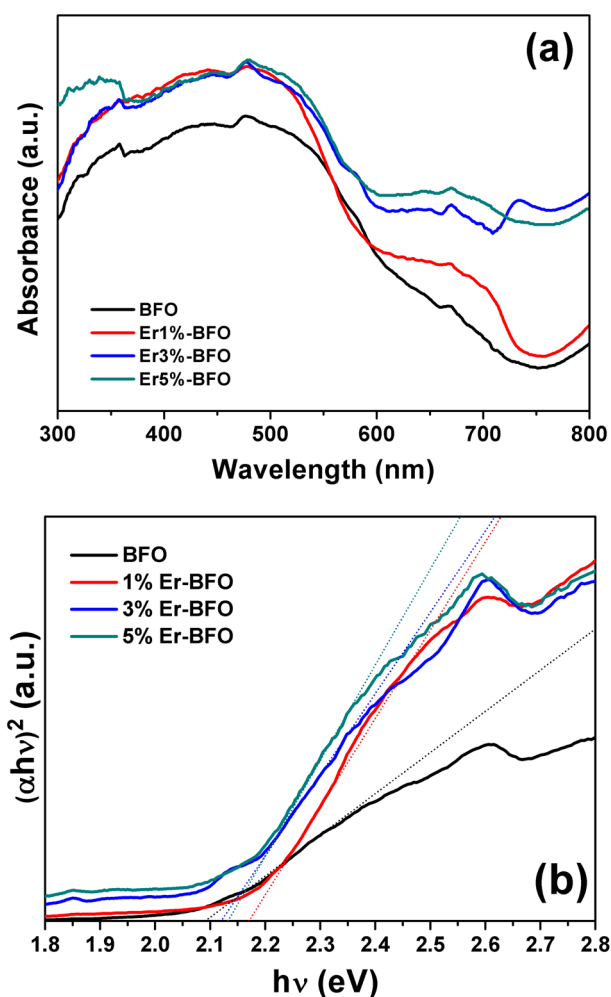
Fig. 5 **a** UV–visible absorbance spectra of the prepared pure BFO, Er1%-BFO, Er3%-BFO, and Er5%-BFO, respectively; **b** the plots to determine the band gaps for each sample

absorption capability ranging from 300 to 600 nm, demonstrating the visible light response of BFO for photocatalytic reaction. In comparison, the Er-doped BFO samples manifested much stronger optical absorption ability especially in the visible light region, and the absorption intensity also increased with the Er dopant concentration. The significantly improved visible light absorption of the Er-doped BFO could be ascribed to the upconversion ability of Er doping, that is, the ability to convert infrared light into visible light [27]. Apparently, the enhanced spectral absorption ability of BFO by Er doping would probably boost the photocatalytic activity of Er-doped BFO for TC removal, as discussed below. However, the band gap values of the pristine BFO, Er1%-BFO, Er3%-BFO, and Er5%-BFO samples calculated from the plots of Kubelka–Munk function [42] were 2.09, 2.16, 2.12, and 2.13 eV, respectively, implying that Er doping could slightly enlarge the band gap of BFO.

To investigate the influence of Er doping on the photocatalytic activities of BFO, the prepared BFO and Er-doped BFO samples were used as the photocatalysts for photocatalytic TC removal upon visible light. As shown in Fig. 6a, the concentration of TC was nearly unchanged in the absence of any photocatalyst, suggesting that the TC structure is stable. When the BFO photocatalyst was added, about 27.3% of TC was decomposed after 180 min irradiation time. In contrast, the Er-doped BFO photocatalysts exhibited much higher TC photodegradation efficiencies. It was found that 49.0%, 75.8%, and 57.8% of TC were decomposed for the Er1%-BFO, Er3%-BFO, and Er5%-BFO samples, respectively, after 180 min visible light irradiation (Table 2). Apparently, the Er3%-BFO sample achieved the highest photocatalytic degradation efficiency of TC, which was ca. 2.8 times that of the prepared BFO and could be also comparable to those photocatalytic TC degradation efficiencies over the previously-reported BFO-based or TiO$_2$-based photocatalysts [43–48] as summarized in Table S1. According to the Langmuir–Hinshelwood model [49], the TC degradation rate constants (k) for the blank sample, the pristine BFO, Er1%-BFO, Er3%-BFO, and Er5%-BFO calculated from the fitting curves of ln(C_0/C) versus irradiation time (t) were $(2.31 \pm 0.07) \times 10^{-4}$, $(1.83 \pm 0.055) \times 10^{-3}$, $(3.65 \pm 0.109) \times 10^{-3}$, $(6.68 \pm 0.204) \times 10^{-3}$, and $(4.64 \pm 0.139) \times 10^{-3}$ min^{-1}, respectively, as shown in Fig. 6b. The TC degradation rate constant of the Er3%-BFO sample was about 3.6 times that of the pristine BFO sample. It should be noted that the photocatalytic activity of Er5%-BFO was on the contrary decreased though the doping amount of Er element was further increased to 5%. This could be attributed to the fact that excess amounts of Er dopant in BFO may act as recombination centers for photogenerated electron–hole pairs [50], thereby resulting in low photoactivity. Thus, the doping amount of Er elements could play an essential role in determining the photocatalytic activities of Er-doped BFO photocatalysts. With a proper doping amount of Er element, a significant improvement of photocatalytic activities of BFO could be achieved. In addition, the photocatalytic stability and reusability were also evaluated by recycling 5 runs for photocatalytic degradation of TC over Er3%-BFO, as depicted in Fig. 6c. As seen, the photocatalytic degradation efficiency of Er3%-BFO had little attenuation after 5 successive runs, implying that the Er-doped BFO photocatalyst was quite stable and reusable. Furthermore, the main reactive species for photocatalytic TC removal catalyzed by Er-doped BFO were determined by the photocatalytic trapping experiments, in order to clarify the photocatalytic mechanism of Er-doped BFO. Figure 6d shows the photocatalytic TC removal results catalyzed by the Er3%-BFO photocatalyst with the addition of different quenchers under visible light irradiation. It was found that the photocatalytic activity of Er3%-BFO for TC
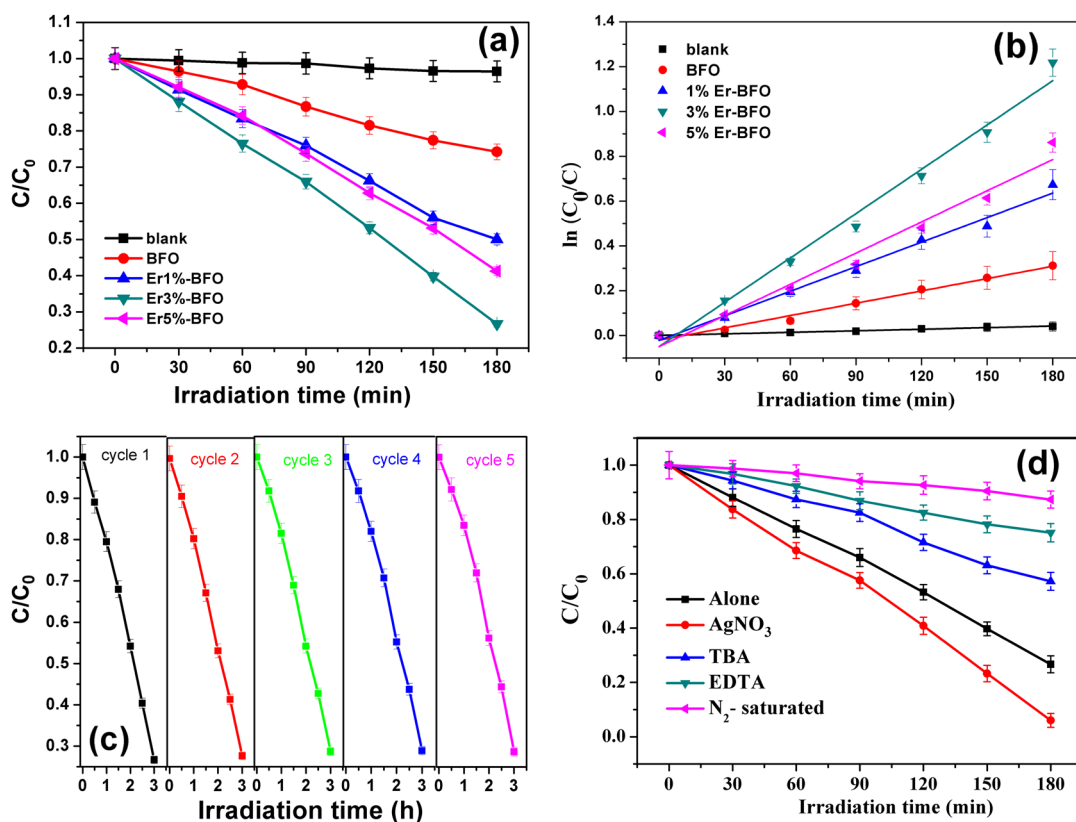
Fig. 6 a TC removal catalyzed by the prepared BFO and Er-doped BFO photocatalysts as a function of the irradiation time under visible light ($\lambda \geq 420$ nm). **b** Pseudo-first kinetics fitting data for the photocatalytic degradation of TC over the prepared samples. **c** Photocatalytic stability of the Er3%-BFO sample by evaluating TC removal for five cycles. **d** Photocatalytic degradation of TC over the Er3%-BFO sample alone, and with the addition of different types of active species scavengers (i.e., AgNO$_3$, EDTA, and TBA) or in the absence of O$_2$ (i.e., N$_2$-saturated solution) under visible light ($\lambda \geq 420$ nm)

removal was suppressed to different extents when adding tert-butyl alcohol (TBA, a hydroxyl radicals (·OH) scavenger [51], 2 mM) or ethylene diamine tetraacetic acid (EDTA, a hole (h$^+$) scavenger [52], 2 mM), whereas the photocatalytic activity was significantly improved when AgNO$_3$ (an electron scavenger [53], 2 mM) was added. More importantly, the photocatalytic TC removal efficiency was found to be dramatically restrained when the trapping experiment was carried out under N$_2$-saturated conditions, suggesting superoxide radicals (O$_2^{-\bullet}$) could play a significant role in the photocatalytic TC removal. From the above trapping experiments, it can be revealed that the predominant reactive species for TC removal catalyzed by the Er-doped BFO were superoxide radicals, photogenerated holes, or hydroxyl radicals rather than photogenerated electrons.

To probe into the enhanced photocatalytic mechanism of Er-doped BFO for TC removal, the photocurrent action spectra, EIS, and PL spectra of the prepared BFO and Er-doped BFO photocatalysts were measured. As known, the charge separation and migration efficiency of the photo-induced carriers within a photocatalyst can be reflected by transient photocurrent [54]. Figure 7a displays the typical

photocurrent action spectra for BFO and Er3%-BFO photo-toelectrodes under chopped visible light ($\lambda \geq 420$ nm) irradiation. As shown, both BFO and Er3%-BFO photoelectrodes could produce transient photocurrents upon visible light irradiation. In comparison with the BFO photoelectrode, the Er3%-BFO photoelectrode manifested a much higher photocurrent intensity, implying a much more efficient charge separation and transfer process and a much longer charge lifetime of the photoinduced carriers in the Er3%-doped BFO sample thus leading to the improved photocatalytic performance. To further reveal the influence of Er doping on the interfacial charge transfer efficiency of BFO, the EIS Nyquist plots for BFO and Er3%-BFO photocatalysts (Fig. 7b) were obtained under visible light ($\lambda \geq$ 420 nm) irradiation. In general, the arc radius at the high-frequency zone in the Nyquist plot is associated with the interfacial charge transfer process on the photoelectrode surface, and a smaller arc radius usually signifies a higher efficient charge separation and transfer process of photo-induced carriers at the electrode/electrolyte interface [55]. As seen, the Er3%-BFO photoelectrode exhibited a relatively smaller arc radius than the BFO photoelectrode,
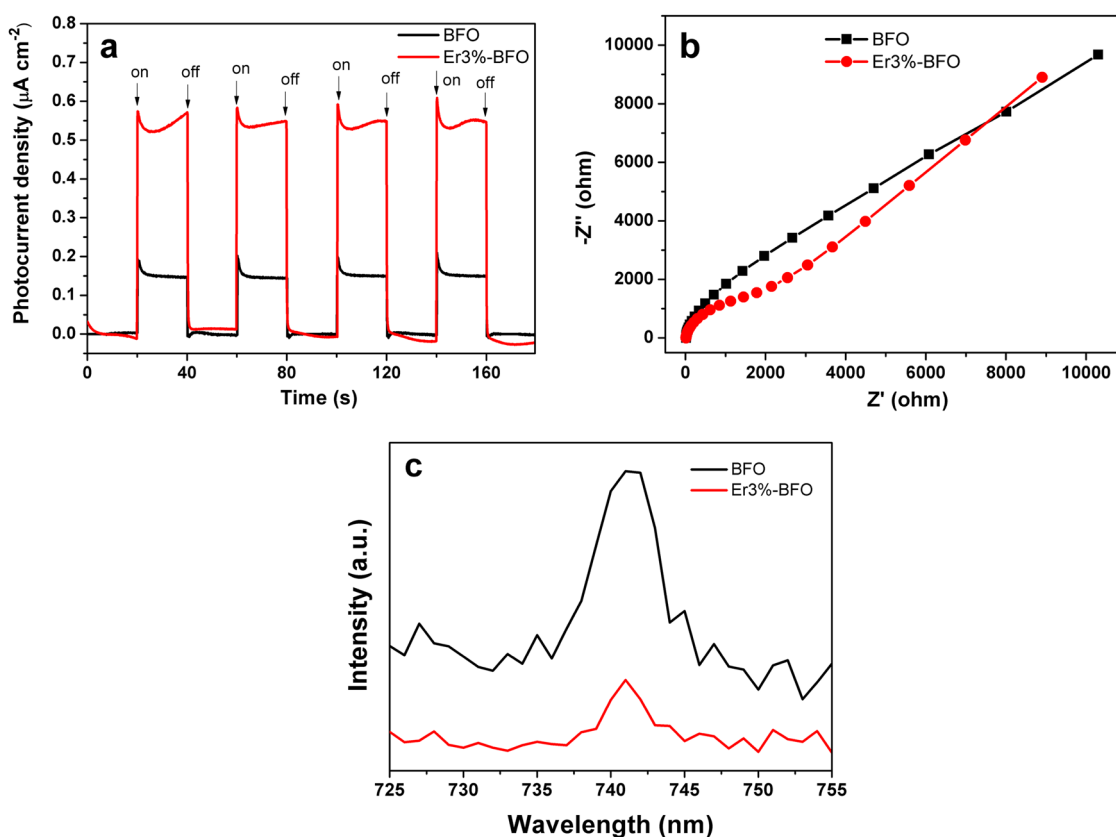
Fig. 7 a Photocurrent response spectra of the pure BFO and Er3%-BFO photoelectrodes upon chopped visible light irradiation ($\lambda \geq 420$ nm). **b** EIS Nyquist plots of the pure BFO and Er3%-BFO photoelectrodes under visible light illumination ($\lambda \geq 420$ nm). **c** PL emission spectra of the prepared BFO and Er3%-BFO samples at an excitation wavelength of 404 nm

confirming that the photogenerated charge separation and migration process of BFO could be effectively promoted by Er doping, which was consistent with the photocurrent result. Furthermore, we also conducted the PL experiments to investigate the recombination process of photogenerated electrons and holes within the BFO and Er3%-BFO samples. The PL emission intensity has been considered to be correlated to the recombination probability of photoexcited electrons and holes, and the lower PL emission intensity implies the decreased recombination probability [56]. Figure 7c displays the PL spectra of the prepared BFO and Er3%-doped BFO photocatalysts. As seen, the Er3%-BFO sample had a PL emission band centered at 741 nm, which was similar to that of BFO. Compared to BFO, the Er3%-BFO sample exhibited a much smaller PL emission intensity, confirming that the Er dopants could reduce the recombination rate of electron–hole pairs. The reason for low recombination rate of electron–hole pairs in the Er-doped BFO nanoparticles could be presumed by two cases. First, the excited electrons were trapped by surface defects induced by the doping of Er, which could decrease the number of recombination of electron–hole pairs [57, 58]. The second reason for the decreased PL intensity of Er3%-BFO was the relatively smaller size of this sample as

compared to the pure BFO sample. The decrease in the PL intensity with decreasing the particle size might be derived from the fact that the defects would increase while reduction in the particle size and hence the quenching centers for non-radiative recombination of electron–hole pairs would also increase [59], thus leading to the quenching of luminescence. Thus, the lower recombination probability of photogenerated electrons and holes within Er3%-BFO would make some important contribution to the boosted photocatalytic performance. Therefore, from these experimental results, it can be demonstrated that the improved photocatalytic activities of Er-doped BFO could be attributed to the augmented optical absorption capability, the promoted charge separation and transfer process as well as the decreased recombination probability of photogenerated electrons and holes arising from the Er doping effect.

On the basis of the above trapping experiments and PEC measurements, the photocatalytic mechanism for TC removal by the Er-doped BFO photocatalysts under visible light irradiation was proposed. Figure 8 schematically illustrates the photocatalytic mechanism of Er-doped BFO for TC removal. Under visible light irradiation, the Er-doped BFO photocatalyst could be excited to produce substantial electron–hole pairs. Subsequently, the
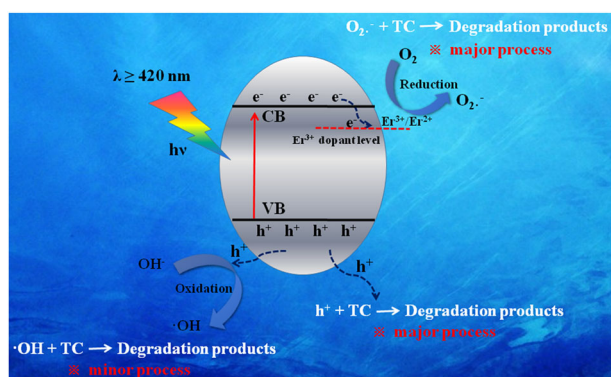
Fig. 8 Schematic illustration of the photocatalytic mechanism for TC removal over the Er-doped BFO photocatalyst

photogenerated electrons would be rapidly transferred from the conduction band (CB) to the Er^{3+} dopant level and then to the photocatalyst surface, where the reactive superoxide radicals ($O_2^{-\bullet}$) would be formed by reacting with the surface-adsorbed O_2 to further participate in the photocatalytic removal of TC. At the same time, the holes remaining in the valence band (VB) would migrate to the photocatalyst surface and thereby react with H_2O to form hydroxyl radicals ($\cdot OH$) for the TC removal or directly oxidize TC. In our case, superoxide radicals ($O_2^{-\bullet}$) and holes (h^+) were the predominant reactive species for TC removal, while hydroxyl radicals ($\cdot OH$) might also make some contribution to the TC removal process. In addition, the TOC removal efficiency during the photocatalytic TC removal process was investigated to determine the degree of mineralization of the pollutant. The TOC removal ratios of TC over the prepared BFO and Er-doped photocatalysts are shown in Figure S1. About 24.4%, 46.2%, 72.6%, and 51.3% were photocatalytically degraded by the prepared BFO, Er1%-BFO, Er3%-BFO, and Er5%-BFO, respectively, and mineralized to CO_2, H_2O, or inorganic ions under visible light irradiation for 180 min. The TOC analysis further indicates that the Er3%-BFO photocatalyst possessed a relatively strong mineralization ability.

4 Conclusions

To summarize, the Er-doped BFO photocatalysts with different Er dopant concentrations ($Bi_{1-x}Er_xFeO_3$, where $x=$ 0, 0.01, 0.03, or 0.05) were successfully synthesized through a simple sol–gel approach. The doping of Er^{3+} into the BFO host was proven by a variety of characterization techniques including XRD, SEM, TEM, and XPS. It was found that the optical absorption capacity of BFO was improved by Er doping especially in the visible light region, and the absorbance value was also gradually increased with

the rise of Er dopant concentration. The photocatalytic experiments reveal that the photocatalytic activities of all the Er-doped BFO photocatalysts for TC removal were much higher than the BFO photocatalyst, and the Er3%-BFO sample achieved the highest photocatalytic TC degradation efficiency of 75.8% which was about 2.8 times that of the prepared BFO sample. On the basis of the photocurrent action spectra, EIS, and PL spectra, the major contributions to the improvement in the photocatalytic activities of Er-doped BFO were the much more spectral absorption capability, the more efficient charge separation and migration process as well as the lower recombination probability of photogenerated electrons and holes, arising from the Er doping effect. Moreover, the stability and reusability of the prepared Er-doped BFO nanoparticles for photocatalytic TC removal were fairly good. Thus, this work manifests a possibility to use Er-doped BFO as an effective visible light photocatalyst for highly efficient photocatalytic degradation or removal of antibiotics from aqueous matrices.

Compliance with ethical standards

Conflict of interest The authors declare that they have no conflict of interest.

Publisher's note: Springer Nature remains neutral with regard to jurisdictional claims in published maps and institutional affiliations.

References

1. Homem V, Santos L (2011) Degradation and removal methods of antibiotics from aqueous matrices—a review. J Environ Manag 92:2304–2347
2. Bagheri S, Termehyousefi A (2017) Photocatalytic pathway toward degradation of environmental pharmaceutical pollutants: structure, kinetics and mechanism approach. Catal Sci Technol 7:4548–4569
3. Chong MN, Jin B, Chow CW, Saint C (2010) Recent developments in photocatalytic water treatment technology, a review. Water Res 44:2997–3027
4. He HY (2016) Facile synthesis of ultrafine CuS nanocrystalline/ TiO2:Fe nanotubes hybrids and their photocatalytic and Fenton-like photocatalytic activities in the dye degradation. Microporous Mesoporous Mater 227:31–38
5. He HY (2017) Facile synthesis of Bi_2S_3 nanocrystalline-modified TiO2:Fe nanotubes hybrids and their photocatalytic activities in dye degradation. Part Sci Technol 35:410–417

6. He HY, Tian CY (2016) Rapid photo- and photo-Fenton-like catalytic removals of malachite green in aqueous solution on undoped and doped TiO_2 nanotubes. Desalin Water Treat 57:14622–14631

7. Pan FM, Zhang B, Cai WH (2017) The effect of hydrophilicity/hydrophobicity of TiO_2–SiO_2 composite aerogels in the epoxidation reaction. Catal Commun 98:121–125

8. Xiang C, Guo RH, Lan JW, Jiang SX, Wang C, Du ZF, Cheng C (2018) Self-assembling porous 3D titanium dioxide-reduced graphene oxide aerogel for the tunable absorption of oleic acid and RhodamineB dye. J Alloys Compd 735:246–252

9. Cho CM, Noh JH, Cho IS, An JS, Hong KS, Kim JY (2008) Low-temperature hydrothermal synthesis of pure $BiFeO_3$ nanopowders using triethanolamine and their applications as visible-light photocatalysts. J Am Ceram Soc 91:3753–3755

10. Joshi UA, Jang JS, Borse PH, Lee JS (2008) Microwave synthesis of single-crystalline perovskite $BiFeO_3$ nanocubes for photoelectrode and photocatalytic applications. Appl Phys Lett 92:242106

11. Huo YN, Jin Y, Zhang Y (2010) Citric acid assisted solvothermal synthesis of $BiFeO_3$ microspheres with high visible-light photocatalytic activity. J Mol Catal A Chem 331:15–20

12. Li ZX, Shen Y, Yang C, Lei YC, Guan YH, Lin YH, Liu DB, Nan W (2013) Significant enhancement in the visible light photocatalytic properties of $BiFeO_3$–graphene nanohybrids. J Mater Chem A 1:823–829

13. Fei LF, Yuan JK, Hu YM, Wu CZ, Wang JL, Wang Y (2011) Visible light responsive perovskite $BiFeO_3$ pills and rods with dominant {111}(c) facets. Cryst Growth Des 11:1049–1053

14. Guo RQ, Fang L, Dong W, Zheng FG, Shen MG (2010) Enhanced photocatalytic activity and ferromagnetism in gd doped $BiFeO_3$ nanoparticles. J Phys Chem C 114:21390–21396

15. Niu F, Chen D, Qin LS, Gao T, Zhang N, Wang S, Chen Z, Wang JY, Sun XG, Huang YX (2015) Synthesis of Pt/$BiFeO_3$ heterostructured photocatalysts for highly efficient visible-light photocatalytic performances. Sol Energy Mater Sol Cells 143:386–396

16. Niu F, Chen D, Qin L, Zhang N, Wang JY, Chen Z, Huang YX (2015) Facile synthesis of highly efficient p–n heterojunction CuO/$BiFeO_3$ composite photocatalysts with enhanced visible-light photocatalytic activity. ChemCatChem 7:3279–3289

17. Mohan S, Subramanian B, Bhaumik I, Gupta PK, Jaisankar SN (2014) Nanostructured $Bi_{(1-x)}Gd_{(x)}FeO_3$—a multiferroic photocatalyst on its sunlight driven photocatalytic activity. RSC Adv 4:16871–16878

18. Pei YL, Zhang C (2013) Effect of ion doping in different sites on the morphology and photocatalytic activity of $BiFeO_3$ microcrystals. J Alloys Compd 570:57–60

19. Bingham S, Daoud WA (2011) Recent advances in making nanosized TiO_2 visible-light active through rare-earth metal doping J Mater Chem 21:2041–2050

20. Weber AS, Grady AM, Koodali RT (2012) Lanthanide modified semiconductor photocatalysts. Catal Sci Technol 2:683–693

21. Ranjit KT, Willner I, Bossmann SH, Braun AM (2001) Lanthanide oxide-doped titanium dioxide photocatalysts: novel photocatalysts for the enhanced degradation of p-chlorophenoxyacetic acid. Environ Sci Technol 35:1544–1549

22. Yang Y, Zhang CC, Xu Y, Wang HY, Li X, Wang C (2010) Electrospun Er:TiO_2 nanofibrous films as efficient photocatalysts under solar simulated light. Mater Lett 64:147–150

23. Bharathkumar S, Sakar M, Ponpandian N, Balakumar S (2018) Dual oxidation state induced oxygen vacancies in Pr substituted $BiFeO_3$ compounds: an effective material activation strategy to enhance the magnetic and visible light-driven photocatalytic properties. Mater Res Bull 101:107–115

24. Chen ZW, Wu YP, Wang X, Jin WL, Zhu CB (2015) Ferromagnetism and enhanced photocatalytic activity in Nd doped $BiFeO_3$ nanopowders. J Mater Sci Mater Electron 26:9929–9940

25. Hu ZJ, Chen D, Wang S, Zhang N, Qin LS, Huang YX (2017) Facile synthesis of Sm-doped $BiFeO_3$ nanoparticles for enhanced visible light photocatalytic performance. Mater Sci Eng B Adv Funct Solid-State Mater 220:1–12

26. Sakar M, Balakumar S, Saravanan P, Bharathkumar S (2015) Compliments of confinements: substitution and dimension induced magnetic origin and band-bending mediated photocatalytic enhancements in $Bi_{1-x}Dy_xFeO_3$ particulate and fiber nanostructures. Nanoscale 7:10667–10679

27. Obregóna S, Colón G (2012) Evidence of upconversion luminescence contribution to the improved photoactivity of erbium doped TiO_2 systems. Chem Commun 48:7865–7867

28. Wang T, Song SH, Xu T, Wang M (2016) Maltose-assisted sol–gel synthesis, structural, magnetic and optical properties of multiferroic $BiFeO_3$ nanopowders. J Sol-Gel Sci Technol 80:675–682

29. Chen C, Cheng JR, Yu SW, Che LJ, Meng ZY (2006) Hydrothermal synthesis of perovskite bismuth ferrite crystallites. J Cryst Growth 291:135–139

30. Maurya D, Thota H, Nalwa KS, Garg A (2009) $BiFeO_3$ ceramics synthesized by mechanical activation assisted versus conventional solid-state-reaction process: a comparative study. J Alloys Compd 477:780–784

31. Wang YP, Zhou L, Zhang MF, Chen XY, Liu JM, Liu ZG (2004) Room-temperature saturated ferroelectric polarization in $BiFeO_3$ ceramics synthesized by rapid liquid phase sintering. Appl Phys Lett 84:1731–1733

32. Shokrollahi H (2013) Magnetic, electrical and structural characterization of $BiFeO_3$ nanoparticles synthesized by co-precipitation. Powder Technol 235:953–958

33. Das N, Majumdar R, Sen A, Maiti HS (2007) Nanosized bismuth ferrite powder prepared through sonochemical and microemulsion techniques. Mater Lett 61:2100–2104

34. Gao T, Chen Z, Zhu YX, Niu F, Huang QL, Qin LS, Sun XG, Huang YX (2014) Synthesis of $BiFeO_3$ nanoparticles for the visible-light induced photocatalytic property. Mater Res Bull 59:6–12

35. Zhang N, Chen D, Niu F, Wang S, Qin LS, Huang YX (2016) Enhanced visible light photocatalytic activity of Gd-doped $BiFeO_3$ nanoparticles and mechanism insight Sci Rep 6:26467

36. Xing WY, Ma Y, Ma Z, Bai YL, Chen JY, Zhao SF (2014) Improved ferroelectric and leakage current properties of Er-doped $BiFeO_3$ thin films derived from structural transformation. Smart Mater Struct 23:085030

37. Yang YC, Zhang T, Le L, Ruan XF, Fang PF, Pan CX, Xiong R, Shi J, Wei JH (2014) Quick and facile preparation of visible light-driven TiO_2 photocatalyst with high absorption and photocatalytic activity. Sci Rep 4:7045–7052

38. Yu CL, Yang K, Xie Y, Fan QZ, Yu JC, Shu Q, Wang CY (2013) Novel hollow Pt-ZnO nanocomposite microspheres with hierarchical structure and enhanced photocatalytic activity and stability. Nanoscale 5:2142–2151

39. Zhao YK, Liu YD, Du XQ, Han RX, Ding Y (2014) Hexagonal assembly of $Co_3V_2O_8$ nanoparticles acting as an efficient catalyst for visible light-driven water oxidation. J Mater Chem A 2:19308–19314

40. Mao CY, Li WJ, Wu F, Dou YY, Fang L, Ruan HB, Kong CY (2015) Effect of Er doping on microstructure and optical properties of ZnO thin films prepared by sol–gel method. J Mater Sci Mater Electron 26:8732–8739

41. Maneeshya LV, Thomas PV, Joy K (2015) Effects of site substitutions and concentration on the structural, optical and visible photoluminescence properties of Er doped $BaTiO_3$ thin films prepared by RF magnetron sputtering. Opt Mater 46:304–309

42. Clementi C, Miliani C, Verri G, Sotiropoulou S, Romani A, Brunetti BG, Sgamellotti A (2009) Application of the Kubelka–

Munk correction for self-adsorption of fluorescence emission in carmine lake paint layers. Appl Spectrosc 63:1323–1329

43. Tao R, Shao CL, Li XH, Li XW, Liu S, Yang S, Zhao CC, Liu YC (2018) Bi_2MoO_6/$BiFeO_3$ heterojunction nanofibers: enhanced photocatalytic activity, charge separation mechanism and magnetic separability. J Colloid Interface Sci 529:404–414

44. Gong YY, Wu YJ, Xu Y, Li L, Li C, Liu XJ, Niu LY (2018) All-solid-state Z-scheme CdTe/TiO_2 heterostructure photocatalysts with enhanced visible-light photocatalytic degradation of antibiotic waste water. Chem Eng J 350:257–267

45. Jiang YH, Jing X, Zhu K, Peng ZY, Zhang JM, Liu Y, Zhang WL, Ni L, Liu ZC (2018) Ta_3N_5 nanoparticles/TiO_2 hollow sphere (0D/3D) heterojunction: facile synthesis and enhanced photocatalytic activities of levofloxacin degradation and H_2 evolution. Dalton Trans 47:13113–13125

46. Shen XF, Song LL, Luo L, Zhang Y, Zhu B, Liu JS, Chen ZG, Zhang LS (2018) Preparation of TiO_2/C_3N_4 heterojunctions on carbon-fiber cloth as efficient filter-membrane-shaped photocatalyst for removing various pollutants from the flowing wastewater. J Colloid Interface Sci 532:798–807

47. He L, Dong YN, Zhang YN, Jia QM, Shan SY, Zhang YQ (2019) A novel magnetic MIL-101(Fe)/TiO_2 composite for photo degradation of tetracycline under solar light. J Hazard Mater 361:85–94

48. Shi YY, Yang ZW, Wang B, An H, Chen ZZ, Cui H (2016) Adsorption and photocatalytic degradation of tetracycline hydrochloride using a palygorskite-supported Cu_2O–TiO_2 composite. Appl Clay Sci 119:311–320

49. Ma SS, Li R, Lv CP, Xu W, Gou XL (2011) Facile synthesis of ZnO nanorod arrays and hierarchical nanostructures for photocatalysis and gas sensor applications. J Hazard Mater 192:730–740

50. Akpan UG, Hameed BH (2010) The advancements in sol–gel method of doped-TiO_2 photocatalysts. Appl Catal A Gen 375:1–11

51. Minero C, Mariella G, Maurino V, Vione D, Pelizzetti E (2000) Photocatalytic transformation of organic compounds in the presence of inorganic ions. 2. Competitive reactions of phenol and alcohols and titanium dioxide–fluoride system. Langmuir 16:8964–8972

52. Tian Y, Chang B, Lu J, Fu J, Xi F, Dong X (2013) Hydrothermal synthesis of graphitic carbon nitride–Bi_2WO_6 heterojunctions with enhanced visible light photocatalytic activities. ACS Appl Mater Interfaces 5:7079–7085

53. Li WJ, Li DZ, Lin YM, Wang PX, Chen W, Fu XZ, Shao Y (2012) Evidence for the active species involved in the photo-degradation process of methyl orange on TiO_2. J Phys Chem C 116:3552–3560

54. Kim HG, Borse PH, Choi W, Lee JS (2010) Photocatalytic nanodiodes for visible-light photocatalysis. Angew Chem Int Ed 117:4661–4665

55. Hong SJ, Lee S, Jang JS, Lee JS (2011) Heterojunction $BiVO_4$/WO_3 electrodes for enhanced photoactivity of water oxidation. Energy Environ Sci 4:1781–1787

56. Shiraishi Y, Takeshita S, Isobe T (2015) Two photoenergy conversion modes of YVO_4:Eu^{3+} nanoparticles: photoluminescence and photocatalytic activity. J Phys Chem C 119:13502–13508

57. Bhethanabotla VC, Russell DR, Kuhn JN (2017) Assessment of mechanisms for enhanced performance of Yb/Er/titania photocatalysts for organic degradation: role of rare earth elements in the titania phase. Appl Catal B Environ 202:156–164

58. Tobaldi DM, Ferreira RAS, Pullar RC, Seabra MP, Carlos LD, Labrincha JA (2015) Nano-titania doped with europium and neodymium showing simultaneous photoluminescent and photocatalytic behaviour. J Mater Chem C 3:4970–4986

59. Chang MQ, Zou HF, Song YH, Chen J, Cui L, Sheng Y, Zheng KY (2019) Photoluminescence and photodegradation properties of SiO_2@TiO_2:Sm^{3+} with different coating effects. J Phys Chem Solids 124:100–110

Photoassisted Electrodeposition of Cobalt-Phosphate Cocatalyst on BiFeO$_3$ Thin Film Photoanode for Highly Efficient Photoelectrochemical Performances of Water Oxidation

Yanze Wang, Da Chen, [z] Sen Wang, Junhui Liang, Laishun Qin,[z] Xingguo Sun, and Yuexiang Huang

College of Materials Science and Engineering, China Jiliang University, Hangzhou, 310018 Zhejiang, People's Republic of China

In this work, cobalt-phosphate (Co-Pi) cocatalyst is deposited on the surface of BiFeO$_3$ (BFO) thin film photoanode for enhanced photoelectrochemical (PEC) performances. The prepared Co-Pi/BFO thin film is composed of irregular rhombohedral BFO nanoparticles which are uniformly covered with a layer of amorphous Co-Pi, and the corresponding PEC performance is remarkably improved with a negatively-shifted onset potential from −0.058 V (BFO) to −0.130 V (Co-Pi/BFO). The photocurrent density of Co-Pi/BFO thin film photoanode measured at 0 V (vs. Ag/AgCl) under visible light irradiation is as high as ~0.050 mA cm^{-2} (nearly 8 times that of the prepared BFO thin film photoanode), which rivals or exceeds those of state-of-the-art BFO-based thin film photoelectrodes. On the basis of PEC measurement results, the enhanced PEC performance of Co-Pi/BFO photoanode can be attributed to the higher carrier concentration, the more efficient separation and transfer process of photogenerated charges and the lower electron/hole recombination probability induced by Co-Pi cocatalyst. In addition, the possible PEC mechanism of the Co-Pi/BFO photoanode is also discussed. The present work validates the feasibility of Co-Pi cocatalysts coupled with other photoanode systems for pursuing highly efficient PEC performances of water oxidation.

© 2019 The Electrochemical Society. [DOI: 10.1149/2.0711908jes]

In recent years, photoelectrochemical (PEC) water splitting has become a type of industrial photosynthesis to produce usable hydrogen and oxygen.[1–3] Since the discovery of PEC water splitting by TiO$_2$ photoanode,[4] many other metal oxide-based photoanodes (such as α-Fe$_2$O$_3$,[5] WO$_3$,[6] BiVO$_4$)[7] have been developed for PEC water splitting. Among the previously-reported oxide semiconductors, perovskite BiFeO$_3$ (BFO) has recently attracted a great concern because of its narrow bandgap, good chemical stability and low cost.[8] More importantly, BFO has also been demonstrated as a promising photoanode for PEC water splitting[9,10] under UV or visible light irradiation. For example, Moniz et al.[9] used the chemical vapor deposition method for the first time to prepare BFO thin film, exhibiting an efficient water oxidation with an average O$_2$ evolution rate of 0.023 μmol h^{-1} under UV light irradiation. Though much progress has been made on the PEC studies of BFO, the PEC activities of BFO thin films are still unsatisfactory because of their poor charge-transport properties and rapid electron-hole recombination.[11,12] Therefore, it is essential to modify the structure of BFO thin film photoanodes for improving their PEC performances.

So far, several strategies have been developed to boost the PEC activities of semiconductor photoanodes by improving the charge separation/migration process and reducing the electron-hole recombination at the semiconductor/electrolyte interface, including surface passivation,[13] heterojunction construction,[14] elemental doping,[15] cocatalyst deposition[16] and so on. Among them, the deposition of cocatalyst on the surface of semiconductor photoanodes has been widely recognized as an effective way for improving PEC activities, since the cocatalyst could reduce the PEC reaction overpotential, accelerate the reaction kinetics, suppress the surface state recombination, as well as probably offer more active sites for redox reactions.[5] The commonly-used cocatalysts are precious metals (such as Pt,[17] Pd,[18] Ru)[19] and their oxides (such as RuO$_2$),[20] showing notable enhancement in PEC activities of a given photoanode. However, these precious metals are not suitable for extensive use as cocatalysts because of the shortage of resources and high cost. Thus, the development of alternative inexpensive cocatalysts with high-efficiency performance is highly desirable. Cobalt-phosphate (Co-Pi), which was firstly reported by Nocea,[21] has been demonstrated as a promising cocatalyst material for improving PEC activities, because of its fascinating advantages including relatively high reactivity, cost effectiveness, natural abundance and self-healing feature.[22] A variety of semiconductor

electrodes, such as BiVO$_4$,[23,24] ZnO,[25] α-Fe$_2$O$_3$,[26,27] WO$_3$,[28] Si,[29] have been modified with the deposition of Co-Pi to enhance their PEC characterics. Moreover, Co-Pi can also form an oxygen-oxygen coupling bond on the photoanode surface and act as an active site to accelerate the redox reaction of charge carriers,[30] thus leading to enhanced PEC performance.

Herein, for the first time Co-Pi was deposited on the surface of BFO thin films as an efficient cocatalyst for purpose of achieving high-efficiency PEC performance. Firstly, the deposition of a Co-Pi cocatalyst layer on the BFO thin film was achieved using a photo-assisted electrodeposition method. Various characterization techniques were then employed to clarify the enhanced PEC performance of BFO thin film photoanodes by Co-Pi modification. In addition, the possible mechanism of Co-Pi/BFO composite photoanode for enhanced PEC performances was also proposed.

Experimental

Preparation of BFO and Co-Pi/BFO thin films.—All chemicals were of analytical grade without further purification. The BFO thin films were prepared on the surface of FTO conductive glass through a sol-gel method. Firstly, the FTO substrates (a size of 1 cm × 3 cm, 8 Ω sq^{-1}) were pretreated by successively cleaning ultrasonically in deionized (DI) water, acetone and ethanol for 10 min followed by drying with N$_2$ flow. The BFO precursor sol for spin coating was obtained as follows. 6 mmol of Bi(NO$_3$)$_3$·5H$_2$O and 6 mmol of Fe(NO$_3$)$_3$·9H$_2$O were dissolved in 20 mL of ethylene glycol, and 1 g of Pluronic P123 (PEO-PPO-PEO) was then added as a surfactant to the above solution with an ultrasonic treatment for 30 min. After aging 24 h, the obtained precursor sol was then spin coated on the pretreated FTO surface at a speed of 1400 rpm for 40 s under ambient conditions. The prepared precursor thin films were dried on a hot plate at 150°C for 30 min, and were then calcined in a muffle furnace at 550°C for 20 minutes. After being cooled to room temperature naturally, the BFO thin films were thus fabricated.

The layer of Co-Pi cocatalyst was deposited on the surface of BFO thin films by the photo-assisted electrodeposition method as described previously.[26] In a typical process, the deposition of Co-Pi was carried out in a home-built three-electrode PEC cell under a 300 W xenon lamp irradiation with an applied bias potential of 1 V (vs. Ag/AgCl) in an electrolyte solution containing 0.5 mM cobalt nitrate and 0.1 M potassium phosphate for 2 h. In the PEC cell, a Pt wire, a saturated Ag/AgCl and the fabricated BFO thin film electrode were used as
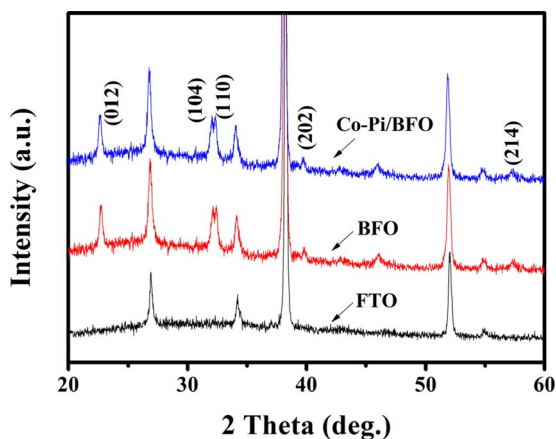
[z]E-mail: dchen_80@hotmail.com; qinlaishun@cjlu.edu.cn

Figure 1. XRD patterns of the FTO substrate, the prepared BFO and Co-Pi/BFO thin film photoanodes.

the counter electrode, the reference electrode and the working electrode, respectively. The obtained Co-Pi/BFO electrode was rinsed with deionized water and dried at room temperature.

Characterizations.—The X-ray powder diffraction (XRD) patterns of the obtained thin films were examined on a Bruker D2 X-ray diffractometer using Cu K_α radiation ($\lambda = 0.15406$ nm) to determine their crystalline structure. The morphological features and elemental compositions of the thin films were characterized by field emission scanning electron microscopy (FESEM, Hitachi SU8010) assembled with energy dispersive X-ray spectroscope (EDS). Transmission electron microscopy (TEM) was operated on a field emission transmission electron microscope (JEOL, JEM-2100). The sample species for TEM measurements were carefully peeled off from the prepared BFO and Co-Pi/BFO thin film photoanodes. X-ray photoelectron spectroscopy (XPS) measurements were performed on a Kratos Axis Ultra instrument with Al K_α radiation to determine the chemical states of the prepared samples. The photoluminescence (PL) spectra were conducted using a Hitachi High-Tech F-7000 fluorescence spectrophotometer under an excitation of 407 nm.

Photoelectrochemical measurements.—The PEC measurements were conducted on a CHI660E electrochemical workstation using a home-built three-electrode PEC cell with a platinum wire as a counter electrode, a saturated Ag/AgCl electrode as reference electrode and the fabricated BFO or Co-Pi/BFO electrode as working electrode in an aqueous electrolyte solution of 0.5 M Na_2SO_4. The visible light source was a 300 W xenon lamp assembled with a 420 nm long-pass filter, and the average irradiance intensity was calibrated to be 100 mW cm^{-2}. The linear scanning voltammetry (LSV) curves were recorded at a scanning rate of 10 mV s^{-1}. The photocurrent response measurements were acquired at 0 V (vs. Ag/AgCl) potential bias under intermittent visible light ($\lambda \geq 420$ nm) irradiation. The Mott-Schottky (M-S) curves were obtained at an applied frequency of 1 kHz from -0.6 V to $+0.2$ V in the dark. Electrochemical impedance spectra (EIS) were collected using an amplitude perturbation of 5 mV in the frequency range from 10 mHz to 100 kHz under visible light ($\lambda \geq 420$ nm) irradiation.

Results and Discussion

Characterizations of BFO and Co-Pi/BFO thin films.—The crystal structure of the prepared BFO and Co-Pi/BFO thin films were characterized by XRD measurements, as shown in Figure 1. It can be seen that the XRD patterns of the two thin film electrodes were almost identical, and the diffraction peaks were well matched with the crystal phase of rhombohedral BFO (JCPDS No.36-1415) except for the FTO substrate, confirming that the BFO thin films were successfully
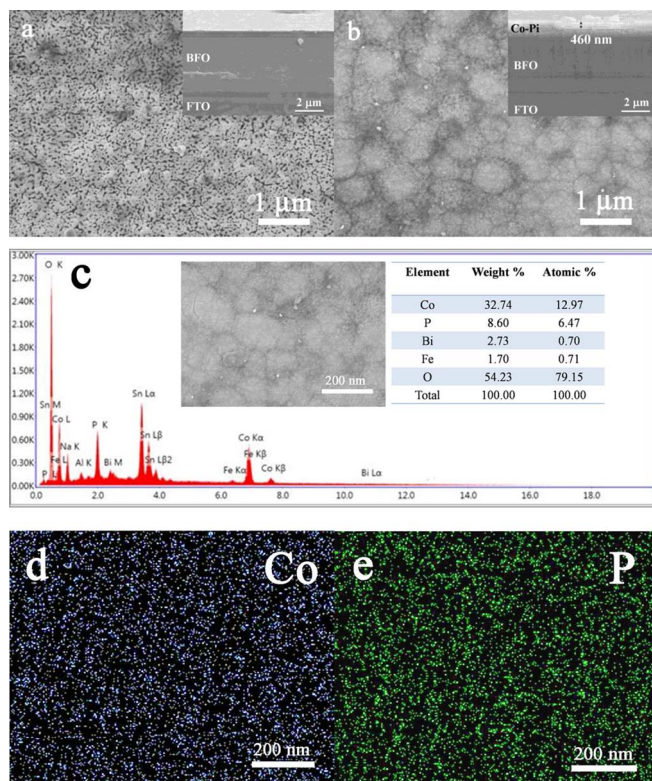

Figure 2. FESEM images of the prepared (a) BFO and (b) Co-Pi/BFO thin film photoanodes (Insets: the corresponding cross-section FESEM images); (c) EDS pattern of the prepared Co-Pi/BFO photoanodes (Inset: SEM micrograph of the selected area of Co-Pi/BFO thin film for EDS mapping of Co and P elements); EDS mapping image of the (d) Co and (e) P elements in the Co-Pi/BFO thin film photoanodes.

fabricated on the FTO surface through a sol-gel method. Meanwhile, no other impurity peaks were found in both BFO and Co-Pi/BFO thin films, implying that the deposition of Co-Pi cocatalyst would not affect the crystal structure of BFO thin films. In addition, the diffraction peaks of Co-Pi were undetected in the Co-Pi/BFO composite thin film probably because of the amorphous or noncrystalline structure of Co-Pi.[21]

The surface morphological features of BFO and Co-Pi/BFO thin films were investigated by FESEM. As seen in Figure 2a, the BFO thin film was composed of numerous irregular nanoparticles with a large number of micropores between each other. The formation of such a porous structure could be ascribed to the thermal decomposition of P123 surfactant. For the Co-Pi/BFO thin film (Figure 2b), however, it can be seen that the BFO surface was covered by semitransparent substance and the surface profile became very blurred, probably because of the deposition of a layer of amorphous Co-Pi on the BFO surface. From the cross-section FESEM images (the insets of Figures 2a and 2b), there appeared a distinct top layer of Co-Pi on the surface of BFO thin film for the Co-Pi/BFO thin film photoanode, and the thickness of the Co-Pi layer was estimated to be about 460 nm. Moreover, the EDS results (Figure 2c) demonstrate that the Co-Pi/BFO thin film consisted of Co, P, Bi, Fe and O elements (Note: the detected other elements (such as Sn, Al, Na) should be derived from the FTO substrate), and the calculated relative atomic percent contents of Co and P were much higher than those of Bi and Fe, implying the coverage of Co-Pi on the BFO surface. Meanwhile, the atomic ratio of Co: Pi was about 2: 1 in accordance with the previously reported proportion of Co-Pi,[21,23] and the atomic ratio of Bi: Fe (about 1: 1) was consistent with the stoichiometric proportion of BFO. Furthermore, the surface elemental scanning analysis (Figures 2d and 2e) proves that the Co and P elements were uniformly distributed on the surface
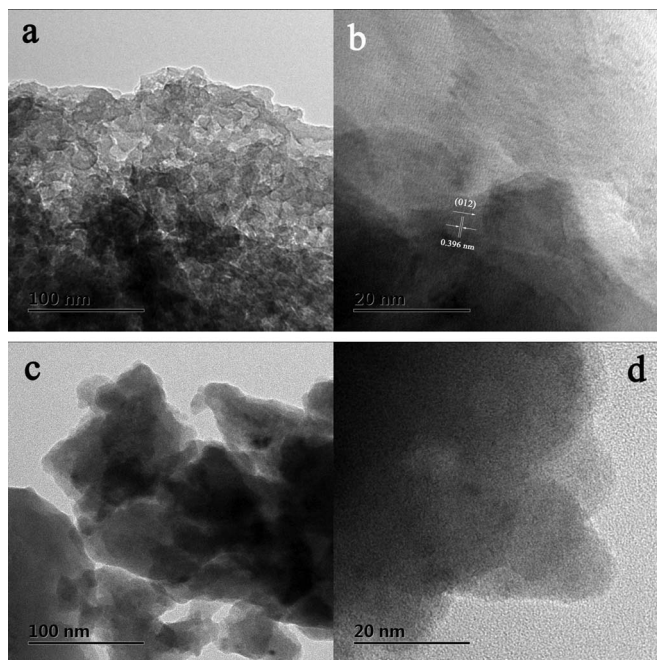
Figure 3. TEM and HRTEM images of the prepared (a, b) BFO and (c, d) Co-Pi/BFO particles peeled from the BFO and Co-Pi/BFO thin film photoanodes.

Figure 4. High resolution XPS spectra of (a) Co 2p and (b) P 2p for the prepared Co-Pi/BFO thin film photoanode.

of the Co-Pi/BFO photoanode. To further reveal the microstructural features of the prepared BFO and Co-Pi/BFO thin films, the TEM measurements were also performed. The BFO thin film (Figure 3a) consisted of a large number of irregular nanoparticles with a particle size of 20~40 nm, which were well connected with each other to form a uniform thin film. The crystal lattices of these nanoparticles were observed with an interplanar spacing of 0.396 nm corresponding to the (012) crystal planes of rhombohedral BFO (Figure 3b), confirming the rhombohedral crystal structure of the prepared BFO thin film. In contrast, the morphological feature of the Co-Pi/BFO thin film was quite different from that of BFO thin film. As shown in Figure 3c, the particles of the Co-Pi/BFO thin films were also irregular in shape with a larger particle size, and these particles were covered with a layer of amorphous substance thus making their surface profiles blurred. There were no crystal lattice fringes detected within the particles of the Co-Pi/BFO thin film (Figure 3d), further implying the coverage of amorphous Co-Pi on the surface of BFO.

The chemical states of Co and P in the Co-Pi/BFO thin film were examined by using XPS measurements. Figure 4 shows the high-resolution XPS spectra of Co and P in the Co-Pi/BFO thin film. The characteristic peaks of Co 2p were split at the binding energies of 780.94 eV and 796.39 eV, corresponding to the Co 2$p_{3/2}$ and Co 2$p_{1/2}$ orbits, respectively. These two split orbits of Co 2$p_{3/2}$ and Co 2$p_{1/2}$ could be assigned to Co^{2+} and Co^{3+}, respectively, in good agreement with the Co-Pi species reported in the literature.[21,31,32] The binding energy of P 2p was located at about 133.2 eV (Figure 4b), which was ascribed to the characteristic peak of P in phosphate.[21,33] These XPS results confirmed the formation of a layer of Co–Pi on the surface of BFO thin film photoanode.

Photoelectrochemical performances.—Figure 5a shows the LSV curves of the prepared BFO and Co-Pi/BFO photoanodes in dark and upon visible light irradiation. As seen, the current densities of both the photoanodes could be gradually enhanced with increasing the applied potential upon visible light illumination, indicating the visible light response characteristics of both photoanodes. The Co-Pi/BFO photoanode exhibited a significant cathodic shift (~72 mV) of the onset potential from −0.058 V (BFO) to −0.130 V (Co-Pi/BFO) for PEC water oxidation compared to the BFO photoanode, validating that the
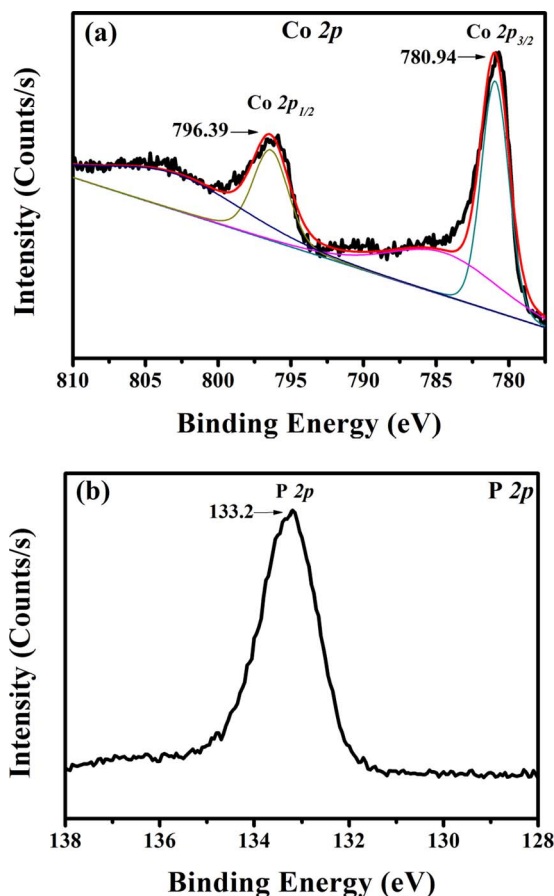
PEC reaction became easier after the deposition of Co-Pi cocatalyst. Moreover, the photocurrent density of Co-Pi/BFO photoanode was greatly improved across the entire potential range in comparison with the BFO photoanode. These observations demonstrate that the PEC performances of the BFO thin film photoanode could be significantly enhanced by the photo-assisted deposition of Co-Pi cocatalyst. To illustrate the enhanced PEC performance of Co-Pi/BFO photoanode, the transient photocurrent responses of BFO and Co-Pi/BFO thin film photoanodes at 0 V (vs. Ag/AgCl) were measured upon intermittent visible light irradiation, and the results were presented in Figure 5b. As shown, a reproducible photocurrent was observed for both BFO and Co-Pi/BFO thin film photoanodes within the five light-on/off cycling measurements, further confirming the photoelectric responses of both BFO and Co-Pi/BFO thin film photoanodes. The measured photocurrent density of Co-Pi/BFO photoanode was ∼0.050 mA cm^{-2} (nearly ca. 8 times that of BFO photoanode), which rivals or exceeds those of previously-reported BFO-based thin film photoelectrodes[10,34–38] (Table I), further demonstrating that the deposition of Co-Pi cocatalyst could significantly boost the PEC performance of BFO thin film photoanode. Moreover, the enhanced photocurrent of the Co-Pi/BFO photoanode also indicated a more efficient photoinduced charge transfer and separation process in the Co-Pi/BFO thin film. Furthermore, the Co-Pi/BFO thin film photoanode presented a relatively good stability of PEC performance with an undiminished photocurrent density for 2000 s (Figure 5c), suggesting the long-term stability of the Co-Pi/BFO photoanode with a great potential for practical PEC applications. In addition, the PEC performance of Co-Pi/BFO thin film photoanodes was significantly affected by the thickness of Co-Pi cocatalyst layer. The thickness of the Co-Pi layer was controlled by adjusting the electrodeposition time, and the three Co-Pi/BFO thin film photoanode samples with different thicknesses of Co-Pi layer were prepared by
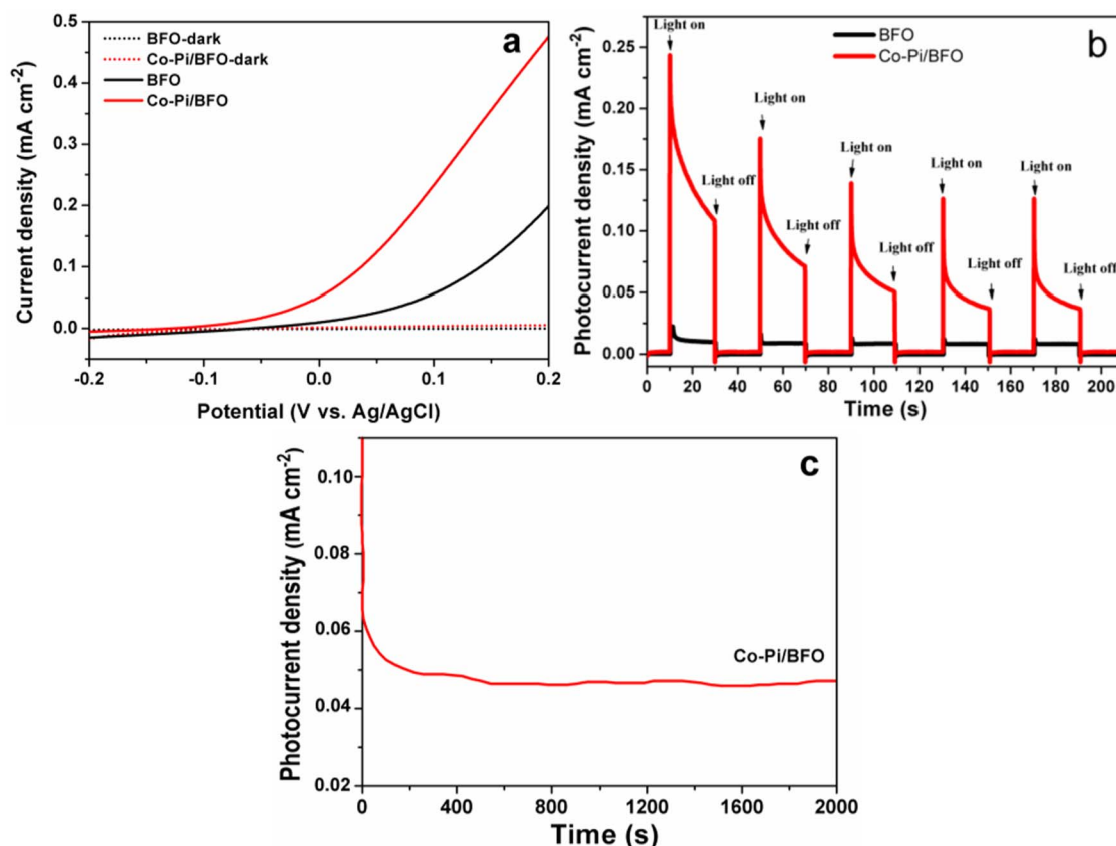
Figure 5. (a) LSV curves obtained from the prepared BFO and Co-Pi/BFO thin film photoanodes in the dark and under visible light ($\lambda \geq 420$ nm) illumination at a scanning rate of 10 mV s^{-1}; (b) Photocurrent response spectra of the prepared BFO and Co-Pi/BFO thin film photoanodes measured at 0 V (vs. Ag/AgCl) with chopped visible light ($\lambda \geq 420$ nm) irradiation; (c) Time-dependent photocurrent density curve of the prepared Co-Pi/BFO thin film photoanode at 0.0 V (vs. Ag/AgCl) under visible light ($\lambda \geq 420$ nm) irradiation.

photoassisted electrodeposition of Co-Pi layer on the surface of BFO thin film photoanode for 1 h, 2 h and 3 h, which were denoted as Co-Pi/BFO-1, Co-Pi/BFO-2 and Co-Pi/BFO-3, respectively. It was found that the thickness of Co-Pi layer was increased with the electrodeposition time, and the PEC performance of the Co-Pi/BFO photoanode increased first and then decreased with increasing the thickness of Co-Pi cocatalyst layer (Figure 6 and Table II). This means that the deposition of Co-Pi cocatalyst layer with an appropriate thickness is vital to achieve the optimized PEC performance of water oxidation for the prepared Co-Pi/BFO photoanode.

To clarify the enhanced PEC performance of the prepared Co-Pi/BFO thin film photoanode, the Mott-Schottky, EIS and PL measurements were performed. As illustrated in Figure 7a, the positive slopes of the M-S plots confirmed the n-type characteristic of the prepared BFO and Co-Pi/BFO thin film photoanodes,[9] implying the

deposition of Co-Pi cocatalyst would not change the n-type characteristic of BFO thin film. According to the Mott-Schottky formula,[39] the slope of the M-S plot is inversely proportional to the carrier concentration (N_D). This means that the Co-Pi/BFO thin film photoanode possessed a higher carrier concentration than the BFO thin film photoanode. Consequently, the higher N_D value of the Co-Pi/BFO thin film indicated a higher charge transfer capability, thus reducing the photogenerated electron/hole recombination and enhancing the PEC performance.[40,41] Moreover, the flatband potentials of the BFO and Co-Pi/BFO thin film photoanode, calculated from the x-intercepts of the linear region in the M-S plots,[42] were found to be -0.35 V and -0.20 V (vs. Ag/AgCl), respectively. Clearly, the flatband potential of the BFO photoanode was positively shifted after the Co-Pi modification, implying that the surface band edge bending of Co-Pi/BFO thin film photoanode was greater than that of the BFO thin film photoanode, which

Table I. The PEC performance of the prepared Co-Pi/BFO thin film photoelectrode in this work in comparison with those of previously-reported BFO-based photoelectrodes.

| Photoelectrode	Electrolyte	Illumination intensity	Photocurrent density (mA cm^{-2})	Onset potential (V vs. Ag/AgCl)	Ref
(001)$_{pc}$ BiFeO$_3$ (photoanode)	1 M Na$_2$SO$_4$	blue light 250 mW/cm^{-2}	0.010 at 0.64 V vs. Ag/AgCl	0.180	34
Polycrystalline BiFeO$_3$ (photoanode)	0.1 M KCl	UV-vis 100 mW/cm^{-2}	0.010 at 0 V vs. Ag/AgCl	0.033	35
Polycrystalline Ti-doped BiFeO$_3$ (photoanode)	1 M NaOH	UV-vis N/A	0.020 at 0 V vs. Ag/AgCl	-0.366	36
Ag/polycrystalline BiFeO$_3$ (photocathode)	0.1 M Na$_2$SO$_4$	UV-vis N/A	-0.035 at 0 V vs. Ag/AgCl	0.080	37
Au/(111)$_{pc}$ BiFeO$_3$ (photocathode)	0.5 M Na$_2$SO$_4$	UV-vis 100 mW/cm^{-2}	-0.055 at 0 V vs. Ag/AgCl	–	38
(111)$_{pc}$ BiFeO$_3$ (photoanode)	0.5 M Na$_2$SO$_4$	UV-vis 100 mW/cm^{-2}	0.080 at 0 V vs. Ag/AgCl	-0.352	10
Co-Pi/BiFeO$_3$ (photoanode)	0.5 M Na$_2$SO$_4$	Visible 100 mW/cm^{-2}	0.050 at 0 V vs. Ag/AgCl	-0.130	This work
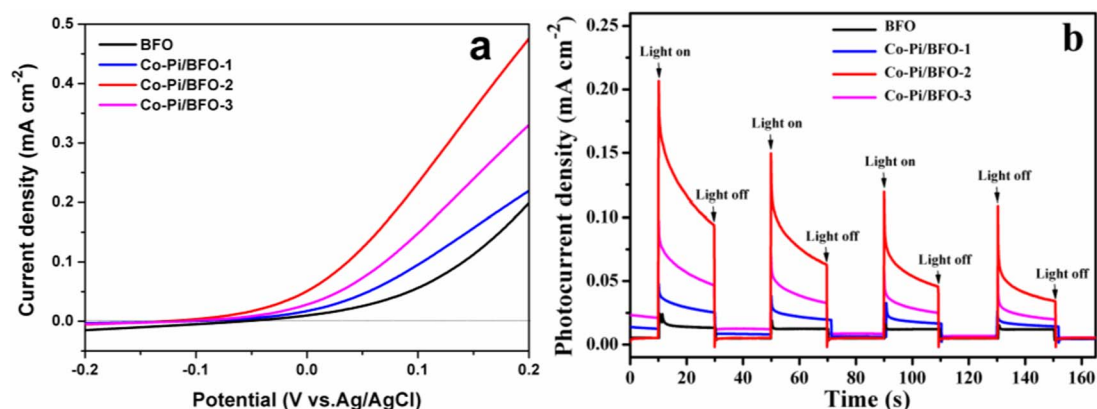
Figure 6. (a) LSV curves obtained from the prepared BFO, Co-Pi/BFO-1, Co-Pi/BFO-2 and Co-Pi/BFO-3 thin film photoanodes in the dark and under visible light ($\lambda \geq 420$ nm) illumination at a scanning rate of 10 mV s^{-1}; (b) Photocurrent response spectra of the prepared BFO Co-Pi/BFO-1, Co-Pi/BFO-2 and Co-Pi/BFO-3 thin film photoanodes measured at 0 V (vs. Ag/AgCl) with chopped visible light ($\lambda \geq 420$ nm) irradiation

Table II. The thicknesses of Co-Pi layer, photocurrent densities and onset potential values for the prepared BFO, Co-Pi/BFO-1, Co-Pi/BFO-2 and Co-Pi/BFO-3 thin film photoelectrodes.

Photoelectrode	Thickness of Co-Pi layer (nm)[#]	Photocurrent density (mA cm^{-2})	Onset potential (V vs. Ag/AgCl)
BFO	/	0.006 at 0.64 V vs. Ag/AgCl	−0.058
Co-Pi/BFO-1	280	0.018 at 0 V vs. Ag/AgCl	−0.108
Co-Pi/BFO-2	460	0.050 at 0 V vs. Ag/AgCl	−0.130
Co-Pi/BFO-3	610	0.034 at 0 V vs. Ag/AgCl	−0.115

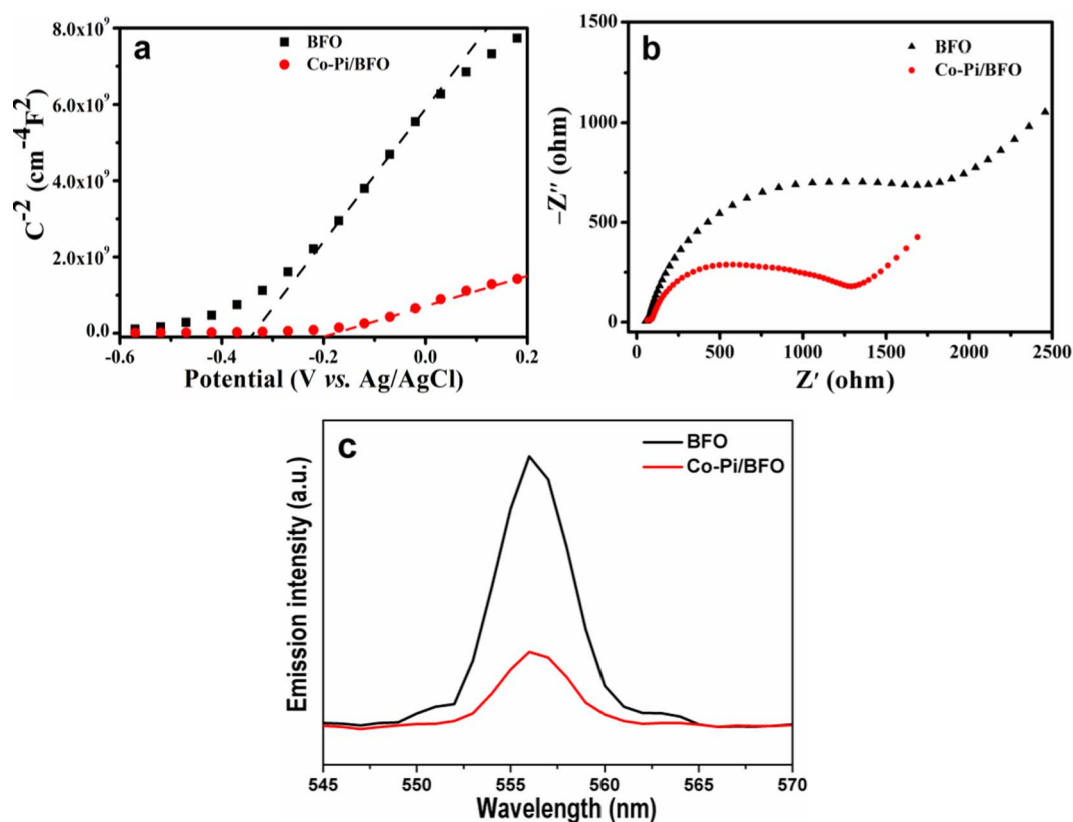*Note:* [#]estimated from the cross-section FESEM images.

Figure 7. (a) The Mott-Schottky plots, (b) EIS Nyquist curves and (c) PL spectra of the prepared BFO and Co-Pi/BFO thin film photoanodes.
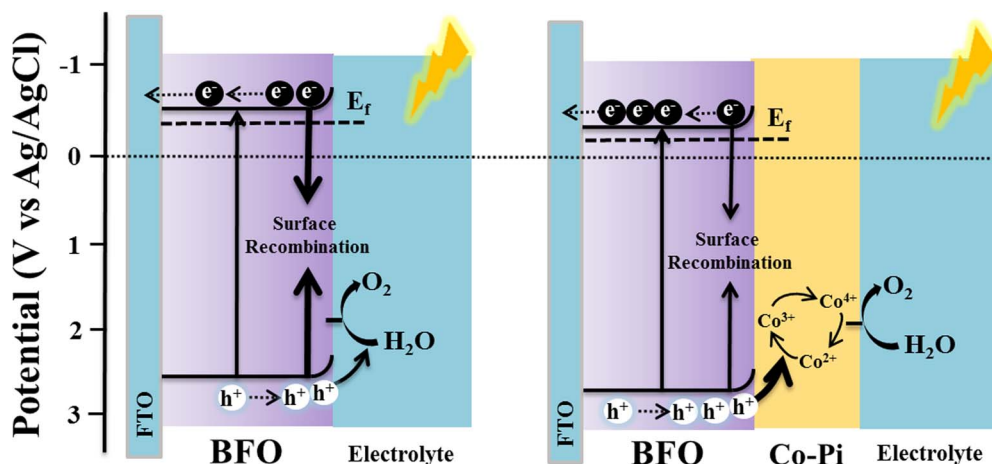
Figure 8. Schematic illustration of the PEC mechanism of the prepared Co-Pi/BFO photoanode in comparison with the prepared BFO photoanode.

could facilitate the charge separation and transfer as well as restrain the electron/hole recombination,[43] thus leading to the enhanced PEC performance. Figure 7b shows the EIS spectra of the prepared BFO and Co-Pi/BFO thin film photoanodes upon visible light irradiation. As shown, the two photoanodes exhibited typical semi-circular arcs with different radii in the measured frequency range, and the arc radius of the prepared Co-Pi/BFO photoanode was much smaller than that of the prepared BFO photoanode. The smaller arc radius of Co-Pi/BFO indicated a more efficient separation and transfer of photogenerated electrons and holes at the electrode/electrolyte interface,[44] which was beneficial to the enhanced PEC performance. In addition, the charge recombination process of a given photoanode can be investigated by PL spectra, in which a higher PL intensity generally means a higher recombination rate of photogenerated charges.[45,46] As seen in Figure 7c, both the BFO and Co-Pi/BFO photoanodes generated a PL emission peak centered at 556 nm at an excitation wavelength of 407 nm. The PL intensity of the Co-Pi/BFO photoanode was much lower than that of the BFO photoanode, indicating a lower recombination probability of photogenerated electrons and holes in the Co-Pi/BFO photoanode which would contribute significantly to the improved PEC performance. Therefore, it is believed that the enhanced carrier concentration, the improved separation and transfer process of photogenerated charges and the decreased photogenerated electron/hole recombination probability induced by the Co-Pi cocatalytst modification would greatly contribute to the boosted PEC performance of the Co-Pi/BFO thin film photoanode.

On the basis of the above PEC results, the possible mechanism of the prepared Co-Pi/BFO photoanode for enhanced PEC performances is tentatively proposed, as schematically illustrated in Figure 8. Upon visible light irradiation, both the BFO and Co-Pi/BFO thin film photoanode would be excited to produce electrons and holes. The photogenerated electrons would be transported to the FTO substrate, while the photogenerated holes would be reversely transported to the electrode/electrolyte interface for participating in the PEC water oxidation at the surface of photoanode. For the bare BFO photoanode, the transfer of the photogenerated holes to the electrode/electrolyte surface was relatively slow because of the slow kinetics of water oxidation as well as the more negative flatband potential of the BFO thin film surface. In this case, the photogenerated holes within the BFO photoanode would be accumulated near the electrode/electrolyte surface thus to increase the recombination of photogenerated electrons and holes at the surface, which could dramatically lower the PEC performance. After the Co-Pi modification, however, the separation and transfer process of photogenerated holes within the BFO photoanode could be effectively promoted, since the deposited Co-Pi cocatalyst could capture the photogenerated holes from the valence band of BFO for water oxidation reaction. During the water oxidation reaction, the Co^{2+} species in the Co-Pi cocatalyst could be oxidized to

Co^{3+} by accepting the photogenerated holes from the valence band of BFO, and the obtained Co^{3+} species could be further oxidized to Co^{4+} by reacting with another hole. These Co^{4+} species, possessing strong oxidization, would then directly react with H_2O for water oxidation, accompanying by reducing Co^{4+} to their original valence state (Co^{2+}).[27] Apparently, the Co-Pi cocatalyst could effectively facilitate the charge separation and transfer of photogenerated holes at the BFO electrode/electrolyte interface and suppress the electron/hole recombination, thus leading to the improvement of the overall PEC performance.

Conclusions

In summary, Co-Pi cocatalyst was successfully deposited on the surface of BFO thin film photoanode by photo-assisted electrochemical deposition for enhanced PEC performance. It was found that the deposited Co-Pi cocatalyst was amorphous and uniformly covered on the BFO thin film surface, and the Co-Pi/BFO thin film photoanode exhibited significantly enhanced PEC performance. After the Co-Pi modification, the photocurrent density of BFO thin film photoanode was remarkably improved within the entire potential range with a remarkable cathodic shift of the onset potential to only ca. 0.24 V (vs. Ag/AgCl). The transient photocurrent measurements reveal that the photocurrent density of Co-Pi/BFO photoanode was ca. 8 times that of the BFO photoanode under visible light irradiation. The Mott-Schottky, EIS and PL measurements confirm that the boosted PEC performance of the Co-Pi/BFO thin film photoanode could be ascribed to the enhanced carrier concentration, the improved separation and transfer process of photogenerated charges and the decreased photogenerated electron/hole recombination probability induced by the Co-Pi cocatalytst. In addition, the possible mechanism of the Co-Pi/BFO thin film photoanode for enhanced PEC performance was also discussed. This work demonstrates that Co-Pi can be an attractive candidate as a highly efficient cocatalyst to couple with other photoanode systems for highly efficient PEC water oxidation.

ORCID

Da Chen https://orcid.org/0000-0001-7854-7135

References

1. D. Wang, X. T. Zhang, P. P. Sun, S. Lu, L. L. Wang, Y. A. Wei, and Y. C. Liu, "Enhanced photoelectrochemical water splitting on hematite thin film with layer-by-layer deposited ultrathin TiO$_2$ underlayer," *Int. J. Hydrogen Energy*, **39**, 16212 (2014).
2. A. Kudo, K. Ueda, H. Kato, and I. Mikami, "Photocatalytic O$_2$ evolution under visible light irradiation on BiVO$_4$ in aqueous AgNO$_3$ solution," *Catal. Lett.*, **53**, 229 (1998).
3. J. A. Seabold and K. S. Choi, "Effect of a cobalt-based oxygen evolution catalyst onthestability and the selectivity of photo-oxidation reactions of a WO$_3$ photoanode," *Chem. Mater.*, **23**, 1105 (2011).
4. A. Fujishima and K. Honda, "Electrochemical photolysis of water at a semiconductor electrode," *Nature*, **238**, 37 (1972).
5. B. Klahr, S. Gimenez, F. Fabregatsantiago, J. Bisquert, and T. W. Hamann, "Photoelectrochemical and impedance spectroscopic investigation of water oxidation with "Co-Pi"-coated hematite electrodes," *J. Am. Chem. Soc.*, **134**, 16693 (2012).
6. R. Solarska, R. Jurczakowski, and J. Augustynski, "A highly stable, efficient visible-light driven water photoelectrolysis system using a nanocrystalline WO$_3$ photoanode and a methane sulfonic acid electrolyte," *Nanoscale*, **4**, 1553 (2012).
7. M. Zhou, J. Bao, W. Bi, Y. Zeng, R. Zhu, M. Tao, and Y. Xie, "Efficient water splitting via a heteroepitaxial BiVO$_4$ photoelectrode decorated with Co-Pi catalysts," *ChemSusChem*, **5**, 1420 (2012).
8. A. Zhu, Q. Zhao, X. Li, and Y. Shi, "BiFeO$_3$/TiO$_2$ nanotube arrays composite electrode construction, characterization, and enhanced photoelectrochemical properties," *ACS Appl. Mater. Interfaces*, **6**, 671 (2014).
9. S. A. Moniz, R. Quesadacabrera, C. Blackman, J. Tang, P. Southern, P. Weaverd, and C. Carmalta, "A simple, low-cost CVD route to thin films of BiFeO$_3$ for efficient water photo-oxidation," *J. Mater. Chem. A*, **2**, 2922 (2013).
10. J. Song, T. L. Kim, J. Lee, S. Y. Cho, J. Cha, S. Y. Jeong, H. An, W. S. Kim, Y. S. Jung, J. Park, G. Y. Jung, D. Y. Kim, J. Y. Jo, S. D. Bu, H. W. Jang, and S. Lee, "Domain-engineered BiFeO$_3$ thin-film photoanodes for highly enhanced ferroelectric solar water splitting," *Nano Res.*, **11**, 642 (2018).
11. H. Y. Shen, X. X. Zhou, W. Dong, X. D. Su, L. Fang, X. Wu, and M. R. Shen, "Dual role of TiO$_2$ buffer layer in Pt catalyzed BiFeO$_3$ photocathodes efficiency enhancement and surface protection," *Appl. Phys. Lett.*, **111**, 123901 (2017).
12. H. M. Xu, Y. H. Lin, T. Harumoto, J. Shi, and C. W. Nan, "Highly (001)-textured tetragonal BiFeO$_3$ film and its photoelectrochemical behaviors tuned by magnetic field," *ACS Appl. Mater. Interfaces*, **9**, 30127 (2017).
13. R. Liu, Z. Zheng, J. Spurgeon, and X. G. Yang, "Enhanced photoelectrochemical water-splitting performance of semiconductors by surface passivation layers," *Energy Environ. Sci.*, **7**, 2504 (2014).
14. J. G. Hou, H. J. Cheng, O. Takeda, and H. M Zhu, "Unique 3D heterojunction photoanode design to harness charge transfer for efficient and stable photoelectrochemical water splitting," *Energy Environ. Sci.*, **8**, 1348 (2015).
15. N. Mirbagheri, D. G. Wang, C. Peng, J. Q. Wang, Q. Huang, C. H. Fan, and E. E. Ferapontova, "Visible light driven photoelectrochemicalwater oxidation by Zn- and Ti-doped hematite nanostructures," *ACS Catal.* **4**, 2006 (2014).
16. S. H. Kim, M. Ebaid, J. H. Kang, and S. W. Ryu, "Improved efficiency and stability of GaN photoanode in photoelectrochemical water splitting by NiO cocatalyst," *Appl. Surf. Sci.*, **305**, 638 (2014).
17. N. P. Dasgupta, C. Liu, S. Andrews, F. B. Prinz, and P. D. Yang, "Atomic layer deposition of platinum catalysts on nanowire surfaces for photoelectrochemical water reduction," *J. Am. Chem. Soc.*, **135**, 12932 (2013).
18. X. W. Cheng, H. L. Liu, Q. H. Chen, J. J. Li, and P. Wang, "Preparation and characterization of palladium nano-crystalline decorated TiO$_2$nano-tubes photoelectrode and its enhanced photocatalytic efficiency for degradation of diclofenac," *J. Hazard. Mater.*, **254**, 141 (2013).
19. M. de Respinis, K. S. Joya, H. J. M. De Groot, F. D'Souza, W. A. Smith, R. van de Krol, and B. Dam, "Solar water splitting combining a BiVO$_4$light absorber with a Ru-based molecular co-catalyst," *J. Phys. Chem. C*, **119**, 7275 (2015).
20. P. Dias, L. Andrade, and A. Mendes, "Hematite-based photoelectrode for solar water splitting with very high photovoltage," *Nano Energy*, **38**, 218 (2017).
21. M. W. Kanan and D. G. Nocera, "In situ formation of an oxygen-evolving catalyst in neutral watercontaining phosphate and Co^{2+}," *Science*, **321**, 1072 (2008).
22. G. Ai, R. Mo, H. Li, and J. Zhong, "Cobalt phosphate modified TiO$_2$ nanowire arrays as co-catalysts for solar water splitting," *Nanoscale*, **7**, 6722 (2015).
23. S. K. Pilli, T. E. Furtak, L. D. Brown, T. G. Deutsch, J. A. Turner, and A. M. Herring, "Cobalt-phosphate (Co-Pi) catalyst modified Mo-doped BiVO$_4$ photoelectrodes for solar water oxidation," *Energy Environ. Sci.*, **4**, 5028 (2011).
24. D. K. Zhong, S. Choi, and D. R. Gamelin, "Near-complete suppression of surface recombination in solar photoelectrolysis by "Co-Pi" catalyst-modified W: BiVO$_4$," *J. Am. Chem. Soc.*, **133**, 18370 (2011).
25. Y. G. Lin, Y. K. Hsu, Y. C. Chen, B. W. Lee, J. S. Hwang, L. C. Chen, and K. H. Chen, "Cobalt-phosphate-assisted photoelectrochemicalwater oxidation by arrays of molybdenum-doped zinc oxide nanorods," *ChemSusChem*, **7**, 2748 (2014).
26. D. K. Zhong, M. Cornuz, K. Sivula, M. Grätzel, and D. R. Gamelin, "Photo-assisted electrodeposition of cobalt-phosphate (Co-Pi) catalyst on hematite photoanodes for solar water oxidation," *Energy Environ. Sci.*, **4**, 1759 (2011).
27. B. Eftekharinia, A. Moshaii, A. Dabirian, and N. Sobhkhiz, "Optimization of charge transport in a Co-Pi modified hematite thin film produced by a scalable electron beam evaporation for photoelectrochemical water oxidation," *J. Mater. Chem. A*, **5**, 3412 (2017).
28. J. A. Seabold and K. S. Choi, "Effect of a cobalt-based oxygen evolution catalyst on the stability and the selectivity of photo-oxidation reactions of a WO$_3$ photoanode," *Chem. Mater.*, **23**, 1105 (2011).
29. E. R. Young, R. Costi, S. Paydavosi, D. G. Nocera, and V. Bulovic, "Photo-assisted water oxidation with cobalt-based catalyst formed from thin-film cobalt metal on silicon photoanodes," *Energy Environ. Sci.*, **4**, 2058 (2011).
30. Y. Surendranath, M. W. Kanan, and D. G. Nocera, "Mechanistic studies of the oxygen evolution reaction by a cobalt-phosphate catalyst at neutral pH," *J. Am. Chem. Soc.*, **132**, 16501 (2010).
31. T. H. Jeon, W. Choi, and H. Park, "Cobalt-phosphate complexes catalyze the photoelectrochemical water oxidation of BiVO$_4$ electrodes," *Phys. Chem. Chem. Phys.*, **13**, 21392 (2011).
32. K. J. McDonald and K. S. Choi, "Photodeposition of co-based oxygen evolution catalysts on α-Fe$_2$O$_3$ photoanodes," *Chem. Mater.*, **23**, 1686 (2011).
33. G. Ai, H. Li, S. Liu, R. Mo, and J. Zhong, "Solar water splitting by TiO$_2$/CdS/Co-Pi nanowire array photoanodeenhanced with Co-Pi as holetransfer relay and CdS as light absorber," *Adv. Funct. Mater.*, **25**, 5706 (2015).
34. W. Ji, K. Yao, Y. F. Lim, Y. C. Liang, and A. Suwardi, "Epitaxial ferroelectric BiFeO$_3$ thin films for unassisted photocatalytic water splitting," *Appl. Phys. Lett.*, **103**, 062901 (2013).
35. D. W. Cao, Z. J. Wang, L. Y. Wen Nasori, Y. Mi, and Y. Lei, "Switchable charge-transfer in the photoelectrochemical energy-conversion process of ferroelectric BiFeO$_3$ photoelectrodes," *Angew. Chem., Int. Ed.*, **53**, 11027 (2014).
36. N. N. Rong, M. S. Chu, Y. L. Tang, C. Zhang, X. Cui, H. C. He, Y. H. Zhang, and P. Xiao, "Improved photoelectrocatalytic properties of Ti-doped BiFeO$_3$ films for water oxidation," *J. Mater. Sci.*, **51**, 5712 (2016).
37. Q. Liu, Y. Zhou, L. You, J. L. Wang, M. R. Shen, and L. Fang, "Enhanced ferroelectric photoelectrochemical properties of polycrystalline BiFeO$_3$ film by decorating with Ag nanoparticles," *Appl. Phys. Lett.*, **108**, 022902 (2016).
38. Y. L. Huang, W. S. Chang, C. N. Van, H. J. Liu, K. A. Tsai, J. W. Chen, H. H. Kuo, W. Y. Tzeng, Y. C. Chen, C. L. Wu, C. W. Luo, Y. J. Hsu, and Y. H. Chu, "Tunable photoelectrochemical performance of Au/BiFeO$_3$ heterostructure." *Nanoscale*, **8**, 15795 (2016).
39. K. P. Parmar, H. J. Kang, A. Bist, P. Dua, J. S. Jang, and J. S. Lee, "Photocatalytic and photoelectrochemical water oxidation over metal-doped monoclinic BiVO$_4$," *ChemSusChem*, **5**, 1926 (2012).
40. J. Poppe, S. G. Hickey, and A. Eychmüller, "Photoelectrochemical investigations of semiconductor nanoparticles and their application to solar cells," *J. Phys. Chem. C*, **118**, 17123 (2014).
41. X. H. Zhou, R. Liu, K. Sun, K. M. Papadantonakis, B. S. Brunschwigad, and N. S. Lewis, "570 mV photovoltage, stabilized n-Si/CoO$_x$ heterojunction photoanodes fabricated using atomic layer deposition," *Energy Environ. Sci.*, **9**, 892 (2016).
42. S. Wang, D. Chen, N. Zhang F.Niu, L. S. Qin, and Y. X. Huang, "Pd cocatalyst on Sm-doped BiFeO$_3$ nanoparticles: Synergetic effect of Pd cocatalyst and samarium doping on photocatalysis," *RSC Adv.* **6**, 34574 (2016).
43. Y. F. Li, C. Cao, X. X. Xie, L. Zhang, and S. W. Lin, "Enhanced photoelectrochemical performance of TiO$_2$ nanotube arrays with coexisted Pt nanoparticles and Co-Pi cocatalysts," *Appl. Surf. Sci.*, **436**, 337 (2018).
44. Y. Lv, Y. Zhu, and Y. Zhu, "Enhanced photocatalytic performance for the BiPO$_{4-x}$nanorod inducedby surface oxygen vacancy," *J. Phys. Chem. C*, **117**, 18520 (2013).
45. E. M. P. Steinmiller and K. S. Choi, "Photochemical deposition of cobalt-based oxygenevolving catalyst on a semiconductor photoanode for solar oxygen production," *Proc. Natl. Acad. Sci. USA*, **106**, 20633 (2009).
46. H. Huang, Y. He, X. Du, P. K. Chu, and Y. Zhang, "A general and facile approach to heterostructured core/shell BiVO$_4$/BiOI p-n junction room-temperature in situ assembly and highly boosted visible-light photocatalysis," *ACS Sustain. Chem. Eng.*, **3**, 3262 (2015).

Available online at www.sciencedirect.com

ScienceDirect

journal homepage: www.elsevier.com/locate/he
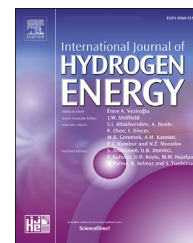
Decoration of WS$_2$ as an effective noble-metal free cocatalyst on ZnIn$_2$S$_4$ for enhanced visible light photocatalytic hydrogen evolution

Jiabo Zhou [a], *Da Chen* [a,*], *Liqun Bai* [b,c], *Laishun Qin* [a,**], *Xingguo Sun* [a], *Yuexiang Huang* [a]

[a] *College of Materials Science and Engineering, China Jiliang University, Hangzhou, Zhejiang 310018, China*
[b] *Zhejiang Provincial Key Laboratory of Chemical Utilization of Forestry Biomass, Zhejiang A & F University, Lin'an, Zhejiang 311300, China*
[c] *Zhejiang Provincial Key Lab. for Chem. & Bio. Processing Technology of Farm Products, Zhejiang University of Science & Technology, Hangzhou, Zhejiang 310023, China*

ARTICLE INFO

ABSTRACT

In this work, a series of WS$_2$/ZnIn$_2$S$_4$ composite photocatalysts containing different WS$_2$ cocatalyst amounts were prepared through a facile hydrothermal approach. The prepared WS$_2$/ZnIn$_2$S$_4$ composite photocatalysts were characterized by means of X-ray diffraction (XRD), scanning electron microscopy (SEM), transmission electron microscopy (TEM) and UV−vis diffuse reflectance spectra (DRS), and their visible-light driven photocatalytic hydrogen evolution performances were also investigated. It was revealed that the loading of WS$_2$ cocatalyst could greatly boost the photocatalytic hydrogen evolution activity of ZnIn$_2$S$_4$, and the 3% WS$_2$/ZnIn$_2$S$_4$ sample achieved the highest hydrogen production rate of 199.1 μmol/h/g, which was nearly 6 times higher than ZnIn$_2$S$_4$ and was even comparable to the conventional Pt/ZnIn$_2$S$_4$ photocatalyst. The improved photocatalytic performance of WS$_2$/ZnIn$_2$S$_4$ could be ascribed to the promotion of separation and migration of photo-generated charge carriers derived from the heterostructure formed at the interface between ZnIn$_2$S$_4$ and WS$_2$. Thus, this work proves a great potential of WS$_2$ as a cost-effective cocatalyst for semiconductor-based photocatalytic hydrogen production.

Introduction

With the rapid increase of global energy demand and environmental pollution, it is urgent to explore a clean renewable energy. Over the last several decades, hydrogen energy has been widely recognized as a potential sustainable and renewable energy resource. Since the discovery of photoelectrochemical hydrogen production from water splitting by titania in 1972 [1], much effort has been made to pursue efficient photocatalytic hydrogen production over semiconductors for producing clean hydrogen energy by utilizing inexhaustible solar energy [2]. So far, a variety of metal oxides, such as TiO$_2$ [3], ZnO [4], titanates [5,6], tantalates [7] and niobates [8], have been explored for photocatalytic hydrogen production. Because of their wide band gaps,

---

however, these photocatalysts can only respond to UV light which occupies merely 4% of the whole solar spectrum, thus greatly restricting the solar energy utilization efficiency. In view of this, it is indispensable to explore visible light photocatalysts covering a wide solar spectrum for pursuing high-efficiency photocatalytic hydrogen evolution.

In recent years, ternary chalcogenide $ZnIn_2S_4$ has been regarded as an excellent photocatalyst because of its good visible light absorption ability, suitable band-edge positions, low toxicity and favorable chemical stability [9]. For example, Lei et al. [10] reported that $ZnIn_2S_4$ nanoparticles were successfully synthesized through a hydrothermal approach for visible light photocatalytic water splitting. Chen et al. [11] synthesized hexagonal $ZnIn_2S_4$ microspheres and cubic $ZnIn_2S_4$ nanoparticles respectively, which exhibited efficient photocatalytic activities for degradation of pollutant organic dyes. Despite these advances, however, the photocatalytic activity of $ZnIn_2S_4$ itself is still not ideal [12] and needs to be further improved for potential practical applications. It is widely accepted that the coupling of cocatalysts can effectively boost the photocatalytic activities of semiconductor photocatalysts for hydrogen evolution, since a suitable cocatalyst can dramatically reduce the hydrogen evolution overpotential, restrain the recombination of photogenerated charge carriers of a given photocatalyst as well as probably offer some redox reaction sites for hydrogen evolution [13]. Currently, the commonly used cocatalysts for photocatalytic hydrogen evolution are noble metals like Pt [14], Pd [15], Au [16] and their oxides like RuO_2 [17] benefiting from their relatively low hydrogen evolution overpotential and outstanding driving dynamics for hydrogen evolution reaction (HER). In 2012, Li et al. [18] prepared $Pt/ZnIn_2S_4$ nanocomposites by depositing Pt nanoparticles as a cocatalyst on the $ZnIn_2S_4$ surface, which exhibited enhanced photocatalytic hydrogen evolution efficiencies. Apparently, these precious metals are too expensive to use widely in photocatalytic hydrogen evolution, and thus the development of inexpensive transition metal cocatalysts is highly desirable.

Recently transition metal sulfides, such as MoS_2 [19−21], NiS [22,23] and WS_2 [24], have been proven as efficient cocatalyst alternatives to noble metals (e.g., Pt, Pd) for photocatalytic hydrogen evolution [25]. Particularly, tungsten disulfide (WS_2) as an emerging layered transition metal dichalcogenide (TMD) has attracted much concern in view of its graphite-like layered structure with unique structural and electrical properties [26], and considerable progress has been made toward the development of WS_2 cocatalyst-coupled photocatalysts for photocatalytic hydrogen production from water splitting [24,27−34]. It has been reported that the WS_2 cocatalyst could provide rich active sites and lower the activation barriers for redox reactions thus to enhance the photocatalytic efficiency [25]. Moreover, the indirect-to-direct gap transition of WS_2 would occur when bulk WS_2 is reduced to few-layer WS_2 nanosheets [35], and the in-plane carrier mobility in WS_2 nanosheets is relatively high [36]. Furthermore, the coupling of WS_2 cocatalyst can enhance the utilization efficiency of light illumination because of its narrow band gap-induced strong absorption in the visible-light region [37], and probably mitigate the photocorrosion issue and improve the photostability of CdS photocatalyst [27]. More

importantly, the WS_2 cocatalyst would readily form the matched junction with sulfide photocatalysts (such as CdS) resulting from the "outer atomic match" structure [25], which would increase the intimate contact between the WS_2 cocatalyst and sulfide photocatalyst thus facilitating the transport of photoexcited carriers at the WS_2/semiconductor interface. These features make WS_2 nanosheets very suitable as a promising noble-metal-free cocatalyst in combination with $ZnIn_2S_4$ photocatalysts for efficient photocatalytic hydrogen evolution. To the best of our knowledge, however, the influence of WS_2 cocatalyst on the photocatalytic hydrogen evolution activity of $ZnIn_2S_4$ has not yet been investigated. Herein, a facile hydrothermal method was adopted to prepare $WS_2/ZnIn_2S_4$ composite photocatalysts where WS_2 was served as a cocatalyst for visible light photocatalytic hydrogen production. As expected, the prepared $WS_2/ZnIn_2S_4$ composite photocatalysts displayed considerably improved photocatalytic hydrogen production efficiency in comparison with $ZnIn_2S_4$ alone. Moreover, the effect of the loading amount of WS_2 cocatalyst on the photocatalytic H_2 production activity of $WS_2/ZnIn_2S_4$ composites was comparatively studied. In addition, a possible photocatalytic mechanism of $WS_2/ZnIn_2S_4$ was also proposed.

Experimental

Synthesis of $WS_2/ZnIn_2S_4$ nanocomposites

WS_2 nanosheets were firstly synthesized by using a simple hydrothermal approach according to the previous report [38]. The $WS_2/ZnIn_2S_4$ composites were also prepared by means of a facile hydrothermal process, and the obtained composite samples containing 1 wt%, 3 wt%, and 5 wt% WS_2 loading amount were named as 1% $WS_2/ZnIn_2S_4$, 3% $WS_2/ZnIn_2S_4$ and 5% $WS_2/ZnIn_2S_4$, respectively. In a typical synthesis process, a certain amount of WS_2 nanosheets was first dispersed by ultrasonication in 100 mL of water for 1 h, followed by successively adding 2.0 mmol of $ZnCl_2$, 4.0 mmol of $In(NO_3)_3 \cdot 4.5H_2O$ and 8 mmol of thioacetamide (TAA), which was kept stirring for 30 min. The obtained solution was then carefully transferred into a 150 mL Teflon-lined stainless steel autoclave. After being sealed, the autoclave was maintained at 160 °C to perform a hydrothermal reaction for 6 h, which was then cooled naturally to room temperature. The resulting precipitates were filtrated and washed with deionized water and absolute ethanol for several times, followed by vacuum drying at 60 °C for 6 h. Thus, the $WS_2/ZnIn_2S_4$ composite photocatalysts were obtained. For comparison, the pure $ZnIn_2S_4$ particles were synthesized using the same process without adding WS_2. Moreover, Pt cocatalyst was also loaded on the $ZnIn_2S_4$ surface by in-situ photodeposition method for comparison, and the loading amount of Pt was determined using the energy dispersive X-ray spectrometry (EDS).

Characterizations

The crystal phase structures of the prepared samples were measured in the range of $2\theta = 10°−80°$ on a Bruker D8 Advance X-ray diffractometer (XRD) by Cu K_α radiation ($\lambda = 0.15418$ nm).

The microstructural morphologies of the obtained samples were analyzed by means of a Hitachi SU8010 field-emission scanning electron microscope (FESEM) equipped with an energy dispersive X-ray spectrometer and a JEOL JEM-2100 transmission electron microscope (TEM). The ultraviolet–visible (UV–vis) spectrometer (Shimadzu UV-3600) was employed to detect the UV–vis diffuse reflectance spectra (DRS) of the prepared samples based on the $BaSO_4$ reflectance standard. The photoluminescence (PL) spectra were measured on a Hitachi High-Tech F-7000 fluorescence spectrometer at room temperature at an excitation wavelength of $\lambda = 298$ nm.

Photoelectrochemical measurements

The photoelectrochemical (PEC) measurements of the obtained samples were carried out on a CHI660E electrochemical workstation (CH Instruments) in a home-built quartz cell with a three-electrode configuration (i.e., a working electrode, a platinum wire counter electrode, and a saturated calomel electrode (SCE) reference electrode), and a 300 W Xe lamp with a cut-off optical filter ($\lambda \geq 420$ nm) was used as a visible light source. To fabricate the working electrode, a slurry was firstly prepared by dispersing 20 mg of the sample powder in 5 ml of a mixed solution of deionized water, isopropanol, and perfluorosulfonic acid in a molar ratio of 40:20:1 under stirring. Subsequently, the slurry was spin-coated five times on a pre-cleaned FTO glass substrate. After vacuum drying at 60 °C overnight, the working electrode was thus obtained. Photocurrent response spectra were tested in a 0.5 M Na_2SO_4 aqueous solution upon intermittent visible light irradiation, and electrochemical impedance spectra (EIS) were examined by imposing an external ac perturbation of 5 mV within a frequency range from 0.01 Hz to 100 kHz upon visible light irradiation. Mott-Schottky analysis was performed from −1.0 V to +1.0 V in the same three-electrode configuration with an applied frequency of 1000 Hz in the dark.

Photocatalytic hydrogen evolution

The photocatalytic measurements for hydrogen production were performed in a closed quartz glass reactor in connection with a gas circulation system, and a 300-W xenon lamp assembled with a UV cut-off filter ($\lambda \geq 420$ nm) was used as the light source which was positioned 25 cm away from the reactor. The average irradiance intensity was measured to be 15 mW cm^{-2} by a radiometer (FZ-A, Photoelectric Instrument Factory of Beijing Normal University, China). Typically, 0.1 g of the prepared photocatalyst powders was fully dispersed in 100 mL of 0.35 M Na_2S and 0.25 M Na_2SO_3 aqueous solution in the quartz reactor by intense magnetic stirring. Prior to the light irradiation, the dispersion was continuously stirred in the dark for 30 min to reach the absorption equilibrium, and meanwhile the whole configured gas-tight system was evacuated several times to get rid of the residual air inside. After that, the light source was switched on to initiate the photocatalytic reaction for hydrogen production, and the hydrogen production amount was analyzed online by using a gas chromatograph (GEL-SPJZN GC-7820). Note that the suspension was kept stirring and the thermal effect of the

photocatalytic reactor was eliminated by refluxing cooling water during the whole photocatalytic process. By contrast, the hydrogen production amount was negligible when the photocatalytic reaction was performed in the dark or without the photocatalyst. To evaluate the photocatalytic stability, the 3%WS_2/$ZnIn_2S_4$ powders in the suspension after the photocatalytic hydrogen evolution test were carefully recovered by centrifugation and washing and used for another photocatalytic reaction. This photocatalytic process was repeated three times.

Results and discussion

The XRD patterns of pure $ZnIn_2S_4$ and WS_2/$ZnIn_2S_4$ composites with different proportions of WS_2 (1%, 3%, 5%) are presented in Fig. 1. As shown, the diffraction peaks of the prepared pure $ZnIn_2S_4$ sample were in good accordance with a hexagonal phase of $ZnIn_2S_4$ (JCPDS No. 65-2023) [39]. For the WS_2/$ZnIn_2S_4$ composites, the XRD patterns were similar to that of the prepared $ZnIn_2S_4$, implying that the loading of WS_2 cocatalyst would not influence the crystal structure of $ZnIn_2S_4$. Notably, in the WS_2/$ZnIn_2S_4$ composites, there occurred a diffraction peak at the position of around 13°, which was indexed to the (002) crystal plane for WS_2 [38]. Moreover, the diffraction peak intensity of (002) crystal plane gradually increased with increasing the WS_2 content in the composites.

Fig. 2 presents the FESEM images of the prepared $ZnIn_2S_4$, WS_2 and 3% WS_2/$ZnIn_2S_4$ samples. As can be seen, the prepared $ZnIn_2S_4$ sample (Fig. 2A) had an irregular granular shape with a wide range of particle size from several hundred nanometers to tens of micrometers, which were prone to agglomerate, and the prepared WS_2 sample (Fig. 2B) was composed of a large number of wrinkled 2D nanosheets in consistent with the previous report [38]. With respect to the sample of WS_2/$ZnIn_2S_4$ composite (Fig. 2C and D), the $ZnIn_2S_4$ particles were coupled with WS_2 nanosheets with no obvious aggregation, indicating that the coupling of WS_2 nanosheets
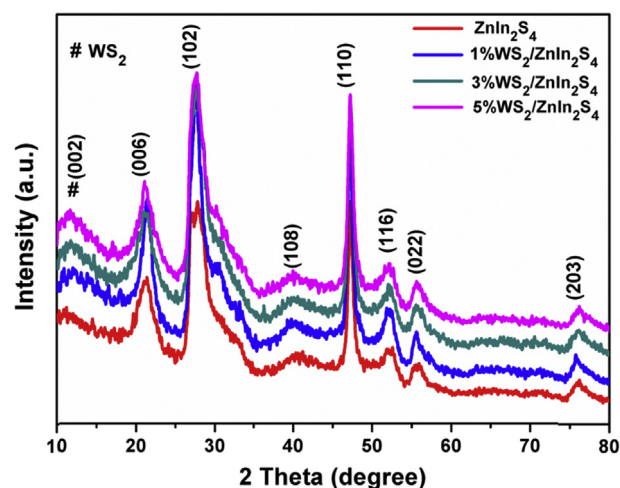

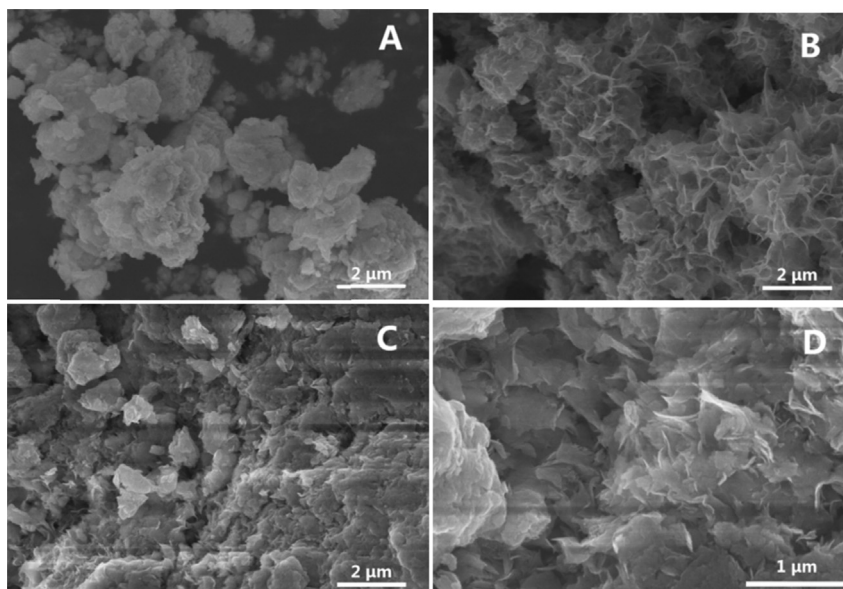Fig. 1 – X-ray diffraction (XRD) patterns of the prepared $ZnIn_2S_4$ and WS_2/$ZnIn_2S_4$ composite photocatalysts.

Fig. 2 – SEM images of the prepared ZnIn$_2$S$_4$ (A), WS$_2$ (B), and 3% WS$_2$/ZnIn$_2$S$_4$ at low (C) and high (D) magnification.

would effectively mitigate the agglomeration of ZnIn$_2$S$_4$ particles. The morphological microstructures of the prepared ZnIn$_2$S$_4$ and 3% WS$_2$/ZnIn$_2$S$_4$ samples were further revealed by TEM and high-resolution TEM (HRTEM) measurements. The prepared ZnIn$_2$S$_4$ particles (Fig. 3A) were irregular in shape, and each particle was made up of numerous three-dimensionally spatially-connected nanocrystals. The HRTEM image of the prepared ZnIn$_2$S$_4$ particles (Fig. 3B) identified the lattice spacing of 0.33 nm, belonging to the (102) crystal plane of hexagonal ZnIn$_2$S$_4$ [40]. Meanwhile, the prepared WS$_2$

nanosheets possessed a wrinkled flaky structure consisting of 5–10 multilayer 2D sheets (Fig. 3C and D). The typical TEM image of WS$_2$/ZnIn$_2$S$_4$ composites (Fig. 3E) confirmed the hybridization structure of WS$_2$ and ZnIn$_2$S$_4$, where ZnIn$_2$S$_4$ nanoparticles were well encapsulated by the wrinkled 2D WS$_2$ nanosheets. This indicates that the agglomeration of ZnIn$_2$S$_4$ nanoparticles was greatly suppressed after the coupling of WS$_2$ nanosheets. Moreover, the HRTEM image (Fig. 3F) revealed the close contact between ZnIn$_2$S$_4$ nanoparticles and WS$_2$ nanosheets, which could make possible the
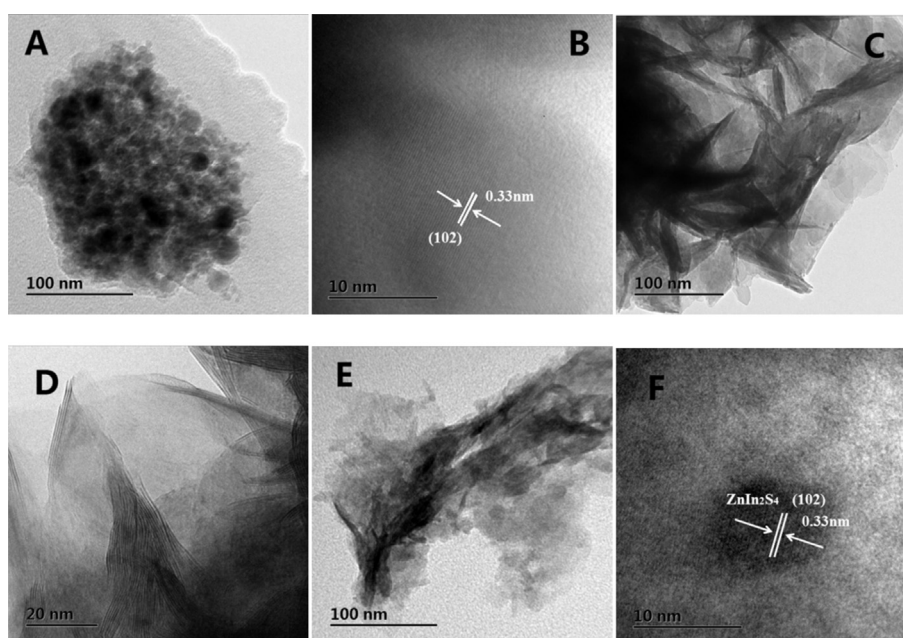

Fig. 3 – TEM and HRTEM images of the prepared (A, B) ZnIn$_2$S$_4$, (C, D) WS$_2$, and (E, F) 3% WS$_2$/ZnIn$_2$S$_4$ composite photocatalyst.
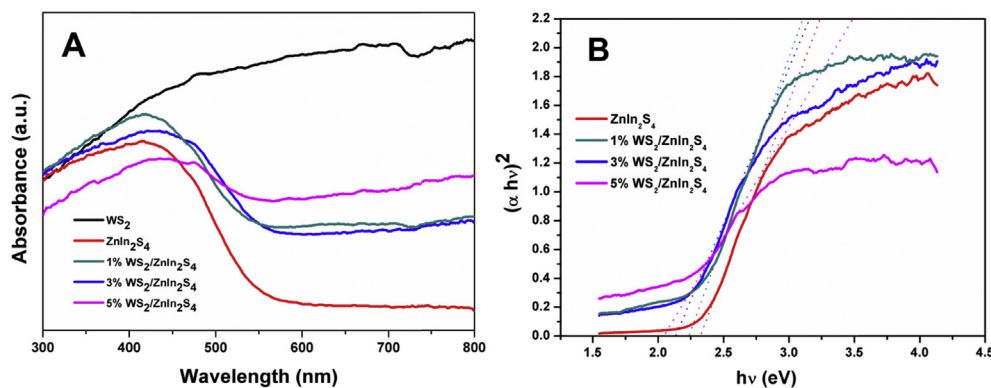
Fig. 4 — (A) UV—vis DRS of the prepared ZnIn$_2$S$_4$ and WS$_2$/ZnIn$_2$S$_4$ composite photocatalysts; (B) the plots to determine the band gaps for each sample.

heterostructure formation between ZnIn$_2$S$_4$ and WS$_2$, thus facilitating the charge separation and improving the photocatalytic activity of ZnIn$_2$S$_4$.

Fig. 4 presents the UV—vis DRS spectra of the prepared samples. As seen, the prepared ZnIn$_2$S$_4$ sample exhibited strong optical absorption from the UV to visible light region with an absorption edge at ca. 520 nm, demonstrating the visible light response of the prepared ZnIn$_2$S$_4$ for photocatalytic reaction. In comparison with the ZnIn$_2$S$_4$ sample, the WS$_2$/ZnIn$_2$S$_4$ composite samples displayed an obvious enhancement in the visible light absorption, which could be ascribed to the coupling of WS$_2$, and the visible light absorption intensity increased with the increase of WS$_2$ amount in the composites. According to the Tauc Plot equation [41], the band gap values of the prepared ZnIn$_2$S$_4$, 1% WS$_2$/ZnIn$_2$S$_4$, 3% WS$_2$/ZnIn$_2$S$_4$ and 5% WS$_2$/ZnIn$_2$S$_4$ samples could be determined to be about 2.32, 2.24, 2.13 and 2.04 eV, respectively (Fig. 4B), confirming that the band gap value was decreased with increasing the WS$_2$ content in the WS$_2$/ZnIn$_2$S$_4$ composites. Obviously, the improved visible light absorption arising from the coupling of WS$_2$ would contribute to the photocatalytic performance of ZnIn$_2$S$_4$, as will be discussed below.

The photocatalytic hydrogen production activities of the prepared ZnIn$_2$S$_4$ and WS$_2$/ZnIn$_2$S$_4$ nanocomposites were examined in the presence of Na$_2$S/Na$_2$SO$_3$ aqueous solution under visible light ($\lambda \geq 420$ nm) irradiation, and the results are shown in Fig. 5(A) and (B). As seen, hydrogen was undetected when using WS$_2$ as a photocatalyst alone, implying that WS$_2$ itself was inactive for photocatalytic hydrogen evolution in agreement with the previous reports [30,32]. In the absence of WS$_2$, the prepared ZnIn$_2$S$_4$ photocatalyst exhibited a comparatively low photocatalytic activity with a hydrogen evolution rate of 33.3 μmol/h/g. In contrast, the photocatalytic activities of WS$_2$/ZnIn$_2$S$_4$ composite photocatalysts were much higher than that of ZnIn$_2$S$_4$. When 1 wt% of WS$_2$ cocatalyst was loaded, the hydrogen evolution rate was enhanced to 59.2 μmol/h/g. With increasing the WS$_2$ loading amount to 3 wt%, the hydrogen evolution rate was further enhanced, reaching the maximum value of 199.1 μmol/h/g. When the loading amount of WS$_2$ in the composite was further increased to 5 wt%, however, the photocatalytic H$_2$

evolution rate on the contrary dropped off to 84.5 μmol/h/g. The decreased photocatalytic activity arising from the heavy loading of WS$_2$ could be attributed to the shading effect of WS$_2$ cocatalyst, which could hinder the light absorption of ZnIn$_2$S$_4$ [42,43]. Moreover, Pt cocatalyst was also loaded on the ZnIn$_2$S$_4$ surface by in-situ photodeposition method for comparison. The 3 wt% Pt/ZnIn$_2$S$_4$ photocatalyst presented a H$_2$ evolution rate of 224.6 μmol/h/g under a similar reaction condition, indicating that WS$_2$ cocatalyst could be comparable to conventional Pt cocatalyst. In addition, the photocatalytic stability of WS$_2$/ZnIn$_2$S$_4$ for hydrogen evolution was also evaluated. As shown in Fig. 5(C), the hydrogen evolution activity of the 3% WS$_2$/ZnIn$_2$S$_4$ photocatalyst after 3 cycling tests was largely retained, revealing the pretty good photocatalytic stability of the composite.

To elucidate the effect of the coupling of WS$_2$ cocatalyst on the photocatalytic activity of ZnIn$_2$S$_4$, the separation and migration of photogenerated charges of the prepared ZnIn$_2$S$_4$ and WS$_2$/ZnIn$_2$S$_4$ photocatalysts were studied by using photoelectrochemical measurements. Fig. 6(A) presents the photocurrent response spectra of the ZnIn$_2$S$_4$ and 3% WS$_2$/ZnIn$_2$S$_4$ photoelectrodes upon intermittent visible light irradiation, respectively. As seen, both the ZnIn$_2$S$_4$ and 3% WS$_2$/ZnIn$_2$S$_4$ photoelectrodes could respond rapidly to the on/off visible light irradiation, confirming the visible light response characteristic of ZnIn$_2$S$_4$. More importantly, the 3% WS$_2$/ZnIn$_2$S$_4$ photoelectrode displayed a much larger photocurrent intensity, which was ca. 7 times that of the ZnIn$_2$S$_4$, implying a much more efficient separation and migration efficiency of the photogenerated charges in the WS$_2$/ZnIn$_2$S$_4$ sample thus leading to the boosted photocatalytic activity. In addition, EIS measurements were also conducted under visible light irradiation to analyze the charge transfer process at the semiconductor/electrolyte interface. As can be seen in Fig. 6(B), the pure ZnIn$_2$S$_4$ presents a larger radius than the 3% WS$_2$/ZnIn$_2$S$_4$ composite, suggesting that the loading of WS$_2$ cocatalyst would facilitate the charge separation and transfer process of ZnIn$_2$S$_4$. Furthermore, the suppression of charge recombination in ZnIn$_2$S$_4$ by the coupling of WS$_2$ was supported by PL emission spectra. Fig. 6(C) shows the PL spectra of the prepared ZnIn$_2$S$_4$ and 3% WS$_2$/ZnIn$_2$S$_4$ samples. As seen, the bare ZnIn$_2$S$_4$ displayed a strong PL emission centered at 545 nm,
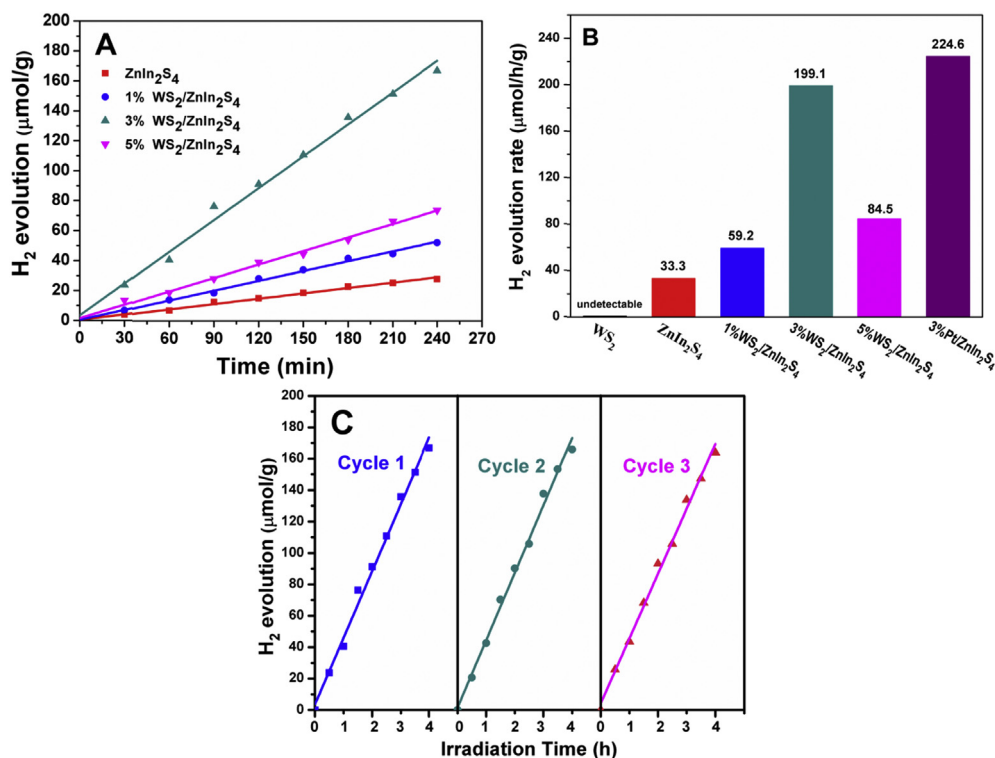
Fig. 5 — (A) The photocatalytic H_2 evolution performance over the prepared $ZnIn_2S_4$ and $WS_2/ZnIn_2S_4$ composite photocatalysts; (B) the histogram of the obtained H_2 evolution rates over the prepared WS_2, $ZnIn_2S_4$, $WS_2/ZnIn_2S_4$ and $Pt/ZnIn_2S_4$ composite photocatalysts; and (C) photocatalytic hydrogen evolution over the 3% $WS_2/ZnIn_2S_4$ photocatalyst for several cycles under visible light ($\lambda \geq 420$ nm) irradiation.

which could be attributed to the intrinsic band gap emission and the defect in $ZnIn_2S_4$ [44]. While the PL emission of the 3% $WS_2/ZnIn_2S_4$ sample was similar to that of bare $ZnIn_2S_4$, a dramatic decrease of PL intensity was observed. The lower PL intensity of $WS_2/ZnIn_2S_4$ sample indicated a delay in recombination rate of photogenerated charges, thus improving the photocatalytic activity.

Furthermore, Mott—Schottky measurements were performed to determine the conduction band (CB) edge potential of the prepared photocatalysts. As shown in Fig. 7, the slopes in the Mott-Schottky plots were positive, indicating the n-type characteristic of the prepared $ZnIn_2S_4$ and 3% $WS_2/ZnIn_2S_4$ samples [45]. Moreover, the flat—band potentials derived from

the x intercepts of the linear region could be approximately considered as the E_{CB} potentials [46]. Thus, the E_{CB} potential of the 3% $WS_2/ZnIn_2S_4$ sample was estimated to be ca. −0.78 V vs. NHE, which was more positive than that of $ZnIn_2S_4$ (−0.94 V vs. NHE). The E_{CB} positive shift of 3% $WS_2/ZnIn_2S_4$ was probably due to the change of the fermi level arising from the interaction between $ZnIn_2S_4$ and WS_2 cocatalyst. Combined with the bandgap values obtained by the DRS result, the valence band (VB) potentials could be estimated as 1.38 eV and 1.35 eV for the prepared $ZnIn_2S_4$ and 3% $WS_2/ZnIn_2S_4$, respectively.

On the basis of the obtained band edge positions of $ZnIn_2S_4$ and $WS_2/ZnIn_2S_4$, the possible photocatalytic mechanism of
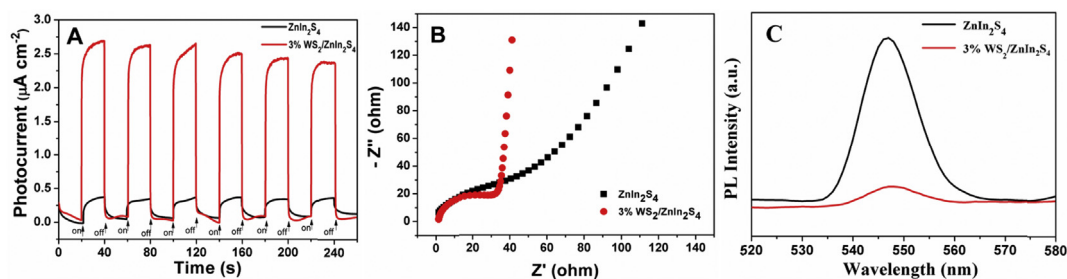

Fig. 6 — (A) Photocurrent-time curves of the prepared $ZnIn_2S_4$ and 3%$WS_2/ZnIn_2S_4$ composites with visible light on/off cycles at 0 V (vs. SCE) in 0.5 M Na_2SO_4 aqueous solution; (B) EIS spectra for the prepared $ZnIn_2S_4$ and 3%$WS_2/ZnIn_2S_4$ samples in 0.5 M Na_2SO_4 aqueous solution under visible light ($\lambda \geq 420$ nm) irradiation; (C) PL emission spectra of the prepared $ZnIn_2S_4$ and 3% $WS_2/ZnIn_2S_4$ samples at an excitation wavelength of 298 nm.
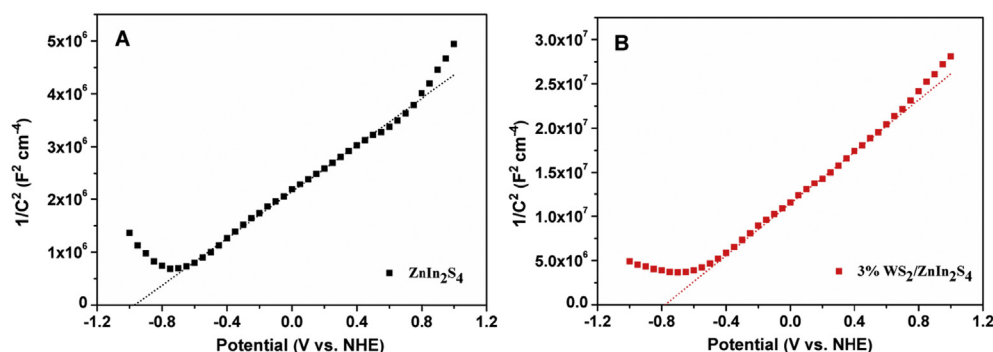
Fig. 7 — Mott-Schottky plots for (A) $ZnIn_2S_4$ and (B) 3% $WS_2/ZnIn_2S_4$ in 0.5 M Na_2SO_4 aqueous solution.

$WS_2/ZnIn_2S_4$ composites was proposed, as schematically illustrated in Fig. 8. Upon visible light illumination, $ZnIn_2S_4$ nanoparticles could be excited to produce photogenerated electrons and holes. The same process would also occur in WS_2 nanosheets. For the pure $ZnIn_2S_4$ sample, the generated electrons and holes could be easily recombined, thus leading to the poor photocatalytic activity. When $ZnIn_2S_4$ was coupled with WS_2, however, the excited electrons from the CB of $ZnIn_2S_4$ would rapidly transfer to WS_2 because of the lower conduction band position of WS_2 [47]. In this case, the separation of photogenerated electron-hole pairs within $ZnIn_2S_4$ would be greatly enhanced, which could be probably ascribed to the heterostructure formed at the interface between $ZnIn_2S_4$ and WS_2. The accumulated electrons in WS_2 would then reduce H^+ to generate H_2 on account of the lower E_{CB} potential of $WS_2/ZnIn_2S_4$ than the reduction potential of H^+/H_2. At the same time, the photogenerated holes would also transfer stepwise from the VB of WS_2 nanosheets to the VB of $ZnIn_2S_4$ nanoparticles because of the more positive E_{VB} potential of WS_2 (1.56 eV vs. NHE) [48] as compared to that of $ZnIn_2S_4$, and these photogenerated holes would further react with the sacrificial agents (such as S^{2-}, SO_3^{2-}) [49] for oxidation process. Consequently, the probability of photogenerated charge recombination considerably decreased, thus leading to

the significantly enhanced photocatalytic activity of $WS_2/ZnIn_2S_4$ for hydrogen evolution.

Conclusions

In summary, a series of $WS_2/ZnIn_2S_4$ composite photocatalysts were successfully synthesized for highly enhanced visible light photocatlaytic H_2 evolution. The WS_2 nanosheets were firstly prepared via a simple hydrothermal method, and the obtained WS_2 cocatalyst was subsequently realized to couple with $ZnIn_2S_4$ by also using a facile hydrothermal method. It was revealed that the $WS_2/ZnIn_2S_4$ composites exhibited much higher photocatalytic activities for hydrogen evolution than pure $ZnIn_2S_4$, and the photocatalytic activity of $ZnIn_2S_4$ was greatly affected by the loading amount of WS_2 cocatalyst. Among all the prepared $WS_2/ZnIn_2S_4$ photocatalysts, the 3% $WS_2/ZnIn_2S_4$ photocatalyst achieved the best hydrogen evolution rate of 199.1 μmol/h/g, which was nearly 6 times higher than pure $ZnIn_2S_4$ and was even comparable to conventional $Pt/ZnIn_2S_4$ photocatalysts. The improved photocatalytic performance of $WS_2/ZnIn_2S_4$ could be ascribed to the efficient separation and migration of photogenerated electron-hole pairs derived from the heterostructure formed at the interface between $ZnIn_2S_4$ and WS_2.
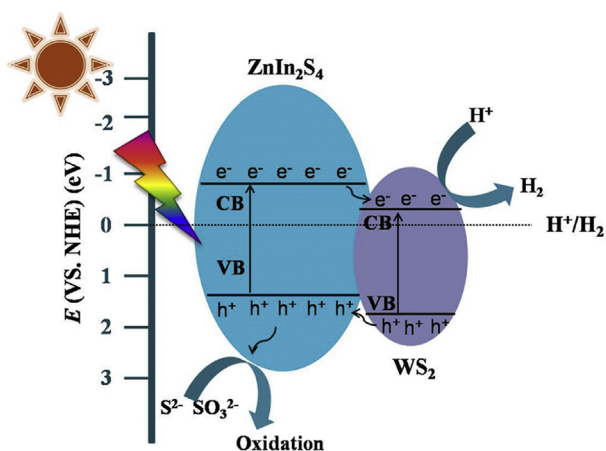
Acknowledgments

Fig. 8 — Schematic illustration of the proposed mechanism for visible light photocatalytic hydrogen evolution over the $WS_2/ZnIn_2S_4$ composite photocatalyst.

REFERENCES

[1] Fujishima A, Honda K. Electrochemical photolysis of water at a semiconductor electrode. Nature 1972;238:37–8.

[2] Hisatomi T, Kubota J, Domen K. Recent advances in semiconductors for photocatalytic and photoelectrochemical water splitting. Chem Soc Rev 2014;43:7520–35.

[3] Ge MZ, Cai JS, Iocozzia J, Cao CY, Huang JY, Zhang XN, et al. A review of TiO_2 nanostructured catalysts for sustainable H_2 generation. Int J Hydrogen Energy 2017;42:8418–49.

[4] Huo JP, Fang LT, Lei YL, Zeng GC, Zeng HP. Facile preparation of yttrium and aluminum co-doped ZnO via a sol-gel route for photocatalytic hydrogen production. J Mater Chem A 2014;2:11040–4.

[5] Miseki Y, Kato H, Kudo A. Water splitting into H_2 and O_2 over niobate and titanate photocatalysts with (111) plane-type layered perovskite structure. Energy Environ Sci 2009;2:306–14.

[6] Qu Y, Zhou W, Ren ZY, Wang GF, Jiang BJ, Fu HG. Facile synthesis of porous Zn_2Ti_3O8 nanorods for photocatalytic overall water splitting. ChemCatChem 2014;6:2258–62.

[7] Zhang P, Zhang JJ, Gong JL. Tantalum-based semiconductors for solar water splitting. Chem Soc Rev 2014;43:4395–422.

[8] Zhou C, Zhao YF, Shang L, Cao YH, Wu LZ, Tung CH, et al. Facile preparation of black Nb^{4+} self-doped $K_4Nb_6O_{17}$ microspheres with high solar absorption and enhanced photocatalytic activity. Chem Commun 2014;50:9554–6.

[9] Shen SH, Zhao L, Guo LJ. Cetyltrimethylammoniumbromide (CTAB)-assisted hydrothermal synthesis of $ZnIn_2S_4$ as an efficient visible-light-driven photocatalyst for hydrogen production. Int J Hydrogen Energy 2008;33:4501–10.

[10] Lei ZB, You WS, Liu MY, Zhou GB, Takata T, Hara M, et al. Photocatalytic water reduction under visible light on a novel $ZnIn_2S_4$ catalyst synthesized by hydrothermal method. Chem Commun 2003:2142–3.

[11] Chen YJ, Huang RK, Chen DQ, Wang YS, Liu WJ, Li XN, et al. Exploring the different photocatalytic performance for dye degradations over hexagonal $ZnIn_2S_4$ microspheres and cubic $ZnIn_2S_4$ nanoparticles. ACS Appl Mater Interfaces 2012;4:2273–9.

[12] Shen J, Zai JT, Yuan YP, Qian XF. 3D hierarchical $ZnIn_2S_4$: the preparation and photocatalytic properties on water splitting. Int J Hydrogen Energy 2012;37:16986–93.

[13] Yang JH, Wang DG, Han HX, Li C. Roles of cocatalysts in photocatalysis and photoelectrocatalysis. Acc Chem Res 2013;46:1900–9.

[14] Wang YB, Wang YS, Xu R. Photochemical deposition of Pt on CdS for H_2 evolution from water: markedly enhanced activity by controlling Pt reduction environment. J Phys Chem C 2013;117:783–90.

[15] Wang S, Chen D, Niu F, Zhang N, Qin LS, Huang YX. Enhancement in visible light photocatalytic activity of $BiFeO_3$ photocatalysts by Pd cocatalyst. Appl Phys A 2016;122:867.

[16] Rayalu SS, Jose D, Joshi MV, Mangrulkar PA, Shrestha K, Klabunde K. Photocatalytic water splitting on Au/TiO_2 nanocomposites synthesized through various routes: enhancement in photocatalytic activity due to SPR effect. Appl Catal B Environ 2013;142–43:684–93.

[17] Nguyen-Phan TD, Luo S, Voychok D, Llorca J, Graciani J, Sanz JF, et al. Visible light-driven H_2 production over highly dispersed ruthenia on rutile TiO_2 nanorods. ACS Catal 2016;6:407–17.

[18] Li YX, Zhang K, Peng SQ, Lu GX, Li SB. Photocatalytic hydrogen generation in the presence of ethanolamines over $Pt/ZnIn_2S_4$ under visible light irradiation. J Mol Catal Chem 2012;363–364:354–61.

[19] Zong X, Yan HJ, Wu GP, Ma GJ, Wen FY, Wang L, et al. Enhancement of photocatalytic H_2 evolution on CdS by loading MoS_2 as cocatalyst under visible light irradiation. J Am Chem Soc 2008;130:7176–7.

[20] Zhou XZ, Huang JJ, Zhang HZ, Sun H, Tu WX. Controlled synthesis of CdS nanoparticles and their surface loading with MoS_2 for hydrogen evolution under visible light. Int J Hydrogen Energy 2016;41:14758–67.

[21] Liu C, Chai B, Wang CL, Yan JT, Ren ZD. Solvothermal fabrication of MoS_2 anchored on $ZnIn_2S_4$ microspheres with boosted photocatalytic hydrogen evolution activity. Int J Hydrogen Energy 2018;43:6977–86.

[22] Zhang W, Wang YB, Wang Z, Zhong ZY, Xu R. Highly efficient and noble metal-free NiS/CdS photocatalysts for H_2 evolution from lactic acid sacrificial solution under visible light. Chem Commun 2010;46:7631–3.

[23] Zhou XZ, Sun H, Zhang HZ, Tu WX. One-pot hydrothermal synthesis of CdS/NiS photocatalysts for high H_2 evolution from water under visible light. Int J Hydrogen Energy 2017;42:11199–205.

[24] Zong X, Han JF, Ma GJ, Yan HJ, Wu GP, Li C. Photocatalytic H_2 evolution on CdS loaded with WS_2 as cocatalyst under visible light irradiation. J Phys Chem C 2011;115:12202–8.

[25] Chang K, Hai X, Ye JH. Transition metal disulfides as noble-metal-alternative Co-Catalysts for solar hydrogen production. Adv Energy Mater 2016;6:1502555.

[26] Chhowalla M, Shin HS, Eda G, Li LJ, Loh KP, Zhang H. The chemistry of two-dimensional layered transition metal dichalcogenide nanosheets. Nat Chem 2013;5:263–75.

[27] Zhong YY, Zhao G, Ma FK, Wu YZ, Hao XP. Utilizing photocorrosion-recrystallization to prepare a highly stable and efficient CdS/WS_2 nanocomposite photocatalyst for hydrogen evolution. Appl Catal B Environ 2016;199:466–72.

[28] Xu DY, Xu PT, Zhu YZ, Peng WC, Li Y, Zhang GL, et al. High yield exfoliation of WS_2 crystals into 1–2 layer semiconducting nanosheets and efficient photocatalytic hydrogen evolution from WS_2/CdS nanorod composites. ACS Appl Mater Interfaces 2018;10:2810–8.

[29] Zhang K, Fujitsuka M, Du YK, Majima T. 2D/2D heterostructured CdS/WS_2 with efficient charge separation improving H_2 evolution under visible light irradiation. ACS Appl Mater Interfaces 2018;10:20458–66.

[30] Zhong YY, Shao YL, Huang BB, Hao XP, Wu YZ. Combining ZnS with WS_2 nanosheets to fabricate a broad-spectrum composite photocatalyst for hydrogen evolution. New J Chem 2017;41:12451–8.

[31] Chu DM, Zhang CY, Yang P, Du YK, Lu C. WS_2 as an effective noble-metal free cocatalyst modified $TiSi_2$ for enhanced photocatalytic hydrogen evolution under visible light irradiation. Catalysts 2016;6:136.

[32] Hou YD, Zhu YS, Xu Y, Wang XC. Photocatalytic hydrogen production over carbon nitride loaded with WS_2 as cocatalyst under visible light. Appl Catal B Environ 2014;156:122–7.

[33] Akple MS, Low JX, Wageh S, Al-Ghamdi AA, Yu JG, Zhang J. Enhanced visible light photocatalytic H_2-production of g-C_3N_4/WS_2 composite heterostructures. Appl Surf Sci 2015;358:196–203.

[34] Chu DM, Li KZ, Liu AJ, Huang L, Zhang CY, Yang P, et al. Zn-doped hematite modified by graphene-like WS_2: a p-type semiconductor hybrid photocathode for water splitting to produce hydrogen. Int J Hydrogen Energy 2018;43:7307–16.

[35] Zhao WJ, Ghorannevis Z, Chu LQ, Toh ML, Kloc C, Tan PH, et al. Evolution of electronic structure in atomically thin sheets of WS_2 and WSe_2. ACS Nano 2013;7:791–7.

[36] Braga D, Lezama IG, Berger H, Morpurgo A. Quantitative determination of the band gap of WS_2 with ambipolar ionic liquid-gated transistors. Nano Lett 2012;12:5218–23.

[37] Sang YH, Zhao ZH, Zhao MW, Hao P, Leng YH, Liu H. From UV to near-infrared, WS_2 nanosheet: a novel photocatalyst for full solar light spectrum photodegradation. Adv Mater 2015;27:363–9.

[38] Yang J, Voiry D, Ahn SJ, Kang D, Kim AY, Chhowalla M, et al. Two-Dimensional hybrid nanosheets of tungsten disulfide

and reduced graphene oxide as catalysts for enhanced hydrogen evolution. Angew Chem 2013;125:13996–9.

[39] Chen ZX, Li DZ, Zhang WJ, Shao Y, Chen TW, Sun M, et al. Photocatalytic degradation of dyes by $ZnIn_2S_4$ microspheres under visible light irradiation. J Phys Chem C 2009;113:4433–40.

[40] Zhang ZY, Liu KC, Feng ZQ, Bao YN, Dong B. Hierarchical sheet-on-sheet $ZnIn_2S_4$/g-C_3N_4 heterostructure with highly efficient photocatalytic H_2 production based on photoinduced interfacial charge transfer. Sci Rep 2016;6:19221.

[41] Tauc J, Grigorovici R, Vancu A. Optical properties and electronic structure of amorphous germanium. Phys Status Solidi 1966;15:627–37.

[42] Wei L, Chen YJ, Lin YP, Wu HS, Yuan RS, Li ZH. MoS_2 as non-noble-metal co-catalyst for photocatalytic hydrogen evolution over hexagonal $ZnIn_2S_4$ under visible light irradiations. Appl Catal B Environ 2014;144:521–7.

[43] Chen GP, Ding N, Li F, Fan YZ, Luo YH, Li DM, et al. Enhancement of photocatalytic H_2 evolution on $ZnIn_2S_4$ loaded with in-situ photo-deposited MoS_2 under visible light irradiation. Appl Catal B Environ 2014;160–161:614–20.

[44] Li WJ, Lin ZY, Yang GW. A 2D self-assembled MoS2/ZnIn2S4 heterostructure for efficient photocatalytic hydrogen evolution. Nanoscale 2017;9:18290–8.

[45] Wolcott A, Smith WA, Kuykendall TR, Zhao YP. Photoelectrochemical study of nanostructured ZnO thin films for hydrogen generation from water splitting. Adv Funct Mater 2009;19:1849–56.

[46] Xia Y, Li Q, Lv K, Tang D, Li M. Superiority of graphene over carbon analogs for enhanced photocatalytic H_2-production activity of $ZnIn_2S_4$. Appl Catal B Environ 2017;206:344–52.

[47] Zhong YY, Shao YL, Ma FK, Wu YZ, Huang BB, Hao XP. Band-gap-matched CdSe QD/WS_2 nanosheet composite: size-controlled photocatalyst for high-efficiency water splitting. Nano Energy 2017;31:84–9.

[48] Zou YJ, Shi JW, Ma DD, Fan ZY, Cheng LH, Sun DK, et al. WS2/Graphitic carbon nitride heterojunction nanosheets decorated with CdS quantum dots for photocatalytic hydrogen production. ChemSusChem 2018;11:1187–97.

[49] Bao NZ, Shen LM, Takata T, Domen K. Self-templated synthesis of nanoporous CdS nanostructures for highly efficient photocatalytic hydrogen production under visible light. Chem Mater 2008;20:110–7.

Facile synthesis of Sm-doped BiFeO$_3$ nanoparticles for enhanced visible light photocatalytic performance

CrossMark

Zijun Hu, Da Chen *, Sen Wang, Ning Zhang, Laishun Qin *, Yuexiang Huang

College of Materials Science and Engineering, China Jiliang University, Hangzhou 310018, Zhejiang, PR China

ABSTRACT

In this work, the effect of Sm doping on the structural and photocatalytic properties of BiFeO$_3$ (BFO) was investigated. A series of Sm doped BFO nanoparticles containing different Sm dopant contents (Bi$_{(1−x)}$Sm$_x$FeO$_3$, x = 0.00, 0.01, 0.03, 0.05, 0.07, 0.10) were synthesized via a simple sol-gel route. It was revealed that Sm^{3+} ions were successfully doped into BFO nanoparticles, and the band gap value was gradually decreased when increasing Sm dopant concentration. The photocatalytic activity of Sm-doped BFO photocatalyst was significantly affected by the Sm doping content. Compared to pure BFO, the Sm-doped BFO samples exhibited much higher photocatalytic activity. The improved photocatalytic activity of Sm-doped BFO could be attributed to the enhanced visible light absorption and the efficient separation of photogenerated electrons and holes derived from Sm dopant trapping level in the Sm-doped BFO samples. In addition, the possible photocatalytic mechanism of Sm-doped BFO photocatalyst was also proposed.

© 2017 Elsevier B.V. All rights reserved.

1. Introduction

As one of the very few multiferroic materials in which coexist ferroelectricity and ferromagnetism behaviors in single phase at the room temperature, perovskite bismuth ferrite (BiFeO$_3$, BFO) has garnered special attention for a wide range of potential applications in data storage, sensors, spintronics devices, etc [1]. Noteworthily, recent research has drawn attention on the photocatalytic activity of BFO, such as photocatalytic splitting water [2] and organics degradation [3,4], owing to its narrow band-gap (E$_g \sim$ 2.2 eV), excellent chemical stability and low cost [5]. The narrow band gap allows carrier excitation in BFO under visible light irradiation, and hence enables us to develop BFO-based visible-light driven photocatalysts. For instance, Gao et al. [3] have revealed that BFO nanoparticles exhibited photocatalytic activities for decomposition of methyl orange under visible light irradiation. Unfortunately, the BFO photocatalyst has fatal drawbacks, such as the poor intrinsic carrier mobility and the fast recombination of photogenerated electron–hole pairs, which seriously restricts the photocatalytic activity of BFO. Therefore, much effort should be made to improve the photocatalytic activity of BFO for practical use.

To date, extensive studies have been performed to improve the optical, ferroelectric polarization, and ferromagnetic properties of BFO by means of metal ion doping at A site or B site or A and B site in the ABO$_3$ lattice [6,7]. In these cases, the lattice structure of perovskite BFO could be distorted by the doping metal ions, which could modulate its electronic band structure and dipole–dipole interaction, thus making it possible to improve the optical, ferroelectric and ferromagnetic properties [7]. Motivated by these studies, metal ion doping could be regarded as an efficient method to improve the photocatalytic activities of BFO [8–11], since doping metal ions have the ability to promote the efficient separation of photoexcited charge carriers during the photocatalytic reaction [8]. Especially, doping of BFO with rare earth elements has proved to be relatively more successful because of their special 4f electron configurations which can facilitate the abruption of photogenerated electron-hole pairs [12]. For example, Sakar et al. [10] reported that the substitution of Dy in the host of BFO nanoparticles and nanofibers was obtained by sol-gel and electrospinning methods respectively, and the photocatalytic efficiency was thus enhanced, which could be attributed to the reduced band gap energy and enhanced delocalization of charge carriers induced by the Dy substitution. Recently, our group [11] also demonstrated the successful substitution of Gd^{3+} in BFO host by a facile sol-gel method for enhanced visible light photocatalytic activity. The Gd-doped BFO sample containing 3% Gd dopant content exhibited the highest photocatalytic RhB degradation efficiency, which was about 2.55 times

that of the pure BFO. The enhanced photocatalytic activities could be ascribed to the increased optical absorption, the efficient separation and migration of photogenerated charge carriers as well as the decreased recombination probability of electron-hole pairs derived from the Gd doping effect. It should be noted that substitution of Bi^{3+} cation with rare earth ions having smaller ionic radii than Bi^{3+} (1.03 Å), such as the above mentioned Dy^{3+} (0.912 Å) [10] or Gd^{3+} (0.938 Å) [11], is requisite to cause a more significant structural distortion in the BFO lattice for improved photocatalytic properties. In this regard, the Sm^{3+} substitution may also introduce sufficient degree of distortion in the BFO lattice because the ionic radius of Sm^{3+} (0.958 Å) [13] is smaller than Bi^{3+}, and thus probably improve the photocatalytic properties of BFO. Though there have been several reports on doping of Sm^{3+} in BFO for improved magnetic and ferroelectric properties [13–15], to the best of our knowledge, the effect of samarium element doping on the photocatalytic activity of BFO has seldom been reported. In fact, samarium ions have been demonstrated as an efficient dopant in other photocatalysts (such as TiO_2 [16], Bi_2O_3 [17]) for enhanced photocatalytic activities. For example, Reddy et al. [17] reported that the photocatalytic activity of Bi_2O_3 was greatly enhanced through the doping of samarium ions for methylene blue dye and phenol degradation under solar irradiation. Therefore, it is of considerable interest to investigate the feasibility of enhanced photocatalytic properties of BFO by doping with samarium element.

To reveal the effect of Sm^{3+} ions doping on the photocatalytic activities of BFO, herein, samarium (Sm)-doped BFO photocatalysts containing different Sm^{3+} doping contents were synthesized through a simple sol-gel method. The obtained Sm-doped photocatalysts were characterized by various techniques, including scanning electron microscopy (SEM), transmission electron microscopy (TEM), X-ray diffraction (XRD), Raman spectroscopy, X-ray photoelectron spectroscopy (XPS) and UV–vis diffuse reflectance spectroscopy (DRS). The photocatalytic activities of the obtained samples were then evaluated by photodegradation of methyl orange (MO) under visible light irradiation. In addition, the photocatalytic mechanism of Sm-doped BFO nanoparticles was also discussed.

2. Experimental

2.1. Preparation of photocatalysts

All chemical reagents were of analytical grade and used without any further purification. A series of samarium (Sm)-doped BFO photocatalysts with different Sm^{3+} doping concentrations ($Bi_{(1-x)}Sm_xFeO_3$) (x = 0.00, 0.01, 0.03, 0.05, 0.07, or 0.10) were prepared by using a simple sol-gel method. Typically, appropriate amounts of $Bi(NO_3)_3 \cdot 5H_2O$ (purity ≥ 99.0%) ($100 \times (1 - x)$ mmol), $Sm(NO_3)_3 \cdot 6H_2O$ (purity ≥ 99.9%) ($100 \times (x)$ mmol) and $Fe(NO_3)_3 \cdot 9H_2O$ (purity ≥ 98.5%) (100 mmol) in the desired stoichiometric ratio were dissolved in 100 mL of ethylene glycol to prepare the precursor solution. Subsequently, citric acid (3 g) was added into the above precursor solution. After a continuous stirring for 3 h, a homogeneous brownish-red-colored solution was achieved. The resulting solution was further stirred vigorously at 80 °C for 1.5 h to form the sol, which was then transferred into an open Petri dish and dried at 100 °C for 24 h. The resultant gel was then calcined at 550 °C for 2 h, and thus the pure BFO or Sm-doped BFO nanoparticles were obtained.

2.2. Characterizations

The crystal structures of the obtained samples were examined by a Bruker D2 X-ray diffractometer (XRD) using Cu K_α radiation.

The morphology and composition of the samples were characterized by the scanning electron microscope (SEM, Hitachi SU8010) equipped with an energy dispersive X-ray spectrometer (EDS), and an emission transmission electron microscope (TEM) (JEOL JEM-2100). Raman spectra were analyzed in the range of 70–700 cm^{-1} by Renishaw inVia Raman Microscope. The chemical elements present in the prepared samples were recorded using a PHI 5000 Versa Probe X-ray photoelectron spectrometer with Al K_α radiation. The optical properties of the samples were determined on a UV–visible spectrophotometer (Shimadzu UV-3600) using $BaSO_4$ as reference.

2.3. Photocatalytic measurements

The photodegradation of methyl orange (MO) aqueous solution was conducted in a quartz glass reactor under a 300 W Xe lamp attached with a cut-off filter ($\lambda \geq 420$ nm) as a light source. In each experiment, a portion of the obtained photocatalyst (0.3 g) was suspended in 100 mL of MO solution (5 mg L^{-1}, pH 6.8), followed by magnetically stirring for 1 h in dark to establish the adsorption-desorption equilibrium. Note that the suspension temperature was kept at room temperature to avoid the thermal effect
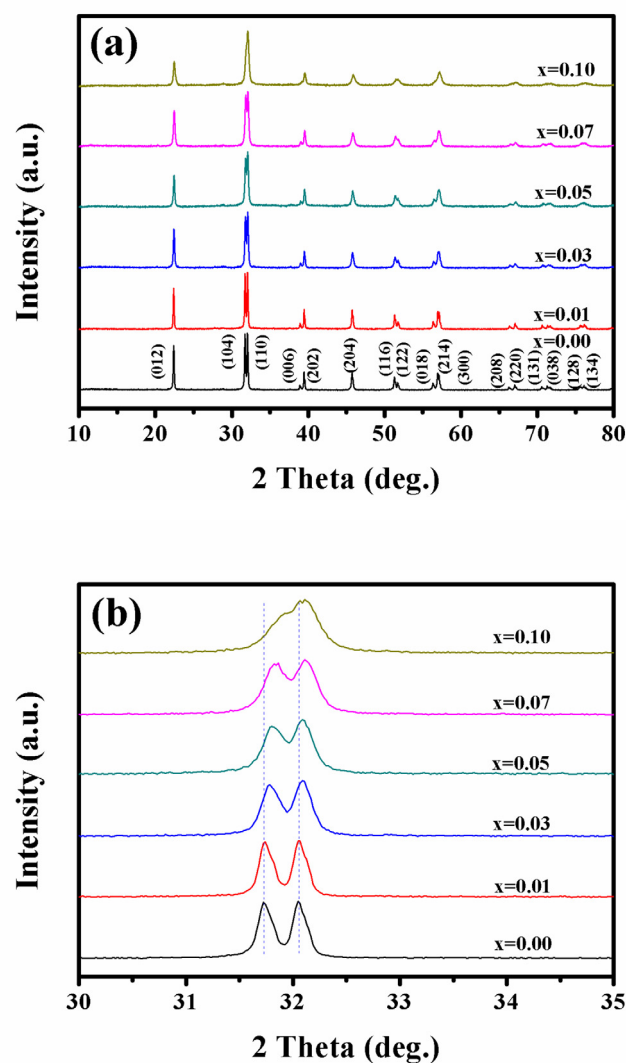

Fig. 1. (a) XRD patterns of the prepared $Bi_{(1-x)}Sm_xFeO_3$ (x = 0.00, 0.01, 0.03, 0.05, 0.07, and 0.10) samples; (b) the magnified patterns of $Bi_{(1-x)}Sm_xFeO_3$ in the range of 30°–35°.

by a cooling water circulation machine during the whole photocatalytic process. At a given interval time, 4 mL of the suspension solution was collected and centrifuged to remove the catalyst particles, and the MO concentration was then determined by measuring the maximum absorbance at 464 nm using a UV–visible spectrophotometer (model: 722, Precision Instruments Co., Ltd. Shanghai, China). In terms of the photocatalytic stability test, the remaining photocatalyst particles in suspension after a photocatalytic experiment were gathered and washed with distilled water to remove the residual MO, and then dried before the next catalytic reaction.

3. Results and discussion

The crystal structures and phase purity of the obtained samples were investigated by XRD measurements. Fig. 1(a) presents the XRD patterns of the prepared $Bi_{(1-x)}Sm_xFeO_3$ (x = 0.00, 0.01, 0.03, 0.05, 0.07, and 0.10) nanoparticles containing different Sm doping concentrations. As seen, all the diffraction peaks of pure BFO sample could be matched to a rhombohedral phase with the space group R3c (JCPDS No. 86-1518), suggesting the successful preparation of pure BFO phase by the present sol-gel process. For the Sm-doped BFO samples, the diffraction peaks were similar to those of
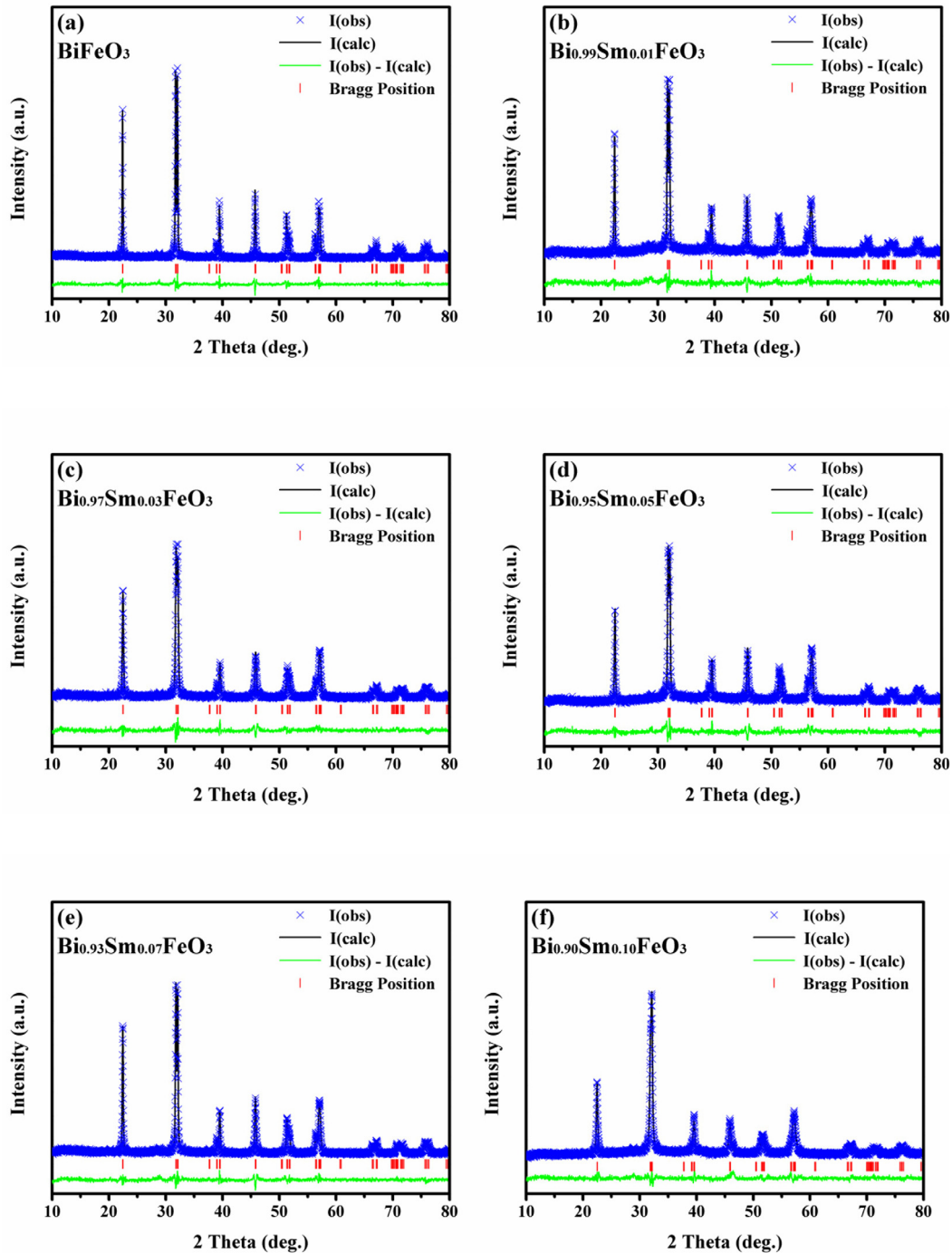

Fig. 2. Rietveld refinement XRD patterns of (a) $BiFeO_3$, (b) $Bi_{0.99}Sm_{0.01}FeO_3$, (c) $Bi_{0.97}Sm_{0.03}FeO_3$, (d) $Bi_{0.95}Sm_{0.05}FeO_3$, (e) $Bi_{0.93}Sm_{0.07}FeO_3$ and (f) $Bi_{0.90}Sm_{0.10}FeO_3$.

pure BFO, and no signals for samarium element or other impurities were detected, implying that the substitution of Sm would not produce the second phase in BFO. From the magnified XRD patterns (Fig. 1(b)), however, it can be seen that the separate (104) and (110) diffraction peaks at around 32° in pure BFO tended to shift toward higher 2θ angles and nearly merge into a single broad peak with increasing Sm doping concentration, suggesting that the rhombohedral BiFeO$_3$ structure underwent some changes by Sm

Table 1
Rietveld structural parameters for Bi$_{(1-x)}$Sm$_x$FeO$_3$ (x = 0.00, 0.01, 0.03, 0.05, 0.07,and 0.10) samples.

Parameters	Bi$_{(1-x)}$Sm$_x$FeO$_3$					
	x = 0.00	x = 0.01	x = 0.03	x = 0.05	x = 0.07	x = 0.10
Space group	*R3c*					
Lattice parameters						
a = b(Å)	5.5781	5.5772	5.5745	5.5743	5.5766	5.5711
c(Å)	13.8678	13.8626	13.8461	13.8402	13.8530	13.8053
Volume(Å^3)	373.68	373.43	372.63	372.44	373.09	371.07
Bond length						
Bi–Fe	3.083	3.055	3.130	3.083	3.084	3.281
Bi–O	2.276	2.359	2.468	2.315	2.312	2.540
Fe–O	1.885	1.770	1.743	1.783	1.838	1.835
R-factors (%)						
R_{wp}	6.46	7.10	6.53	7.07	6.40	6.04
R_p	5.03	5.54	5.18	5.54	5.03	4.72
χ^2	1.665	1.736	1.660	1.720	1.647	1.519
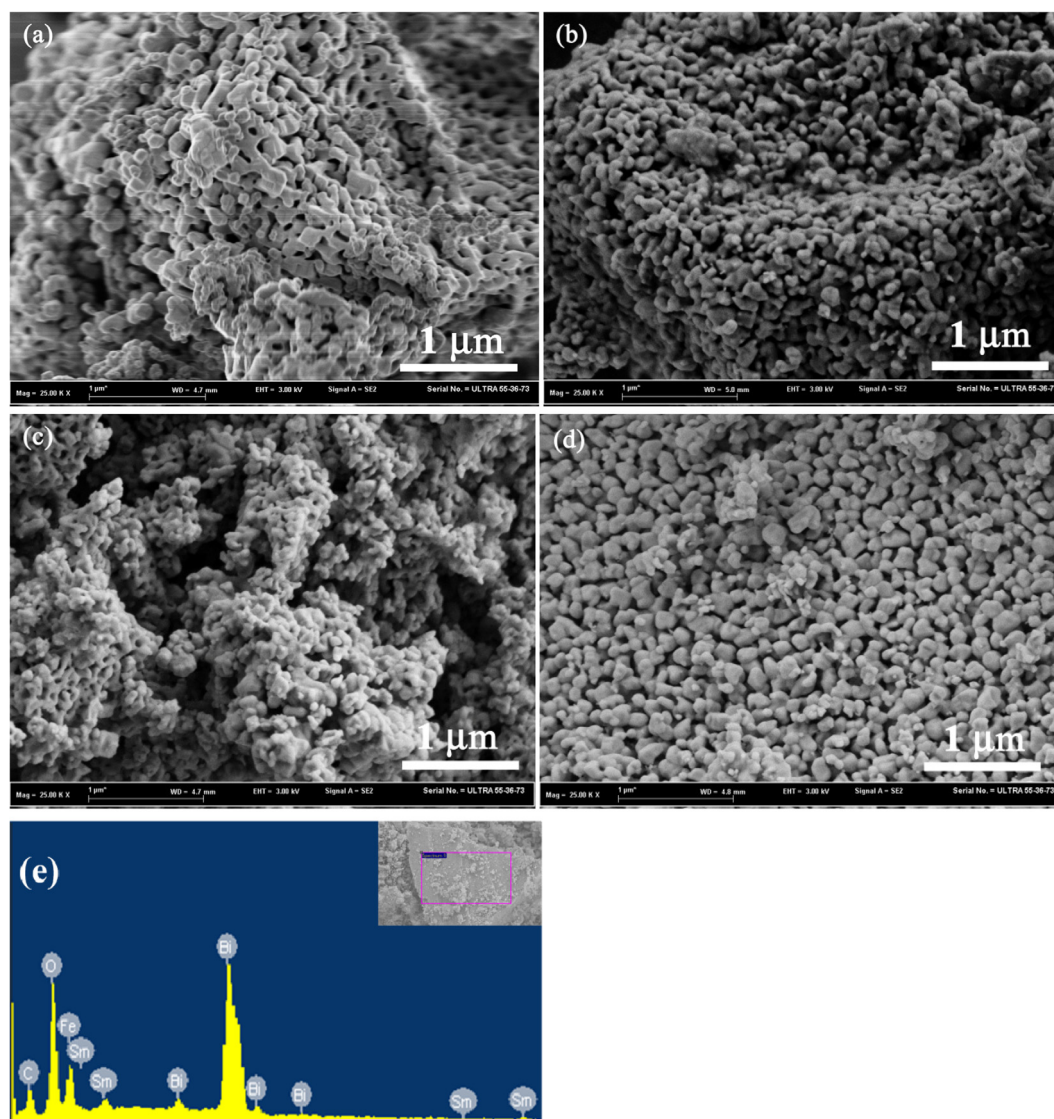
Fig. 3. SEM images of as-prepared Bi$_{(1-x)}$Sm$_x$FeO$_3$ nanoparticles (a) pure BFO, (b) Bi$_{0.97}$Sm$_{0.03}$FeO$_3$ nanoparticles, (c) Bi$_{0.93}$Sm$_{0.07}$FeO$_3$ nanoparticles, (d) Bi$_{0.90}$Sm$_{0.10}$FeO$_3$ nanoparticles and (e) EDS spectrum of the Bi$_{0.90}$Sm$_{0.10}$FeO$_3$ nanoparticles (*Note*: the labeled element carbon (C) was detected from the conductive tapes).

substitution in accordance with the previously reported other metal ions doped BFO ceramics [18]. Note that the perovskite structure (ABO$_3$) could be described by the following Goldschmidt's tolerance factor (Eq. (1)) [19]:

$$t = \frac{(r_A + r_O)}{\sqrt{2}(r_B + r_O)} \tag{1}$$

where r_A, r_B and r_O are the ionic radii of A, B and O in ABO$_3$ perovskite structure, respectively. As the ionic radius of Sm^{3+} ions (0.958 Å) is smaller than that of Bi^{3+} ions (1.03 Å) [13], the substitution of Sm^{3+} ions in place of Bi^{3+} ions would decrease the tolerance factor, thus leading to the compression in Fe–O bond and tension in Bi–O bond and hence the lattice distortion in BFO. In addition, the characteristic peaks corresponding to (110), (012) and (204) in Sm-doped BFO became broader compared with pure BFO, indicating that the crystalline size of Sm-doped BFO was decreased. In order to obtain more accurate structural information of all the samples, the Rietveld refinement of X-ray diffraction pattern was also performed by using GSAS software [20], as shown in Fig. 2. The refined structural parameters along with the profile R-factors obtained from the Rietveld refinement of the XRD patterns are listed in Table 1. From Table 1, the fitting parameters (R_{wp}, R_p, and χ^2) indicate good agreement between the refined and observed XRD patterns. The crystalline structure of all the samples is the typical rhombohedral phase with the R3c space group, and the distortions created on doping Sm in BFO can be seen clearly from the small variations in lattice parameters and unit cell volumes. This structure distortion could be attributed to the differences between bismuth and samarium ionic radii.

The typical SEM images of as-prepared Bi$_{(1-x)}$Sm$_x$FeO$_3$ (x = 0.00, 0.03, 0.07, 0.10) are shown in Fig. 3(a)–(d). Both pure BFO and Sm-doped BFO exhibited an irregular shape with a relatively narrow size distribution. For pure BFO, the particles were easily agglomerated, and the average particle size was about 80–150 nm. Compared to pure BFO, the Sm-doped BFO particles showed similar morphological features, and the average particle size was also ca. 80–150 nm. The EDS pattern of Bi$_{(1-x)}$Sm$_x$FeO$_3$ (x = 0.10) (Fig. 3 (e)) confirms that the obtained sample was composed of Bi, Fe, O and Sm elements. To further study the morphological feature of the Sm-doped BFO nanoparticles, TEM images of the pure BFO and Bi$_{0.97}$Sm$_{0.03}$FeO$_3$ samples were measured, as shown in Fig. 4 (a) and (b). The pure BFO and Bi$_{0.97}$Sm$_{0.03}$FeO$_3$ particles were irregular in shape, and the morphological structure of the Bi$_{0.97}$Sm$_{0.03}$-FeO$_3$ sample was similar to that of pure BFO, which was in agreement with the SEM results. The SEM and TEM images imply that the doping of Sm would not change the morphological feature of BFO. In addition, the high-resolution TEM (HRTEM) images
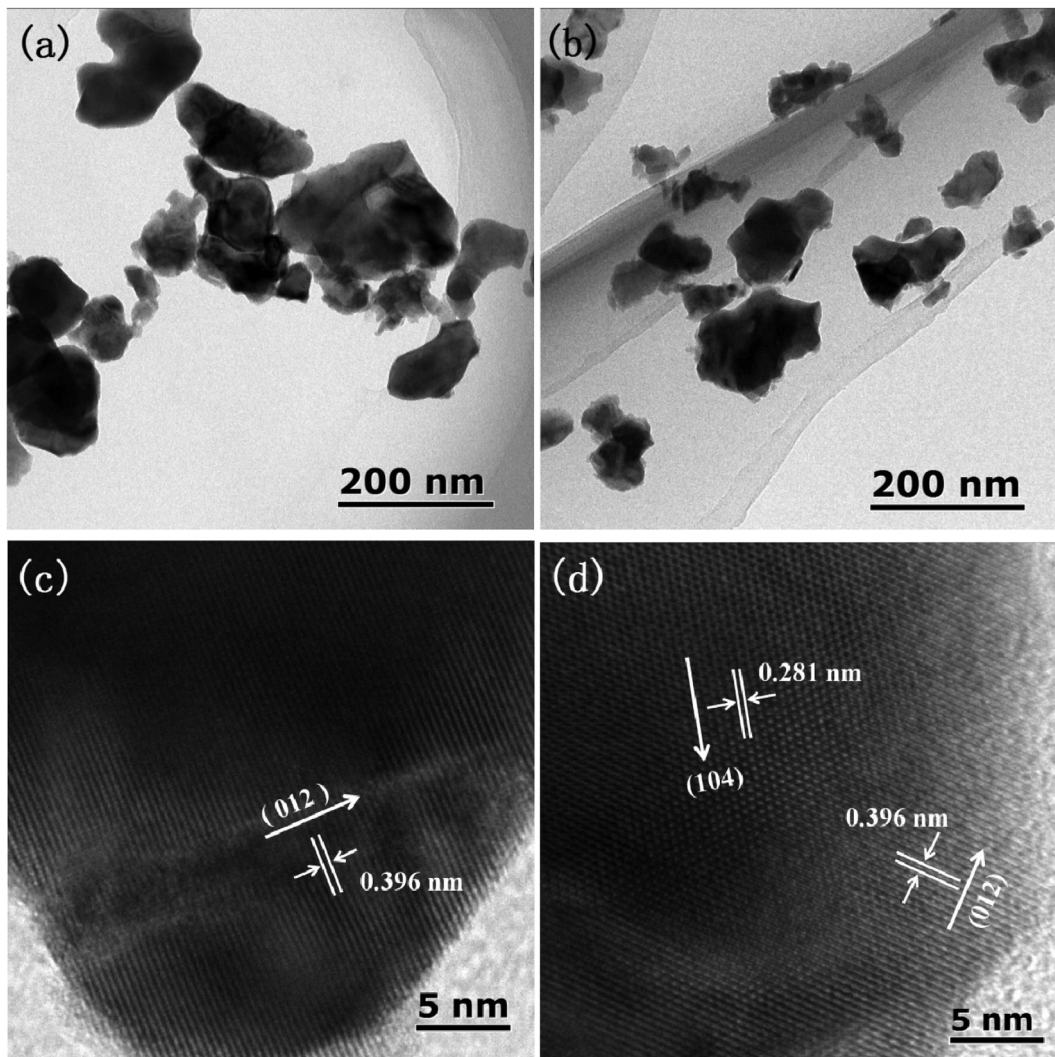

Fig. 4. TEM images of (a) BFO, (b) Bi$_{0.97}$Sm$_{0.03}$FeO$_3$; and HRTEM images of (c) BFO, (d) Bi$_{0.97}$Sm$_{0.03}$FeO$_3$.

(Fig. 4(c) and (d)) reveal that the interplanar spacings for the pure BFO and $Bi_{0.97}Sm_{0.03}FeO_3$ sample were 0.396 nm and 0.281 nm, which could be corresponding to the (012) and (104) crystal planes of the rhombohedral BFO, respectively. The HRTEM images further confirm the rhombohedral crystal structure of pure BFO and $Bi_{0.97}Sm_{0.03}FeO_3$ nanoparticles.

To further verify the chemical state and elemental composition of Sm-doped BFO, XPS measurements were performed on the pure BFO and Sm-doped BFO samples. Fig. 5 shows the core level Sm 3d, Bi 4f, Fe 2p and O 1 s XPS spectra of the $Bi_{0.97}Sm_{0.03}FeO_3$ sample. In the Sm 3d core level spectrum (Fig. 5(a)), the doublet peaks for Sm $3d_{5/2}$ and Sm $3d_{3/2}$ were located at 1083.5 and 1110.8 eV, respectively, indicating that the dopant Sm ion was in the trivalent oxidation state and no other valence state of Sm present in the sample [21]. For the Bi 4f core level state (Fig. 5(b)), the two peaks appearing at 158.3 and 163.9 eV corresponded to Bi $4f_{7/2}$ and Bi $4f_{5/2}$, respectively, confirming that the chemical state of Bi was trivalent oxidation in the Sm-doped BFO sample [6,22]. The representative Fe 2p core level spectrum (Fig. 5(c)) presented a doublet peaks at 709.8 and 723.6 eV corresponding to Fe $2p_{3/2}$ and Fe $2p_{1/2}$, respectively, and a satellite peak appearing at 717.8 eV ($\sim$8 eV above the Fe $2p_{3/2}$ peak) was regarded as the characteristic of the valence state of Fe, suggesting that the Fe element was in the form of Fe^{3+} in the obtained Sm-doped BFO sample [23]. The O 1s spectrum (Fig. 5(d)) could be resolved into three peaks centered around 528.9, 531.0, and 532.5 eV, corresponding to the lattice oxygen, chemisorbed oxygen and physically adsorbed oxygen, respectively [24]. Thus, the above XPS results demonstrate the presence of Sm, Bi and Fe in the obtained $Bi_{0.97}Sm_{0.03}FeO_3$ sample in a form of Sm^{3+}, Bi^{3+} and Fe^{3+}, respectively. In addition, to reveal the variation of oxidation states in Sm-doped BFO samples with Sm dopant con-

centration, the XPS spectra of pure BFO, $Bi_{0.99}Sm_{0.01}FeO_3$, and $Bi_{0.90}Sm_{0.10}FeO_3$ samples were also examined and compared with those of the $Bi_{0.97}Sm_{0.03}FeO_3$ sample, as shown in Fig. 6. It can be seen that the Bi 4f, Fe 2p, O 1s and Sm 3d core level XPS spectra of the pure BFO, $Bi_{0.99}Sm_{0.01}FeO_3$, and $Bi_{0.90}Sm_{0.10}FeO_3$ samples were similar to those of the $Bi_{0.97}Sm_{0.03}FeO_3$ sample, indicating that Bi, Fe and Sm were also present in the +3 oxidation states in the $Bi_{0.99}Sm_{0.01}FeO_3$ and $Bi_{0.90}Sm_{0.10}FeO_3$ samples. When increasing the Sm doping concentration, however, the Bi 4f peaks in Sm-doped BFO samples were slightly shifted toward higher binding energies in comparison with the pure BFO counterpart. This energy shift could be ascribed to the change of electronic structures of Bi due to the doping of Sm atoms into the lattice of BFO [17]. The XPS results further confirm the successful doping of Sm in BFO.

As known, Raman spectra are sensitive to atomic displacements, and the evolvement of Raman normal modes with increasing doping concentration would probe into the lattice properties, structural phase transitions, and spin-phonon coupling in the doped samples [25]. Fig. 7 shows the typical Raman spectra of the prepared pure BFO and Sm-doped BFO samples. According to the group theory, the pure BFO with rhombohedral structure R3c space group should generally have 13 Raman active modes (i.e., $4A_1 + 9E$), where the A_1 and E modes are Raman and infrared active, respectively [26]. In the Raman spectrum of pure BFO (Fig. 7 (a)), however, there were only ten active modes, and the other three active modes were missing. The absence of the three Raman peaks may be due to the higher local stress and the existence of point defects in the pure BFO sample [6]. According to the earlier reported data [6,27,28], the Raman peaks at 137, 178, and 218 cm^{-1} for pure BFO could be ascribed to longitudinal-optical (A_1) phonon modes, and the other Raman peaks at 77, 267, 329,
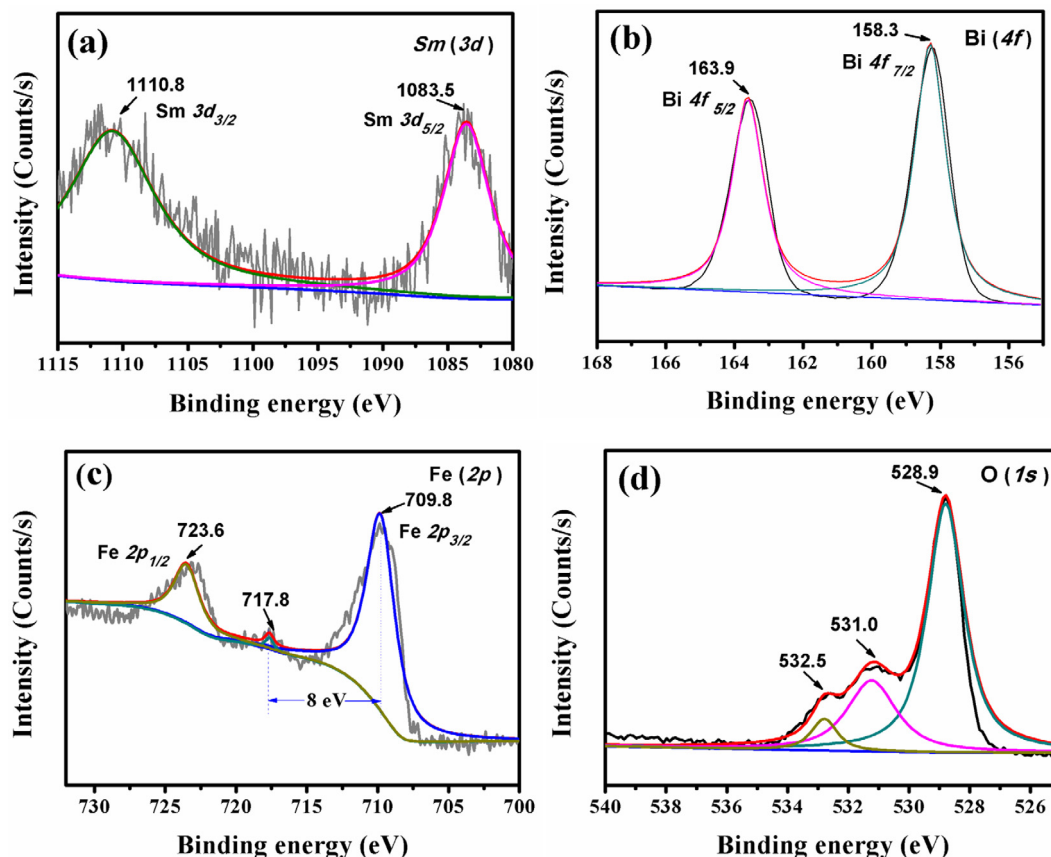

Fig. 5. XPS spectra of (a) Sm, (b) Bi, (c) Fe and (d) O elements for the $Bi_{0.97}Sm_{0.03}FeO_3$ sample.

372, 463, 523, and 605 cm^{-1} could be regarded as transverse-optical (E) phonon modes. Fig. 7(b) shows the Raman spectra of Sm-doped BFO samples in comparison with pure BFO. The dependence of the mode frequency on Sm concentration is summarized in Table 2. With the increase of Sm concentrations from x = 0.00 to x = 0.10, the E-1, A$_1$-1, A$_1$-2, A$_1$-3 and E-3 modes, which were subjected to Bi-O covalent bonds [26,29], shifted gradually to higher mode frequencies, and the corresponding peaks were also broadened. As known, the frequency of Raman modes is closely related to the atomic masses and force constant [30]. With the substitution of Sm^{3+} ions in BFO, the average mass on A-site of ABO$_3$ lattice would decrease because the atomic weight of Sm^{3+} (150.36 g/mol) is smaller than that of Bi^{3+} (208.98 g/mol), thus leading to the frequency shift of the E-1, A$_1$-1, A$_1$-2, A$_1$-3, and E-3 modes. The shifting and broadening of the Raman modes with increasing Sm concentration further demonstrate the successful doping of Sm into BFO in accompany with the increased lattice distortion [25], which was in accordance with the XRD results.

To study the optical absorption characteristic of photocatalysts, the UV–Vis DRS spectra of as-prepared Bi$_{1-x}$Sm$_x$FeO$_3$ (x = 0.00, 0.01, 0.03, 0.05, 0.07, and 0.10) samples were examined and the results are displayed in Fig. 8. Clearly, all the photocatalyst samples exhibited strong light absorption both in the UV and visible light region (Fig. 8(a)), demonstrating that the as-prepared Bi$_{1-x}$Sm$_x$FeO$_3$ could respond to visible light for photocatalytic reaction. Compared to BFO, the Sm-doped BFO samples showed improved absorption in visible light region, especially for the x = 0.10 sample. According to the Tauc Plot equation ($\alpha h\nu = A(h\nu - E_g)^{n/2}$) [31], the

band gap values of pure BFO and Sm-doped BFO samples could be estimated to be about 2.17, 2.15, 2.14, 2.13, 2.12 and 2.06 eV for the x = 0.00, 0.01, 0.03, 0.05, 0.07 and 0.10 sample, respectively (Fig. 8(b)). Obviously, the band gap value decreased with increasing Sm concentration. The decrease in the band gap could be ascribed to the rearrangement of the molecular orbital and distortion in FeO$_6$ octahedral with the doping of Sm ions [32]. Thus, the improved visible light absorption would be beneficial for the photocatalytic performance of BFO, as will be demonstrated below.

The photocatalytic performances of the obtained photocatalysts were evaluated by photocatalytic degradation of MO under visible light ($\lambda \geq 420$ nm) irradiation. Fig. 9(a) displays the photodegradation efficiencies of MO over the obtained samples as a function of illumination time. When no photocatalyst was added, the change of MO concentration was negligible during the whole irradiation time, suggesting that MO is a stable pollutant. With the addition of pure BFO or Sm-doped BFO, the MO degradation took place upon the visible light irradiation, and the dye was photodegraded in a stepwise manner with the color of the solution changing from an initial deep orange to nearly colorless (inset of Fig. 9(a)). After 120 min, 58.8%, 65.4%, 86.9%, 63.4%, 62.1% and 31.5% of MO were decomposed for the x = 0.00, 0.01, 0.03, 0.05, 0.07, and 0.10 sample, respectively. It is obvious that the photocatalytic performances of obtained Bi$_{1-x}$Sm$_x$FeO$_3$ photocatalyst were significantly affected by the Sm doping concentration. With the increase of the Sm doping concentration from 0.00% to 10%, the degradation efficiency of as-prepared Bi$_{1-x}$Sm$_x$FeO$_3$ photocatalyst first increased and then decreased. When the Sm doping concentration was 3%, the catalyst gave the highest degradation efficiency, which was about 1.5 times
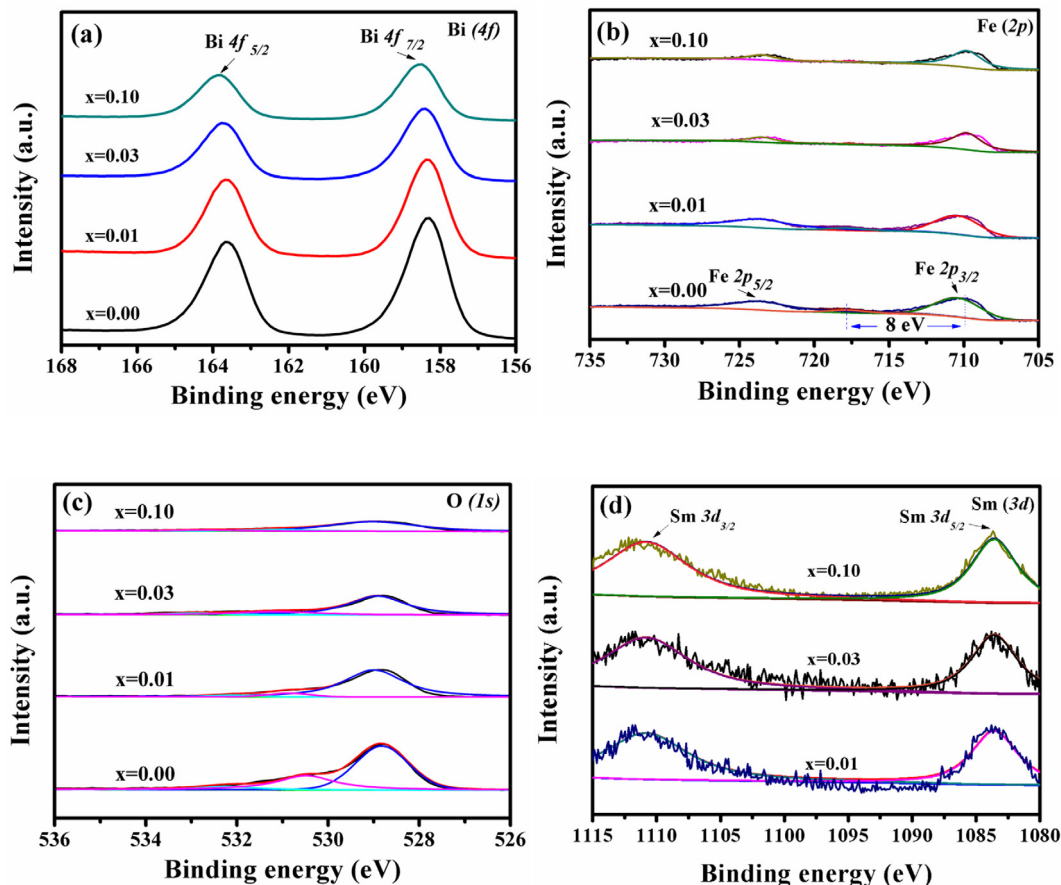
Fig. 6. XPS spectra of (a) Bi, (b) Fe and (c) O elements for BFO, Bi$_{0.99}$Sm$_{0.01}$FeO$_3$, Bi$_{0.97}$Sm$_{0.03}$FeO$_3$ and Bi$_{0.90}$Sm$_{0.10}$FeO$_3$ samples; Sm *3d* XPS spectra (d) for Bi$_{0.99}$Sm$_{0.01}$FeO$_3$, Bi$_{0.97}$Sm$_{0.03}$FeO$_3$ and Bi$_{0.90}$Sm$_{0.10}$FeO$_3$ samples.

that of pure BFO. Moreover, the linear fitting curves of $\ln(C_0/C)$ versus irradiation time (t) (Fig. 9(b)) indicate that the photocatalytic reaction followed pseudo-first-order reaction kinetics, as fitted by the following Langmuir-Hinshelwood model (Eq. (2)) [33]:

$$\ln \frac{C}{C_0} = kt \qquad (2)$$

where C_0 and C are the MO concentration (mg L^{-1}) at different irradiation time of t_0 and t, respectively, and k is the pseudo-first-order rate constant of photodegradation. The corresponding reaction rate constant (k) values were calculated to be 783×10^{-5}, 879×10^{-5}, 1510×10^{-5}, 860×10^{-5}, 835×10^{-5}, and 389×10^{-5} min^{-1} for the x = 0.00, 0.01, 0.03, 0.05, 0.07, and 0.10 sample, respectively (Fig. 9(c)). This further confirms that the Sm^{3+} doping concentration could significantly affect the photocatalytic activity of BFO photocatalyst, and that there was an optimum doping concentration of Sm^{3+} ions in BFO nanoparticles for photocatalytic performances. The discrepancy in photocatalytic activities of as-prepared Bi$_{1-x}$Sm$_x$FeO$_3$ photocatalyst might be attributed to the following reasons. Firstly, for the Sm-doped BFO photocatalysts, the decreased band gap in accompany with the enhanced optical absorption in visible light region imply that the photodegradation efficiency could
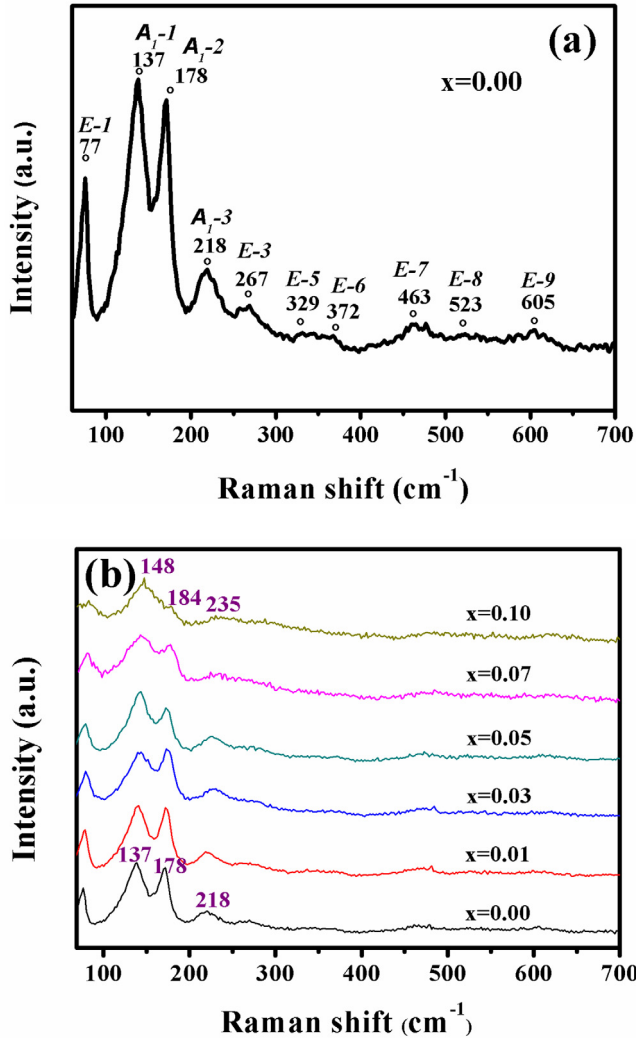
Fig. 7. Raman spectroscopy of (a) pure BFO, and (b) as-prepared Bi$_{(1-x)}$Sm$_x$FeO$_3$ nanoparticles.
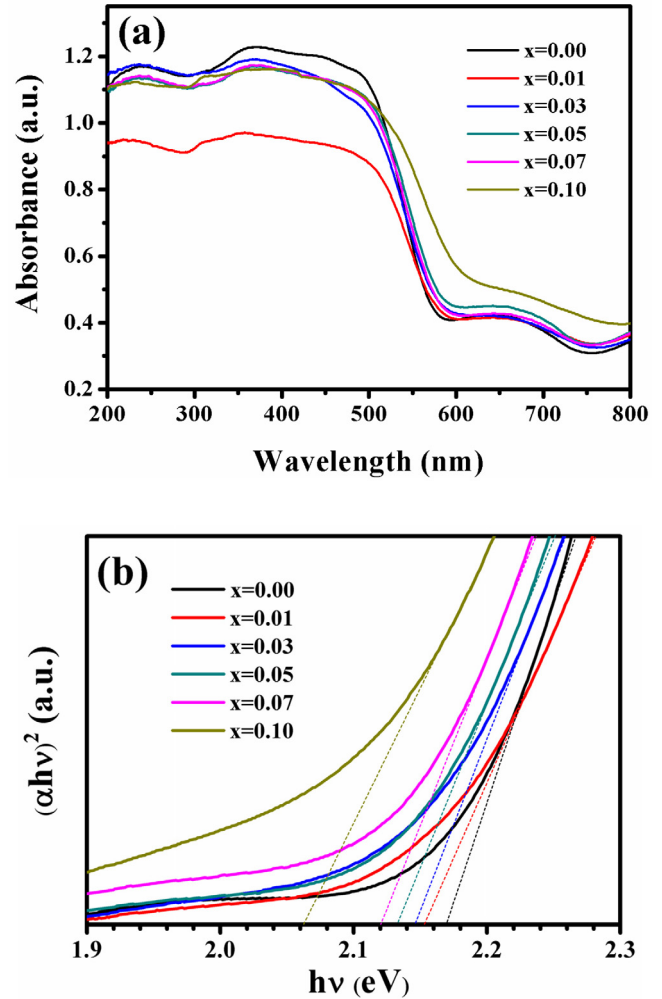
Fig. 8. UV–vis diffuse reflectance spectra of as-prepared samples; (b) The plots to determine the band gaps for the as-prepared Bi$_{(1-x)}$Sm$_x$FeO$_3$ (x = 0.00, 0.01, 0.03, 0.05, 0.07, and 0.10) samples.

Table 2
Raman modes of pure and Sm-doped BFO nanoparticles.

Samples	Assigned modes or frequencies (cm^{-1})									
	A$_1$-1	A$_1$-2	A$_1$-3	E-1	E-3	E-5	E-6	E-7	E-8	E-9
x = 0.00	137	178	218	77	267	329	372	463	523	605
x = 0.01	138	179	221	78	268	330	372	464	524	607
x = 0.03	141	180	225	80	269	331	–	466	524	609
x = 0.05	143	182	229	81	271	–	–	467	526	610
x = 0.07	145	183	231	84	272	–	–	468	–	611
x = 0.10	148	184	235	85	273	–	–	–	–	–

be enhanced consequently because more charge carriers would be probably produced upon visible light irradiation. Secondly, the Sm^{3+} doping could cause a lattice deformation and produce defects in the BFO crystal. As rare earth elements are known to be good electron acceptors [17], the defects derived from Sm dopants would act as trapping sites to capture the excited electron, which would probably facilitate the separation of photogenerated electron-hole pairs and extend the lifetime of charge carriers [34], thus eventually enhancing the photocatalytic activity. However, excess amounts of the Sm^{3+} dopant may act as a recombination center in BFO, thereby resulting in low photoactivity. So it is not a surprise that there was an optimum concentration of Sm dopants in the as-prepared $Bi_{1-x}Sm_xFeO_3$ photocatalysts for MO photodegradation under visible light irradiation.

In practical use, the photocatalyst stability is crucial. To evaluate the stability of Sm-doped BFO photocatalyst, the $Bi_{0.97}Sm_{0.03}FeO_3$ photocatalyst was recycled 5 runs for MO degradation, as shown in Fig. 10(a). The photocatalytic activity of the $Bi_{0.97}Sm_{0.03}FeO_3$ photocatalyst after five runs could be largely maintained, implying a good stability and reusability. Moreover, the XRD patterns (Fig. 10(b)) and UV–Vis DRS spectra (Fig. 10(c)) of the $Bi_{0.97}Sm_{0.03}FeO_3$ sample after 5 run photodegradation of MO were almost the same as those before photodegradation, further confirming the excellent stability, reusability and less photocorrosion of the prepared $Bi_{1-x}Sm_xFeO_3$ photocatalysts.

The photocatalytic degradation of organic pollutants is generally controlled by different kinds of reactive species, such as photo-generated electrons (e^-), photo-generated holes (h^+), hydroxyl radicals ($\cdot OH$) and superoxide radicals ($O_2\cdot^-$) [35]. To elucidate the reaction mechanism over Sm-doped BFO photocatalysts, the trapping experiments were carried out to identify the dominant reactive species of Sm-doped BFO for MO photodegradation. Fig. 11 shows the trapping experimental results over the $Bi_{0.97}Sm_{0.03}FeO_3$ photocatalyst with addition of different reactive species scavengers. The addition of $AgNO_3$ (an electron scavenger [36], 2 mM) could accelerate the MO degradation efficiency, indicating that the consumption of electrons could facilitate the separation of photogenerated electron-hole pairs and hence result in the enhanced photodegradation efficiency. When KI (a hole-scavenger [37], 2 mM) was added, the photodegradation efficiency of MO was significantly decreased to 12.8%, suggesting that the consumption of excited holes could remarkably affect the photodegradation efficiency. When tert-butyl alcohol (TBA, a hydroxyl radicals ($\cdot OH$) scavenger [38], 2 mM) was added, the photodegradation efficiency of MO was slightly suppressed, indicating the minor role of hydroxyl radicals in the MO photodegradation process. Additionally, the addition of benzoquinone (BQ, a superoxide radicals ($O_2\cdot^-$) scavenger [39], 0.5 mM) dramatically suppressed the MO photodegradation efficiency, demonstrating that the superoxide radicals were also of great importance in MO photocatalytic process. Consequently, the dominant reactive species were h^+ and $O_2\cdot^-$ rather than e^- or $\cdot OH$ during the MO photodegradation over the Sm-doped BFO photocatalyst.

On the basis of the above trapping experiments, the photocatalytic mechanism for MO degradation by the Sm-doped BFO photocatalysts under visible light irradiation was proposed. Fig. 12(a) schematically illustrates the energy band structures for pure BFO and Sm-doped BFO. As previously reported [1], the band gap
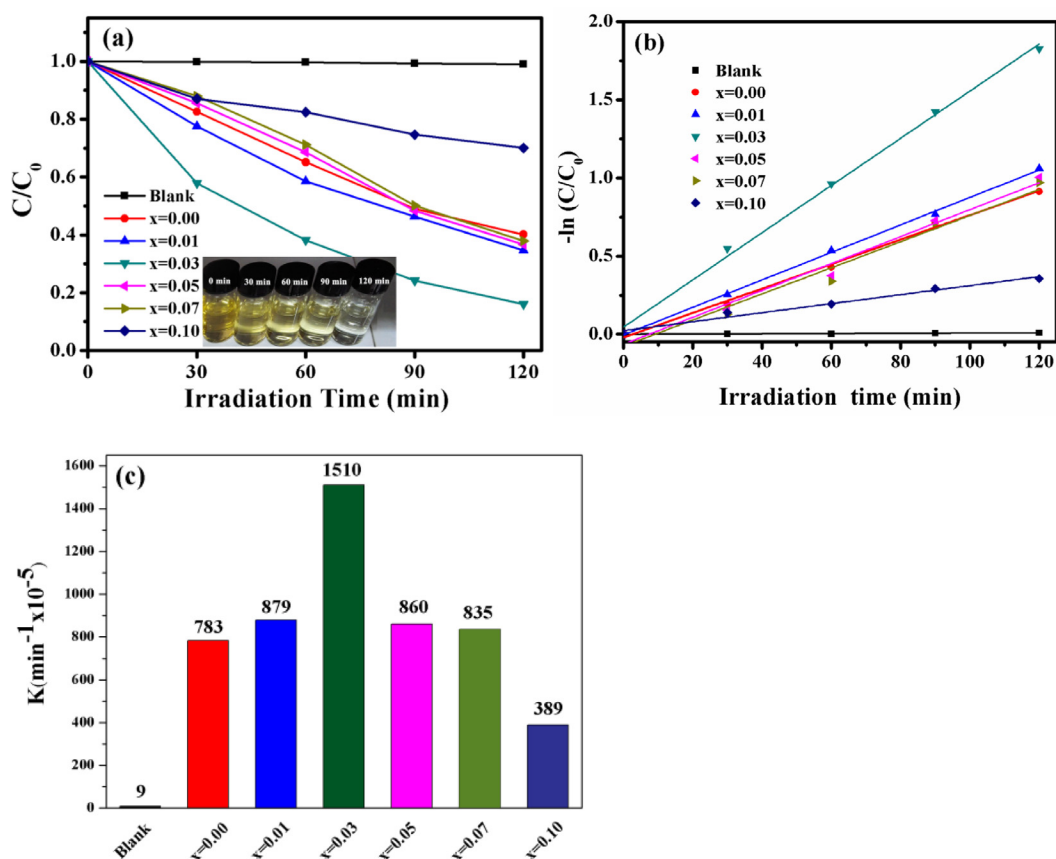
Fig. 9. (a) Photocatalytic degradation of MO as a function of the irradiation time under visible light for the as-prepared photocatalysts; (The inset shows the color change of MO solution during the photodegradation process by the Sm-doped BFO (x = 0.03) sample upon different irradiation time.) (b) Pseudo first order kinetics fitting data, and (c) Rate constant k for the photodegradation of MO over pure BFO and Sm-doped BFO samples. (For interpretation of the references to color in this figure legend, the reader is referred to the web version of this article.)

structure of BFO could be determined by the orbital overlap between the O $2p$ and Fe $3d$ levels. With respect to the Sm-doped BFO photocatalyst, its band gap structure could be modulated by the Sm dopant ions. In Sm-doped BFO, the Sm $4f$ level was located below the conduction band of host BFO [40], which would play as an acceptor lever for photoexcited electrons, as shown in Fig. 12(a). Therefore, compared to the pure BFO, the band gap of Sm-doped BFO would be reduced, which might promote the transport and separation of photogenerated carriers and thus improve the photocatalytic activity. Fig. 12(b) shows the schematic diagram of the proposed photocatalytic mechanism for MO degradation over the Sm-doped BFO photocatalyst under visible light irradiation. Upon the visible light irradiation, the Sm-doped BFO photocatalyst would receive photon energy greater than or equal to its bandgap energy, and hence substantial electron-hole pairs were excited (Eq. (3)) [41]. Subsequently, the photogenerated electrons transferred from the Sm^{3+} dopant level to the photocatalyst surface could react with the surface-adsorbed O_2 to form reactive superoxide radicals $(O_2 \cdot^-)$ (Eq. (4)), which could further participate in the photocatalytic degradation of MO (Eq. (6)). Simultaneously, the holes after migrating to the photocatalyst surface could react with H_2O to form $\cdot OH$ (Eq. (5)) for the degradation of MO (Eq. (7)) or directly oxidize MO (Eq. (8)). On the basis of the trapping experiments, superoxide radicals $(O_2 \cdot^-)$ and holes (h^+) were the predominant reactive species for MO degradation (Eqs. (6) and (8)), while hydroxyl radicals $(\cdot OH)$ might also contribute a little to the MO degradation process (Eq. (7)). The proposed photocatalytic mechanism of Sm-doped BFO for MO degradation could be described as follows:

$$Bi_{(1-x)}Sm_{(x)}FeO_3 + h\nu \rightarrow e^- (Sm\ dopant\ level) + h^+ \quad (3)$$

$$e^- (Sm\ dopant\ level) + O_2 \rightarrow O_2^- \quad (4)$$

$$h^+ + H_2O \rightarrow \cdot OH \quad (5)$$

$$O_2^- + MO \rightarrow degradation\ products \quad (6)$$

$$\cdot OH + MO \rightarrow degradation\ products \quad (7)$$

$$h^+ + MO \rightarrow degradation\ products \quad (8)$$
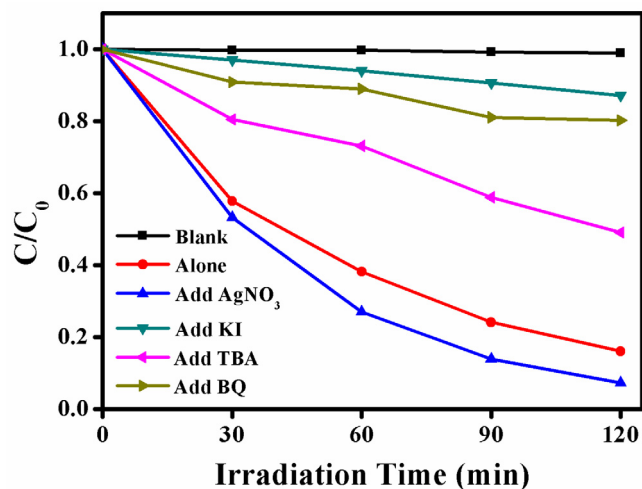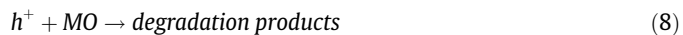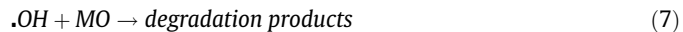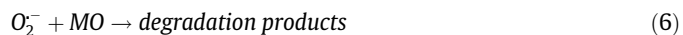
Fig. 11. Photodegradation of MO over the $Bi_{0.97}Sm_{0.03}FeO_3$ sample alone, and with the addition of different types of active species scavengers (i.e., $AgNO_3$, KI, TBA, or BQ).
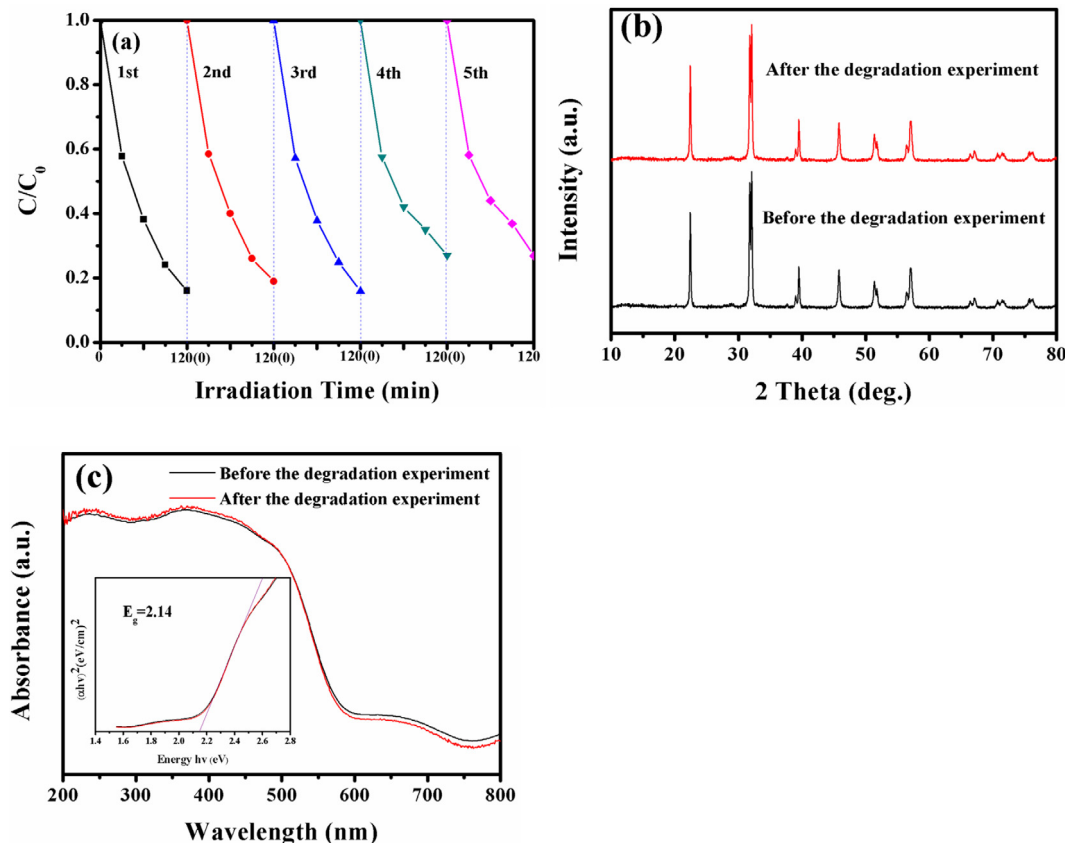
Fig. 10. (a) Photodegradation performance for MO with the $Bi_{0.97}Sm_{0.03}FeO_3$ sample for five cycles; (b) XRD patterns and (c) UV-DRS spectra (Insets are the plots to determine the band gaps) of the $Bi_{0.97}Sm_{0.03}FeO_3$ sample before and after the photocatalytic degradation experiments for five cycles.
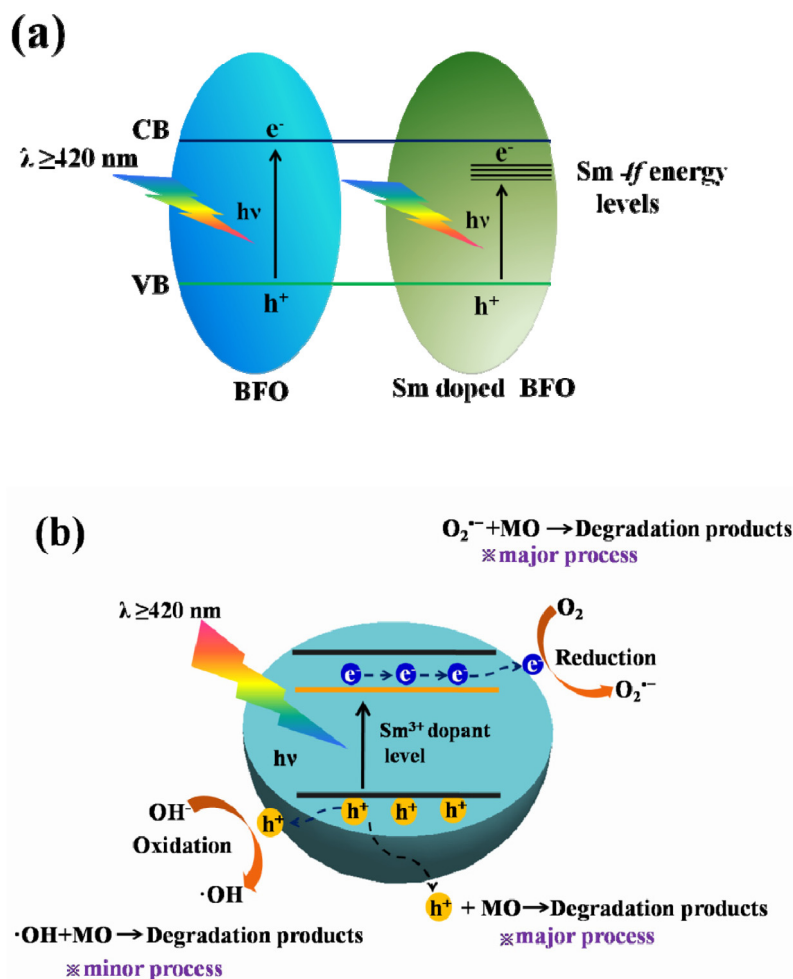
Fig. 12. (a) Schematic diagram of energy band structure for pure BFO and Sm-doped BFO; (b) Schematic illustration of the mechanism for the photocatalytic degradation of MO on the Sm-doped BFO photocatalyst.

4. Conclusions

In summary, Sm-doped BFO ($Bi_{1-x}Sm_xFeO_3$ (x = 0, 0.01, 0.03, 0.05, 0.07, 0.10)) nanoparticles containing different Sm doping concentrations were prepared by a sol-gel method, and the effect of Sm doping concentration on their photocatalytic properties was studied for the first time. The XRD, Raman and XPS measurements confirmed the successful substitution of Sm^{3+} in the BFO crystal structure. The UV–vis DRS spectra manifested that the band gap of the $Bi_{(1-x)}Sm_xFeO_3$ nanoparticles decreased when increasing Sm doping concentration. The photocatalytic experiments demonstrated that the photocatalytic performances of the $Bi_{1-x}Sm_xFeO_3$ photocatalysts were significantly affected by the Sm doping concentration. With increasing Sm doping concentration from 0% to 10%, the MO photodegradation efficiency of $Bi_{1-x}Sm_xFeO_3$ photocatalysts first increased and then decreased. When the Sm doping concentration was 3%, the optimal photocatalytic degradation efficiency was achieved. The optimal photocatalytic performance of the $Bi_{0.97}Sm_{0.03}FeO_3$ photocatalyst may be ascribed to the increased optical absorption as well as the efficient migration and separation of photogenerated electron-hole pairs derived from Sm dopant trapping level in BFO. On the basis of the trapping experiments, the predominant reactive species in the photocatalytic process were photogenerated holes and superoxide radicals (O_2·$^-$) rather than photogenerated electrons or hydroxyl radicals (·OH), and the photocatalytic mechanism was also proposed. The present work may promote understanding of scientific aspects of

Sm doping in oxide photocatalysts, and the significantly improved photocatalytic performance of Sm-doped BFO nanoparticles suggests its promising applications in water treatment and environmental remediation.

References

[1] G. Catalan, J.F. Scott, Physics and applications of bismuth ferrite, Adv. Mater. 21 (2009) 2463–2485.
[2] W. Ji, K. Yao, Y.F. Lim, Y.C. Liang, A. Suwardi, Epitaxial ferroelectric BiFeO₃ thin films for unassisted photocatalytic water splitting, Appl. Phys. Lett. 103 (2013) 062901.
[3] B.F. Gao, X.Y. Chen, K.B. Yin, S. Dong, Z.F. Ren, F. Yuan, T. Yu, Z.G. Zou, J.M. Liu, Visible-light photocatalytic properties of weak magnetic BiFeO₃ nanoparticles, Adv. Mater. 19 (2007) 2889–2892.
[4] S. Li, Y.H. Lin, B.P. Zhang, Y. Wang, C.W. Nan, Controlled fabrication of BiFeO₃ uniform microcrystals and their magnetic and photocatalytic behaviors, J. Phys. Chem. C 114 (2010) 2903–2908.
[5] I. Grinberg, D.V. West, M. Torres, G.Y. Gou, D.M. Stein, L.Y. Wu, G. Chen, E.M. Gallo, A.R. Akbashev, P.K. Davies, J.E. Spanier, A.M. Rappe, Perovskite oxides for

visible light absorbing ferroelectric and photovoltaic materials, Nature 503 (2013) 509–512.

[6] R. Das, G.G. Khan, S. Varma, G.D. Mukherjee, K. Mandal, Effect of quantum confinement on optical and magnetic properties of Pr-Cr-codoped bismuth ferrite nanowires, J. Phys. Chem. C 117 (2013) 20209–20216.

[7] B.D. Kan, L.P. Lova, V. Anbusathaiah, C.J. Cheng, S. Fujino, V. Nagarajan, K.M. Rabe, I. Takeuchi, Universal behavior and electric-field-induced structural transition in rare earth substituted BiFeO₃, Adv. Funct. Mater. 20 (2010) 1108–1115.

[8] S. Mohan, B. Subramanian, I. Bhaumik, P.K. Gupta, S.N. Jaisankar, Nanostructured $Bi_{(1-x)}Gd_{(x)}FeO_3$ – a multiferroic photocatalyst on its sunlight driven photocatalytic activity, RSC Adv. 4 (2014) 16871–16878.

[9] Y.L. Pei, C.L. Zhang, Effect of ion doping in different sites on the morphology and photocatalytic activity of BiFeO₃ microcrystals, J. Alloys. Compd. 570 (2013) 57–60.

[10] M. Sakar, S. Balakumar, P. Saravanan, S. Bharathkumar, Compliments of confinements: substitution and dimension induced magnetic origin and band-bending mediated photocatalytic enhancements in $Bi_{1-x}Dy_xFeO_3$ particulate and fiber nanostructures, Nanoscale 7 (2015) 10667–10679.

[11] N. Zhang, D. Chen, F. Niu, S. Wang, L.S. Qin, Y.X. Huang, Enhanced visible light photocatalytic activity of Gd-doped BiFeO₃ nanoparticles and mechanism insight, Sci. Rep. 6 (2016) 26467.

[12] S.X. Wu, J.Z. Fang, X.X. Xu, Z. Liu, X.M. Zhu, W.C. Xu, Microemulsion synthesis, characterization of highly visible light responsive rare earth-doped Bi₂O₃, Photochem. Photobiol. 88 (2012) 1205–1210.

[13] S. Pattanayak, R.N.P. Choudhary, P.R. Das, Effect of Sm-substitution on structural, electrical and magnetic properties of BiFeO₃, Electron. Mater. Lett. 10 (2014) 165–172.

[14] K.S. Nalwa, A. Garg, A. Upadhyaya, Effect of samarium doping on the properties of solid-state synthesized multiferroic bismuth ferrite, Mater. Lett. 62 (2008) 878–881.

[15] C. Anthonyraj, M. Muneeswaran, S. Gokul Raj, N.V. Giridharan, V. Sivakumar, G. Senguttuvan, Effect of samarium doping on the structural, optical and magnetic properties of sol–gel processed BiFeO₃ thin films, J. Mater. Sci.: Mater. Electron. 26 (2015) 49–58.

[16] J. Thomas, K.P. Kumar, S. Mathew, Hydrothermal synthesis of samarium doped nanotitania as highly efficient solar photocatalyst, Sci. Adv. Mater. 2 (2010) 481–488.

[17] J.K. Reddy, B. Srinivas, V.D. Kumari, M. Subrahmanyam, Sm^{3+}-doped Bi₂O₃ photocatalyst prepared by hydrothermal synthesis, ChemCatChem 1 (2009) 492–496.

[18] J. Liu, L. Fang, F.G. Zheng, S. Ju, M.R. Shen, Enhancement of magnetization in Eu doped BiFeO₃ nanoparticles, Appl. Phys. Lett. 95 (2009) 022511.

[19] T.D. Rao, R. Ranjith, S. Asthana, Enhanced magnetization and improved insulating character in Eu substituted BiFeO₃, J. Appl. Phys. 115 (2014) 124110.

[20] A.C. Larson, R.B. Von Dreele, General Structure Analysis System technical manual LANSCE, MS-H805, Los Almos National Laboratory LAUR (2000) 86–748.

[21] T.D. Nguyen, D. Mrabet, T.O. Do, Controlled self-assembly of Sm₂O₃ nanoparticles into nanorods: simple and large scale synthesis using bulk Sm₂O₃ powders, J. Phys. Chem. C 112 (2008) 15226–15235.

[22] F. Niu, D. Chen, L.S. Qin, N. Zhang, J.Y. Wang, Z. Chen, Y.X. Huang, Facile synthesis of highly efficient p–n heterojunction CuO/BiFeO₃ composite photocatalysts with enhanced visible-light photocatalytic activity, ChemCatChem 7 (2015) 3279–3289.

[23] P.S.V. Mocherla, C. Karthik, R. Ubic, M.S.R. Rao, C. Sudakar, Tunable bandgap in BiFeO₃ nanoparticles: the role of microstrain and oxygen defects, Appl. Phys. Lett. 103 (2013) 022910.

[24] Y.B. Ding, F. Yang, L.H. Zhu, N. Wang, H.Q. Tang, Bi^{3+} self doped NaBiO₃ nanosheets: facile controlled synthesis and enhanced visible light photocatalytic activity, Appl. Catal. B 164 (2015) 151–158.

[25] R.Q. Guo, L. Fang, W. Dong, F.G. Zheng, M.G. Shen, Enhanced photocatalytic activity and ferromagnetism in Gd doped BiFeO₃ nanoparticles, J. Phys. Chem. C 114 (2010) 21390–21396.

[26] R. Haumont, J. Kreisel, P. Bouvier, F. Hippert, Phonon anomalies and the ferroelectric phase transition in multiferroic BiFeO₃, Phys. Rev. B 73 (2006) 132101.

[27] H. Fukumura, H. Harima, K. Kisoda, M. Tamada, Y. Noguchi, M. Miyayam, Raman scattering study of multiferroic BiFeO₃ single crystal, J. Magn. Magn. Mater. 310 (2007) 367–369.

[28] A. Jaiswal, R. Das, K. Vivekanand, P.M. Abraham, S. Adyanthaya, P. Poddar, Effect of reduced particle size on the magnetic properties of chemically synthesized BiFeO₃ nanocrystals, J. Phys. Chem. C 114 (2010) 2108–2115.

[29] T.J. Park, G.C. Papaefthymiou, A.J. Viescas, A.R. Moodenbaugh, S.S. Wong, Size-dependent magnetic properties of single-crystalline multiferroic BiFeO₃ nanoparticles, Nano. Lett. 7 (2007) 766–772.

[30] M. Arora, P.C. Sati, S. Chauhan, H. Singh, K.L. Yadav, S. Chhoker, M. Kumar, Structural, magnetic and optical properties of $Bi_{1-x}Dy_xFeO_3$ nanoparticles synthesized by sol-gel method, Mater. Lett. 96 (2013) 71–73.

[31] L.F. Fei, J.K. Yuan, Y.M. Hu, C.Z. Wu, J.L. Wang, Y. Wang, Visible light responsive perovskite BiFeO₃ pills and rods with dominant $\{111\}_c$ facets, Cryst. Growth Des. 11 (2011) 1049–1053.

[32] M. Arora, M. Kumar, Structural, magnetic and optical properties of Ce substituted BiFeO₃ nanoparticles, Ceram. Int. 41 (2015) 5705–5712.

[33] J.C. Yu, J.G. Yu, W.K. Ho, Z.T. Jiang, L.Z. Zhang, Effects of F- doping on the photocatalytic activity and microstructures of nanocrystalline TiO₂ powders, Chem. Mater. 14 (2002) 3808–3816.

[34] W. Choi, A. Termin, M.R. Hoffmann, The role of metal ion dopants in quantum-sized TiO₂: correlation between photoreactivity and charge carrier recombination dynamics, J. Phys. Chem. 9 (1994) 13669–13679.

[35] A.W. Xu, Y. Gao, H.Q. Liu, The preparation, characterization, and their photocatalytic activities of rare-earth-doped TiO₂ nanoparticles, J. Catal. 207 (2002) 151–157.

[36] W.J. Li, D.Z. Li, Y.M. Lin, P.X. Wang, W. Chen, X.Z. Fu, Y. Shao, Evidence for the active species involved in the photodegradation process of methyl orange on TiO₂, J. Phys. Chem. C 116 (2012) 3552–3560.

[37] R. Palominos, J. Freer, M.A. Mondaca, H.D. Mansilla, Evidence for hole participation during the photocatalytic oxidation of the antibiotic flumequine, J. Photochem. Photobiol. A 193 (2008) 139–145.

[38] K.L. Lv, Y.M. Xu, Effects of polyoxometalate and fluoride on adsorption and photocatalytic degradation of organic dye X3B on TiO₂: the difference in the production of reactive species, J. Phys. Chem. B 110 (2006) 6204–6212.

[39] Y.C. Huang, H.B. Li, M.S. Balogun, W.Y. Liu, Y.X. Tong, X.H. Lu, H.B. Ji, Oxygen vacancy induced bismuth oxyiodide with remarkably increased visible-light absorption and superior photocatalytic performance, ACS Appl. Mater. Interfaces 6 (2014) 22920–22927.

[40] N.H. Hong, Tuning magnetic properties of BiFeO₃ thin films by controlling rare-earth doping: experimental and first-principles studies, J. Phys. Chem. C 119 (2015) 14351–14357.

[41] Z.Y. Wang, Y.Y. Liu, B.B. Huang, Y. Dai, Z.Z. Lou, G. Wang, X.Y. Zhang, X.Y. Qin, Progress on extending the light absorption spectra of photocatalysts, Phys. Chem. Chem. Phys. 16 (2014) 2758–2774.
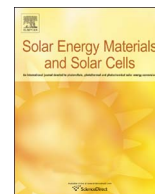
Contents lists available at ScienceDirect

Solar Energy Materials and Solar Cells

Defective BiFeO$_3$ with surface oxygen vacancies: Facile synthesis and mechanism insight into photocatalytic performance

CrossMark

Da Chen, Feng Niu, Laishun Qin*, Sen Wang, Ning Zhang, Yuexiang Huang*

College of Materials Science and Engineering, China Jiliang University, Hangzhou 310018, Zhejiang, PR China

ARTICLE INFO

ABSTRACT

Oxygen vacancies particularly for those located on the photocatalyst surface are believed to play an important role in its photocatalytic process. In this work, surface oxygen vacancies were introduced into hydrothermally-synthesized BiFeO$_3$ (BFO) nanocrystals through high pressure hydrogenation treatment, and with increasing hydrogenation temperature the oxygen vacancy concentration would increase. The X-ray diffraction (XRD) results indicated no pronounced structure change when the hydrogenation temperature was below 200 °C. The formation of surface oxygen vacancies on BFO nanocrystals was verified by a variety of techniques such as high-resolution transmission electron microscopy (HRTEM), X-ray photoelectron spectroscopy (XPS), electron paramagnetic resonance (EPR) and Kelvin probe force microscopy (KPFM). The hydrogenated BFO nanocrystals exhibited nearly four times methyl orange (MO) photodegradation efficiency higher than pristine BFO under visible light irradiation, and the inherent correlation between surface oxygen vacancies and enhanced photocatalytic activity was established. Our findings demonstrate that the formation of surface oxygen vacancies on the hydrogenated BFO nanocrystals could narrow the band gap of BFO resulting in the improved light absorption capability, act as trapping centers for photoinduced electrons thus to facilitate the separation of the photogenerated electron-hole pairs as well as the production of predominant active species (hydroxyl radicals) for MO photodegradation, suppress the recombination of photogenerated electrons and holes, and also favor the adsorption of MO molecules. All these factors could contribute to the observed enhanced photocatalytic activity of the hydrogenated BFO nanocrystals for MO degradation. In addition, the as-formed surface oxygen vacancies were also stable at room temperature.

1. Introduction

The interest of developing semiconductor metal oxides as photocatalysts for environmental purification and solar energy conversion arises from their good chemical stability, simplicity of synthesis, and relatively low cost [1]. For example metal oxide photocatalysts including TiO$_2$ [2], ZnO [3], WO$_3$ [4], BiVO$_4$ [5], Fe$_2$O$_3$ [6] have been explored for applications in removal or degradation of environmental pollutants, splitting water to generate hydrogen energy and reducing carbon dioxide to fuel molecules. Bismuth ferrite (BiFeO$_3$, noted as BFO), which is well-recognized as a multiferroic material used in multiferroic memories [7], has been considered as a potential photocatalyst largely due to its narrow band gap (~ 2.5 eV) [8]. In contrast to the wide band gap (~ 3.2 eV) of the most-investigated TiO$_2$ photocatalyst which can only respond to ultraviolet irradiation, the narrow band gap of BFO allows its visible light response to be possible which apparently will increase solar light harvesting efficiency. In fact, the visible light photocatalytic activities of BFO for organic pollutants

degradation have been already demonstrated in recent reports [9–11]. However, the photocatalytic efficiency of BFO is still low. This is largely attributed to the poor carrier mobility in BFO material which limits the separation and transport efficiency of photo-induced electron/hole carriers. Therefore, further improving the photocatalyitc activity of BFO materials is still a big challenge.

It is widely recognized that oxygen vacancies especially for those located in particle surfaces would play an important role in photocatalytic process [12]. Mao and co-workers [13] used a high pressure hydrogenation process to yield a disorder layer on TiO$_2$ nanoparticle surface where substantial oxygen vacancies were formed. The obtained black TiO$_2$ demonstrated considerable solar-driven hydrogen evolution capability from water splitting. Wang et al. [14] used a simple heat treatment process to prepare oxygen vacancy-rich ZnO nanocrystals. The presence of oxygen vacancies in ZnO led to a narrow band gap and thus facilitate its visible light absorption. Lv and co-workers [15] reported that the introduction of oxygen vacancies in BiPO$_4$ nanorods by a vacuum deoxidation process could broaden the valence band, thus

* Corresponding authors.
  E-mail addresses: qinlaishun@cjlu.edu.cn (L. Qin), yuexiang65@hotmail.com (Y. Huang).

leading to an enhanced photocatalytic performance. Recently Tan et al. [16] also introduced oxygen vacancies into pervoskite $SrTiO_3$ nanocrystals using $NaBH_4$ as a reducing agent, and further confirmed the favorable effect of oxygen vacancies on the photocatalytic activity. Though the favorable effect of oxygen vacancies on photocatalytic activity have been observed in various metal oxides, it is important to note that the understanding of such a favorable effect is still very poor, especially for the relationship between oxygen vacancies and photocatalytic activities.

Herein, surface oxygen vacancies were introduced into hydrothermally-synthesized BFO nanocrytals by a high pressure hydrogenation process. The presence and enhanced density of surface oxygen vacancies by hydrogenation were then verified via various characterization techniques. The inherent correlation between surface oxygen vacancies and photocatalytic activities of the hydrogenated BFO nanocrystals for the first time was established.

2. Experimental

2.1. Hydrothermal synthesis of BiFeO₃ nanoparticles

All chemicals were of analytical grade without any further purification. BFO nanoparticles were synthesized through a hydrothermal process. Typically, bismuth nitrate ($Bi(NO_3)_3 \cdot 5H_2O$) and ferric nitrate ($Fe(NO_3)_3 \cdot 9H_2O$) with a stoichiometric ratio were dissolved in distilled water. The NaOH aqueous solution (7.5 M) was dropwisely added into the mixed solution at a rate of 1 mL min^{-1} through a burette to get a yellowish-brown-colored precipitate. After being washed with distilled water and ethyl alcohol several times, dried in an oven at 70 °C for 5 h and ground by a pestle and mortar, the precipitate was dispersed in polyvinyl pyrrolidone (PVP) aqueous solution under stirring, and the stirring was kept for 10 h to obtain a suspension. 3 M NaOH solution as a mineralizer was then added to the above suspension, and finally the mixed suspension was transferred into a hydrothermal reactor. The reactor was then sealed and maintained at 200 °C for 3 h. After being cooled down to room temperature, the process of filtration, washing with distilled water and drying in an oven at 80 °C for 12 h was operated to obtain BFO nanoparticles.

2.2. Hydrogenation of BiFeO₃ nanoparticles

Hydrogenation of BFO nanoparticles was performed in a hydrogenation furnace. 1 g of as-prepared $BiFeO_3$ powder was put in a stainless steel reactor which was then connected to the vacuum system. After being evacuated by a vacuum pump to 10 Pa, the reactor was heated to a given temperature at a heating rate of 5 °C min^{-1} and then was filled with hydrogen (purity higher than 99.99%) at a pressure of 2.0 MPa. After being kept for 8 h, the high pressure hydrogen was relieved and the BFO sample was taken out from the reactor after the reactor was cooled down to room temperature. The as-hydrogenated BFO samples were denoted as HB-T-P-t, where T, P and t were the reaction temperature (T = 120, 150, 180, 200 °C), pressure (P = 2.0 MPa) and hydrogenation time (t = 8 h), respectively.

2.3. Characterizations

X-ray powder diffraction (XRD) was performed on a Bruker D2 X-ray diffractometer using Cu Kα radiation. The UV–visible diffuse reflectance spectra (UV–vis DRS) of the samples were recorded on a UV–visible spectrophotometer (Shimadzu UV-3600) equipped with an integrating sphere. High resolution transmission electron microscopy (TEM) was operated on a field emission transmission electron microscope (JEOL, JEM-2100) at an accelerating voltage of 200 kV. The chemical states present in BFO and the hydrogenated samples were analyzed using a PHI 5000 Versa Probe X-ray photoelectron spectrometer with Al Kα radiation, and C 1s (284.6 eV) was used to calibrate

the peak position. In situ electron paramagnetic resonance (EPR) was recorded at ambient temperature on a Bruker EPR A300 spectrometer. Kelvin probe force microscopy (KPFM) experiments were performed at room temperature and under ambient conditions using an Atomic Force Microscope (Veeco Multimode V). A conductive Co/Cr-coated tip with a resonant frequency of 75 kHz and a spring constant of 2.8 N/m (MESP cantilever, Bruker) was used for KPFM measurement in noncontact mode operation. For KPFM experiments, the sample powder was carefully dispersed on the surface of precleaned ITO conductive glass. Thermogravimetric analysis (TGA) was carried out in a temperature range of 25–800 °C under flowing O_2 with a heating rate of 10 °C min^{-1} on a Mettler Toledo SMP/PF7458/MET/600 W instrument. Room temperature photoluminescence (PL) spectra were recorded on a Hitachi High-Tech F-7000 fluorescence spectrophotometer with a xenon lamp as an excitation source (Excitation wavelength λ = 404 nm).

2.4. Photoelectrochemical evaluation

The photocatalytic activities of pristine BFO and hydrogenated BFO samples were evaluated by monitoring the photocatalytic degradation of methyl orange (MO) in aqueous solutions under visible light irradiation under a neutral pH condition. A 300 W Xe lamp equipped with an optical filter (λ ≥ 420 nm) was employed as the visible light source. An amount of 0.3 g of the catalyst was added into 100 mL of 5 mg L^{-1} MO solution in a quartz glass reactor, which was cooled by refluxing water to prevent any thermal catalytic effect. The photoreaction vessel was then exposed to visible light irradiation under ambient conditions with an average intensity of 15 mW cm^{-2} produced by a 300-W Xenon lamp equipped with an optical filter (λ ≥ 420 nm), which was positioned 25 cm away from the vessel. The irradiance intensity was measured by a radiometer (FZ-A, Photoelectric Instrument Factory of Beijing Normal University, China). Before the light irradiation, the suspension was ultrasonically dispersed in dark for 30 min and then magnetically stirred for 30 min to achieve the adsorption-desorption equilibrium. At given time intervals, 4 mL of suspension was collected and centrifuged at 10,000 rpm for 30 min to remove the catalyst powders. To estimate the degradation efficiency, the absorbancy of the supernatant was detected by measuring the maximum absorbance at 464 nm using a spectrophotometer (model: 722, Precision Instruments Co., Ltd. Shanghai, China).

For photocurrent measurements, the working photoelectrodes were fabricated by doctor blading a slurry, which was prepared by mixing the obtained photocatalyst powder and a polymer binder (PVDF) at a weight ratio of 90:10 using N-methyl-2-pyrrolidinone (NMP) as a solvent, on F-doped SnO_2 (FTO) conductive glass with an active area of 1.0 × 2.0 cm^2, followed by drying in vacuum at 60 °C for 24 h. Photocurrent measurements were recorded on a CHI660E electrochemical station at 0.0 V potential bias (vs. SCE) using the standard three electrode system with the working photoelectrode, a saturated calomel electrode (SCE) as the reference electrode, and a platinum wire as counter electrode in 0.5 M Na_2SO_4 aqueous solution under visible light (λ ≥ 420 nm) irradiation.

3. Results and discussion

3.1. Structure evolution

Fig. 1 shows the XRD patterns of the BFO nanoparticles before and after high pressure hydrogenation under different temperatures. It can be seen that all diffraction peaks of the pristine BFO nanoparticles could be indexed by a rhombohedral phase with the space group $R3c$ (JCPDS no. 86-1518), indicating that single crystalline BFO phase was obtained by the present hydrothermal process. Such a BFO crystal structure would be maintained when the hydrogenation temperature was below 200 °C. When the hydrogenation temperature was increased to 200 °C,
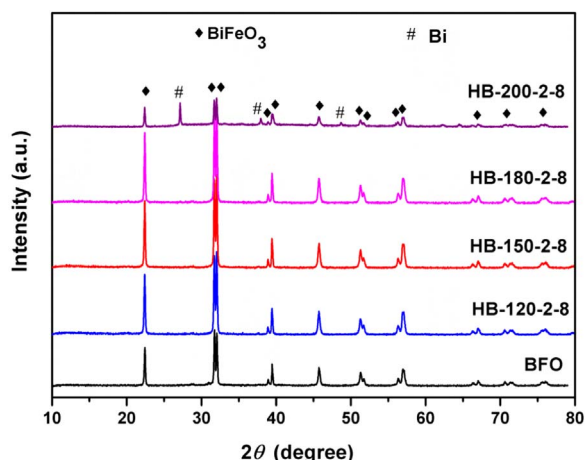
Fig. 1. XRD patterns of pristine BFO and samples hydrogenated under different temperature.

however, the predominant BFO phase with a trace of Bi crystalline phase was observed. This indicates that the reduction of BFO particles took place when they were hydrogenated under 2.0 MPa hydrogen pressure and 200 °C temperature for 8 h.

Fig. 2 shows the TEM and high-resolution TEM (HRTEM) images of the pristine and as-hydrogenated BFO particles (HB-180-2-8). As shown in Fig. 2(a), the pristine BFO particles exhibited a spherical morphology with a size of around 20 nm. After hydrogenation (Fig. 2(c)), no significant change in particle morphology and size was observed. However comparing with the HRTEM images in Fig. 2(b) and (d), a disordered layer with ~ 1.0 nm thickness was clearly observed on the as-hydrogenated BFO nanocrystals while it was still highly crystalline inside the BFO nanocrystals. This indicates that the present hydrogenation

treatment would mainly change the surface structures of BFO nanocrystals rather than inside parts. The measured crystal interplanar spacing was 0.396 nm for both pristine Fig. 2(b) and hydrogenated BFO nanocrystals Fig. 2(d), further verifying that hydrogenation would not alter the inside part of BFO nanocrystals.

3.2. Oxygen vacancies

Among all possible defects present on the surface of metal oxides, oxygen vacancy is supposed to be the prevalent defect, which is generally one of the most important defects in determining the surface related material properties including photocatalysis [17]. Considering that the reduction reaction of Bi^{3+} or Fe^{3+} by hydrogen would be certainly associated with the formation of oxygen vacancies according to defect chemistry, it is reasonable to assume that oxygen vacancies are the predominant defects formed on BFO nanocrystal surfaces during the hydrogenation process. Since the formation of oxygen vacancy is generally associated with changes in chemical states of Bi and Fe in BFO nanocrytals, the X-ray photoelectron spectroscopy (XPS) was employed to monitor such a change. Fig. 3(a) and (b) give the high resolution spectra of Bi 4f and Fe 2p of the pristine and hydrogenated BFO samples, respectively. In Fig. 3(a), the two peaks of pristine BFO centered at around 157.9 and 163.2 eV could be identified as the binding energies of Bi $4f_{7/2}$ and Bi $4f_{5/2}$, respectively, which is correlated to the Bi^{3+} valence state [18]. In Fig. 3(b), the binding energies of Fe 2p corresponding to the Fe $2p_{3/2}$ and Fe $2p_{1/2}$ peaks with a satellite peak indicates that the Fe element was in the Fe^{3+} valence state in the pristine BFO [19]. After hydrogenation treatment, however, some peak shifts to high binding energy were observed for both Bi and Fe spectra. The shift of these XPS peaks could be generally ascribed to the formation of oxygen vacancy which would increase the equilibrium electron density and thus make the binding energies increase [16]. Meanwhile, the peak shift of both Bi and Fe to high binding energy would gradually
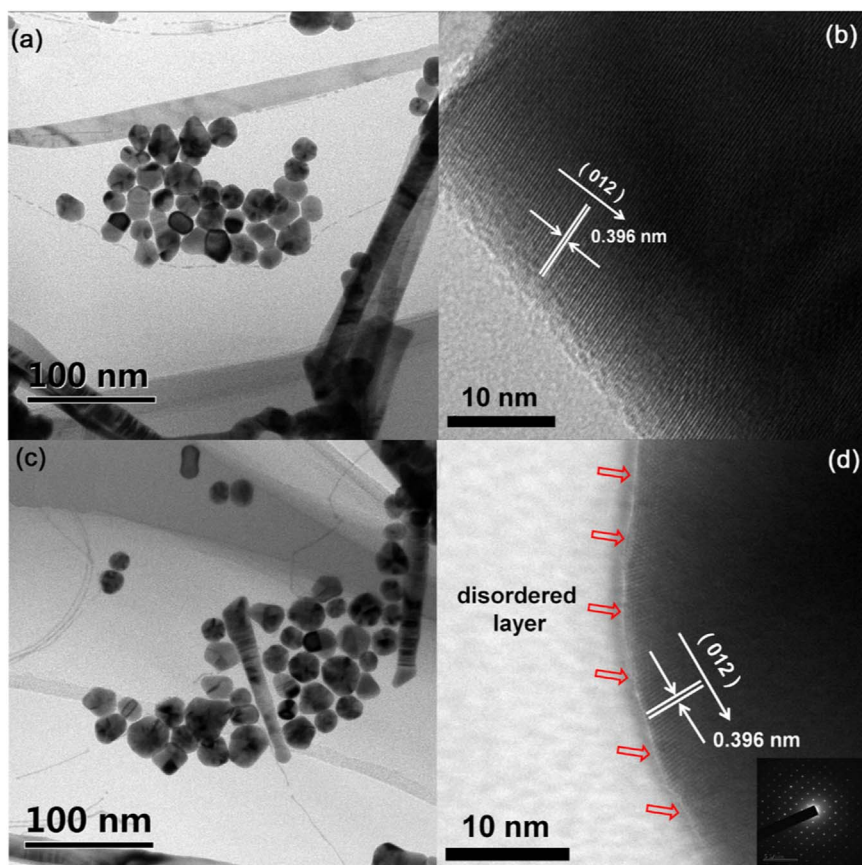

Fig. 2. TEM and HRTEM images of pristine BFO (a, b) and HB-180-2-8 (c, d). The inset in (d) is the electron diffraction patterns of HB-180-2-8, suggesting the high crystallinity of the bulk, and the red arrows in (d) indicate the disordered layer at the boundary of crystalline.
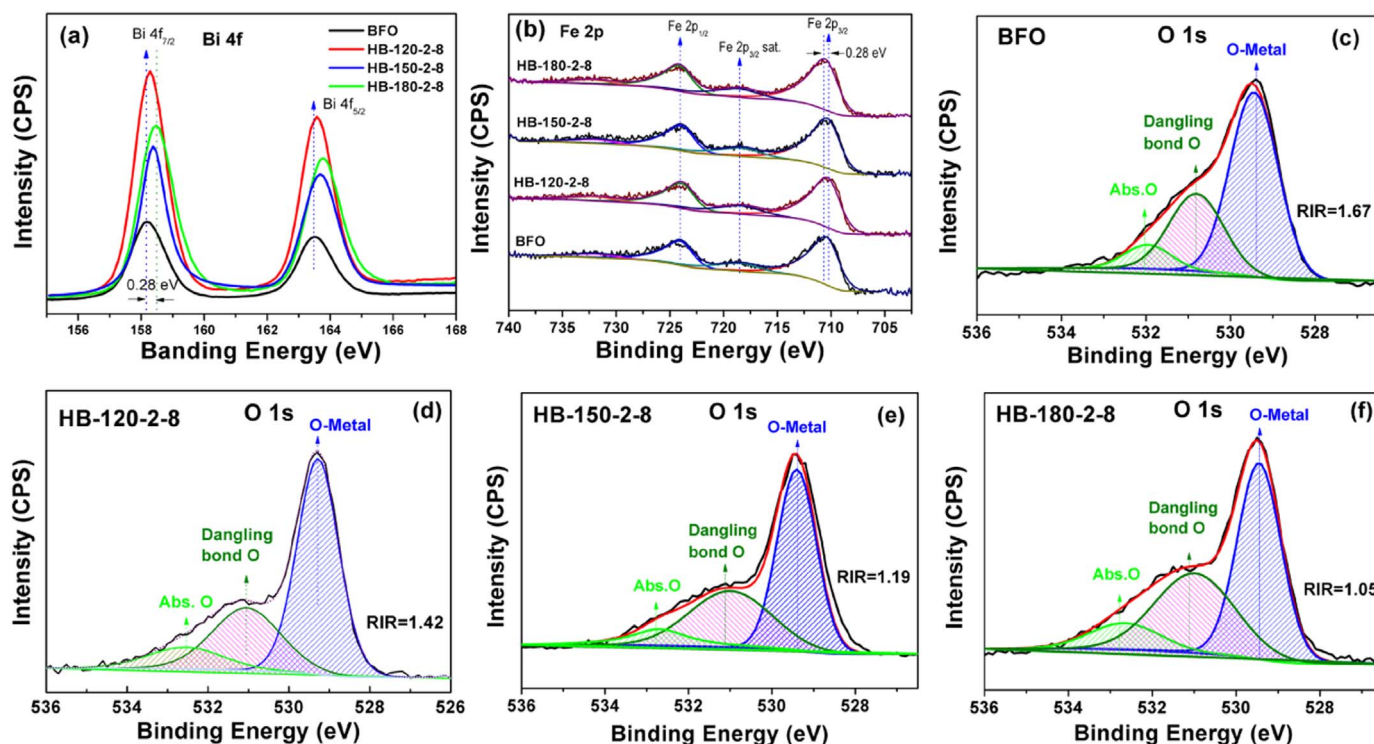
Fig. 3. High resolution XPS of (a) Bi 4f and (b) Fe 2p for the pristine and as-hydrogenated BFO samples, respectively; (c)–(f) O 1s core-level XPS spectra for different samples along with the splitted peaks and calculated relative intensity ratio (RIR) of lattice oxygen / (dangling bonds and adsorptional oxygen).

aggrandize with the increase hydrogenation temperature, and the largest shift of about 0.28 eV was observed for the HB-180-2-8 sample. Fig. 3(c)–(f) show the O 1s core-level XPS spectra for the pristine and hydrogenated BFO samples. It is seen that all O 1s spectra showed three peaks. The major peak located at around 529.0 eV could be associated with the lattice oxygen in BFO, which is the characteristic of chemical bonding between metal and oxygen atom, while the smaller two peaks located at around 531.2 eV and 532.4 eV were corresponding to the dangling bonds and surface adsorption oxygen, respectively [20,21]. Generally, the presence of the dangling bonds and absorbed species (O$^-$, O$_2^-$, and O^{2-}) in XPS spectra were supposed to be due to the formation of surface oxygen vacancies in perovskite oxides [22]. According to the relative intensity ratio (RIR) of O 1s (lattice oxygen)/O 1s (dangling bonds and adsorption oxygen), the relative concentration of surface oxygen vacancies can be roughly estimated [23]. The calculated RIR values were 1.67, 1.42, 1.19 and 1.05 respectively for pristine BFO, HB-120-2-8, HB-150-2-8, and HB-180-2-8, suggesting that increasing hydrogenation temperature would lead to a higher surface oxygen vacancy concentration in BFO.

Kelvin probe force microscopy (KPFM), which holds great promise for determining the contact potential difference (CPD), is becoming a popular tool for electronic characterization of semiconductor surfaces that is sensitive to the local oxygen vacancy concentration [24,25]. To provide direct evidence of the hydrogenation-induced oxygen vacancy on the BFO surface, KPFM measurements were also performed. Fig. 4 shows simultaneously obtained topography and CPD images of as-prepared BFO and hydrogenated BFO (HB-180-2-8) nanocrystals on ITO surface measured by KPFM. In topography images, the deposited sample particles (bright spots, indicative of an abnormal rise in surface roughness) on the ITO surface were relatively uniform with a particle size of 20–40 nm in agreement with the TEM results for both pristine BFO and hydrogenated BFO (HB-180-2-8). Nevertheless, the CPD images of the pristine BFO and hydrogenated BFO were quite different. The typical cross-sectional CPD profiles along the lines indicated by numbers 1, 2 and 3 in CPD images clearly demonstrate that the values of CPD change (ΔV_{CPD}) were ~ 40 mV and ~ 140 mV for pristine BFO

and hydrogenated BFO (HB-180-2-8), respectively. As expected, the surface potential of hydrogenated BFO nanocrystals was much more negative than that of pristine BFO nanocrystals. The negatively-shifted surface potential of hydrogenated BFO identified the presence of a large amount of oxygen vacancies on the particle surface [26], which could act as active sites for electron trapping thus making the surface potential of hydrogenated BFO nanocrystals significantly decrease. The KPFM results confirm that the hydrogenation treatment would really change the electronic structure of the BFO particle surface. In addition, the in situ electron paramagnetic resonance (EPR) is another sensitive characterization technique which is extensively used to identify the formation of oxygen vacancy defects [27]. Fig. 5(a) shows the EPR spectra of the pristine and hydrogenated BFO nanocrystals. For each sample, a strong broad and symmetric signal characteristic for BiFeO$_3$ was observed, which is consistent with the literature [28,29]. The ferromagnetic spin-wave resonance in EPR spectra could be divided into two resonances segments, i.e., low field (LF) (g = ~ 2.70) and high field (HF) (g = ~ 2.04) resonance shoulders, corresponding to the resonance absorption in the cycloidal spin structure (P_{cyc}) and the defect-induced free spins (P_{def}), respectively [29]. Specifically, the HF resonance signals (P_{def}) are supposed to be correlated with the free spins induced by oxygen-vacancy related defects [29,30]. As seen, the EPR resonance magnitudes of the hydrogenated BFO sample (HB-180-2-8) including LF (P_{cyc}) and HF (P_{def}) resonance signals were greatly larger than those of pristine BFO, which could be attributed to the hydrogenation induced changes in spin structure. It was suggested that a partial transformation of spin structure from cycloid to a canted anti-ferromagnetic state induced by hydrogenation would happen, since the g-factor/linewidth value of EPR spectra of the hydrogenated BFO sample became smaller than that of pristine BFO as similar to the discussion in the previous work [29]. Meanwhile, the much stronger HF resonance signal intensity of the hydrogenated BFO sample also implies that the surface oxygen vacancy concentration in hydrogenated BFO samples was significantly improved.

In order to further understand the concentration variation of surface oxygen vacancy in as-hydrogenated BFO samples, the TGA curves were
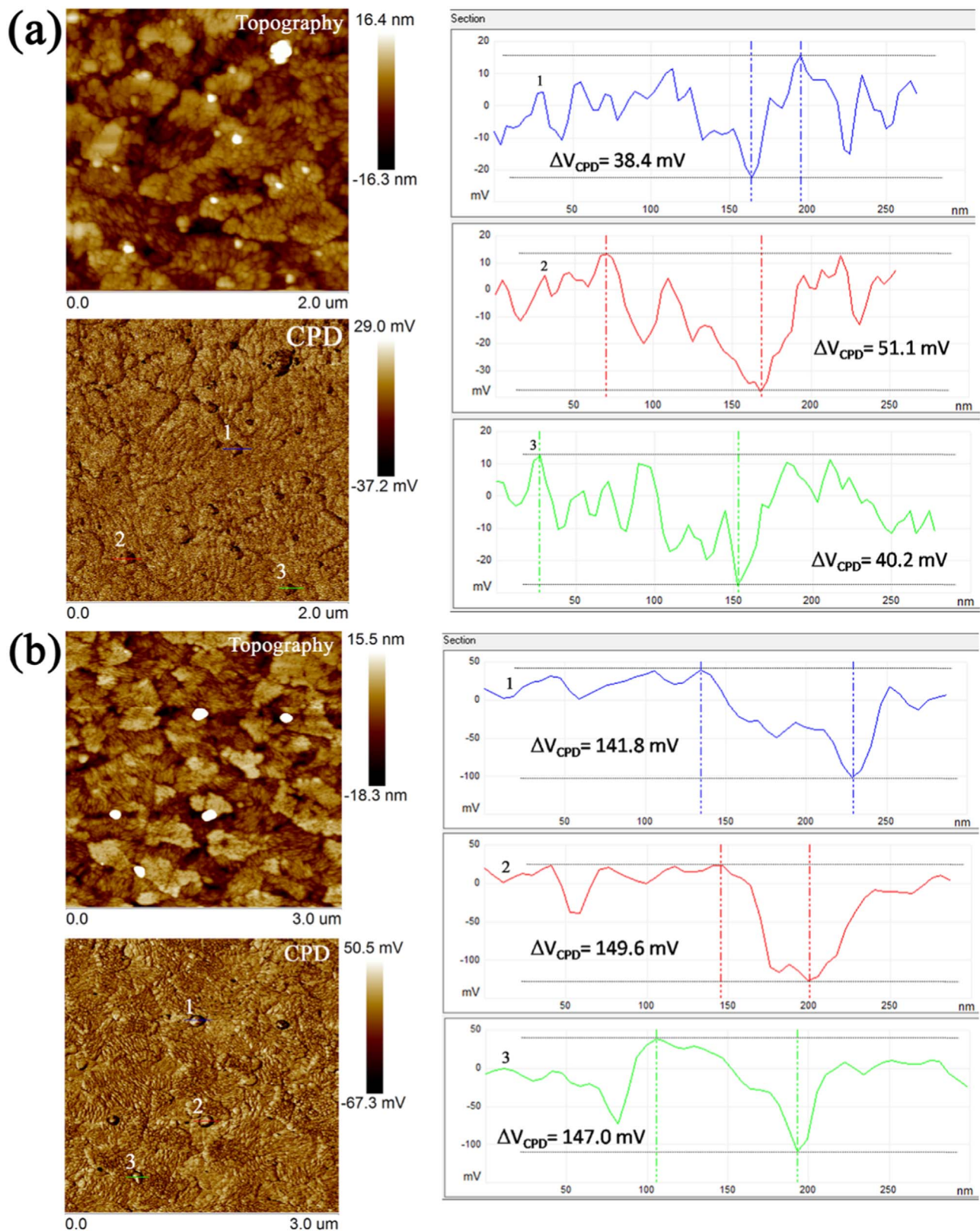
Fig. 4. Topography and contact potential difference (CPD) images of as-prepared (a) BFO and (b) hydrogenated BFO (HB-180-2-8) nanoparticles on ITO surface measured by KPFM. The cross-sectional line profiles of CPD are achieved along the lines indicated by numbers 1, 2 and 3 in CPD images.

measured in flowing O_2 atmosphere. As shown in Fig. 5(b), for the pristine BFO the weight loss in the temperature range of 25–800 °C could be roughly classified into two weight loss stages, which could be ascribed to the removal of physical adsorption water and chemical absorbed water respectively. For the hydrogenated BFO samples,

however, a weight gain was observed between 500 °C and 800 °C. Such a weight gain was apparently caused by the oxygen refilling on the as-formed oxygen vacancies during high temperature, which has been also observed in the literature [16]. The percentage of weight gain for HB-120-2-8, HB-150-2-8 and HB-180-2-8 were 0.1 wt%, 0.3 wt% and
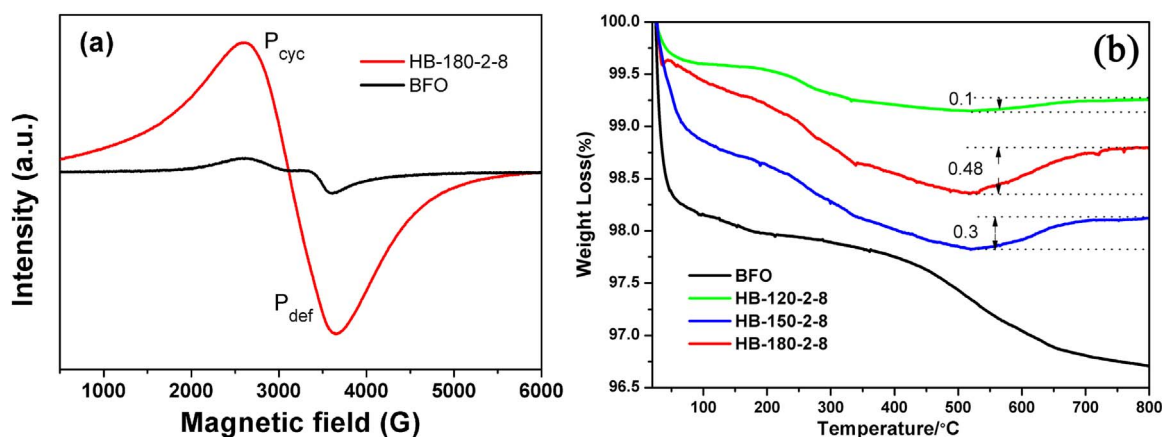
Fig. 5. (a) EPR spectra of pristine BFO and hydrogenated BFO (HB-180-2-8) samples; (b) TGA curves of pristine BFO and hydrogenated BFO.

0.48 wt%, respectively, further confirming that the surface oxygen vacancy concentration in the hydrogenated BFO samples would increase with the hydrogenation temperature. As expected, however, only two weight loss stages, arising from the elimination of physical and chemical absorbed water, and no weight gain were observed in the whole temperature range from the TGA curves obtained under Ar atmosphere for both pristine BFO and hydrogenated BFO (HB-180-2-8) samples (Fig. S1). This means no filling of oxygen vacancies under Ar atmosphere during the whole temperature range, thus also demonstrating that oxygen refilling could happen on the as-formed oxygen vacancies in the hydrogenated BFO samples when TGA experiments were performed under oxygen atmosphere.

3.3. Effect of oxygen vacancy

The presence and concentration of oxygen vacancy in metal oxides

would significantly influence their optical properties [31]. Fig. 6(a) shows the UV–vis diffuse reflectance spectra (DRS) of the pristine and hydrogenated BFO samples. As shown, the hydrogenation treatment could expand the light absorption band of BFO nanocrystals, and with the increase of hydrogenation temperature the light absorption band would further expand. The color change of BFO nanocrystals, seen from the insets in Fig. 6(a), turned from light brown yellow to brownish black with the increase of hydrogenation temperature, also confirming the extended light absorption capability by hydrogenation. As have been discussed above, it can be concluded that such an enhanced light absorption capability of BFO nanocrystals could be mainly caused by the increased concentration of surface oxygen vacancy during hydrogenation. According to the classical Tauc plots [32,33] shown in Fig. 6(b), the band gaps for the pristine BFO, HB-120-2-8, HB-150-2-8, and HB-180-2-8 were calculated as 2.17, 2.07, 2.06 and 1.97 eV, respectively. To define the electronic details of hydrogenated BFO
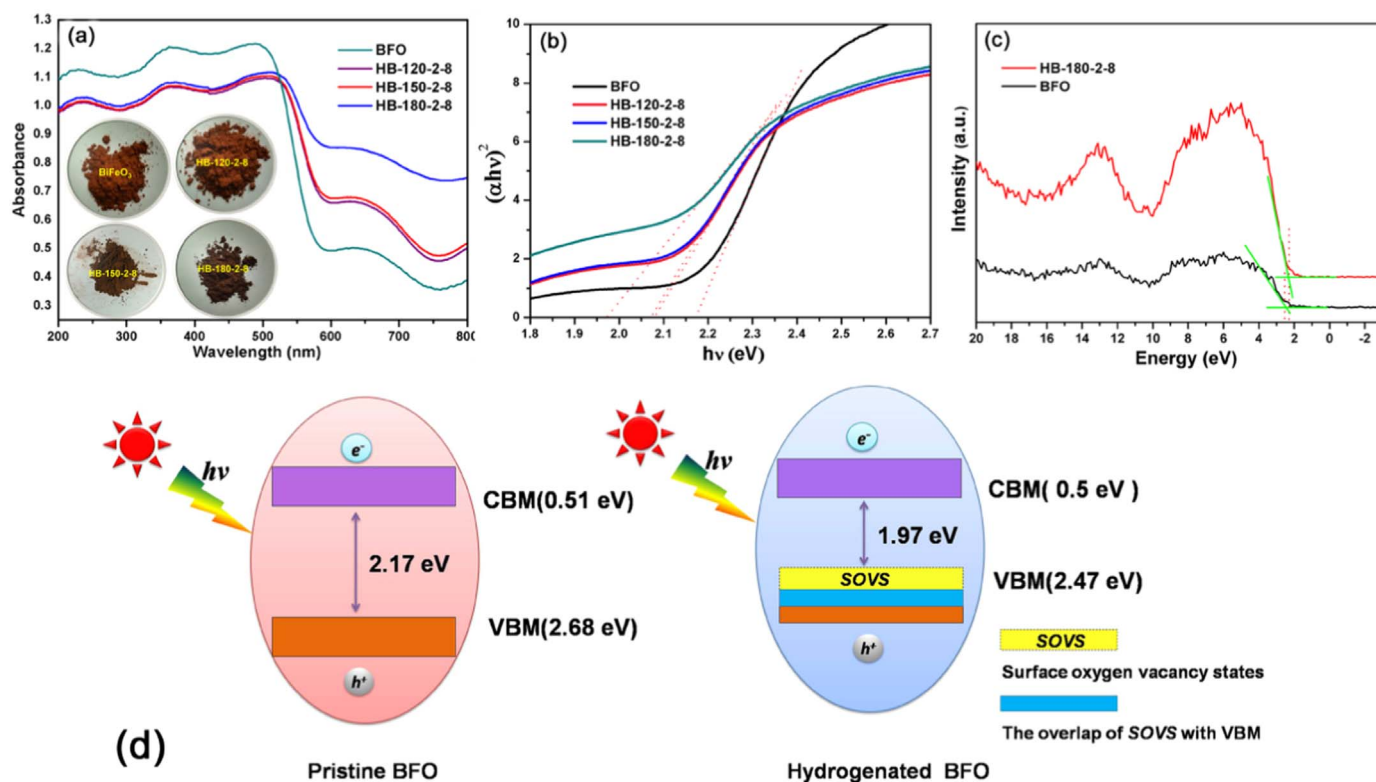

Fig. 6. (a) UV–vis diffuse reflectance spectra of pristine BFO and hydrogenated samples; (Insets are photographs of pristine BFO and hydrogenated powders.) (b) Tauc plots to determine the band gaps for the each sample; (c) VB XPS spectra of the pristine and HB-180-2-8 BFO nanocrystals; (d) illustration of energy band for pristine BFO and hydrogenated BFO with oxygen vacancies.

nanocrystals for specific measurement of conduction-band minimum (CBM) and valence-band maximum (VBM), VB XPS spectra were examined. Fig. 6(c) shows the VB XPS spectra of the pristine and hydrogenated BFO (HB-180-2-8) nanocrystals. The pristine BFO displayed the VB band edge at ~ 2.68 eV below the Fermi level, which was the same as the previous report [18]. Because the UV–vis DRS shown in Fig. 6(b) has revealed that the band gap of pristine BFO is 2.17 eV, the CBM would locate at about 0.51 eV. After hydrogenation treatment, the VBM showed a slightly decrease for the HB-180-2-8 sample, in which the VBM and CBM positions were 2.47 eV and 0.5 eV, respectively. The decreased VBM was probably due to the presence of delocalized surface impurity states arising from surface oxygen vacancies in the hydrogenated BFO sample, as previously reported in similar VB spectra for other hydrogenated photocatalysts [14,34]. These delocalized surface impurity states would overlap with the VB edge, and raise the position of the valence band, thus leading to the decreased VBM in the hydrogenated BFO sample. The VB XPS results further confirm that the increased surface oxygen vacancy concentration by hydrogenation did alter the band structure of BFO nanocrystals, leading to the variation of light absorption capability. Such a band structure variation could be illustrated in Fig. 6(d). Since substantial oxygen vacancies were formed on the BFO particle surfaces during hydrogenation treatment, the corresponding band gap was decreased, i.e. the VBM energy level was raised, which was above and partially overlapping with the VB of pristine BFO.

Except the above-mentioned band gap-related light absorption capability, the transport and recombination of the photogenerated electron-hole pairs is another important factor that determines the quantum efficiency and then the degradation capability of the photocatalyst. In the present case, the effect of the oxygen vacancies of BFO nanocrystals on the separation, transport and recombination of photogenerated charges was evaluated by photoluminescence (PL) emission spectra and photocurrent response spectra. The PL spectra (Fig. 7(a)) of the pristine and hydrogenated BFO nanocrystals were centered at around 406 nm, and the PL emission intensity gradually decreased with the increase of hydrogenation temperature. The PL emission intensity generally reflects the recombination probability of photo-induced electrons and holes, and a low emission intensity means a low recombination probability [35]. Therefore, the increase of oxygen vacancy concentration by increasing hydrogenation temperature in BFO nanocrystals could enhance the suppression of charge recombination. Meanwhile, as shown in Fig. 7(b), the transient photocurrent intensities of the hydrogenated BFO samples were larger than that of pristine BFO sample, implying a more efficient photoinduced charge separation and transfer process in the hydrogenated BFO sample. Moreover, the photocurrent intensity also increased with the increase of hydrogenation temperature, and the HB-180-2-8 sample exhibited the highest

photocurrent intensity. This confirms that the improved concentration of surface oxygen vacancies in the BFO nanocrystals could favor the photoinduced charge separation and transfer process, and thus would probably enhance the photo-quantum efficiency and photocatalytic activity of BFO.

The photocatalytic activities of the pristine and as-hydrogenated BFO nanocrystals were evaluated by degradation of pollutant MO under visible light irradiation ($\lambda \geq 420$ nm). As shown in Fig. 8(a), in the absence of photocatalyst, MO self-degradation was almost negligible. The pristine BFO sample exhibited low photocatalytic activity for MO photodegradation, and only about 19% of MO was decomposed after 4 h visible light irradiation. In contrast, the hydrogenated BFO nanocrystals showed an enhanced photocatalytic activity for MO degradation. For the hydrogenated BFO nanocrystals (HB-180-2-8), 75.8% of MO was decomposed, which was nearly four times that of pristine BFO. In addition, to determine the main active species of hydrogenated BFO for the degradation of MO, the trapping experiments were performed with addition of various quenchers or under anoxic condition, and the results are given in Fig. 8(b). It can be seen that the photocatalytic efficiency was accelerated or nearly unchanged with addition of ethylene diamine tetraacetic acid (EDTA, a hole scavenger [36], 2 mM) or in the absence of O_2, whereas the photocatalytic efficiency was restrained when adding tert-butyl alcohol (TBA, a hydroxyl radicals (•OH) scavenger [37], 2 mM). The trapping experiments reveal that the predominant active species for MO photodegradation by hydrogenated BFO were hydroxyl radicals (•OH) rather than $O_2^{-\bullet}$ or photogenerated holes.

Based on the discussion above, the observed enhanced photocatalytic activity for MO degradation by hydrogenated BFO nanocrystals could be explained as follows. Firstly, oxygen vacancies particularly surface oxygen vacancies were generated on BFO nanocrystals during high pressure hydrogenation process (Figs. 2 and 3) and thus altered their light absorption band structure. The narrowed band gap by oxygen vacancies as a result of hydrogenation (Fig. 6) led to an enhanced light absorption capability and would thus contribute to photocatalytic degradation activity (Fig. 8(a)). Secondly, the generated surface oxygen vacancies on the hydrogenated BFO nanocrystals could act as trapping centers for photogenerated electrons (as discussed in the KPFM measurements, Fig. 4), which would on one hand facilitate the separation of photogenerated electron-hole pairs and on the other hand make the photoinduced holes conducive to producing the predominant active species (hydroxyl radicals, •OH) with H_2O on the hydrogenated BFO surface for MO photodegradation (as demonstrated by the trapping experiments, Fig. 8(b)). Thirdly, the formation of oxygen vacancies generated on BFO nanocrystal surfaces could suppress the recombination of photogenerated electrons and holes and facilitate the photoinduced charge separation and transfer process, as verified by PL and
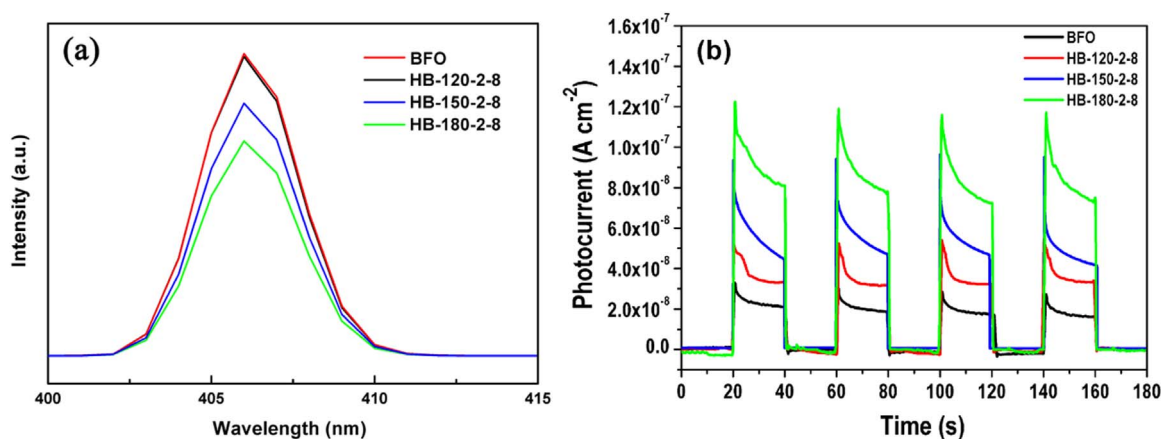
Fig. 7. (a) Photoluminescence (PL) emission spectra of pristine BFO and hydrogenated samples; (b) Photocurrent response spectra of pristine BFO and hydrogenated samples measured at 0.0 V potential bias (vs. SCE) with several light on/off cycles under visible light irradiation ($\lambda \geq 420$ nm).
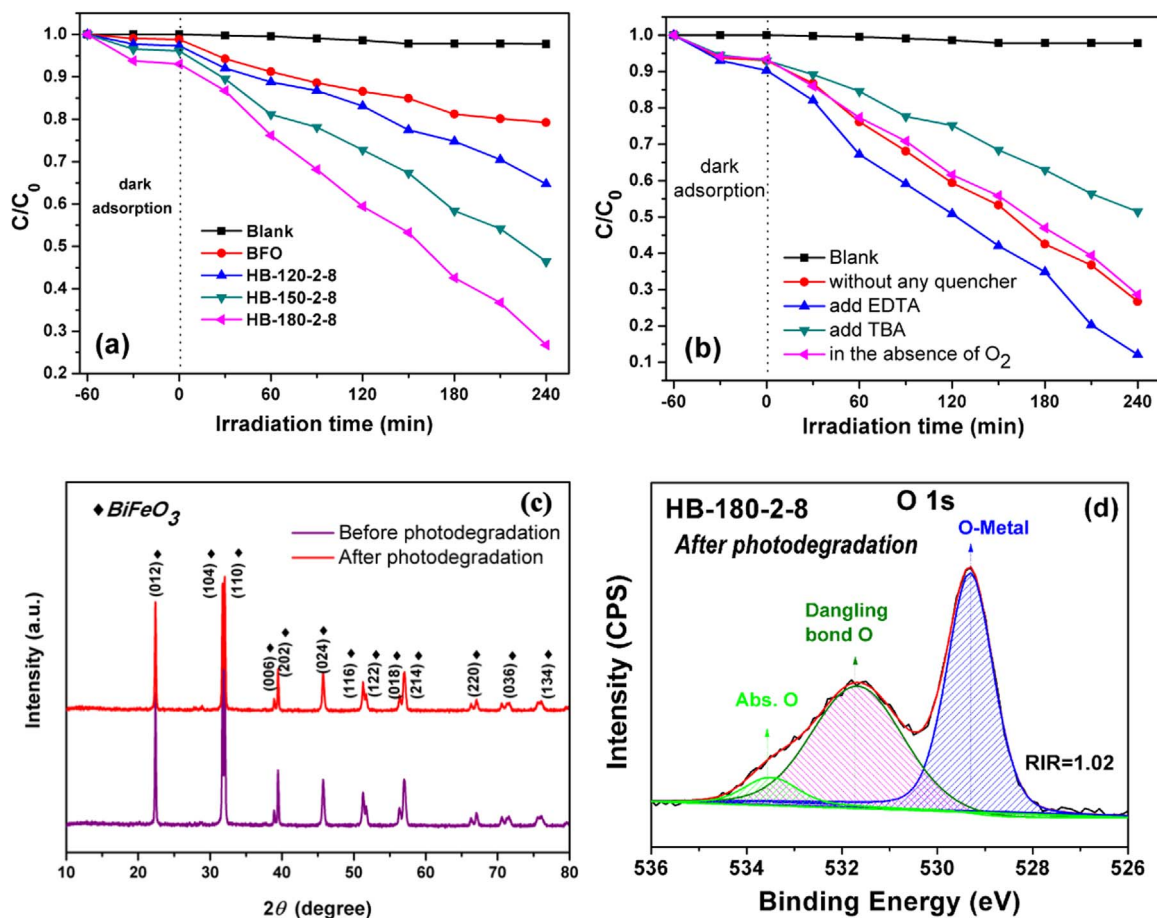
Fig. 8. (a) Photocatalytic degradation efficiency of MO by different photocatalysts under visible light irradiation; (b) The trapping experiments are performed by photodegradation of MO over the hydrogenated BFO sample (HB-180-2-8) alone, and with the addition of EDTA, TBA, or in the absence of O_2; (c) XRD patterns of HB-180-2-8 detected before and after photocatalytic degradation; and (d) O 1s core-level XPS spectra of HB-180-2-8 detected after photocatalytic degradation.

photocurrent results (Fig. 7). The suppression of charge recombination obviously would strengthen photocatalytic degradation activity of BFO nanocrystals. Fourthly, the presence of oxygen vacancies on BFO nanocrystal surfaces could also favor the adsorption of MO molecules, as seen in the dark adsorption area in Fig. 8(a). More MO molecules adsorbed by BFO nanocrystals would accelerate the degradation reaction. All these factors contributed to the observed enhanced photocatalytic activity of hydrogenated BFO for MO degradation.

To evaluate the stability of surface oxygen vacancies in BFO, the XRD patterns and O 1s core-level XPS spectra of HB-180-2-8 detected before and after degradation reaction were performed, as shown in Fig. 8(c)–(d). It is seen that no crystal structure change occurred before and after degradation reaction. The calculated RIR value of HB-180-2-8 after photodegradation was 1.02, which was close to that of before photodegradation. This indicates that the surface oxygen vacancies in BFO introduced by hydrogenation process were stable under room temperature. However, the as-generated oxygen vacancies would be refilled if the sample was treated at a high temperature under oxygen atmosphere. Fig. 9 shows the photocatalytic activity for MO degradation by the hydrogenated BFO nanocrystals before and after being heat treated at 800 °C in air. It is evident that when the as-formed surface vacancies on BFO nanocrystals were recovered by heat treatment in air, the photodegradation capability was subsequently deteriorated. This again verifies that the observed enhanced photodegradation activity by hydrogenation was originated from the presence of oxygen vacancies.

4. Conclusions

To summarize, oxygen vacancies were introduced into
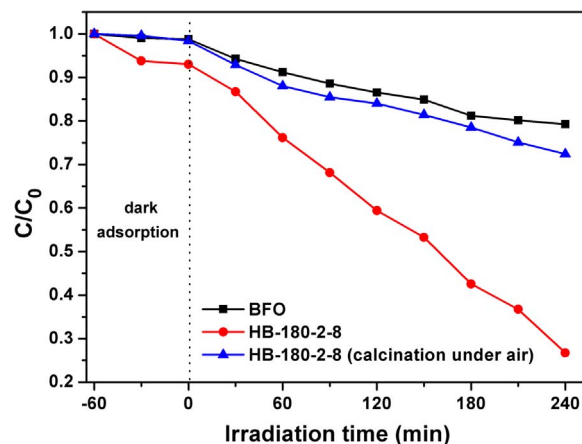
Fig. 9. Photocatalytic degradation activity for MO by the as-hydrogenated BFO nanocrystals (HB-180-2-8) before and after being heat treated at 800 °C in air.

hydrothermally-synthesized $BiFeO_3$ nanocrystals by a high pressure hydrogenation process. HRTEM, XPS, EPR and KPFM results reveal that substantial surface oxygen vacancies were formed on the surfaces of $BiFeO_3$ nanocrystals during the hydrogenation process. With increasing hydrogenation temperature, the oxygen vacancy concentration increased. The formation of surface oxygen vacancies on BFO nanocrystals was found to narrow BFO band gap, leading to an enhanced light absorption capability. During the photocatalytic process, the generated surface oxygen vacancies played the role of the trapping centers for photoinduced electrons, thus promoting the separation of

photogenerated electron-hole pairs and the production of predominant active species (hydroxyl radicals, •OH) for MO photodegradation. The presence of surface oxygen vacancies could also suppress the re-combination of photogenerated electrons and holes, and facilitate the photoinduced charge separation and transfer process. In addition, the adsorption capability for MO molecules was also enhanced due to the presence of surface oxygen vacancies. All these factors contributed to the observed enhanced photocatalytic activity of the hydrogenated BFO nanocrystals. Meanwhile, the as-formed surface oxygen vacancies were also stable at room temperature.

Acknowledgments

Appendix A. Supplementary material

Supplementary data associated with this article can be found in the online version at http://dx.doi.org/10.1016/j.solmat.2017.06.021.

References

[1] Y.Q. Qu, X.F. Duan, Progress, challenge and perspective of heterogeneous photo-catalysts, Chem. Soc. Rev. 42 (2013) 2568–2580.

[2] M. Pelaez, N.T. Nolan, S.C. Pillai, M.K. Seery, P. Falaras, A.G. Kontos, P.S.M. Dunlop, J.W.J. Hamilton, J.A. Byrne, K. O'Shea, M.H. Entezari, D.D. Dionysiou, A review on the visible light active titanium dioxide photocatalysts for environmental applications, Appl. Catal. B: Environ. 125 (2012) 331–349.

[3] S.G. Kumar, K.S.R.K. Rao, Zinc oxide based photocatalysis: tailoring surface-bulk structure and related interfacial charge carrier dynamics for better environmental applications, RSC Adv. 5 (2015) 3306–3351.

[4] H.D. Zheng, J.Z. Ou, M.S. Strano, R.B. Kaner, A. Mitchell, K. Kalantar-Zadeh, Nanostructured tungsten oxide – properties, synthesis, and applications, Adv. Funct. Mater. 21 (2011) 2175–2196.

[5] H.M. Fan, D.J. Wang, L.L. Wang, H.Y. Li, P. Wang, T.F. Jiang, T.F. Xie, Hydrothermal synthesis and photoelectric properties of BiVO$_4$ with different morphologies: an efficient visible-light photocatalyst, Appl. Surf. Sci. 257 (2011) 7758–7762.

[6] M. Mishra, D.M. Chun, Alpha-Fe$_2$O$_3$ as a photocatalytic material: a review, Appl. Catal. A: Gen. 498 (2015) 126–141.

[7] G. Catalan, J.F. Scott, Physics and applications of bismuth ferrite, Adv. Mater. 21 (2009) 2463–2485.

[8] B.F. Gao, X.Y. Chen, K.B. Yin, S. Dong, Z.F. Ren, F. Yuan, T. Yu, Z.G. Zou, J.M. Liu, Visible-light photocatalytic properties of weak magnetic BiFeO$_3$ nanoparticles, Adv. Mater. 19 (2007) 2889–2892.

[9] Y.N. Huo, M. Miao, Y. Zhang, J.A. Zhu, H.X. Li, Aerosol-spraying preparation of a mesoporous hollow spherical BiFeO$_3$ visible photocatalyst with enhanced activity and durability, Chem. Commun. 47 (2011) 2089–2091.

[10] C. Reitz, C. Suchomski, C. Weidmann, T. Brezesinski, Block copolymer-templated BiFeO$_3$ nanoarchitectures composed of phase-pure crystallites intermingled with a continuous mesoporosity: effective visible-light photocatalysts? Nano Res. 4 (2011) 414–424.

[11] F. Niu, D. Chen, L.S. Qin, T. Gao, N. Zhang, S. Wang, Z. Chen, J.Y. Wang, X.G. Sun, Y.X. Huang, Synthesis of Pt/BiFeO$_3$ heterostructured photocatalysts for highly efficient visible-light photocatalytic performances, Sol. Energy Mater. Sol. Cells 143 (2015) 386–396.

[12] G. Wang, Y. Ling, Y. Li, Oxygen-deficient metal oxide nanostructures for photo-electrochemical water oxidation and other applications, Nanoscale 4 (2012) 6682–6691.

[13] X.B. Chen, L. Liu, P.Y. Yu, S.S. Mao, Increasing solar absorption for photocatalysis

[14] with black hydrogenated titanium dioxide nanocrystals, Science 331 (2011) 746–750.

[14] J.P. Wang, Z.Y. Wang, B.B. Huang, Y.D. Ma, Y.Y. Liu, X.Y. Qin, X.Y. Zhang, Y. Dai, Oxygen vacancy induced band-gap narrowing and enhanced visible light photocatalytic activity of ZnO, ACS Appl. Mater. Interfaces 4 (2012) 4024–4030.

[15] Y.H. Lv, Y.Y. Zhu, Y.F. Zhu, Enhanced photocatalytic performance for the BiPO$_{4-x}$ nanorod induced by surface oxygen vacancy, J. Phys. Chem. C 117 (2013) 18520–18528.

[16] H.Q. Tan, Z. Zhao, W.B. Zhu, E.N. Coker, B.S. Li, M. Zheng, W.X. Yu, H.Y. Fan, Z.C. Sun, Oxygen vacancy enhanced photocatalytic activity of pervoskite SrTiO$_3$, ACS Appl. Mater. Interfaces 6 (2014) 19184–19190.

[17] X.Y. Pan, M.Q. Yang, X.Z. Fu, N. Zhang, Y.J. Xu, Defective TiO$_2$ with oxygen vacancies: synthesis, properties and photocatalytic applications, Nanoscale 5 (2013) 3601–3614.

[18] F. Niu, D. Chen, L.S. Qin, N. Zhang, J.Y. Wang, Z. Chen, Y.X. Huang, Facile synthesis of highly efficient p–n heterojunction CuO/BiFeO$_3$ composite photocatalysts with enhanced visible-light photocatalytic activity, ChemCatChem 7 (2015) 3279–3289.

[19] T. Yamashita, P. Hayes, Analysis of XPS spectra of Fe^{2+} and Fe^{3+} ions in oxide materials, Appl. Surf. Sci. 254 (2008) 2441–2449.

[20] F.C. Lei, Y.F. Sun, K.T. Liu, S. Gao, L. Liang, B.C. Pan, Y. Xie, Oxygen vacancies confined in ultrathin indium oxide porous sheets for promoted visible-light water splitting, J. Am. Chem. Soc. 136 (2014) 6826–6829.

[21] N. Zhang, D. Chen, F. Niu, S. Wang, L.S. Qin, Y.X. Huang, Enhanced visible light photocatalytic activity of Gd-doped BiFeO$_3$ nanoparticles and mechanism insight, Sci. Rep. 6 (2016) 26467.

[22] Y. Teraoka, M. Yoshimatsu, N. Yamazoe, T. Seiyama, Oxygen-sorptive properties and defect structure of perovskite-type oxides, Chem. Lett. 13 (1984) 893–896.

[23] L. Qiao, X.F. Bi, Direct observation of oxygen vacancy and its effect on the micro-structure, electronic and transport properties of sputtered LaNiO$_{3-δ}$ films on Si substrates, Thin Solid Films 519 (2010) 943–946.

[24] W. Melitz, J. Shen, A.C. Kummel, S. Lee, Kelvin probe force microscopy and its application, Surf. Sci. Rep. 66 (2011) 1–27.

[25] M. Andra, F. Gunkel, C. Baumer, C.C. Xu, R. Dittmann, R. Waser, The influence of the local oxygen vacancy concentration on the piezo response of strontium titanate thin films, Nanoscales 7 (2015) 14351–14357.

[26] S. Nandy, R. Thapa, M. Kumar, T. Som, N. Bundaleski, O.M.N.D. Teodoro, R. Martins, E. Fortunato, Efficient field emission from vertically aligned Cu$_2$O$_{1-δ}$(111) nanostructure influenced by oxygen vacancy, Adv. Funct. Mater. 25 (2015) 947–956.

[27] Y.S. Chen, H.Y. Guo, J.C. Yang, Y.H. Chu, W.F. Wu, J.G. Lin, Electron paramagnetic resonance probed oxygen deficiency in SrTiO$_3$ with different cap layers, J. Appl. Phys. 112 (2012) 123720.

[28] I. Szafraniak-Wiza, W. Bednarski, S. Waplak, B. Hilczer, A. Pietraszko, L. Kepinski, Multiferroic BiFeO$_3$ nanoparticles studied by electron spin resonance, X-ray diffraction and transmission electron microscopy methods, J. Nanosci. Nanotechnol. 9 (2009) 3246–3251.

[29] J.W. Lin, Y.H. Tang, C.S. Lue, J.G. Lin, Electron spin resonance probed suppressing of the cycloidal spin structure in doped bismuth ferrites, Appl. Phys. Lett. 96 (2010) 232507.

[30] F. Yan, G.Z. Xing, R.M. Wang, L. Li, Tailoring surface phase transition and magnetic behaviors in BiFeO$_3$ via doping engineering, Sci. Rep. 5 (2015) 9128.

[31] H. Tan, Z. Zhao, M. Niu, C. Mao, D. Cao, D. Cheng, P. Feng, Z. Sun, A facile and versatile method for preparation of colored TiO$_2$ with enhanced solar-driven photocatalytic activity, Nanoscale 6 (2014) 10216–10223.

[32] J. Tauc, R. Grigorovici, A. Vancu, Optical properties and electronic structure of amorphous germanium, Phys. Status Solidi 15 (1966) 627–637.

[33] B. Zhou, X. Zhao, H.J. Liu, J.H. Qu, C.P. Huang, Visible-light sensitive cobalt-doped BiVO$_4$ (Co-BiVO$_4$) photocatalytic composites for the degradation of methylene blue dye in dilute aqueous solutions, Appl. Catal. B: Environ. 99 (2010) 214–221.

[34] A. Naldoni, M. Allieta, S. Santangelo, M. Marelli, F. Fabbri, S. Cappelli, C.L. Bianchi, R. Psaro, V. Dal Santo, Effect of nature and location of defects on bandgap narrowing in black TiO$_2$ nanoparticles, J. Am. Chem. Soc. 134 (2012) 7600–7603.

[35] Y. Yao, G.H. Li, S. Ciston, R.M. Lueptow, K.A. Gray, Photoreactive TiO$_2$/carbon nanotube composites: synthesis and reactivity, Environ. Sci. Technol. 42 (2008) 4952–4957.

[36] Y.L. Tian, B.B. Chang, J.L. Lu, J. Fu, F.N. Xi, X.P. Dong, Hydrothermal synthesis of graphitic carbon nitride-Bi$_2$WO$_6$ heterojunctions with enhanced visible light photocatalytic activities, ACS Appl. Mater. Interfaces 5 (2013) 7079–7085.

[37] C. Minero, G. Mariella, V. Maurino, D. Vione, E. Pelizzetti, Photocatalytic transformation of organic compounds in the presence of inorganic ions. 2. Competitive reactions of phenol and alcohols an a titanium dioxide-fluoride system, Langmuir 16 (2000) 8964–8972.

国家自然科学基金委员会

资助项目计划书

资助类别： 面上项目

亚类说明：

附注说明：

项目名称： 双读出闪烁晶体Cs2LiLaBr6:Ce的结晶行为与高光学质量单晶生长

直接费用： 60万元　　　　　　执行年限： 2020.01-2023.12

负 责 人： 秦来顺

通讯地址： 浙江省杭州市下沙高教园区学源街258号

邮政编码： 310018　　　　　　电　　话： 0571-86875607

电子邮件： qinlaishun@126.com

依托单位： 中国计量大学

联 系 人： 韩亮　　　　　　　　电　　话： 0571-87676317

填表日期： 2019年08月20日

190

国家自然科学基金委员会制

国家自然科学基金委员会资助项目计划书填报说明

一、项目负责人收到《关于国家自然科学基金资助项目批准及有关事项的通知》（以下简称《批准通知》）后，请认真阅读本填报说明，参照国家自然科学基金相关项目管理办法及《国家自然科学基金资助项目资金管理办法》（请查阅国家自然科学基金委员会官方网站首页"政策法规"栏目），按《批准通知》的要求认真填写和提交《国家自然科学基金委员会资助项目计划书》（以下简称《计划书》）。

二、填写《计划书》时要求科学严谨、实事求是、表述清晰、准确。《计划书》经国家自然科学基金委员会相关项目管理部门审核批准后，将作为项目研究计划执行和检查、验收的依据。

三、《计划书》各部分填写要求如下：

（一）简表：由系统自动生成。

（二）摘要及关键词：各类获资助项目都必须填写中、英文摘要及关键词。

（三）项目组主要成员：计划书中列出姓名的项目组主要成员由系统自动生成，与申请书原成员保持一致，不可随意调整。如果批准通知中"项目评审意见及修改意见表"中"对研究方案的修改意见"栏目有调整项目组成员相关要求的，待项目开始执行后，按照项目成员变更程序另行办理。

（四）资金预算表：根据批准资助的直接费用，按照《国家自然科学基金项目预算表编制说明》填报资金预算表和预算说明书。国家重大科研仪器研制项目、重大项目还应按照预算评审后批复的直接费用各科目金额填报资金预算表、预算说明书及相应的预算明细表。

（五）正文：

1. 面上项目、青年科学基金项目、地区科学基金项目：如果《批准通知》中没有修改要求的，只需选择"研究内容和研究目标按照申请书执行"即可；如果《批准通知》中"项目评审意见及修改意见表"中"对研究方案的修改意见"栏目明确要求调整研究期限和研究内容等的，须选择"根据研究方案修改意见更改"并填报相关修改内容。

2. 重点项目、重点国际（地区）合作研究项目、重大项目、国家重大科研仪器研制项目：须选择"根据研究方案修改意见更改"，根据《批准通知》的要求填写研究（研制）内容，不得自行降低、更改研究目标（或仪器研制的技术性能与主要技术指标以及验收技术指标）或缩减研究（研制）内容。此外，还要突出以下几点：

    （1）研究的难点和在实施过程中可能遇到的问题（或仪器研制风险），拟采用的研究（研制）方案和技术路线；

    （2）项目主要参与者分工，合作研究单位之间的关系与分工，重大项目还需说明课题之间的关联；

    （3）详细的年度研究（研制）计划。

3. 国家杰出青年科学基金、优秀青年科学基金和海外及港澳学者合作研究基金项目：须选择"根据研究方案修改意见更改"，按下列提纲撰写：

    （1）研究方向；

    （2）结合国内外研究现状，说明研究工作的学术思想和科学意义（限两个页面）；

    （3）研究内容、研究方案及预期目标（限两个页面）；

    （4）年度研究计划；

    （5）研究队伍的组成情况。

4. 国家自然科学基金基础科学中心项目：须选择"根据研究方案修改意见更改"，应当根据评审委员会和现场考察专家组的意见和建议，进一步完善并细化研究计划，作为评估和验收的依据。按下列提纲撰写：

    （1）五年拟开展的研究工作（包括主要研究方向、关键科学问题与研究内容）；

    （2）研究方案（包括骨干成员之间的分工及合作方式、学科交叉融合研究计划等）；

    （3）年度研究计划；

    （4）五年预期目标和可能取得的重大突破等；

    （5）研究队伍的组成情况。

5. 对于其他类型项目，参照面上项目的方式进行选择和填写。

简表

	姓　　　名	秦来顺	性　别	男	出生年月	1978年10月	民　族	汉族
申请者信息	学　　　位	博士			职称	教授		
	是否在站博士后	否			电子邮件	qinlaishun@126.com		
	电　　　话	0571-86875607			个人网页	http://clxy.cjlu.edu.cn/content.jsp?urltype=news.NewsContentUrl&wbtreeid=1067&wbnewsid=1650		
	工　作　单　位	中国计量大学						
	所 在 院 系 所	材料科学与工程学院						

	名　　　称	中国计量大学		代码	31001808A1235
依托单位信息	联　系　人	韩亮	电子邮件	hl@cjlu.edu.cn	
	电　　　话	0571-87676317	网站地址	www.cjlu.edu.cn	

	单　位　名　称
合作单位信息	

	项　目　名　称	双读出闪烁晶体Cs2LiLaBr6:Ce的结晶行为与高光学质量单晶生长	
项目基本信息	资　助　类　别	面上项目	亚 类 说 明
	附　注　说　明		
	申　请　代　码	E0201：人工晶体	
	基　地　类　别		
	执　行　年　限	2020.01-2023.12	
	直　接　费　用	60万元	

项目摘要

中文摘要：

　　n/γ双读出闪烁晶体Cs2LiLaBr6:Ce（CLLB:Ce）具有光输出高、衰减时间快、能量分辨率优、α/β高等优点，而且光输出均一性和温度依赖性极佳，综合性能优异、应用前景明确，然而生长高光学质量CLLB:Ce单晶困难，疑因CLLB非一致熔融导致多晶失透，但目前缺乏包含CLLB相的二元或者三元相图，结晶行为尚不明晰，晶体生长得不到科学的理论指导。本项目立足应用需求、以期突破瓶颈，拟以CLLB:Ce为研究对象，研究晶体生长中遇到的核心基础科学问题：包含CLLB相的二元相图的绘制和CLLB的结晶行为，从而进行CLLB:Ce晶体的组分设计、生长优化，制备大尺寸、高光学质量的CLLB:Ce晶体，研究其组分分布与光学性能、双读出性能的关系，为CLLB:Ce等冰晶石型闪烁晶体生长奠定坚实的基础，以期为中子探测技术装备的开发与产业发展贡献关键的高端材料。

Abstract：

Cs2LiLaBr6:Ce (CLLB:Ce) is a comprehensively excellent potential n/γ dual readout scintillation crystal with high light output, fast decay time, excellent energy resolution and high α/β ratio as well as excellent light output uniformity and temperature dependence. However, it is difficult to grow high optical quality CLLB:Ce single crystals. It is suspected that CLLB is so incongruent as to polycrystalline, but there is no binary or ternary phase diagram including CLLB compound at present, and the crystallization behavior of CLLB is not clear, so that the crystal growth of CLLB cannot be guided by reasonable theory. Based on the application requirement and the wish to break through the bottleneck, in this project CLLB:Ce will be taken as the research object, and the core basic academic question is investigated, which is to draw binary phase diagram including CLLB phase and disclose crystallization behavior of CLLB, encountered in crystal growth. Then to design the composition and optimize the growth process of CLLB:Ce crystals, prepare large-sized and high-quality CLLB:Ce crystals, and study the relationship between composition distribution and optical properties and dual readout performance, are performed afterwards. Consequently the project lead to solid foundation for the growth of Elpasolite scintillation crystals such as CLLB:Ce, as well as contributing materials for the development of neutron detection technological equipment and high-tech industry.

关键词(用分号分开)： 核辐射探测；光输出

Keywords(用分号分开)： Nuclear Radiation Detection; Light Output

项目组主要成员

编号	姓名	出生年月	性别	职称	学位	单位名称	电话	证件号码	项目分工	每年工作时间（月）
1	秦来顺	1978.10	男	教授	博士	中国计量大学	0571-86875607	142330197810232 41X	项目负责人	8
2	魏钦华	1985.07	男	讲师	博士	中国计量大学	0571-86835738	330226198507291597	晶体生长与闪烁性能研究	8
3	唐高	1981.11	男	副研究员	博士	中国计量大学	0571-86835738	430202198111222010	相图与光学性能研究	8
4	许振霞	1992.05	女	硕士生	学士	中国计量大学	0571-86875612	412724199205062124	化合物制备	10
5	宁佩	1995.11	女	硕士生	学士	中国计量大学	0571-86875612	142322199511103027	晶体生长	10
6	胡亦谦	1995.10	男	硕士生	学士	中国计量大学	0571-86875612	330781199510162012	晶体生长	10

总人数	高级	中级	初级	博士后	博士生	硕士生
6	2	1				3

国家自然科学基金项目直接费用预算表 （定额补助）

项目批准号：51972291　　　　　　　项目负责人：秦来顺　　　　　　　金额单位：万元

序号	科目名称	金额
1	项目直接费用合计	60.0000
2	1、 设备费	0.0000
3	(1)设备购置费	0.0000
4	(2)设备试制费	0.0000
5	(3)设备升级改造与租赁费	0.0000
6	2、 材料费	28.0000
7	3、 测试化验加工费	7.0000
8	4、 燃料动力费	1.0000
9	5、 差旅/会议/国际合作与交流费	10.0000
10	6、 出版/文献/信息传播/知识产权事务费	5.0000
11	7、 劳务费	8.0000
12	8、 专家咨询费	1.0000
13	9、 其他支出	0.0000

预算说明书（定额补助）

（请按照《国家自然科学基金项目预算表编制说明》等的有关要求，对各项支出的主要用途和测算理由，以及合作研究外拨资金、单价≥10万元的设备费等内容进行必要说明。）

（1）材料费

主要用于购买高纯无水卤化物晶体制备原料和各种辅助材料，共28万元。

无水卤化物原料主要为溴化镧、溴化铈、溴化铯、溴化锂等，该类原料极易潮解，无水和含结晶水原料价格差异巨大，目前国内晶体生长用无水卤化物原料依然需要购买国外进口原料，价格主要参照Sigma-Aldrich西格玛奥德里奇、艾璞尔（上海）商贸有限公司（美国APL子公司）和有研稀土新材料股份有限公司等的报价，预算为：溴化镧：8kg*1.5万元/kg=12万；溴化铈：1kg*2万元kg=2万元；溴化铯：15kg*0.4万元/kg=6万元；溴化锂：8kg*0.5万元/kg=4万元。合计24万元。

卤化物晶体生长采用高纯石英坩埚，一次性消耗使用，预算200根*500元/根=1万元。维护手套箱正常使用的氮气、晶体生长用热电偶、耐火砖、耐火棉、晶体加工所需辅材，预算3万元。合计4万元。

（2）测试化验加工费

晶体测试样品的加工，常规测试样品本实验室加工完成，大尺寸高精度晶体仍需委托加工，预算1万元；晶体物相、成分、微观结构的分析测试，包括DSC-TG、XRD、SEM、EDS、XPS、EPMA、拉曼、IR等，预算3万元；闪烁和光学性能的测试，包括光输出、能量分辨率、衰减时间、荧光光谱、X射线激发发射谱、伽玛能谱测试等，共3万元。合计7万元。

（3）燃料动力费，晶体生长电费、水费等，共1万元。

（4）差旅/会议/国际合作与交流费，共10万元。

差旅费主要用于科研调研、交流、实验等差旅产生的住宿费、交通费，预计20人次*0.2万元/人次=4万元，合计4万元。会议费主要是参加国内外的闪烁晶体及应用、晶体生长会议和核探测与应用技术会议的差旅费、注册费，国内会议预计8人次*0.5万元/人次=4万元，国际合作与交流费用于1人次的国际会议，1人次*2万元/人次=2万元，合计6万元。

（5）出版/文献/信息传播/知识产权事务费

包括发表论文所需的版面费，通过论文发表不需要版面费，但是中文期刊和个别外文期刊尚需付版面费，预算控制在2万元以内；专利申请及保护费，专利4个*0.5万元/个=2万元；信息交流与通话费及科技检索查询费等1万元。共5万。

（6）劳务费，用于直接参加项目的研究生劳务费用，4人*4年*10月/年*500元/月·人=8万元。

（7）专家咨询费，预算1万元。

项目负责人签字：　　　　　　科研部门公章：　　　　　　财务部门公章：

报告正文

研究内容和研究目标按照申请书执行。

报告正文

国家自然科学基金资助项目签批审核表

我接受国家自然科学基金的资助，将按照申请书、项目批准意见和计划书负责实施本项目（批准号：51972291），严格遵守国家自然科学基金委员会关于资助项目管理、财务等各项规定，切实保证研究工作时间，认真开展研究工作，按时报送有关材料，及时报告重大情况变动，对资助项目发表的论著和取得的研究成果按规定进行标注。

项目负责人（签章）：秦志鹏
2019年9月10日

我单位同意承担上述国家自然科学基金项目，将保证项目负责人及其研究队伍的稳定和研究项目实施所需的条件，严格遵守国家自然科学基金委员会有关资助项目管理、财务等各项规定，并督促实施。

依托单位（公章）
2019年9月10日

本栏目由基金委填写	科学处审查意见：

同意按计划执行

建议年度拨款计划（本栏目为自动生成，单位：万元）：

年度	总额	第一年	第二年	第三年	第四年	第五年
金额						

负责人（签章）：
2019年月日

科学部审查意见：

同意按计划执行

负责人（签章）：
2019年月日

本栏目主要用于重大项目等	相关局室审核意见：

负责人（签章）：
年　月　日

委领导审批意见：

委领导（签章）：
年　月　日

浙江省科技计划项目

合 同 书

项 目 编 号： 2022C01046

项 目 名 称： 面向成像诊疗技术的高性能射线探测材料
与元件产业化关键技术

计 划 类 别： 工业领域

项目委托单位(甲方)： 浙江省科学技术厅

项目承担单位(乙方)： 中国科学院宁波材料技术与工程研究所

起 止 年 月： 2022-01-01 至 2024-12-31

浙 江 省 科 学 技 术 厅

２０２１ 年 制

一、项目基本情况

项目名称	面向成像诊疗技术的高性能射线探测材料与元件产业化关键技术		
组织方式	择优委托项目	榜单类型	尖兵计划
项目主管处室	高新处	项目主管	沈维强
项目计划类别	工业领域	项目管理领域	无机材料
项目开始日期	2022-01-01	项目完成日期	2024-12-31

项目承担单位	单位名称	中国科学院宁波材料技术与工程研究所		
	单位类型	科研院所	统一社会信用代码	121000007178168758
	法人代表	黄政仁	所属行业	其他
	通信地址	宁波市镇海区中官西路1219号		
	联系人	王晶	联系人手机号码	15757456069

参与单位		单位名称	统一社会信用代码
	1	中国计量大学	123300004700090698
	2	中国科学院上海硅酸盐研究所	12100000425006547H
	3	上海御光新材料科技股份有限公司	91310000561853177T

鼓励在本项目实施过程中，设置科研助理岗位，聘用高校应届毕业生，预计开发科研助理岗位数 2 个，吸纳应届毕业生人数 20 人。

二、项目负责人及项目组成员

<table>
<tr><td rowspan="6">项目负责人</td><td colspan="2">姓名</td><td colspan="2">蒋俊</td><td colspan="2">证件号码</td><td colspan="3">429001197705073811</td></tr>
<tr><td colspan="2">最高学位</td><td colspan="2">博士</td><td colspan="2">职称</td><td colspan="3">正高级</td></tr>
<tr><td colspan="2">年龄</td><td colspan="2">43</td><td colspan="2">性别</td><td colspan="3">男</td></tr>
<tr><td colspan="2">工作单位</td><td colspan="2">中国科学院宁波材料技术与工程研究所</td><td colspan="2">手机号码</td><td colspan="3">13486492179</td></tr>
<tr><td colspan="2">现从事专业</td><td colspan="2">材料研发与应用</td><td colspan="2">年参加项目工作时间</td><td colspan="3">8</td></tr>
<tr><td colspan="2">姓名</td><td colspan="2">证件号码</td><td colspan="2">工作单位</td><td>职称</td><td>从事专业</td><td>年参加项目工作时间(月)</td></tr>
<tr><td rowspan="9">项目组成员</td><td colspan="2">唐高</td><td colspan="2">430202198111222010</td><td colspan="2">中国计量大学</td><td>副高级</td><td>材料研发</td><td>8</td></tr>
<tr><td colspan="2">吴云涛</td><td colspan="2">330103198406151317</td><td colspan="2">中国科学院上海硅酸盐研究所</td><td>正高级</td><td>材料研发与性能评测</td><td>6</td></tr>
<tr><td colspan="2">唐华纯</td><td colspan="2">513021197910290219</td><td colspan="2">上海御光新材料科技股份有限公司</td><td>中级</td><td>产业化与应用示范</td><td>6</td></tr>
<tr><td colspan="2">尹亦农</td><td colspan="2">15040419940829004X</td><td colspan="2">中国科学院宁波材料技术与工程研究所</td><td>中级</td><td>材料研发</td><td>8</td></tr>
<tr><td colspan="2">刘泽华</td><td colspan="2">412828198911153919</td><td colspan="2">中国科学院宁波材料技术与工程研究所</td><td>中级</td><td>材料研发</td><td>8</td></tr>
<tr><td colspan="2">何益锋</td><td colspan="2">330227199006086334</td><td colspan="2">中国科学院宁波材料技术与工程研究所</td><td>初级</td><td>器件制备</td><td>8</td></tr>
<tr><td colspan="2">秦来顺</td><td colspan="2">14233019781023241X</td><td colspan="2">中国计量大学</td><td>正高级</td><td>晶体生长</td><td>6</td></tr>
<tr><td colspan="2">魏钦华</td><td colspan="2">330226198507291597</td><td colspan="2">中国计量大学</td><td>副高级</td><td>材料研发</td><td>8</td></tr>
<tr><td colspan="2">陈振华</td><td colspan="2">330106198808115211</td><td colspan="2">中国计量大学</td><td>中级</td><td>材料发光性能研究</td><td>6</td></tr>
</table>

李中波	511026197812274813	上海御光新材料科技股份有限公司	副高级	产业化与技术开发	6
罗朝华	430524198401288178	中国科学院宁波材料技术与工程研究所	正高级	材料研发与应用	6
李宇焜	430702198411044030	中国科学院宁波材料技术与工程研究所	其他	材料制备工艺调节与性能优化	10
李瑞阳	330822199708300922	中国科学院宁波材料技术与工程研究所	其他	发光机理研究	10
胡盼	420703199708204065	中国科学院宁波材料技术与工程研究所	其他	材料制备工艺优化	10
姜杭杰	330281199701061313	中国科学院宁波材料技术与工程研究所	其他	闪烁陶瓷材料制备	10
武涛	342601199609025014	中国计量大学	其他	晶体生长工艺调节	10
华哲浩	330922199612243017	中国计量大学	其他	晶体生长设备设计	10
何君雨	411425199603103322	中国计量大学	其他	晶体生长	10
童宇枫	330226199710254331	中国计量大学	其他	晶体生长	10

六、项目经费来源

1、本项目研发总经费 <u>1000</u> 万元，其中：甲方补助 <u>325</u> 万元，乙方自筹 <u>675</u> 万元，丙方共同支持 <u>0</u> 万元。

2、甲方经费拨付计划（参与单位经费由承担单位转拨）

单位：万元

	首期	二期	合计
甲方资金	190	135	325

	甲方补助	承担单位	参与单位1	参与单位2	参与单位3
首期	190	114	76	0	0
二期	135	81	54	0	0
合计	325	195	130	0	0

3、乙方自筹和共同支持资金到位计划

单 位：万元

	首期	二期	合计
乙方自筹资金	300	375	675
丙方共同支持资金	0	0	0

	乙方自筹	承担单位	参与单位1	参与单位2	参与单位3
首期	300	40	35	0	225
二期	375	50	50	0	275
合计	675	90	85	0	500

	丙方共同支持	承担单位	参与单位1	参与单位2	参与单位3
首期	0	0	0	0	0
二期	0	0	0	0	0
合计	0	0	0	0	0

国防科技工业核材料技术创新中心文件

核材原发〔2021〕1号

关于批准"用于中子/伽马双读出的大尺寸、高质量 CLLB:Ce 闪烁晶体的研制"项目提前启动的通知

中国计量大学：

你单位《用于中子/伽马双读出的大尺寸、高质量 CLLB:Ce 闪烁晶体的研制》项目申请书收悉，经研究同意该项目提前启动，现将任务书和有关要求下达你单位，请据此开展工作，确保完成任务。

一、任务书

《用于中子/伽马双读出的大尺寸、高质量 CLLB:Ce 闪烁晶体的研制》项目

1、目标

采用非化学计量比配料结合坩埚旋转下降法制备出直径和长度均为 1.5 英寸、高质量的 CLLB:Ce 闪烁晶体，获得最佳生长工艺和组分配制，拥有良好的 n/γ 分辨能力，γ 光输出达到 40000 Ph./Mev，中子光输出达到 80000 Ph./中子，满足 n/γ 双模式探测器的应用要求。

2、考核指标

1）获得 CLLB:Ce 晶体毛坯，尺寸大于Φ1.5 英寸×1.5 英寸。

2）γ射线下（^{137}Cs 源），晶体的光输出≥40000 Ph./Mev，能量分辨率 6%以内；中子源下，光输出≥80000 Ph./中子，能量分辨率 5%以内。

3）提供 2 根Φ1.5 英寸×1.5 英寸的 CLLB:Ce 晶体封装件。

4）发表学术论文 2 篇。

3、内容

主要研发内容：

1）非化学计量比配料结合坩埚旋转下降进行 CLLB:Ce 晶体生长。

2）CLLB:Ce 晶体组分和工艺的优化。

3）CLLB:Ce 晶体双读出性能与晶体组成的关系。

4）CLLB:Ce 晶体防潮切割、抛光和封装。

主要创新点：

1）项目研究对象 CLLB:Ce 为新型 n/γ双读出闪烁晶体，提出采用非化学计量比配比生长高质量 CLLB:Ce 晶体，本项目立足应用需求，以期突破瓶颈。

2）项目提出采用坩埚旋转辅助和温度梯度调控来优化生长工艺，以获得大尺寸、高质量 CLLB:Ce 晶体。

（二）进度及经费

以创新中心下达的任务书为准。提前启动资金由中国计量大学自行垫付，待经费到位后，进行归垫。

二、有关要求

1.请你单位严格按照《国防科技工业核材料技术创新中心管理办法》、《国防科技工业核材料技术创新中心科研项目管理办法》和《国防科技工业核材料技术创新中心项目经费管理办法》的有关要求，加强对项目的管理。

2.请你单位相关项目负责人将项目进展报告定期报送核材料技术创新中心。

附件：

《用于中子/伽马双读出的大尺寸、高质量 CLLB: Ce 闪烁晶体的研制》项目任务书

国防科技工业核材料技术创新中心

2021 年 3 月 24 日

合同登记编号：

2021-HCL-Ⅱ-KYHZ-FWCG-7

技 术 服 务 合 同 书

项目名称：<u>用于中子/伽马双读出的大尺寸、高质量 CLLB:Ce</u>

<u>闪烁晶体的研制</u>

委 托 方：　　<u>中国原子能科学研究院</u>

<u>（国防科技工业核材料技术创新中心）（简称甲方）</u>

研究开发方：　<u>中国计量大学　　　　（简称乙方）</u>

签订地点：北京

签订日期：2021 年 9月27日

有效期限：自生效之日起至 2023 年 7 月 31 日止。

依据《中华人民共和国民法典》的规定，合同双方就 用于中子/伽马双读出的大尺寸、高质量 CLLB:Ce 闪烁晶体的研制 项目的服务，经协商一致，签订本合同。

一、合同内容

（一）《用于中子/伽马双读出的大尺寸、高质量 CLLB:Ce 闪烁晶体的研制》项目

1、研究内容

（1）非化学计量比配料结合坩埚旋转下降进行 CLLB:Ce 晶体生长

（2）CLLB:Ce 晶体组分和工艺的优化

（3）CLLB:Ce 晶体双读出性能与晶体组成的关系

（4）CLLB:Ce 晶体防潮切割、抛光和封装

2、关键技术

（1）通过非化学计量配比和坩埚设计，结合结晶习性，生长界面等生长工艺上的调控克服由于组分的非一致熔融问题导致晶体生长阶段的组分偏析和相分离问题。

（2）通过非化学计量比配比结合优化后的生长条件来获得大尺寸（≥1.5 英寸）、高质量的 $Cs_2LiLaBr_6$:Ce 晶体。

3、创新点

（1）本项目研究对象 CLLB:Ce 为新型 n/γ 双读出闪烁晶体，提出采用非化学计量比配比生长高质量 CLLB:Ce 晶体，本项目立足应用需求，以期突破瓶颈。

（2）本项目提出采用坩埚旋转辅助和温度梯度调控来优化生长工

艺，以获得大尺寸、高质量 CLLB:Ce 晶体。

二、应达到的技术指标和要求：

（一）《用于中子/伽马双读出的大尺寸、高质量 CLLB:Ce 闪烁晶体的研制》项目

（1）获得 CLLB:Ce 晶体尺寸≥1.5 英寸，γ 射线下（^{137}Cs 源），晶体的光输出≥ 40000 Ph./Mev，能量分辨率 6%以内；中子源下，光输出≥80000 Ph./中子，能量分辨率 5%以内

（2）提供 2 根 1.5 英寸的 CLLB:Ce 晶体

（3）提供 1 份研究报告，研究报告要求内容详尽、思路清晰、观点明确，文字简洁，图表清晰，提出的意见与建议具有较强的操作性和实际意义，正文中标注参考文献。

（4）发表学术论文 2 篇，凡发表与项目相关的论文或申请与项目相关的专利等，需按统一规定，署名"国防科技工业核材料技术创新中心"。

三、研究开发计划：

（一）《用于中子/伽马双读出的大尺寸、高质量 CLLB:Ce 闪烁晶体的研制》项目

1、2021年1月1日---2021年12月31日

（1）；基于包含 CLLB 相的二元相图和 CLLB 的结晶行为，合理配置晶体生长原料和非化学计量配比，研究自发成核坩埚下降法生长非化学计量比的 CLLB:Ce 晶体，探讨非化学计量比配比、坩埚形状、温场、下降速度、温度梯度、界面结构等坩埚下降法工艺条件对 CLLB:Ce 晶体生长的影响，获得 CLLB:Ce 单晶，初步确定适合 CLLB:Ce 单晶生长的

原料配比，提交阶段性研究报告 1 份。

2、2022年 1月1日---2022年12月31日

（1）研究非化学计量比配比的 CLLB:Ce 系列晶体样品，通过光学显微镜、SEM、TEM、EDS、常温和变温 XRD、ICP-MS 等手段分析非化学计量配比晶体中的生长缺陷及其分布和成分组成。根据晶体的原料组成、结构和生长工艺条件，分析生长缺陷产生的原因和演化过程以及与相分离之间的联系。

（2）分析晶体生长中出现的问题，调节晶体原料非化学计量配比和优化生长工艺，获得 1.5 英寸高质量 CLLB:Ce 单晶，揭示非化学计量比对晶体生长的影响因素，获得最佳原料配比，并对加工好的晶体进行封装。提交加工和封装好的尺寸为 1.5 英寸的晶体样品 1 个，阶段性研究报告 1 份和发表论文 1 篇

（3）选取非化学计量比配比的 CLLB:Ce 系列晶体样品，在不同测试温度和不同激发源下，获得不同 CLLB:Ce 晶体样品的荧光光谱、衰减时间以及双读出性能，研究非化学计量比对晶体的荧光性能和双读出性能的影响，确定最佳的化学计量比并顺利结题。提交封装好的尺寸为 1.5 英寸的晶体样品 1 个，发表论文 1 篇和结题报告 1 份。

四、履行期限、地点和方式

本合同自生效之日起至 2023 年 7 月 31 日止。在北京履行。

本合同履行的方式：按照本合同的规定执行。

五、验收方式

课题研究完成后，由乙方提交研究成果和技术资料，甲方验收合格后，向乙方支付相应的报酬。

六、报酬及其支付方式

1、本项目报酬（大写）总计为：肆拾捌万陆仟元整（￥ 486000.00），包括专家咨询费、会议费、调研差旅费、文本印刷费、办公耗材费、研究人员成本支出等。

2、支付方式：

（1）合同签订后，乙方按税率 3%开具增值税专用发票贰拾肆万叁仟元整（￥ 243000 元），甲方收到发票 1 个月内支付合同总额的 50%首款，即人民币金额（大写）：贰拾肆万叁仟元整；

（2）乙方根据研究内容要求，完成委托研究内容，并提交成果，经甲方验收合格后，乙方按税率3%开具增值税专用发票贰拾肆万叁仟元整（￥ 243000 元），甲方收到发票 1 个月内支付合同总额的 50%尾款，即人民币金额（大写）：贰拾肆万叁仟元整。

遇有特殊情况另议。

七、保密条款

（一）本技术服务项目为（☑不涉及国家秘密 □秘密 □机密 □绝密）级项目。

本合同文本为（☑不涉及国家秘密 □秘密 □机密 □绝密）级。

（二）甲乙双方应当按照国家保密法律法规的要求开展本技术服务项目的相关工作。

（三）乙方对本合同所列研究的内容、成果，以及甲方所提供的文件、资料和数据负有保密义务，并按保密规定妥善保管。未经甲方事先批准，乙方不得向任何第三方扩散、提供，不得用于本合同之外的其他目的，也不得私自复制、备份或留存。

（四）在本合同终止、解除、撤销、失去效力或无效等情形下，本第六条的条款依然有效。

八、技术成果的归属和分享：

加工数据及知识产权的使用权为双方共有，未经对方书面同意，任何一方不得以对方名义进行广告宣传和商业活动。未经甲方同意，乙方不得擅自将有关资料和数据提供给第三方。该数据成果及知识产权双方各占比 50%。

九、违约责任及合同解除

（一）违反本合同约定，违约方应当按照《中华人民共和国民法典》有关条款的规定承担违约责任。

（二）违反本合同第一至第八条约定，乙方应承担以下违约责任：退还合同款，承担违约金（合同款的 10%）。

（三）违反本合同第一至第八条约定，甲方应承担以下违约责任：承担乙方项目研究过程中垫付的所有支出。

（四）不可抗力

甲乙双方的任何一方由于不可抗力的原因逾期、不能或不能完全履行合同时，应及时向对方通知逾期、不能或不能完全履行的理由，在取得有关主管机关证明以后，允许延期履行、部分履行或者不履行合同，并根据情况可部分或全部免于承担违约责任。

	名称（或姓名）	中国原子能科学研究院		（签章）
委托方（甲方）	法定代表人	罗琦（签章）	委托代理人	（签章） 2021. 9.14
	联 系 人	刘微（签章）		
	住 所 （通信地址）	北京市房山区新镇		
	电 话	010-69357907	传 真	
	纳税人识别号	12100000400000309R		
	开户银行	工商银行北京二六六支行		
	帐 号	0200026609008800252	邮政编码	102413
研究开发方（乙方）	名称（或姓名）	中国计量大学		（签章）
	法定代表人	宋明顺（签章）	委托代理人	（签章） 2021.9.27
	联 系 人	秦来顺（签章）		
	住 所 （通信地址）	浙江省杭州市钱塘区学源街 258 号		
	电 话		传 真	
	纳税人识别号	12330000470009069B		
	开户银行	工行高新支行		
	帐 号	1202026209008932114	邮政编码	310018

浙江省基础公益研究计划项目批准通知

秦来顺同志：

根据浙江省自然科学基金相关管理规定，浙江省自然科

学基金委员会会同相关部门决定资助您申请的以下项目：

项目批准号	LY19E020003		依托单位	中国计量大学	
项目名称	红外光响应的多元金属氧化物光催化制氢材料的构建				
项目负责人	秦来顺		证件号码	14233019781023241X	
项目类别	省自然科学基金/一般项目		研究期限	2019 年 1 月 至 2021 年 12 月	
总经费（万元）	10.00	省财政资助经费（万元）	10.00	联合资助经费（万元）	0.00
序号	其他主要成员	证件号码	性别	单位名称	
1	陈达	510703198001180511	男	中国计量大学	
2	梁俊辉	410482198809265513	男	中国计量大学	
3	蒋力栋	330483199302250532	男	中国计量大学	
4	许振霞	412724199205062124	女	中国计量大学	
5					
6					

浙江省自然科学基金委员会办公室

2018 年 11 月 30 日

浙江省教育厅

浙教办函〔2019〕365号

浙江省教育厅办公室关于公布高等教育"十三五"人才培养项目建设名单的通知

各高等学校：

根据《关于开展高等教育"十三五"人才培养项目立项建设工作的通知》（浙教办函〔2019〕316号）文件精神，我厅组织开展了高等教育"十三五"人才培养项目申报工作，经高校申报、专家评审、厅长办公会议审议，认定省课堂教学创新校51所，省高校教师教学发展示范中心31个；立项建设省级产教融合示范基地（第二批人才培养类示范基地）25个，"十三五"第二批教学改革研究项目1082项，省级虚拟仿真实验教学项目585项（其中认定163项，立项建设422项），省产学合作协同育人项目240项，现将名单予以公布（详见附件）。

各高校应加大对各类人才培养项目的组织实施和经费支持，加强过程管理，深化教育教学改革，确保项目取得实效，不断提高人才培养质量。

附件：1.浙江省课堂教学创新校名单

2.浙江省高校教师教学发展示范中心名单

3.浙江省高等学校省级产教融合示范基地(第二批人才培养类示范基地）立项名单

4.浙江省高等教育"十三五"第二批教学改革研究项目

5.浙江省"十三五"高校虚拟仿真实验教学项目

6.浙江省"十三五"省级产学合作协同育人项目

浙江省教育厅办公室

2019 年 12 月 31 日

（此件公开发布）

浙江省高等教育"十三五"第二批教学改革研究项目

序号	项目编号	项目主持学校	项目名称	主持人	参与人
1	jg20190001	浙江大学	面向通识教育的逻辑教学改革	黄华新	金立、廖备水、徐慈华、胡龙彪
2	jg20190002	浙江大学	面向新时代的通识课程体系优化与质量保障机制研究	金娟琴	王英芳、姚立敏、胡家钰
3	jg20190003	浙江大学	大学生学业负担的研究：现状与对策	胡吉明	杨旸、王珹、刘有恃、张良
4	jg20190004	浙江大学	基于一流专业评估体系的探索与实践	谢桂红	谷辉、宓旭峰、毛水生、马英梅
5	jg20190005	浙江大学	应用贝叶斯定理对医学生进行临床思维培训的研究	王筝扬	方向前、赖东武、生金、徐文斌
6	jg20190006	浙江大学	线上线下混合教学效果影响因素探索	邢以群	施杰、周亚庆、张大亮、戚振江
7	jg20190007	浙江大学	土木水利与交通工程专业优化与新工科教改实践	罗尧治	吕朝锋、段元锋、许贤、路琳琳
8	jg20190008	浙江大学	电子信息类主干课程贯穿实验实践的教改研究	史治国	杨建义、陈积明、章献民、周金芳
9	jg20190009	浙江大学	面向自主可控核心关键安全技术，基于开源硬件的信息安全专业计算机系统类课程教学改革	任奎	韩劲松、卜凯、常瑞、申文博
10	jg20190010	浙江大学	即时反馈型客观结构化临床教考模式对提高实习生自信的实证研究	虞洪	杨瑾、沈波、沈吉良、俞图南
11	jg20190011	浙江大学	专业基础与前沿相结合的新工科机械制造课程体系改革与实践	汪延成	梅德庆
12	jg20190012	浙江大学	面向国家战略的"三位一体"多元化药学创新人才培养模式改革	范骁辉	王芳、张翔南、朱卡林、沈丽娟

193	jg20190193	中国计量大学	新工科视域下混合式教学研究——以电气专业核心课程为例	王颖	谢岳、蔡慧、胡晓静、郭倩
194	jg20190194	中国计量大学	基于高水平学生项目的新工科人才培养研究与实践	赵明岩	梁明轩、胡剑虹、王宗炼、林盛
195	jg20190195	中国计量大学	基于需求导向的智能感知方向课程体系构建	郭天太	谷伟、黄咏梅、刘维、郭世旭
196	jg20190196	中国计量大学	专业认证背景下《光学原理》教学改革	沈常宇	李晨霞、沈为民、楼俊、陈义
197	jg20190197	中国计量大学	材料计量与标准化特色创新人才的培养	秦来顺	唐高、卫国英、金杰、程芳
198	jg20190198	中国计量大学	基于 OBE 理念的材料类专业校外工程实践教学质量评价体系构建	唐高	卫国英、秦来顺、魏钦华、陈振华
199	jg20190199	中国计量大学	面向金课的高质量多数据源课程教学质量诊断模型构建与应用——以测量系统分析课程为例	项荣	洪涛、洪雪珍、曾其勇、张茂琛
200	jg20190200	中国计量大学	"一带一路"倡议下标准化教育国际化的机制和路径研究	宋明顺	余晓、刘欣、周立军、许丹
201	jg20190201	中国计量大学	新工科背景下大学生数学知识、能力、素质培养体系构建与实践	王义康	曹飞龙、张宝琳、刘学艺、吴龙树
202	jg20190202	中国计量大学	基于 OBE 理念的汉语国际教育研究生创新实践型课程改革——以《课堂观察与实践》课程为例	林雅	姚岚、周海英、彭飞、刘博宇
203	jg20190203	中国计量大学	工科高校艺术类通识课程改革与实践——以中国计量大学为例	魏殿林	徐向纮、徐莉莉、倪旭前、左冕
204	jg20190204	中国计量大学	对分课堂在"中国近现代史纲要"课程中的实践探索	周爽	兰婷、雷家军、时会永、刘鑫昊
205	jg20190205	中国计量大学	基于"互联网+"的"智慧体育"与传统体育俱乐部教学融合与创新	李文川	张英英、李水强、全先成、陈保磊
206	jg20190206	中国计量大学	循证视角下高校大学生竞赛评价研究	赵春鱼	孙卫红、李战国、张艳、杨璐
207	jg20190207	中国计量大学	地方院校创新创业教育体系研究与实践	金尚忠	张艳、汪俊斐、沈常宇、李佳

合同编号：

技术开发（委托）合同

项目名称：_____ 重稀土扩散 NdFeB 基体研究 _____

委托方（甲方）：_____ 浙江鑫盛永磁科技有限公司 _____

受托方（乙方）：_____ 中国计量大学 _____

_____

签订时间：_____ 2022.3.15 _____

签订地点：_____ 中国计量大学 _____

有效期限：_____ 2022.3.15 - 2023.3.15 _____

中华人民共和国科学技术部印制

填 写 说 明

一、本合同为中华人民共和国科学技术部印制的技术开发（委托）合同示范文本，各技术合同登记机构可推介技术合同当事人参照使用。

二、本合同书适用于一方当事人委托另一方当事人进行新技术、新产品、新工艺、新材料或者新品种及其系统的研究开发所订立的技术开发合同。

三、签约一方为多个当事人的，可按各自在合同关系中的作用等，在"委托方"、"受托方"项下（增页）分别排列为共同委托人或共同受托人。

四、本合同书未尽事项，可由当事人附页另行约定，并可作为本合同的组成部分。

五、当事人使用本合同书时约定无需填写的条款，应在该条款处注明"无"等字样。

技术开发（委托）合同

委托方（甲方）：__浙江鑫盛永磁科技有限公司__

住　所　地：__浙江省湖州市安吉天子湖镇南店村吟诗路 1988 号__

法定代表人：__鲍金胜__

项目联系人：__张伟华__

联系方式：__13355826593__

通讯地址：__浙江省湖州市安吉天子湖镇南店村吟诗路 1988 号__

电　话：__0572 5907089__　　　传　真：__0572 5907666__

电子信箱：__admin@xs-magnetics.com__

受托方（乙方）：__中国计量大学__

住　所　地：__浙江省杭州市下沙高教园区学源街 258 号__

法定代表人：__徐江荣__

项目联系人：__秦来顺__

联系方式

通讯地址：__浙江省杭州市下沙高教园区学源街 258 号__

电　话：__0571－86875607__　　传　真：__0571－86875607__

电子信箱：__qinlaishun@cjlu.edu.cn__

本合同甲方委托乙方研究开发　__重稀土扩散 NdFeB 基体研究__　项目，并支付研究开发经费和报酬，乙方接受委托并进行此项研究开发工作。双方经过平等协商，在真实、充分地表达各自意愿的基础上，根据《中华人民共和国合同法》的规定，达成如下协议，并由双方共同恪守。

第一条　本合同研究开发项目的要求如下：

1. 技术目标：__探究 NdFeB 基体化学成分对重稀土晶界扩散效率的影响及机理，提高重稀土晶界扩散效率，降低高矫顽力 NdFeB 对重稀土元素的需求量。__
2. 技术内容：__合作开发并优化重稀土（Tb 或 Dy）元素渗透新工艺，明确 NdFeB 基体成分与重稀土晶界扩散效率以及磁体性能之间的相互关系。__
3. 技术方法和路线：__采用蒸汽热处理晶界扩散 Tb 或 Dy 工艺开展研究。__

第二条　乙方应在本合同生效后____30____日内向甲方提交研究开发计划。研究开发计划应包括以下主要内容：

1. __研发方案__　　　　　　　　　　　　　　　　　　　　　　　；
2. __研究进度__　　　　　　　　　　　　　　　　　　　　　　　；

第三条　乙方应按下列进度完成研究开发工作：

1.　**2022.3-2022.5，配合甲方进行市场调研，开展相关文献的调研和专利检索，并在前期研究基础和工厂的生产需求上提出研究开发计划；**

2.　**2022.6-2022.9，开展重稀土（Tb 或 Dy）元素渗透新工艺的开发与优化；**

3.　**2022.10-2023.3，开展 NdFeB 基体化学成分对重稀土晶界扩散效率的影响及机理的研究，开发满足客户要求的低重稀土高矫顽力的烧结 NdFeB 磁体产品，并做研究总结报告。**

第四条　甲方应向乙方提供的技术资料及协作事项如下：

1. 技术资料清单：　　**重稀土（Tb 或 Dy）元素渗透现阶段工艺**　　。
2. 提供时间和方式：　　**双方协商**　　。
3. 其他协作事项：　**为乙方开展项目研究提供相关试验场地和设备**　。
本合同履行完毕后，上述技术资料按以下方式处理：　　**双方协商处理**　　。

第五条　甲方应按以下方式支付研究开发经费和报酬：

1. 研究开发经费和报酬总额为　　**100 万元**　　　　　　　。
其中：（1）**主要用于材料费、检验费、技术劳务费、科研活动费等**　　；
　　　　（2）　　　　　　　　　　　　　　　　　　　　　。
2. 研究开发经费由甲方　　**分期**　　　　（一次、分期或提成）支付乙方。具体支付方式和时间如下：

（1）　**第一笔：银行转账支付 40 万，2022 年 5 月 15 日前资金到账**
（2）　**第二笔：银行转账支付 30 万，2022 年 9 月 15 日前资金到账**
（3）　**第三笔：银行转账支付 30 万，2022 年 12 月 15 日前资金到账**

乙方开户银行名称、地址和帐号为：

开户银行：　　**工行杭州市高新技术开发区支行**　　　
地　　址：　　**浙江省杭州市下沙高教园区学源街 258 号**　　

帐　　号：　**12020262090008932114**　

3.双方确定，甲方以实施研究开发成果所产生的利益提成支付乙方的研究开发经费和报酬的，乙方有权以　　　　／　　　　　的方式查阅甲方有关的会计帐目。

第六条　本合同的研究开发经费由乙方以　　**符合所在单位对研究开发经费的管理文件**　的方式使用。甲方有权以　**交流**　的方式检查乙方进行研究开发工作和使用研究开发经费的情况，但不得妨碍乙方的正常工作。

第七条　本合同的变更必须由双方协商一致，并以书面形式确定。但有下列情形之一的，一方可以向另一方提出变更合同权利与义务的请求，另一方应当在　　**15**　　日内予以答复；逾期未予答复的，视为同意。

第八条　未经甲方同意，乙方不得将本合同项目部分或全部研究开发工作转让第三人承担。但有下列情况之一的，乙方可以不经甲方同意，将本合同项目部分或全部研究开发工作转让第三人承担：

1.　**材料测试及分析**　　　　　　　。

乙方可以转让研究开发工作的具体内容包括：__材料测试及分析__。

第九条 在本合同履行中，因出现在现有技术水平和条件下难以克服的技术困难，导致研究开发失败或部分失败，并造成一方或双方损失的，双方按如下约定承担风险损失：__双方协商解决__。

双方确定，本合同项目的技术风险按_____双方协商_____的方式认定。认定技术风险的基本内容应当包括技术风险的存在、范围、程度及损失大小等。认定技术风险的基本条件是：

1. 本合同项目在现有技术水平条件下具有足够的难度；
2. 乙方在主观上无过错且经认定研究开发失败为合理的失败。

一方发现技术风险存在并有可能致使研究开发失败或部分失败的情形时，应当在__15__日内通知另一方并采取适当措施减少损失。逾期未通知并未采取适当措施而致使损失扩大的，应当就扩大的损失承担赔偿责任。

第十条 在本合同履行中，因作为研究开发的技术已经由他人公开（包括以专利权方式公开），一方应在__15__日内通知另一方解除合同。逾期未通知并致使另一方产生损失的，另一方有权要求予以赔偿。

第十一条 双方确定因履行本合同应遵守的保密义务如下：

甲方：
1. 保密内容（包括技术信息和经营信息）：__重稀土（Tb 或 Dy）元素渗透工艺__。
2. 涉密人员范围：__甲方项目组成员__。
3. 保密期限：__2022.3-2023.3__。
4. 泄密责任：__双方协商确定__。

乙方：
1. 保密内容（包括技术信息和经营信息）：__重稀土（Tb 或 Dy）元素渗透工艺__。
2. 涉密人员范围：__乙方项目组成员__。
3. 保密期限：__2022.3-2023.3__。
4. 泄密责任：__双方协商确定__。

第十二条 乙方应当按以下方式向甲方交付研究开发成果：
1. 研究开发成果交付的形式及数量：__研究报告一份（内含：开发的重稀土（Tb 或 Dy）元素渗透工艺）__。
2. 研究开发成果交付的时间及地点：__2023.3，浙江鑫盛永磁科技有限公司__。

第十三条 双方确定，按以下标准及方法对乙方完成的研究开发成果进行验收：__研究开发所完成的技术成果，由甲方验收并出具验收证明__。

第十四条 乙方应当保证其交付给甲方的研究开发成果不侵犯任何第三人的合法权益。如发生第三人指控甲方实施的技术侵权的，乙方应当__向甲方提供相应的材料，以证明研究开发结果具有自主创新性__。

第十五条 双方确定，因履行本合同所产生的研究开发成果及其相关知识产权权利归属，按下列第__1__种方式处理：
1. ____双____（甲、乙、双）方享有申请专利的权利。

专利权取得后的使用和有关利益分配方式如下：__由双方共同使用__。

 2. 按技术秘密方式处理。有关使用和转让的权利归属及由此产生的利益按以下约定处理：

 （1）技术秘密的使用权：__双方协商__

 （2）技术秘密的转让权：__双方协商__

 （3）相关利益的分配办法：__双方协商__

双方对本合同有关的知识产权权利归属特别约定如下：__双方共同使用__。

 第十六条 乙方不得在向甲方交付研究开发成果之前，自行将研究开发成果转让给第三人。

 第十七条 乙方完成本合同项目的研究开发人员享有在有关技术成果文件上写明技术成果完成者的权利和取得有关荣誉证书、奖励的权利。

 第十八条 乙方利用研究开发经费所购置与研究开发工作有关的设备、器材、资料等财产，归____乙____（甲、乙、双）方所有。

 第十九条 双方确定，乙方应在向甲方交付研究开发成果后，根据甲方的请求，为甲方指定的人员提供技术指导和培训，或提供与使用该研究开发成果相关的技术服务。

 1. 技术服务和指导内容：__重稀土（Tb 或 Dy）元素渗透工艺__。

 2. 地点和方式：__浙江鑫盛永磁科技有限公司，现场指导__
 _____。

 3. 费用及支付方式：__另行商定__
 _____。

 第二十条 双方确定：任何一方违反本合同约定，造成研究开发工作停滞、延误或失败的，按以下约定承担违约责任：

 1. _____方违反本合同第____条约定，应当_____无_____
 _____（支付违约金或损失赔偿额的计算方法）。

 2. _____方违反本合同第____条约定，应当_____无_____
 _____（支付违约金或损失赔偿额的计算方法）。

 3. _____方违反本合同第____条约定，应当_____无_____
 _____（支付违约金或损失赔偿额的计算方法）。

 4. _____方违反本合同第____条约定，应当_____无_____
 _____（支付违约金或损失赔偿额的计算方法）。

 5. _____方违反本合同第____条约定，应当_____无_____
 _____（支付违约金或损失赔偿额的计算方法）。

 6. _____方违反本合同第____条约定，应当_____无_____
 _____（支付违约金或损失

赔偿额的计算方法)。

第二十一条　双方确定，甲方有权利用乙方按照本合同约定提供的研究开发成果，进行后续改进。由此产生的具有实质性或创造性技术进步特征的新的技术成果及其权利归属，由 甲 （甲、乙、双）方享有。具体相关利益的分配办法如下： 无 。

乙方有权在完成本合同约定的研究开发工作后，利用该项研究开发成果进行后续改进。由此产生的具有实质性或创造性技术进步特征的新的技术成果，归 乙 （甲、乙、双）方所有。具体相关利益的分配办法如下： 无 。

第二十二条　双方确定，在本合同有效期内，甲方指定 张伟华 为甲方项目联系人，乙方指定 秦来顺 为乙方项目联系人。项目联系人承担以下责任：
1. 负责项目的总体实施及双方的沟通交流 ；
2. 双方人员安排 ；
3. 双方工作安排 。
一方变更项目联系人的，应当及时以书面形式通知另一方。未及时通知并影响本合同履行或造成损失的，应承担相应的责任。

第二十三条　双方确定，出现下列情形，致使本合同的履行成为不必要或不可能的，一方可以通知另一方解除本合同；
1. 因发生不可抗力或技术风险；
2. ；
3. 。

第二十四条　双方因履行本合同而发生的争议，应协商、调解解决。协商、调解不成的，确定按以下第 1 种方式处理：
1. 提交 杭州市 仲裁委员会仲裁；
2. 依法向人民法院起诉。

第二十五条　双方确定：本合同及相关附件中所涉及的有关名词和技术术语，其定义和解释如下：
1. 无 ；
2. ；
3. 。

第二十六条　与履行本合同有关的下列技术文件，经双方以 共同协商 方式确认后，为本合同的组成部分：
1. 技术背景资料： ；
2. 可行性论证报告： ；
3. 技术评价报告： ；
4. 技术标准和规范： ；
5. 原始设计和工艺文件： ；
6.其他： 。
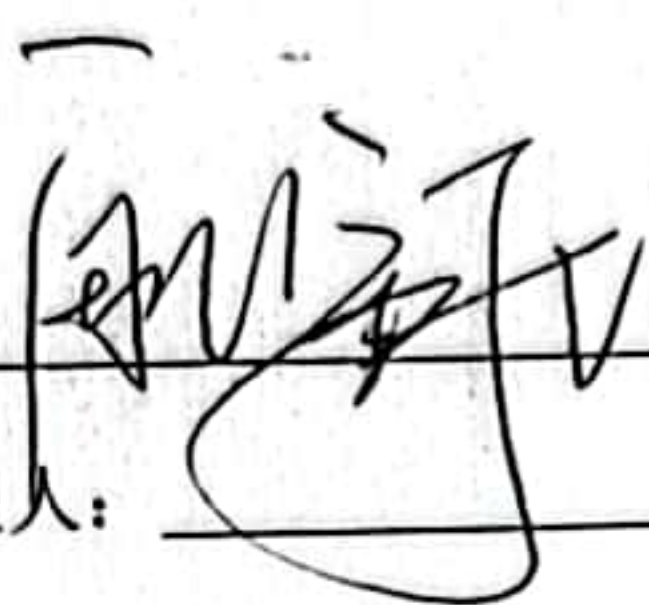
第二十七条　双方约定本合同其他相关事项为：＿＿＿无＿＿＿。

第二十八条　本合同一式＿＿＿七＿＿＿份，具有同等法律效力。

第二十九条　本合同经双方签字盖章后生效。

甲方：＿＿＿＿＿＿＿＿＿＿＿＿＿＿＿＿＿＿＿＿＿＿＿（盖章）

法定代表人/委托代理人：＿＿＿＿＿＿＿＿＿＿＿＿＿＿（签名）

年　　　月　　　日

乙方：＿＿＿＿＿中国计量大学＿＿＿＿＿＿＿＿＿＿＿（盖章）
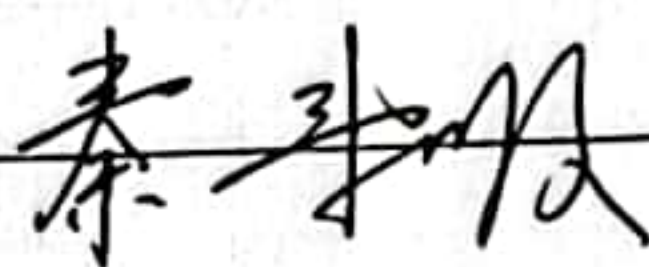
法定代表人/委托代理人：＿＿＿＿＿＿＿＿＿＿＿＿＿＿（签名）

2022年　3月　8日
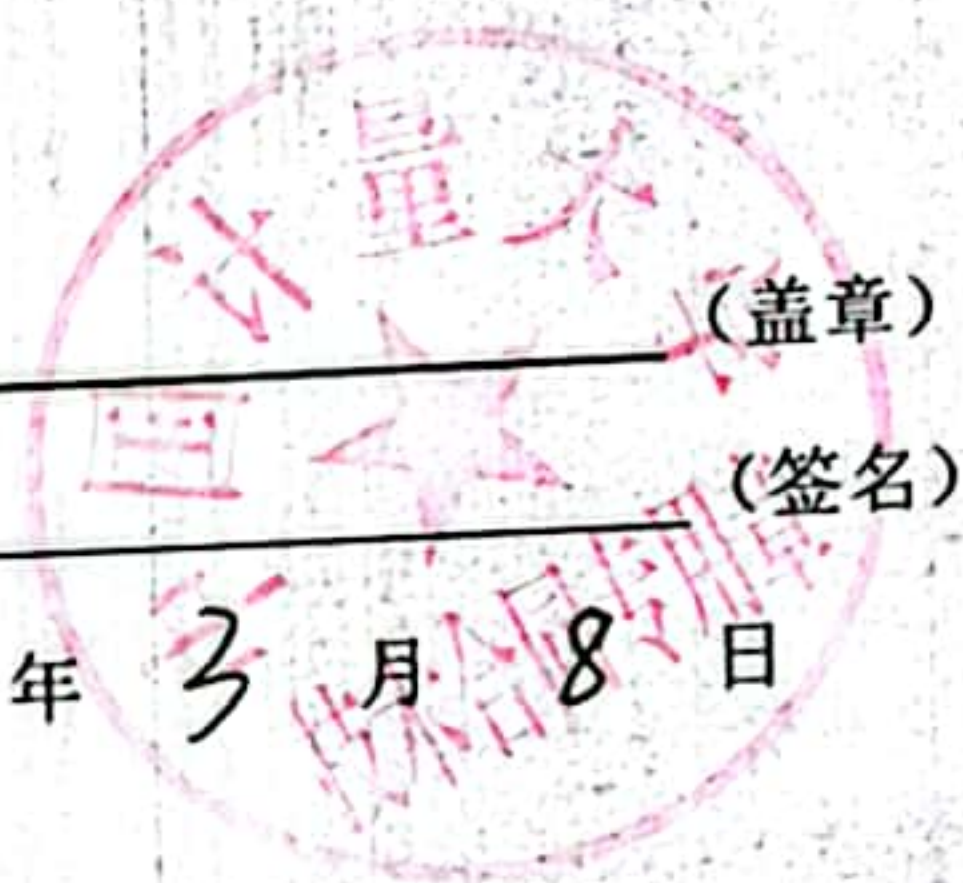
标准样品概论

INTRODUCTION TO REFERENCE MATERIALS

田世宏　陈洪俊　高建忠　俞晓平　王丽敏　胡晓燕 等◎编著

中国标准出版社

编 委 会

（按姓氏笔画排序）

标准样品概论

INTRODUCTION TO REFERENCE MATERIALS

为加深读者对各章内容的理解，各章最后设置有二维码，扫码后您可观看学习约 10 分钟的视频，视频内容为各章重要知识点、拓展知识或典型应用案例。